Applications and Characterization of a Confocal Scanning Laser MACROscope/Microscope

by

Alfonso Carlos Ribes

A thesis
presented to the University of Waterloo
in fulfillment of the
thesis requirement for the degree of

Doctor of Philosophy

in

Physics

Waterloo, Ontario, Canada, 1997

© Alfonso Carlos Ribes 1997

National Library of Canada
Bibliothèque nationale du Canada

Acquisitions and Bibliographic Services
Acquisitions et services bibliographiques

395 Wellington Street
Ottawa ON K1A 0N4
Canada

395, rue Wellington
Ottawa ON K1A 0N4
Canada

Your file Votre référence

Our file Notre référence

The author has granted a non-exclusive licence allowing the National Library of Canada to reproduce, loan, distribute or sell copies of this thesis in microform, paper or electronic formats.

L'auteur a accordé une licence non exclusive permettant à la Bibliothèque nationale du Canada de reproduire, prêter, distribuer ou vendre des copies de cette thèse sous la forme de microfiche/film, de reproduction sur papier ou sur format électronique.

The author retains ownership of the copyright in this thesis. Neither the thesis nor substantial extracts from it may be printed or otherwise reproduced without the author's permission.

L'auteur conserve la propriété du droit d'auteur qui protège cette thèse. Ni la thèse ni des extraits substantiels de celle-ci ne doivent être imprimés ou autrement reproduits sans son autorisation.

0-612-30638-0

Canada

The University of Waterloo requires the signatures of all persons using or photocopying this thesis. Please sign below, and give address and date.

ABSTRACT

APPLICATIONS AND CHARACTERIZATION OF A CONFOCAL SCANNING LASER MACROSCOPE/MICROSCOPE

Confocal scanning laser microscopes are typically limited to small fields of view less than 5 x 5 mm in size. Scanning stage microscopes can scan very large areas (many centimeters) but are unfortunately slow. An image can be acquired in seconds on a scanning beam instrument while it can take minutes on a scanning stage microscope. The confocal scanning laser MACROscope was designed previously by the University of Waterloo's Confocal Microscopy Group (UW-CMG) to combine the large scanning area capability of scanning stage microscopes with the fast scanning rates of scanning beam instruments. The prototype MACROscope, described in this thesis, provides 5 and 200 μm lateral and axial resolution, respectively, using reflected light. It can generate reflected-light, photoluminescence, and optical beam induced current (OBIC) images of areas up to 7.5 x 7.5 cm in less than 10 s. When used in combination with a conventional scanning beam instrument, submicron resolutions are possible and the field of view can be as small as 25 x 25 μm representing a zoom factor of 3000.

A brief introduction to optics and confocal microscopy is given. The MACROscope as well as the UW-CMG confocal microscope are characterized with respect to efficiency, lateral resolution, axial resolution, and limitations.

Imaging applications are illustrated for two semiconductor materials: solar cells and porous silicon. Various microscopic and macroscopic, confocal and non-confocal, reflected-light, photoluminescence and OBIC images of solar cells, porous silicon materials, and porous silicon devices are shown. Brief introductions to both solar cells and porous silicon are given as well as a comparison between OBIC and electron beam induced current.

A relay lens consisting of a unitary telescope made with two achromats is examined on CODE V, a lens design and analysis program. This relay lens is known to cause problems on the UW-CMG confocal microscope and it is compared with an all-reflecting telescope made with off-axis parabolic mirrors. CODE V is also used to examine a detector mirror, a 30X all-reflecting beam expander, and an inexpensive ultraviolet objective.

A design for a proposed fully integrated, single-instrument confocal scanning laser MACROscope-Microscope is presented. The design is based on years of experience working with the MACROscope and the UW-CMG confocal microscope as well as ideas adopted from commercial confocal microscopes. The MACROscope-Microscope has proven to be a versatile, efficient instrument combining scanning beam and scanning stage capabilities and has been demonstrated to be useful in imaging a wide range of specimens.

Several new contributions were made to scanning microscopy:

1) Construction of a prototype MACROscope.
2) Subsequent development and improvement of the MACROscope.
3) Experimental characterization of the MACROscope and cslm with respect to throughput, lateral resolution, and axial resolution including relative intensity measurements.
4) Experimental evidence and analysis of non-telecentric operation.
5) Demonstration of two imaging applications for the MACROscope: solar cells and porous silicon.
6) Evidence of lateral etching and enhanced photoluminescence in porous silicon specimens was shown.
7) Characterization of a porous silicon device and solar cell with reflected light, photoluminescence, and OBIC.
8) Analysis of the current unitary telescope configuration as well as a reflecting telescope, and an eyepiece telescope with CODE V. The eyepiece optical relay is especially innovative. Experimental evidence of unitary telescope aberrations was also shown.
9) Analysis of a detector mirror and a UV singlet, for use in imaging, with CODE V.
10) Several suggestions to develop a fully-integrated cslM/m were made.

ACKNOWLEDGMENTS

In many ways this thesis has been a collaborative effort. I could not have completed many experiments or fully understood many of the concepts in this thesis without the help and support from my colleagues.

I would first like to thank Ted Dixon for allowing me to join the University of Waterloo's Confocal Microscopy Group (UW-CMG) and for putting me to work on the MACROscope. Ted provided a very active research environment where I learned from a wide variety of topics like optics, semiconductors, electronics, and biology. I would also like to thank Ted for sending me to several conferences especially the 1997 Confocal Microscopy Conference in Buffalo, New York which turned out to be the most interesting one.
I would like to thank my committee members: Don Brodie, Melanie Campbell, Ted Dixon and Jim Webb for their guidance and suggestions and also P.C. Cheng for agreeing to be my external examiner.

Savvas Damaskinos has been a constant source of help and enthusiasm, and has taken an interest in any and all experiments I have performed. Savvas has shown me that many innovations come about by trying, and trying again, and then trying the unexpected or the unconventional. I have learned from him to examine everything and not be afraid of change. Thanks to John Bowron for advice and guidance early on in my thesis.

Thanks to Gary Carver for bringing the first porous silicon specimen.
I would like to thank Phillippe Fauchet's group at the University of Rochester for collaborating with UW-CMG. A special thanks to Sid Duttagupta for putting extra effort in manufacturing many porous silicon materials and devices specifically suited for imaging on the MACROscope and the confocal microscope.

Thanks to Henry Tiedje for doing all of the I-V and spectral response measurements in addition to many instructive conversations on solar cells and electronics.

Thanks to Paul Dube for help with the spectrally resolved MACROscope. Thanks to Kevin Ellis for writing the piezo calibration program and helping with 3-D imagery.
Thanks to Rob Roorda and James Jonkman for the LSL specification measurements and many discussions on optics.
Thanks to my proof readers: Rob Roorda, Savvas Damaskinos, Henry Tiedje, Denise King, and James Jonkman.

Finally thanks to Lisa Miolo for help with the typing and printing of this thesis.

TABLE OF CONTENTS

Abstract iv
Acknowledgments vi
List of Tables xi
List of Figures xii
Abbreviations xvii

1.0 Introduction 1
1.1 Motivation for Research 1
1.2 Contributions: Past and Present 3
1.2.1 Past Contribution 4
1.2.2 Present - UW-CMG 6
1.3 The MACROscope: Just Another cslm? 7
1.4 Thesis Overview 9

2.0 Introduction to Confocal Microscopy 13
2.1 Optics Review 13
2.2 Confocal Microscopy 17
2.2.1 Confocal Optics 18
2.2.2 Lateral and Axial Resolution 20
2.2.3 Confocal Slicing 24
2.3 The Confocal Microscope System 28
2.3.1 Light Sources 29
2.3.2 Beam Splitter Assembly 31
2.3.3 x-y Scan Arm 33
2.3.4 Microscope Objective and Specimen Stage 37
2.3.5 Detector Arm 39
2.3.6 Computer and Electronics 41
2.4 Summary and Discussion 42

3.0 Characterization of the Confocal Scanning Laser Microscope and MACROscope 45
3.1 The cslm 46
3.1.1 cslm Component Breakdown 46
3.1.1.1 Laser Source Arm 48
3.1.1.2 Scanning Mirrors and Telescopes 50
3.1.1.3 Microscope Objectives 50
3.1.1.4 Detector Arm 52
3.1.2 cslm Characterization 58
3.1.2.1 cslm Collection Efficiency 59
3.1.2.2 cslm Lateral Resolution 60

3.1.2.3 cslm Axial Resolution 63
3.1.2.4 The Effects of the Unitary Telescopes 79
3.2 The MACROscope 85
3.2.1 The MACROscope Components 88
3.2.2 MACROscope Efficiency 91
3.2.3 MACROscope Lateral Resolution 93
3.2.4 MACROscope Axial Resolution 95
3.2.5 MACROscope Telecentricity 98
3.3 Spectral Characterization on the MACROscope 103
3.4 Summary and Discussion 106

4.0 MACROscope/cslm Applications and Imaging Results 110
4.1 Solar Cells 111
4.1.1 Imaging Results 117
4.1.2 OBIC Limitations 128
4.1.3 Comparison of OBIC with EBIC 131
4.2 Porous Silicon 135
4.2.1 PSi Materials 141
4.2.2 PSi Devices 156
4.3 Summary and Discussion 165

5.0 Quantitative Lens Analysis and Design With Code V 170
5.1 Seidel Aberrations 171
5.1.1 Paraxial Image - The Airy Disk 172
5.1.2 Spherical Aberration 173
5.1.3 Coma 175
5.1.4 Astigmatism and Petzval Field Curvature 176
5.1.5 Distortion 180
5.2 Chromatic Aberrations 181
5.3 Aberrations in Lens Systems 183
5.4 CODE V Results Part I—Analysis and Design 184
5.4.1 Achromat 187
5.4.2 Reflecting Detector Mirror 192
5.4.3 30X Reflecting Beam Expander 198
5.5 CODE V Results Part II—Telescope and UV Objective 200
5.5.1 Refracting and Reflecting Telescopes 201
5.5.2 Low Cost UV Objective 215
5.6 The Erfle Eyepiece Telescope 223
5.7 Summary and Discussion 227

6.0 The Fully Integrated Confocal Scanning Laser MACROscope/Microscope 231
6.1 Commercial Confocal Microscopes 233
6.2 Possible Improvements for the MACROscope and cslm 238

6.2.1 Laser Arm 238
6.2.2 x-y Scanner 239
6.2.3 Objective and Specimen Stage 243
6.2.4 Detector Arm 245
6.3 The cslM/m 250
6.4 Summary and Discussion 254

7.0 Discussion, Personal Contributions and Recommendations 256
7.1 Discussion, Conclusions and Personal Contributions 256
7.1.1 Chapter 2 - Introduction to Confocal Microscopy 256
7.1.2 Chapter 3 - Characterization of the Confocal Scanning Laser Microscope and MACROscope 257
7.1.3 Chapter 4 - MACROscope/cslm Applications and Imaging Results 259
7.1.4 Chapter 5 - Quantitative Lens Analysis with CODE V 261
7.1.5 Chapter 6 - The Fully Integrated Confocal Scanning Laser MACROscope-Microscope 262
7.2 Recommendations 264
7.2.1 Laser Arm 265
7.2.2 Scanning Arm 265
7.2.3 Microscope Objective, Relay Optics, and Specimen Stage 266
7.2.4 Detector Arm 267
7.2.5 Top 5 Recommendations 267

Appendix 1 Using a Wide-Field Microscope as a cslm 269
Appendix 2 Infinity-Corrected Objectives 271
Appendix 3 Effective NA 273
Appendix 4 Estimate of Quantum Efficiency 274
Appendix 5 Intensity versus NA 276
Appendix 6 Lens Data from CODE V 277

LIST OF TABLES

3.1	UW-CMG lasers	49
3.2	Specifications for UW-CMG microscope objective	52
3.3	Specifications for the R292 and R2228 Hamamatsu PMT tubes	54
3.4	Specifications for Standford current-to-voltage preamplifier	58
3.5	Effective NAs for the 0.42 and 0.14 underfilled objectives	61
3.6	Axial resolution vs. pinhole for the 0.42 NA objective	72
3.7	Axial resolution vs. pinhole for the 0.7 NA objective	74
3.8	Axial resolution vs. pinhole for the 0.9 NA objective	75
3.9	Experimental and theoretical FWHM values for the 0.42, 0.7, and 0.9 NA objectives	76
3.10	Axial resolution vs. pinhole with spatial filtering	77
3.11	Axial resolution vs. pinhole without spatial filtering	77
3.12	FWHM for 0.42, 0.7 and 0.9 NA objectives using the no detector lens setup	78
3.13	Comparison between an SSM, a cslm, and the MACROscope	85
3.14	Specifications for the LSL	90
3.15	MACROscope axial resolution and intensity for reflective detector arm at 488 nm	95
3.16	MACROscope axial resolution and intensity for reflective detector arm at 647 nm	95
3.17	MACROscope axial resolution and intensity for refractive detector arm	98
3.18	MACROscope spectral resolution	104
5.1	Primary aberrations as a function of aperture and field size	183
5.2	Third order transverse aberrations for the refracting telescope	202
5.3	Comparison of reflecting and refracting telescopes using 546.1 nm light at best focus	209
5.4	Comparison of encircled energy diameters for 30 and 90° off-axis parabolic mirror telescopes	209
5.5	Encircled energies for UV singlets	222
5.6	Third order transverse aberrations for the Erfle eyepiece telescope	224
5.7	Encircled energy diameters for the Erfle eyepiece telescope using 10 and 15 mm diameter entrance pupils	226
5.8	Encircled energy diameters for the Erfle eyepiece telescope using a 20 mm diameter entrance pupils	226
6.1	Comparison of R292, R228, R928 Hamamatsu PMTs	249

LIST OF FIGURES

1.1	Leica INM-200	3
1.2	Sawyer's and Hughes' laser scanners	5
1.3	Relationship between NA, focal length, beam diameter, and scan angle	8
2.1	Thin lenses	14
2.2	The compound microscope	15
2.3	Minsky's confocal microscope	17
2.4	The confocal effect with a non-infinity-corrected objective	18
2.5	The confocal effect with an infinity-corrected objective	19
2.6	Definition of numerical aperture	21
2.7	Crossections of a diffraction spot	23
2.8	Wide field vs. scanning microscopy	24
2.9	Example of scanning microscopy	25
2.10	Confocal slicing example test object	26
2.11	Confocal slicing example	27
2.12	Block diagram of cslm	28
2.13	Types of light sources	29
2.14	Beam splitter assembly	31
2.15	Telecentric operation	33
2.16	Unitary telescope	34
2.17	x-y scanner with telescope	35
2.18	x-y scanner with two closely spaced mirrors	36
2.19	x-y scanner paddle arrangement	36
2.20	Single mirror x-y scanner	37
2.21	The specimen stage and objective lens	38
2.22	Two possible arrangements for detector arms	40
2.23	The Leica confocal microscope	41
3.1	The UW-CMG cslm	47
3.2	Schematic diagram of a typical microscope objective	51
3.3	PL image of 550 nm longpass filter	53
3.4	Spectral response curves for the R292 and R2228 Hamamatsu PMT tubes	55
3.5	PMT linearity graphs	57
3.6	cslm collection efficiency	60
3.7	RL image of a resolution target taken with the 0.9 NA objective	61
3.8	RL image of a resolution target taken with the 0.42 and 0.14 NA objectives	62
3.9	Axial resolution measurement setup for the cslm	63
3.10	cslm z-scan	65
3.11	Michelson interferometer on the cslm	66
3.12	Image from Michelson interferometer	67

3.13 Diagram showing how x-scan sampling works 69
3.14 z-displacement vs. piezo voltage for displacements < 10 μm 70
3.15 z-displacement vs. piezo voltage for displacements > 10 μm 71
3.16 Intensity and FWHM vs. pinhole for the 0.42 NA objective 72
3.17 Intensity and FWHM vs. pinhole for the 0.7 NA objective 74
3.18 Intensity and FWHM vs. pinhole for the 0.9 NA objective 75
3.19 Intensity distribution for a flat mirror image 80
3.20 False colour mirror imaging with a 0.7 NA objective with different pinholes 81
3.21 Confocal slicing of a flat mirror illustrating off-axis aberrations on the cslm 82
3.22 The effect of astigmatism on the confocal image of a flat mirror 84
3.23 Intermediate form of the MACROscope 86
3.24 The confocal scanning laser MACROscope 87
3.25 Mirror detector arm configuration 88
3.26 The telecentric f-theta laser scan lens 89
3.27 The effect of chromatic aberrations on the LSL 90
3.28 Efficiency for MACROscope illumination and collection arm 92
3.29 MACROscope lateral resolution images 94
3.30 MACROscope axial resolution and intensity graphs 96
3.31 The non-telecentric effect 99
3.32 Non-telecentric effect images using the reflective detector arm 100
3.33 Non-telecentric effect images using the refractive detector arm 102
3.34 The spectrally-resolved MACROscope 103
3.35 Lambda-scan of the 647 nm laser line 105
3.36 Diagram of halogen light source 106

4.1 Solar cell band diagram 111
4.2 Minority carrier collection probability 112
4.3 Solar cell IV-curve 113
4.4 Solar cell equivalent circuit 115
4.5 Description of OBIC imaging 116
4.6 Four $CdS/CuInSe_2$ thin film solar cells 118
4.7 MACROscope images of a polycrystalline silicon solar cell 119
4.8 Cslm images of a polycrystalline silicon solar cell 121
4.9 Schematic diagram of a $CdS/CuInSe_2$ thin film solar cell 122
4.10 Images of a $CdZnS/CuInSe_2$ thin film solar cell 123
4.11 Photocurrent profiles of a $CdZnS/CuInSe_2$ thin film solar cell 124
4.12 Spectral response for the cell in Fig. 4.10 125
4.13 I-V plot for the cell in Fig. 4.10 127
4.14 Image of 'ringing' effect 129
4.15 Image of an amorphous silicon solar cell 129
4.16 OBIC vs. laser power 130
4.17 Schematic diagram illustrating EBIC 131
4.18 Carrier generation by a focused electron beam 132
4.19 Two commonly used configurations in OBIC and EBIC imaging 133

4.20 PSi etching setup 136
4.21 PSi quantum confinement 137
4.22 PSi pore formation process 139
4.23 PSi quantum wires 140
4.24 MACROscope images of an early LEPSi specimen 142
4.25 Confocal images of LEPSi islands 143
4.26 MACROscope images of LEPSi squares 145
4.27 MACROscope images of LEPSi lines 146
4.28 Cslm images of 'gray back' LEPSi lines 148
4.29 Cslm images of 'blue back' LEPSi lines 150
4.30 PL images of round LEPSi specimen 152
4.31 Spectral data for Fig. 4.30 specimen 153
4.32 Clear evidence of bleaching 154
4.33 Evidence of photon induced passivation 155
4.34 Gold-coated PSi solar cell 157
4.35 Polycrystalline PSi solar cell 158
4.36 Spectral response for Fig. 4.35 cell 159
4.37 I-V curve for Fig. 4.35 cell 160
4.38 Structure of 'Dot' devices 161
4.39 Cslm images of 'Dot' devices 163
4.40 OBIC image of 5 μm LEPSi devices 164

5.1 Diagram of coordinate system 171
5.2 The Airy disk 173
5.3 Spherical aberration 174
5.4 The effect of spherical aberration on the Airy disk 174
5.5 Coma 175
5.6 The coma patch 176
5.7 The effect of coma on the Airy disk 176
5.8 Astigmatism 177
5.9 The effect of astigmatism at the image screen 177
5.10 Diagram of astigmatic and Petzval curvature of field 178
5.11 Astigmatic and Petzval radius of curvature 179
5.12 The effect of astigmatism on the Airy disk 180
5.13 Distortion 181
5.14 Axial chromatic aberration 181
5.15 Lateral colour aberration 182
5.16 Construction of an achromat 184
5.17 Schematic diagram of a thick lens 185
5.18 Entrance and exit pupils illustrated 186
5.19 LAO138 achromat as defined by CODE V 187
5.20 LAO138 achromat as drawn by CODE V 189
5.21 PSFs for the LAO138 achromat 190
5.22 Encircled energy vs. diameter for the LAO138 achromat 190

5.23 Encircled energy for the Airy disk 191
5.24 CODE V field plot for the LAO138 achromat 191
5.25 Diagram of an off-axis parabolic mirror 193
5.26 Parabola with various defining quantities 194
5.27 Decenter-tilt equivalence for spherical mirrors 195
5.28 Enc. energy plot for detector mirror with an 18 mm diameter entrance pupil 196
5.29 MTF for detector mirror with an 18 mm diameter entrance pupil 197
5.30 Encircled energy plot for detector mirror with a 7 mm diameter entrance pupil 198
5.31 30X all-reflecting beam expander 199
5.32 PSFs for the 30X all-reflecting beam expander 200
5.33 Refracting telescope 201
5.34 Field plot for the refracting telescope 203
5.35 Construction of the reflecting telescope 203
5.36 Reflecting telescope 204
5.37 Refractive equivalent of the off-axis parabolic reflecting telescope 204
5.38 Field plot for the reflecting telescope 205
5.39 PSFs at the edge position for refracting and reflecting telescopes 207
5.40 PSFs at the corner position for refracting and reflecting telescopes 207
5.41 Encircled energy plot for refractive and reflective telescopes 208
5.42 Single parabolic mirror reflecting telescope 210
5.43 Encircled energy plot for the single parabolic mirror reflecting telescope 211
5.44 1.5X reflecting telescope 213
5.45 Encircled energy plot for the 1.5X reflecting telescope 214
5.46 Double refracting telescope 214
5.47 PSFs for the double refracting telescope 215
5.48 UV triplet made up of stock item singlets 216
5.49 Reflecting macroscopic objective 217
5.50 f=150 mm fused silica singlet 218
5.51 Field plot for UV singlet 218
5.52 Simple mirror objective 219
5.53 PSFs at the center position for the UV singlet and the simple mirror objective 221
5.54 PSFs at the corner position for the UV singlet and the simple mirror objective 221
5.55 Erfle eyepiece telescope 223
5.56 Field plot for the Erfle eyepiece telescope 225
5.57 Encircled energy plot for the Erfle eyepiece telescope 225

6.1 Patent diagram of the fully-integrated cslM/m 232
6.2 The BioRad confocal microscope 234
6.3 The PMT prismatic enhancer 236
6.4 Confocal images of a flat mirror taken with BioRad and Zeiss cslms 237
6.5 'Golf-club' and 'beam-conditioner' two-scanning mirror configurations 240
6.6 Simple single mirror x-y scanner 241
6.7 Single mirror x-y scanners 242
6.8 Scanning mirror - objective lens configurations 243
6.9 Beam expander configuration 246

6.10 Pinhole alignment 247
6.11 Spectral response curve for the R298 Hamamatsu PMT 249
6.12 Proposed fully integrated csIM/m 252

ABBREVIATIONS

AM - Air mass
BFL - Back focal length
BPI - Biomedical Photometrics
BW - Band width
BWD - Back working distance
cslm - Confocal scanning laser microscope
cslM - Confocal scanning laser MACROscope
cslM/m - Confocal scanning laser MACROscope/Microscope
CW - Continuous wave
EE - Encircled energy
EFL - Effective focal length
EL - Electroluminescence
FFL - Front focal length
FWD - Forward working distance
FWHM - Full-width at half maximum
GaAs - Gallium arsenide
HeCd - Helium-Cadmium
HeNe - Helium-Neon
HF - Hydrofluoric acid
HWHM - Half-width at half maximum
IEC - Institute of Energy Conversion
IR - Infra-red
ITO - Indium tin oxide
I-V - Current - voltage
L·AX - Longitudinal axial chromatic aberration
LEPSi - Light emitting porous silicon
LSL - Laser scan lens
MP - Magnifying power
MTF - Modulation transfer function
MXI - Maximum intensity image
NA - Numerical aperture
NDF - Neutral density filter
NEAT - New England Affiliated Technologies
OBIC - Optical beam induced current
OD - Optical density
OTF - Optical transfer function
PL - Photoluminescence
PMT - Photomultiplier tube
PSF - Point spread function
PSi - Porous silicon
PTF - Phase transfer function

RIE	-	Reactive ion etching
RL	-	Reflected light
SEM	-	Scanning electron microscope
SSM	-	Scanning stage microscope
T·AX	-	Transverse axial chromatic aberration
TCO	-	Tangential coma
T·SA	-	Transverse spherical aberration
UW-CMG	-	The University of Waterloo's Confocal Microscopy Group
UV	-	Ultraviolet
WD	-	Working distance

CHAPTER 1

INTRODUCTION

In the early 1990s the University of Waterloo's Confocal Microscopy Group (UW-CMG) developed the idea of a large field-of-view (several centimeters), confocal, fast (several seconds for image acquisition) imaging system. Shortly thereafter a confocal scanning beam MACROscope was designed and constructed. The heart of the MACROscope consists of a relatively inexpensive, prototype, f-theta, telecentric laser scan lens able to accommodate a 7.5 x 7.5 cm (3 x 3 inch) field of view. The MACROscope combines the large area scanning capability of scanning stage microscopes with the short image acquisition time of scanning beam microscopes. This thesis documents the characterization of the prototype MACROscope and the UW-CMG confocal scanning laser microscope (cslm), in addition to showing imaging applications involving solar cells and porous silicon.

1.1 Motivation for Research

Large area scanning microscopy spanning several centimeters has been traditionally done with scanning stage[1,2,3,4] microscopes (SSMs). A SSM generates an image by scanning the specimen under a stationary diffraction-limited laser spot. Due to the stationary nature of the beam, optics are used exclusively on-axis which greatly reduces aberrations. SSMs are very simple instruments which provide high throughput, high resolution, large area scans. Unfortunately SSMs can be very slow in acquiring images, taking as long as several minutes for centimeter-size specimens. The scan speed is limited by the scanning stages. This is especially true at high resolution where excessive speeds can cause vibrations. In some cases centimeter-size confocal images consisting of several slices can take several hours to obtain. Confocal imaging is impractical on SSMs and is limited to the very patient, the very desperate, and graduate students. SSMs are also unable to utilize immersion optics, such as water or oil immersion, due to the moving specimen.

Confocal scanning laser microscopes[5,6,7,8,9] (cslms) have been commercially available since the mid-1980s and provide very fast image acquisition at the highest resolutions. Scan times

are seldom more than 5 seconds and immersion optics can have numerical apertures (NAs) as large as 1.4. Unlike SSMs, cslms are commonly built around conventional wide-field microscopes and are uniquely suited to examine biological specimens (e.g. suspended in aqueous media). Cslms are unfortunately limited to fields of view common to microscope objectives, typically less than 5 x 5 mm.

The MACROscope[10,11,12,13,14,15,16,17] was specifically developed to fuse the large field-of-view capabilities of a SSM with the scanning beam features of a cslm. The first prototype MACROscope uses an f-theta, telecentric laser scan lens able to scan specimens as large as 7.5 x 7.5 cm in less than ten seconds. The MACROscope has lateral and axial resolutions equal to 5 and 200 μm, respectively, under optimum conditions. Under 'normal' conditions lateral and axial resolutions are 20 and 500 μm, respectively, which can be achieved with reflected light on a regular basis. The greatly enhanced scan speed (compared to SSMs) allows for confocal slicing to be done in minutes rather than hours. Finding the optimum focal plane can be done quickly and adjustments, to obtain better images, are easy to make. Decreased image acquisition time contributes directly to increased productivity and enhanced image quality. The MACROscope provides optical beam induced current (OBIC), confocal reflected light and confocal photoluminescence imaging at a macroscopic level with the convenience attributed to cslms.

Early on in the characterization of the MACROscope it became evident that an instrument combining macroscopic and microscopic operation would be the next logical development. Patents[18,19] have been granted and are in the process of being accepted for various designs of the MACROscope and a combined confocal scanning laser MACROscope/Microscope (cslM/m). A company called Biomedical Photometrics (BPI) has been created for the purpose of commercializing the MACROscope and related instruments. Chapter 6 (this thesis) deals with proposed improvements to the cslM/m, while the rest of this thesis deals with the MACROscope and cslm as separate instruments.

A significant amount of time was spent imaging various specimens, notably solar cells and porous silicon (material and devices). The motivation here was two-fold:

1) To characterize the MACROscope and cslm via imaging in addition to identifying limitations in each system.
2) To contribute to the study of solar cells and especially porous silicon with the cslm and the MACROscope. Porous silicon is a novel form of silicon which was discovered in 1990 to luminescence in the visible at room temperature. It could lead to the development of all-silicon optoelectronics, effectively revolutionizing the industry.

1.2 Contributions: Past and Present

The total quantity of research related to the MACROscope and similar devices depends upon the definition of confocal macroscopy. Section 1.3 attempts to distinguish the MACROscope from conventional cslms, and therefore this section will treat the MACROscope as an instrument distinct from cslms.

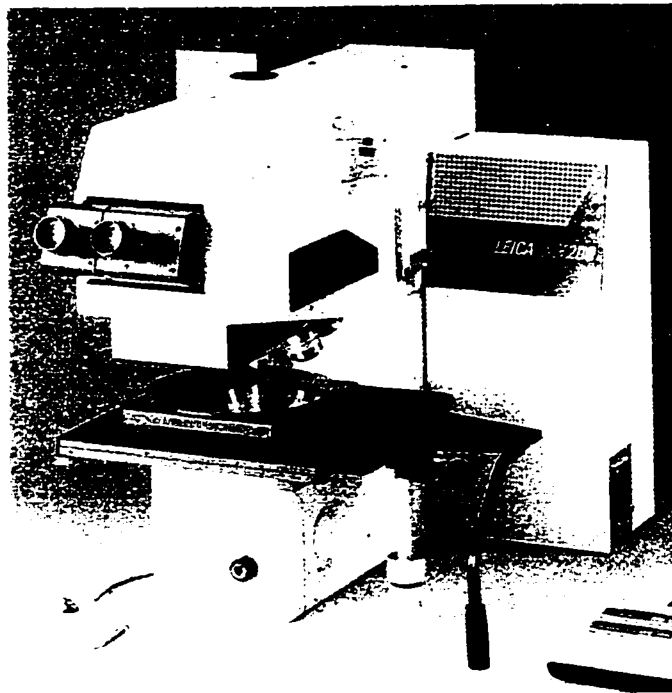

Figure 1.1 Leica INM 200. This microscope combines a confocal scanning beam microscope with a scanning stage. This allows it to scan areas as large as 20x20 cm. Figure taken from the 1996 Leica INM-200 brochure.

1.2.1 Past Contribution

The MACROscope was designed to provide large area scanning available on SSMs, however, it has little relation to SSMs and has directly evolved from cslms. For a list of various commercial cslms see Appendix 2 in the Confocal Handbook[5].

An intermediate step between the MACROscope and cslms & SSMs is a hybrid microscope (Fig. 1.1). Fig. 1.1 shows a Leica INM-200, taken from the 1996 Leica INM-200 brochure, which combines a cslm with a scanning stage microscope. This hybrid offers many features such as imaging exclusively as an SSM or a cslm. The combined imaging mode is probably the most powerful, where many confocal scanning laser images are taken of small parts on the specimen by utilizing the scanning stage. The set of images can be assembled together with suitable software in order to create a single image of the entire specimen. This process is sometimes referred to as tiling. Tiling significantly reduces high NA image acquisition times for large specimens. Under the right circumstances confocal imaging of large specimens is also possible.

Interestingly enough, papers by Sawyer[20] and by Hughes[21], dealing with OBIC imaging of solar cells, come closest to resembling the MACROscope and cslM/m. Fig. 1.2a shows a schematic diagram of a laser scanner taken from the article written by Sawyer. Light from a He-Ne laser is fed into vertical and horizontal scanning mirrors (V and H) where lens L_1 is supposedly a unitary telescope. The scanning beam goes either into a conventional microscope, as shown in Fig. 1.2a, or into a camera lens. This arrangement effectively makes this instrument a Macroscope/Microscope. Reflected light from the specimen can be collected non-confocally by L_2 and a photocell. An OBIC signal can also be collected from the solar cell specimen. Another schematic diagram of a MACROscope-like instrument is shown in Fig. 1.2b, taken from the article by Hughes. In this case the scanner can only be used for OBIC imaging since there are no other detectors except for the solar cell specimen itself. Notice the imaging optics seem to consist of an objective lens and an eyepiece which is not equivalent to a laser scan lens since an intermediate image is formed.

Research related to macroscopic OBIC imaging is quite limited although this is not true of microscopic OBIC imaging. Even more common is electron beam induced current (EBIC)[22,23] imaging which is the scanning electron microscope equivalent to OBIC.

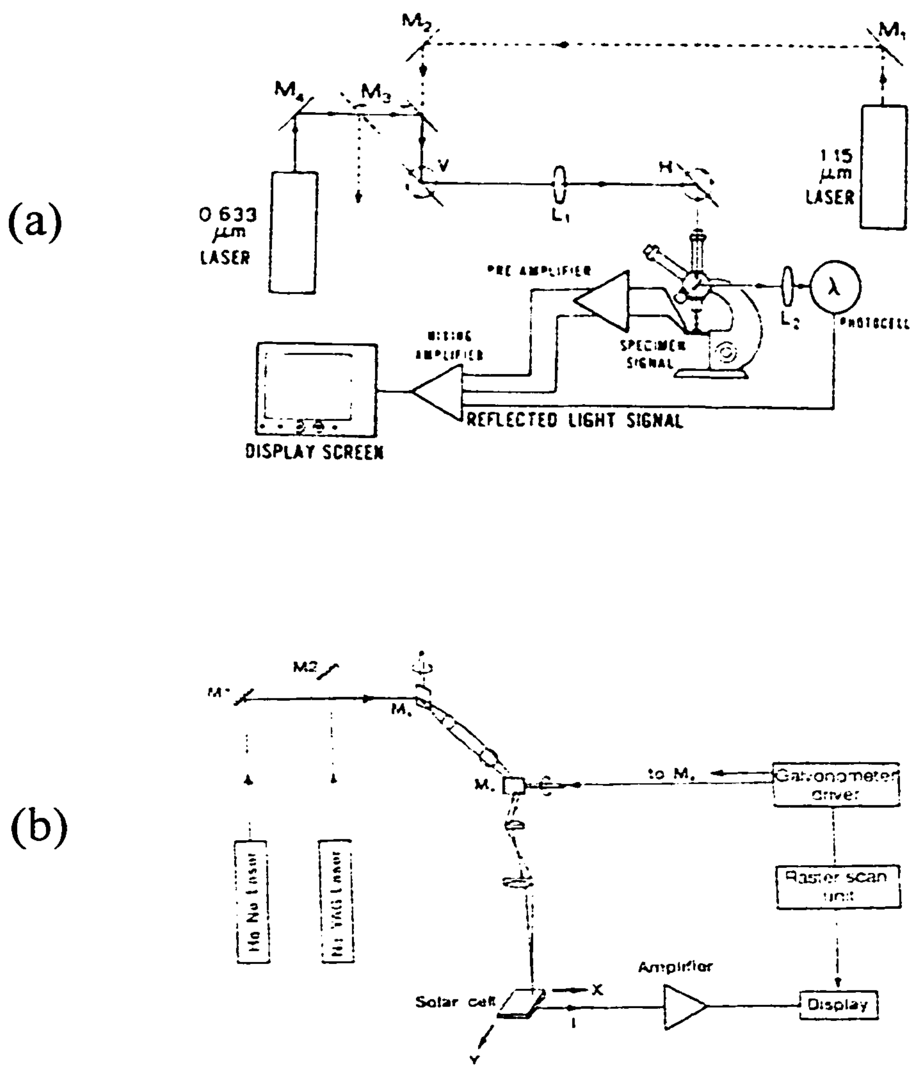

Figure 1.2 (a) Sawyer's[20] scanning beam microscope used primarily for OBIC imaging of solar cells. This instrument is in effect a macroscope-microscope since the above microscope can be interchanged with a camera lens. (b) A scanning beam macroscope developed by Hughes[21]. This instrument can only be used in OBIC mode.

In EBIC, an electron beam is used to create electron-hole pairs in a specimen which in turn generates a photocurrent. EBIC imaging is more common than OBIC mainly because electron microscopes are readily available and well accepted as characterization instruments.

Research dealing with light emitting porous silicon (LEPSi)[24,25,26,27,28,29,30] only really started in the 1990s. A wide variety of characterization techniques have been used to study LEPSi including confocal scanning beam microscopy. Carver[31,32] has imaged LEPSi with a scanning beam microscope but only Nassiopoulos[33] has imaged LEPSi with a cslm. This is not surprising since confocal microscopes are commonly found in biology rather than chemistry or physics, and sometimes they are never even considered as a characterization tool. Imaging systems such as the MACROscope are even more scarce in physics and chemistry research environments.

1.2.2 Present - UW-CMG

UW-CMG has designed and constructed a confocal scanning laser MACROscope able to provide OBIC, confocal reflected-light, or confocal photoluminescence images in less than 10 s with 7.5 x 7.5 cm fields of view and 5 μm lateral and 200 μm axial resolution. Very simply, there is nothing in the literature or in patents that can match this. The Sawyer[20] article comes closest in duplicating the MACROscope and cslm at UW-CMG, however, there are several key differences:

1) The UW-CMG cslM/m offers confocal operation. This inherently requires high quality optics throughout the instrument when compared to non-confocal operation.
2) UW-CMG uses a f-theta, telecentric laser scan lens in order to ensure diffraction-limited operation over the entire field of view, instead of using an arbitrary, off-the-shelf camera lens.
3) The placement and alignment of all the optical components is carefully considered in order to ensure proper telecentric and aberration-free operation. Sawyer's scanner was mainly intended for OBIC imaging and therefore did not need to operate perfectly telecentrically.

1.3 The MACROscope: Just Another cslm?

YES.

In many respects the MACROscope looks like a scaled-up cslm. Its beam size, beam-splitter, scan mirrors, scan angles, and detector lens are all about four times larger than a 'normal' cslm. The reason for the scale-up is the f-theta laser scan lens. The main question can therefore be simplified to: is the f-theta, telecentric laser scan lens just another objective?

NO.

First of all, the laser scan lens (LSL) measures 30 cm long and 12.5 cm in diameter which makes it much too large for any conceivable microscope. The beam size and more importantly the scan angles are too large for any cslm to handle. The LSL is specifically designed to be f-theta and to be operated in telecentric mode with the entrance pupil located several centimeters outside of its case. For conventional objectives f-theta operation is achieved due to the fact that scan angles are small and $\tan\theta \cong \sin\theta \cong \theta$. While any lens can be operated in telecentric mode, most objectives are designed not to operate as such. For example, the Mitutoyo objectives used by UW-CMG were designed to be parfocal and, unfortunately, slightly non-telecentric. Large field-of-view microscope objectives do in fact exist; both Nikon and Mitutoyo sell objectives with 25 and 24 mm diameter fields of view, respectively, and it is probable that most microscope companies will offer similar objectives in the near future. The Mitutoyo 1X objective provides a 17x17 mm field of view at 0.025 NA while the LSL provides more than 4 times the field of view and twice the NA making it a low magnification, 'high' NA lens. Basically, the LSL falls outside the restrictions imposed by commercial cslms and commercial objectives.

The ideal objective, at least from the point of view of this author, is one with the highest NA and the lowest magnification possible. With this kind of lens the entire specimen could be viewed by electronically zooming-in. Unfortunately, in the real world, while a 0.95 NA objective with a 500 μm field of view can be successfully manufactured, it cannot be easily scaled up.

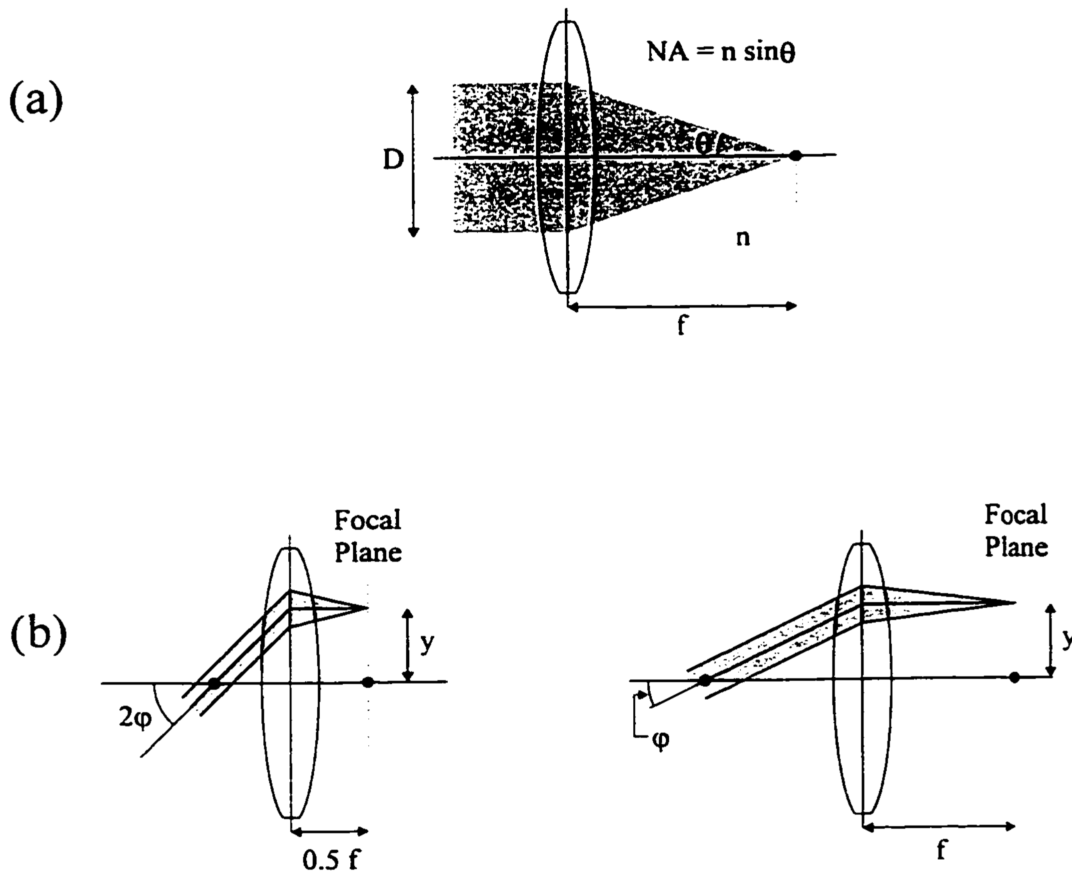

Figure 1.3 (a) To increase NA the focal length, f, must be reduced and/or the beam diameter, D, must be increased. (b) The field angle must be increased to maintain the same field of view when the focal length is decreased.

The reason for this is that linear aberrations scale with size[34] but the diffraction-limited spot size does not, hence, the objective will not work if a simple scaling (upwards) is done.

Fig. 1.3a shows, as a first approximation, in order to increase NA the beam diameter must be increased and the focal length must be decreased. If a large field of view is required then the scan angle must be increased as the focal length is decreased (Fig. 1.3b). For the LSL once the maximum beam size and scan angle (20 mm diameter and ±10°) were agreed upon, the focal length and NA were determined by the materials, surface tolerances, and best achievable aberrations.

1.4 Thesis Overview

Chapter 2 - Introduction to Confocal Microscopy

This chapter begins with an introduction to simple, thin lenses which will be used throughout the thesis to illustrate various optical concepts. The confocal principle is explained followed by a definition of confocal lateral and axial resolution, in turn followed by an example of confocal slicing with a hypothetical test specimen. The last section in the chapter gives an overview of the various parts making up a cslm. This chapter is intended to introduce many basic concepts as well as serve as a knowledge base for other chapters.

Chapter 3 - Characterization of the Confocal Scanning Microscope and MACROscope

A component by component description of the UW-CMG cslm and MACROscope are given based on their standard configurations used throughout the past four years. Throughput, lateral, and axial resolution data are shown for both instruments. Images illustrating some limitations for both instruments are also shown, specifically, the off-axis aberrations associated with the unitary telescopes on the cslm, and the non-telecentric error on the MACROscope. Preliminary data from a spectrally resolved MACROscope is also given. The goal for this chapter is to characterize the cslm and MACROscope with respect to performance and limitations for two primary reasons:

1) To obtain a better feel of the optical quality for both instrument which can serve as a benchmark for future innovations.
2) To define the resolutions and limitations of the instruments with respect to the images shown in the applications chapter (chapter 4)

Chapter 4 - MACROscope/cslm Applications and Imaging Results

This chapter shows imaging results from two types of semiconductor specimens: solar cells and porous silicon. Solar cells proved to be excellent specimens for the MACROscope and in some cases the cslm. A brief introduction to solar cells is given followed by a set of images illustrating the various imaging capabilities of the MACROscope and cslm.

The second part of the chapter deals with a novel material, porous silicon. A brief introduction is given followed by a series of images from various porous silicon materials and devices. The emphases here is not so much MACROscope/cslm characterization, but rather the specimens themselves. UW-CMG aided in characterizing porous silicon materials and devices provided via a collaboration with P.M. Fauchet's research group at the University of Rochester.

Chapter 5 - Quantitative Lens Analysis and Design with CODE V

Significant off-axis aberrations associated with the achromatic, unitary telescopes of chapter 3 prompted a more in-depth investigation of the telescopes with the aid of a lens design/analysis program, CODE V. In addition to studying the aberrations associated with the refracting telescopes, a comparison is made with reflecting telescopes made with off-axis parabolic mirrors. Reflecting telescopes are successfully utilized on the BioRad cslm. CODE V is also used to evaluate designs for all-reflecting detector arms and a 30X beam expander, as well as designs for very inexpensive macroscopic UV objectives.

Chapter 6 - The Fully Integrated Confocal Scanning Laser MACROscope/Microscope

In this chapter, the data from previous chapters is used to develop a proposed improved design for a fully integrated, single instrument cslM/m. A component by component analysis is made of the cslM/m and various features from commercial cslms are integrated into the design. The final design emphasizes simplicity and optical quality.

References

[1] M. Tajima, T. Masui, T. Abe, Proceedings of the Sixth International Symposium on Silicon Materials Science and Technology, The 177th Electrochemical Society Meeting, Montreal, Canada, 1990.

[2] E. Erman, G. Gillardin, J. LeBris, M. Renaud, E. Tamzig, Journal of Crystal Growth, **96** (1989) 469.

[3] C.J.L. Moore, C.J. Miner, Journal of Crystal Growth, **103** (1990) 21.

[4] J.W. Bowron, Ph.D. Thesis, 1993, Physics Department, University of Waterloo, Waterloo, Canada.

[5] J.B. Pawley (Editor), Handbook of Biological Confocal Microscopy, 2nd Edition, (Plenum, New York, 1995).

[6] T.R. Corle, G.S. Kino, Confocal Scanning Optical Microscopy and Related Imaging Systems, (Academic Press, San Diego, 1996).

[7] J.K. Stevens, L.R. Mills, J.E. Trogodis, Three-Dimensional Confocal Microscopy: Volume Investigation of Biological Specimens, (Academic Press, San Diego, 1994).

[8] P.C. Cheng, T.H. Lin, W.L. Wu, J.L. Wu (Editors) Multidimensional Microscopy, (Springer-Verlag, New York, 1993).

[9] T. Wilson (Editor), Confocal Microscopy, (Academic Press, London, 1990).

[10] K.M. Beesley, S. Damaskinos, and A.E. Dixon, J. Forensic Sciences **40** (1995) 10.

[11] A.E. Dixon, S. Damaskinos, A.C. Ribes and K.M. Beesley, J. Microscopy **3** (1995) 178.

[12] A.C. Ribes, S. Damaskinos, H.F. Tiedje, A.E. Dixon, D.E. Brodie, S.P. Duttagupta, and P.M. Fauchet, Materials Research Society Symposium Proceedings, **426** (1996) 581.

[13] A.C. Ribes, S. Damaskinos, A.E. Dixon, and D.E. Brodie, Solar Energy Materials and Solar Cells **44** (1996) 439.

[14] A.C. Ribes, S. Damaskinos, A.E. Dixon, K.A. Ellis, S.P. Duttagupta, and P.M. Fauchet, Progress in Surface Science, **50** (1995) 295.

[15] A.C. Ribes, S. Damaskinos, A.E. Dixon, G.E. Carver, C. Peng, P.M. Fauchet, T.K. Sham, and I. Coulthard, Applied Physics Letters, **66** (1995) 2321.

[16] S. Damaskinos, A.E. Dixon, K.A. Ellis, and W.L. Diehl-Jones, Micron, **26** (1995) 493.

[17] E.K. Seto, S. Damaskinos, A.E. Dixon, W.L. Diehl-Jones, and C.A. Mandato, Electrophoresis **16** (1995) 934.

[18] A.E. Dixon, S. Damaskinos, U.S. Patent #5381224, 1995.

[19] A.E. Dixon, U.S. Patent #5532873, 1996.

[20] D.E. Sawyer, H.K. Kessler, IEEE Transaction on Electron Devices, **27** (1980) 864.

[21] A.E. Hughes, B.M. Neville, K.C. Heasman, and M.P. Lesniak, 10th E.C. Photovoltaic Solar Energy Conference, (1991) 644.

[22] D.B. Holt and D.C. Joy (Editors), SEM Microcharacterization of Semiconductors, (Academic Press, New York, 1989).

[23] B. Sieber, J-L Farvacque (Editors), Journal de Physique, Volume 1, Colloque 6, 1991.

[24] L.T. Canham, Applied Physics Letters, **57** (1990) 1046.

[25] R.L. Smith and S.P. Collins, Journal of Applied Physics, **71** (1992) 121.

[26] P.M. Fauchet, L. Tsybeskov, C. Peng, S.P. Duttagupta, J. van Behren, Y. Kostoulas, J.M. Vandyshev, and K.D. Hirschman, IEEE Journal of Selected Topics in Quantum Electronics, **1** (1995) 1126.

[27] B. Hamilton, Semicond. Sci. Technol., **10** (1995) 1187.

[28] Y. Kanemitsu, Physics Reports, **263** (1995) 1.

[29] J. Kocka, I. Pelant, and A. Fejfar, Journal of Non-Crystalline Solids **198** (1996) 857.

[30] K.H. Jung, S. Shih, and D.L. Kwong, Journal of the Electrochemical Society, **140** (1993) 3046.

[31] G.E. Carver, Y.H. Xie, M.S. Hybertsen, W.L. Wilson, S.A. Ipri, W.L. Brown, E. Dons, B.E. Weir, A.R. Kortan, G.P. Watson, and A.J. Liddle, Physical Review B, **49** (1994) 5386.

[32] G.E. Carver, E. Ettedgui, C. Peng, L. Tsybeskov, Y. Gao, P.M. Fauchet, and H.A. Mizes, Materials Research Society Proceedings, **283** (1993) 173.

[33] A.G. Nassiopoulos, S. Grigoropoulos, L.T. Canham, A. Halimaoui, I. Berbezier, E. Godolides, D. Papadimitrious, Thin Solid Films, **255** (1995) 329.

[34] W.J. Smith, Modern Optical Engineering - The Design of Optical Systems, 2nd Edition, (McGraw-Hill, New York, 1990), p75.

CHAPTER 2

INTRODUCTION TO CONFOCAL MICROSCOPY

A confocal microscope can be simplistically thought of as a conventional or wide-field microscope with the addition of scanning optics and a confocal pinhole. The confocal effect allows the user to image photoluminescent objects with much greater clarity than is possible on a non-confocal microscope. Optical tomography or 3-D imaging with reflected light (RL) and nonconfocal optical beam induced current (OBIC) mapping are also possible with confocal microscopes. Confocal microscopes have been very successful in areas such as immunofluorescence and metallurgy. The attributes and characteristics of confocal microscopes can, for the most part, be illustrated with simple thin lenses. A brief review of simple lenses, including a schematic of a wide-field microscope will be given. Variations on Minsky's[1] original patent diagrams will be used to illustrate the confocal effect. Wide-field microscopy will be compared and contrasted with scanning laser confocal microscopy. Confocal slicing as well as lateral and axial resolution will be illustrated and defined. Finally, a block diagram of a generic cslm will be shown with comments on each of its major components.

2.1 Optics Review

Throughout this thesis most optical effects and properties will be described using simple thin lenses. Fig. 2.1a shows a simple, double-convex, thin lens surrounded by air. A lens that has only two refracting surfaces, thereby consisting of only one element, is called a simple lens. Since both surfaces 'bulge out' this is a double convex, converging, or positive lens. A thin lens is considered to have a thickness, d, which approaches zero. Thin lenses, therefore, have one principal plane coinciding with the center of the lens. In air, the distances from this central plane to either the object focal point, f_o, or the image focal point, f_i, are the same and equal to f, the focal distance. For a thin lens the resulting image of an object can be easily obtained via a graphical method[2] as shown in Fig. 2.1a.

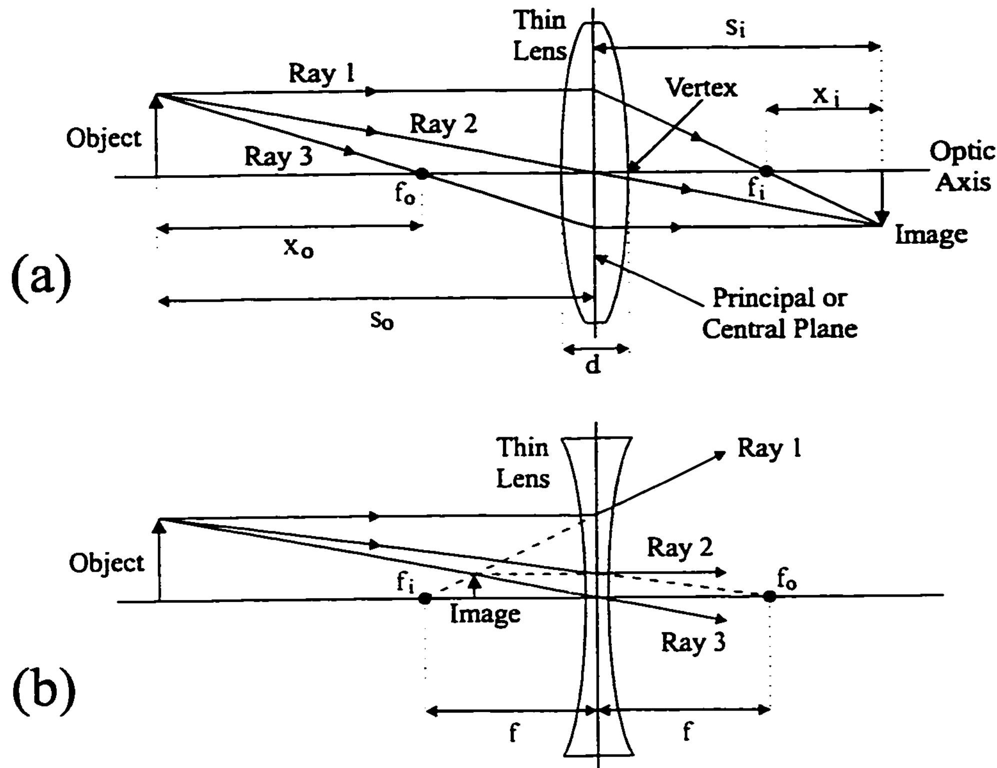

Figure 2.1 (a) Graphical determination of an image formed by a thin, positive lens. Several ways of measuring the object and image distance are also shown where s_o, s_i, x_o, and x_i are positive. (b) Graphically determined image formed by a thin, negative lens.

Starting from the top of the object, three unique rays can be drawn whose intersection will determine the position and size of the image. Ray 1 is drawn parallel to the optic axis and strikes the central plane refracting downwards such that it passes through f_i. A ray which passes through the center of the lens, such as Ray 2, will emerge undeviated. Ray 3 is made to pass through f_o so that when it intersects the central plane, it emerges parallel to the optic axis. The intersection of any two of the above rays determines the resulting image. The position and height of the image can also be calculated using the following formulas:

$$\frac{1}{f} = \frac{1}{s_0} + \frac{1}{s_i} \tag{2.1}$$

$$M_T = \frac{-s_i}{s_o} = \frac{-x_i}{f} = \frac{-f}{x_o} \tag{2.2}$$

where s_o and s_i are the object and image distances respectively, x_o and x_i are as shown in Fig. 2.1a, and M_T is the transverse magnification which defines the image height (image height = $M_T \cdot$ object height).

Fig. 2.1b shows a simple, double concave or negative thin lens with a graphically constructed image. Note in this case that the positions of f_i and f_o have been reversed with respect to the lens in Fig. 2.1a. The projection of Ray 1 from the central plane to f_i determines the direction of Ray 1 after the central plane. Ray 2 is initially drawn such that it would pass through f_o, if there were no lens, emerging parallel to the optic axis. The above graphical methods and formulas have proven invaluable in the initial design and analysis of existing and proposed lens systems in this thesis.

Fig. 2.2 shows a simplified schematic of a compound microscope which consists of two thin lenses: the objective and eyepiece. The objective lens has a focal length f_o and acts as the limiting aperture or aperture stop of the system. The object lies a distance greater than f_o but less than $2f_o$ from the principal plane of the objective, hence a real, inverted, magnified image is produced at which point a field stop is placed in order to limit the size of the image. The eyepiece, with a focal length f_e, is placed such that its focal point is coincident with the intermediate image. The intermediate image is further magnified by the eyepiece and the final image resides at infinity, which is best viewed by a normal, relaxed eye.

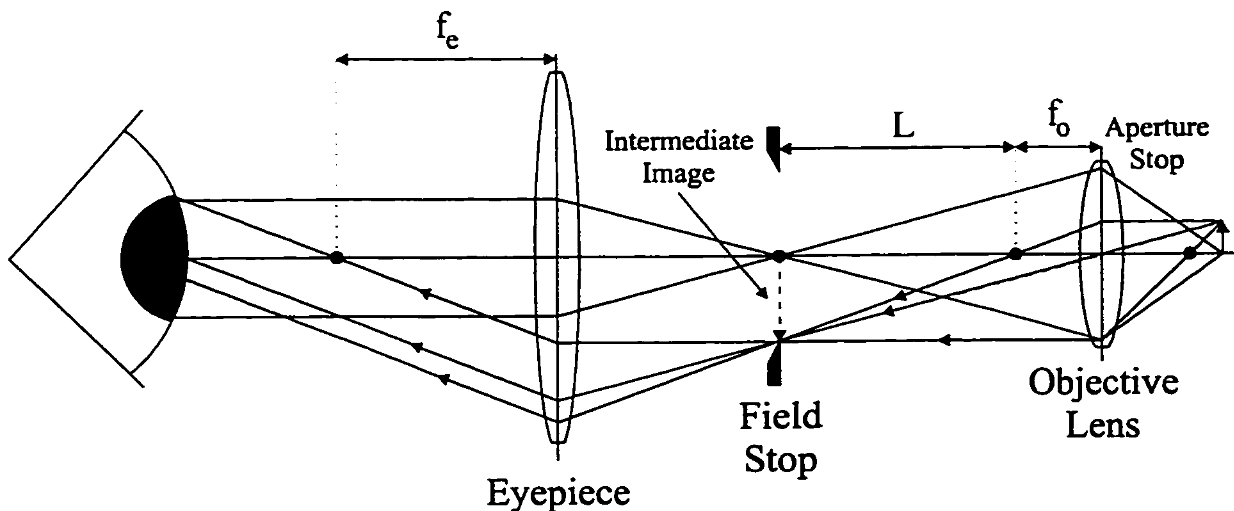

Figure 2.2 Simplified diagram of a compound microscope. The focal point of the eyepiece is coincident with the intermediate image formed by the objective lens.

It can be shown[3] that the magnifying power of the microscope is given by:

Magnifying Power = MP = $M_{TO}\, M_{ae}$ **(2.3)**

where M_{TO} = the transverse linear magnification of the objective, and M_{ae} = the angular magnification of the eyepiece. In turn, M_{TO} and M_{ae} can be expressed as:

$$M_{TO} = \frac{-L}{f_0} \quad \textbf{(2.4)}$$

$$M_{ae} = \frac{254}{f_e} \quad \textbf{(2.5)}$$

where L is the optical tube length (typically 160 mm) as shown in Fig. 2.2, and 254 mm (10 inches) is assumed to be the standard near point (the closest point on which the eye can focus) for a normal eye. Notice that the image generated by the microscope is viewed by the human eye all at once which is quite different from what happens in a cslm as will be seen shortly. In some cases it is useful to consider the eyepiece and objective as a combined system with a single focal length. The effective focal length for two lenses of focal lengths f_1 and f_2 in combination is given by[4]:

$$\frac{1}{f} = \frac{1}{f_1} + \frac{1}{f_2} - \frac{d}{f_1 f_2} \quad \textbf{(2.6)}$$

where d is the separation between the principal planes of the lenses and f is measured with respect to the principal planes of the combined system. At this point it is useful to define back and front focal lengths. The back focal length (BFL) is the distance from the vertex of the last surface of an optical system to the second focal point of that system. Similarly, the front focal length (FFL) is the distance from the first focal point of the system to the vertex of the first surface. Using the above example of two thin lenses in combination, these two quantities can be written as follows[5]:

$$FFL = \frac{f_1(d - f_2)}{d - (f_1 + f_2)} \quad \textbf{(2.7)}$$

$$BFL = \frac{f_2(d - f_1)}{d - (f_1 + f_2)} \quad \textbf{(2.8)}$$

Appendix 1 shows how these formulas can be applied to Fig. 2.2.

2.2 Confocal Microscopy

In 1957, Marvin Minsky (as a postdoc at Harvard University) submitted a patent[1] for a scanning stage confocal microscope. Fig. 2.3 is one of Minsky's patent diagrams showing an epi-illuminated (lens O acts as a condenser and objective) confocal microscope. Lens O forms an image of the illuminating pinhole A at point D.

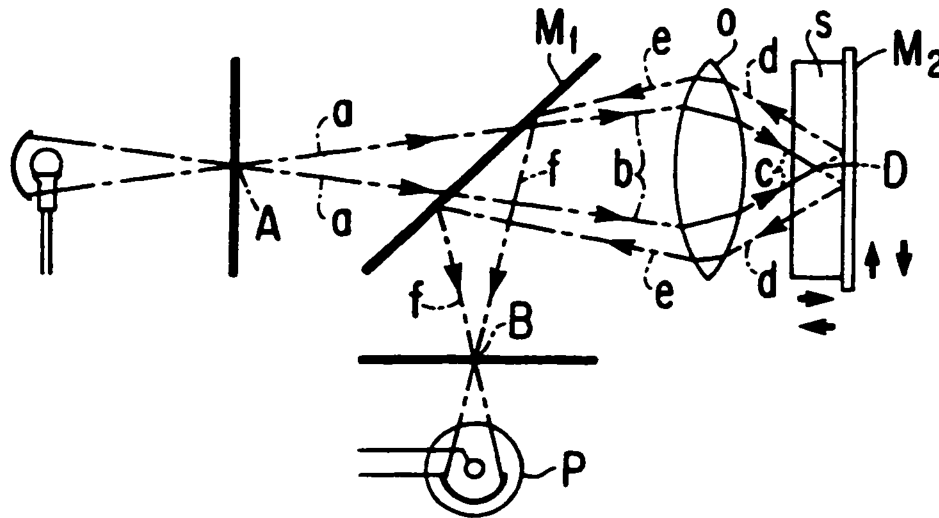

Figure 2.3 A simple scanning stage confocal microscope taken from patent diagrams originally drawn by Marvin Minsky. Figure taken from Minsky's[1] patent.

The image of point D is in turn formed at the detector or confocal pinhole B. Points A, D, and B are said to be confocal. The implications of this confocal microscope will be treated in the next section. The next three decades following Minsky's patent saw significant developments in confocal microscopy leading up to commercialization in the mid-1980s. Inoué gives a brief historic overview[6] in chapter 1 of the Confocal Handbook. It is interesting to note that current commercial versions of confocal microscopes utilize lasers, digital scanning mirrors, and micro-computers which did not exist in 1957. Since their commercialization, confocal microscopes have seen extensive use in biology. Recently confocal microscopes have appeared in areas such as materials research and electronics characterization.

2.2.1 Confocal Optics

Fig. 2.4 shows Minsky's patent diagram redrawn for greater clarity. This is a very simple confocal system using a non-infinity corrected objective lens similar to the one shown in Fig. 2.2. A non-infinity corrected objective will produce a diffraction-limited spot when fully illuminated by a point source at a specific optical tube length distance from the objective.

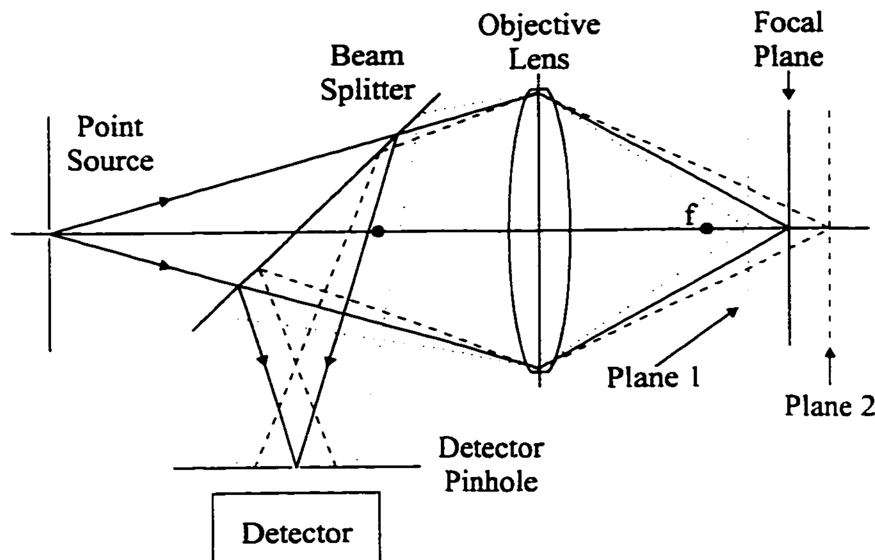

Figure 2.4 A simple confocal microscope illustrating how the confocal effect works. Light from objects in the focal plane will be detected while light originating from points outside the focal plane will be stopped by the confocal pinhole. Objects are therefore in focus or appear black.

In Fig. 2.4 a point source illuminates the objective lens which focuses the light down to a diffraction-limited point on the focal plane. The specimen is assumed to be flat and diffusely reflecting. The confocal effect will in general work the same for specular reflection and photoluminescence (PL), however, the rays in Fig. 2.4 have been drawn assuming diffuse reflection. Light from the specimen at the focal plane (solid black lines) will return through the objective lens and will be partially reflected by the beam splitter. The light is then focused through the detector pinhole and strikes the detector. If the specimen is moved to plane 1 then reflected light (dotted red lines) will pass through the objective which will focus it at a point behind the detector pinhole.

A large area on the detector pinhole is illuminated such that very little or effectively no light reaches the detector from plane 1. Similarly, light reflected by an object at plane 2 (dashed green lines) will be focused in front of the detector pinhole and will not reach the detector. The detector or confocal pinhole is responsible for the confocal effect: objects in the focal plane will be imaged while objects outside the focal plane, such as those at planes 1 and 2, will not be imaged by the detector. For both Figs. 2.4 and 2.5, the optics are only capable of looking at one point at a time on the specimen. An image of the entire specimen can be produced by either raster-scanning the specimen under a stationary beam (the scanning stage method) or by raster-scanning a beam over a stationary specimen which is referred to as scanning beam imaging. A confocal image will contain only in-focus parts and black or empty areas unlike a non-confocal image which has in-focus and blurry parts.

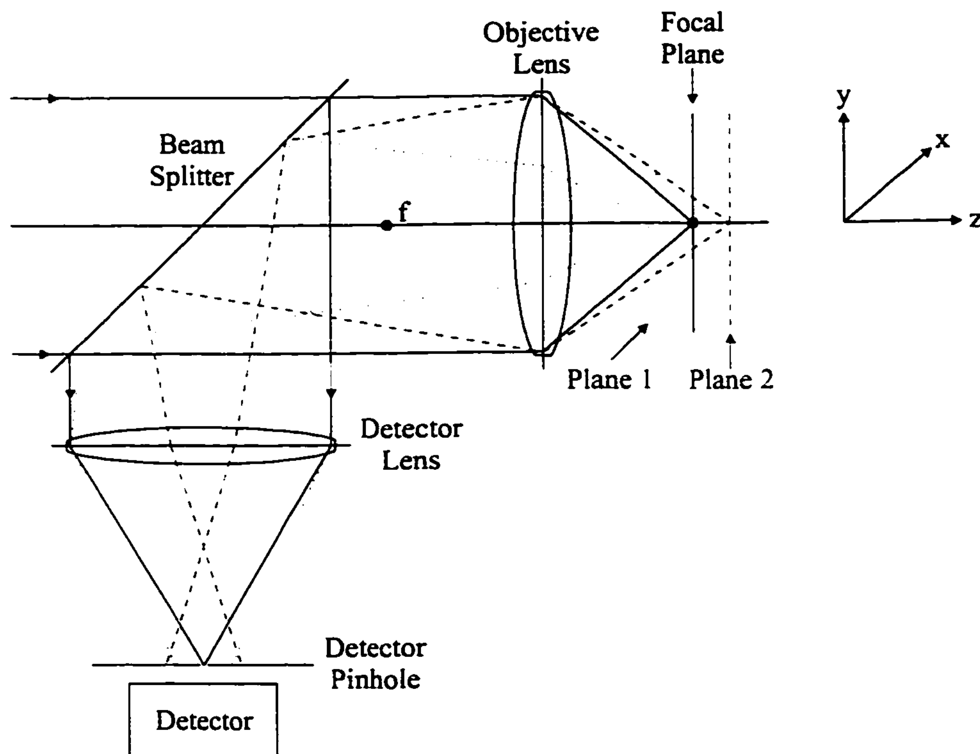

Figure 2.5 A simple confocal microscope using an infinity-corrected objective. A detector lens is needed to refocus the collimated beam onto the confocal pinhole. Filters and beam splitter placed in the collimated beam will not affect the overall beam path.

Fig. 2.5 shows an infinity-corrected version of the system shown in Fig. 2.4. The objective lens in Fig. 2.5 has been designed to accept a collimated beam of light and produce a diffraction-limited spot at its focal point. An infinity-corrected objective requires a detector lens to re-focus the collimated light onto the detector pinhole. The confocal effect is still present, as expected, where light from plane 1 is focused behind the detector pinhole and light from plane 2 is focused in front of the pinhole. Once again, only light from the focal plane of the system enters the pinhole and is detected. The infinity-corrected configuration is relevant since the University of Waterloo's Confocal Microscopy Group (UW-CMG) uses infinity-corrected objectives almost exclusively in all of its microscopes. The reason for this is convenience: optical components such as filters, beam-splitters, polarizers, etc., can be placed between the objective and detector lens without producing aberrations or affecting optical beam paths. Such optical components placed anywhere in the system shown in Fig. 2.4 would create aberrations and distort the existing optical path lengths. Interestingly enough, a non-infinity corrected objective can be converted to a virtual infinity-corrected objective by adding an appropriate eyepiece. The combination of eyepiece and objective in Fig. 2.2 effectively produces an infinity-corrected system. A collimated beam entering the eyepiece will end up focused at the specimen which corresponds to the focal point of the system as a whole. BioRad, a commercial confocal microscope manufacturer, utilizes this fact by attaching a box containing confocal optics to an existing conventional microscope which allows 'normal' and confocal operation with the same instrument.

2.2.2 Lateral and Axial Resolution

The smallest separation between two point objects while still allowing them to be resolved is referred to as the limit of resolution. In confocal microscopy this is referred to as lateral resolution, distinguishing it from axial resolution which is measured along the optic axis. According to Rayleigh's criterion, two point objects are said to be just resolved when the center of one Airy disk falls on the first minimum of the other Airy disk. The Airy disk[7] is simply the image of a point object which comes about due to diffraction from the objective, hence this is an optimized or diffraction-limited image of the point object.

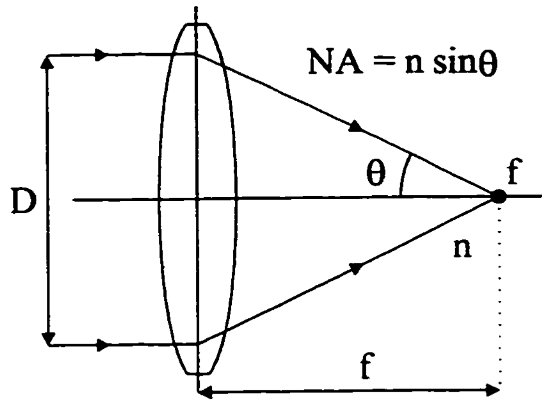

Figure 2.6 The numerical aperture (NA) of a microscope objective is a measure of its light gathering ability. Another measure is the f-number which is equal to f/D. The higher the NA and the lower the f-number, the more light that is collected.

The radius of an Airy disk is commonly defined to be the distance from its center to the first minimum and is equal to the lateral resolution of an objective lens. The Airy disk radius is given by:

$$\text{Limit of resolution} = r_{AIRY} = \frac{1.22\lambda}{2\,NA} \qquad \textbf{(2.9)}$$

where λ = wavelength of light and, NA = numerical aperture of the objective lens.

The numerical aperture of an objective lens is a measure of the angular size of the focusing cone of light as seen in Fig. 2.6 and is defined as follows:

$$NA = n\sin\theta \qquad \textbf{(2.10)}$$

where θ is the half-angle of the cone and n is the index of refraction of the medium encompassing the cone.

Another measure of the light gathering ability of a microscope objective is its f-number (f_{no}):

$$f_{no} = \frac{f}{D} \cong \frac{1}{2\,NA} \qquad \textbf{(2.11)}$$

where D and f refer to the diameter and focal length in Fig. 2.6. f_{no} equals $(2NA)^{-1}$ only for small θ. The lateral resolution of a microscope also depends on the field of view. As the confocal pinhole size is decreased the field of view becomes vanishingly small at which point Ingelstam[8] argues, on the basis of information theory, that the lateral resolution improves by a factor of $\sqrt{2}$.

Assuming a high level of confocality, the lateral resolution can be written as follows:

$$\text{Confocal lateral resolution} = \frac{r_{AIRY}}{\sqrt{2}} = \frac{1}{1.4} \cdot \frac{1.22\,\lambda}{2NA} \quad \textbf{(2.12)}$$

The raster-scanned image of a non-planar object obtained with either the system in Figs. 2.4 or 2.5 will consist of in-focus parts and black or empty areas since the detector pinhole only accepts light from objects 'near' the focal plane. Axial resolution defines what 'near' means. Equation 2.12 gives an unambiguous expression for confocal lateral resolution. It is much more difficult to obtain an equivalent expression for axial resolution especially when dealing with photoluminescent or diffusely reflecting specimens. The Confocal Handbook gives several expressions for the axial resolution, d_z, but two in particular are most relevant[9]:

$$d_z(PL) = \frac{1.77\,\lambda}{(NA)^2} \quad \textbf{(2.13)}$$

$$d_z(RL) = FWHM = \frac{0.22\,\lambda}{n \sin^2(\theta / 2)} \quad \textbf{(2.14)}$$

where θ refers to the angle in Fig. 2.6, and both formulas assume ideal or zero-size pinholes. Eqn. 2.13 is the Rayleigh criterion applied along the optic axis (this direction is generally referred to as the z-direction, while the plane perpendicular to the optic axis is the x-y plane). A microscope objective focused in air will produce a 3-D diffraction-limited spot with an Airy disk cross-section at the focal point in the x-y plane and another distribution along the x-z or y-z plane as shown in Fig. 2.7 (taken from the Confocal Handbook[9]). In Fig. 2.7b the distance from Z_1, the first minimum, to the center of the distribution is analogous to the Airy radius and equals $2\lambda/(NA)^2$. This formula must be further normalized to agree with low NA values from Eqn. 2.14 in order to obtain Eqn. 2.13. Eqn. 2.13 best describes the axial resolution in photoluminescence imaging. Eqn. 2.14 is derived using paraxial (small angle) theory assuming the object being viewed is a perfect planar mirror. Eqn. 2.14 represents the full-width at half-maximum (FWHM) for a distribution like that of Fig. 2.7b which is then taken to be the axial resolution for a specular reflector. At low NA Eqn. 2.14 agrees with Eqn. 2.13 except for a factor of two due to specular reflection[10]. Eqns. 2.13 and 2.14 should be considered only approximations which in some circumstances will fail to predict resolutions very accurately.

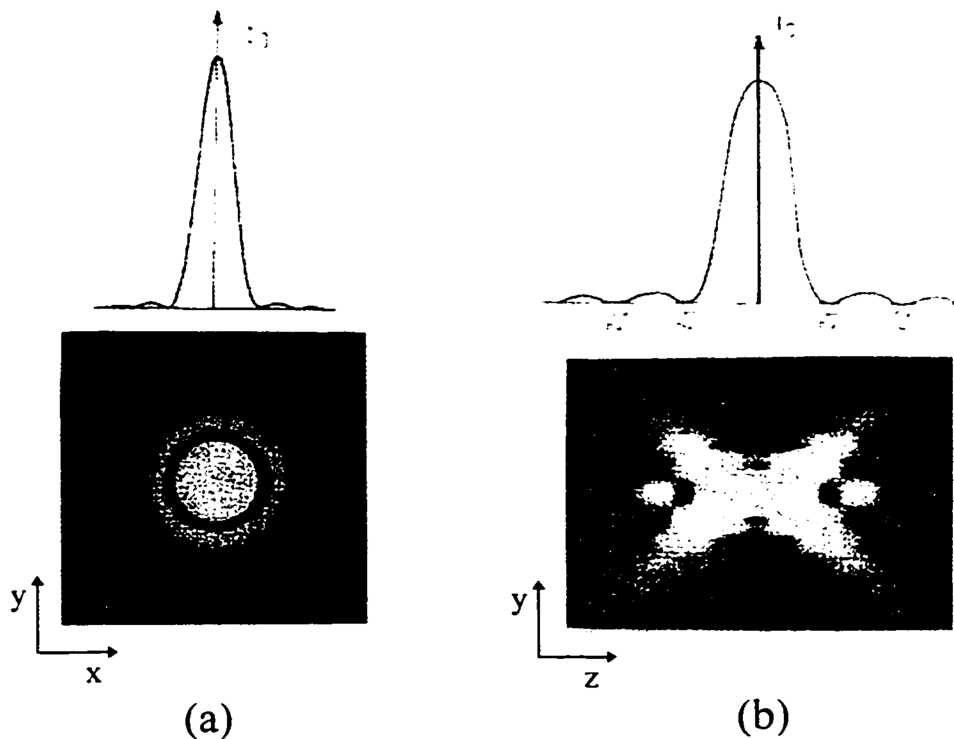

Figure 2.7 (a) An Airy disk image with the corresponding graph plotting intensity vs. position along a diameter. (b) The intensity distribution of a diffraction-limited point along the optic or z-axis. Figures taken from the Confocal Handbook[9].

A good source illustrating the various proposed axial resolution theories along with each of their particular assumptions is a short technical note by Sheppard[11]. Bowron[12] has shown that a proper treatment of axial resolution using finite size pinholes, even for plane reflectors, requires a model that considers the specific optical parameters, setup, etc., of the particular confocal microscope in question. In this thesis, axial resolutions quoted will assume the full-width at half maximum (FWHM) intensity measurement with a mirror where Eqn. 2.14 is the most relevant. Axial resolutions involving photoluminescent specimens are expected to be worse than the ones quoted.

It is important to always measure the lateral and axial resolutions experimentally for the various microscope objective, pinhole size and detector lens combinations in order to properly characterize the confocal microscope in question. Lateral resolution can be measured by imaging an appropriate test target such as one with a series of highly reflective horizontal and vertical lines of known spacing. A measure of axial resolution, which agrees

with Eqn. 2.14, is obtained by imaging a flat mirror at various positions along the optic axis (z-direction). Plotting an intensity versus z-position graph will result in a curve such as the one shown in Fig. 2.7b. The FWHM, for such a distribution, is defined to be the axial resolution.

2.2.3 Confocal Slicing

As was mentioned in section 2.2.1, most confocal microscopes raster scan a diffraction-limited spot over a specimen in order to generate a confocal image. Fig. 2.8a illustrates how a wide-field microscope obtains an image all at once by illuminating the entire specimen. This form of imaging is inherently a parallel or an analog process and requires the use of a CCD camera, for example, to convert it to a digital image. Scanning microscopy (Fig. 2.8b) is inherently a serial or a digital process as shown in Fig. 2.9a. By illuminating one point at a time, the scanning microscope gains a tremendous increase in light intensity when compared to a wide-field microscope. The scanning microscope scans the spot (or the specimen) over a square grid area. The grid size in this case is 16 x 16 where each individual square is referred to as a pixel. Therefore this microscope will generate a 16 x 16 pixel image. The grid in Fig. 2.9a is as large as possible because the corners touch the borders on the objective's field of view.

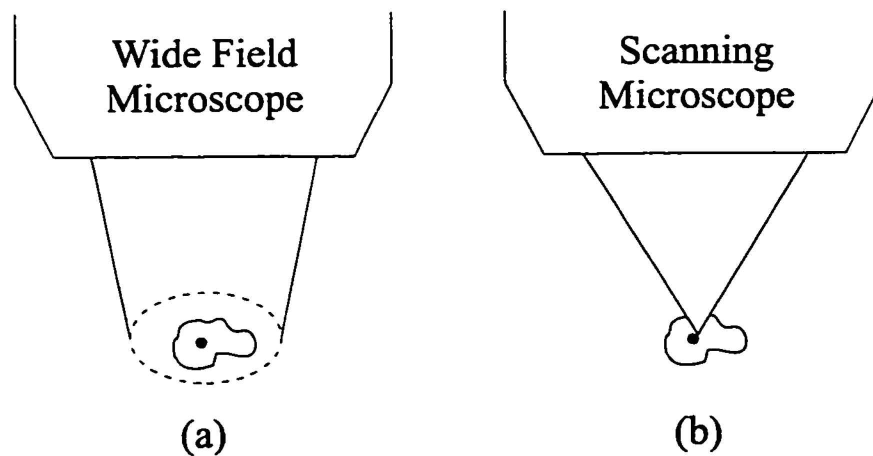

Figure 2.8 (a) A wide-field microscope views the entire image all at once. (b) The scanning microscope looks at one point at a time such that a digital image can be assembled by raster scanning the diffraction-limited spot.

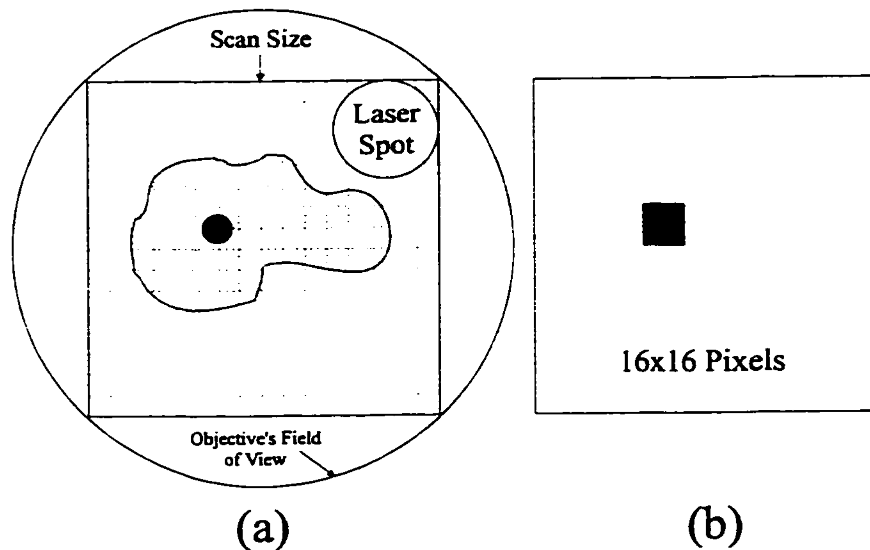

Figure 2.9 (a) A scanning microscope generates an image by moving a laser spot over every pixel position on a grid. (b) The 16x16 grid is too coarse and produces a very boxy or pixelated image. Common image sizes range from 256x256 to 2048x2048 pixels.

This grid size corresponds to zoom 1, zoom 2 is obtained by reducing the grid size by a factor of 2 while maintaining the same number of pixels. This sort of electronic zoom is distinctly different from a wide-field microscope where a greater magnification is achieved by changing to different objective lenses or eyepieces. In order to obtain an image of the amoeba in Fig. 2.9a, the laser spot must be moved to each pixel position on the grid. Each pixel position will generate a particular reflectivity, photoluminescence, etc., which is recorded digitally. Typically the detector signal is represented by one of 256 gray levels. The laser spot size in Fig. 2.9a was chosen to satisfy the Nyquist theorem[13], which states that at least 2.3 samples should be taken for each resel (resolution limit distance). Assuming that the laser spot or disk in Fig. 2.9a has a diameter equal to twice the Airy radius, then the pixel size should be at least 4.6 times smaller than the disk in confocal mode and there should be $1.4 \times 4.6 \cong 6.4$ pixels per Airy disk diameter. Fig. 2.9b shows what the resultant image of the amoeba might look like using the very course 16 x 16 grid. Clearly a finer grid is required. Typical grid sizes range from 256 x 256 up to 2048 x 2048 pixels, where UW-CMG typically uses 512 x 512 pixel grids.

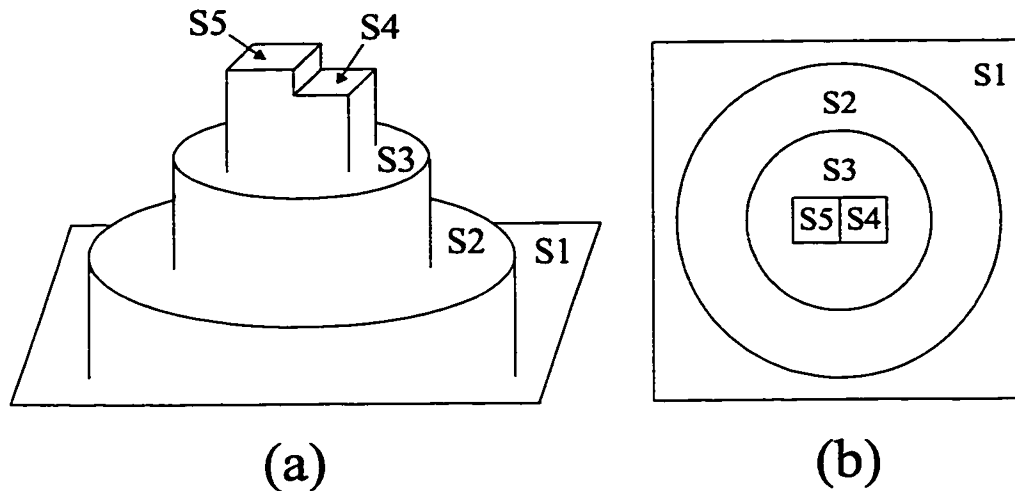

Figure 2.10 (a) Side and (b) top views of a test object used in a confocal slicing example. All surfaces are assumed to be flat and of equal reflectivity.

An image generated with the confocal system of Fig. 2.5 using either a scanning stage or a scanning beam is referred to as a confocal slice. By moving the objective lens or the specimen in the z-direction, several confocal slices can be taken which will contain in-focus information for all parts of the specimen. These slices can be assembled to produce 3-D topographical and extended focus images of the specimen.

Fig. 2.10a and 2.10b show the side and top view, respectively, of an imaginary test object which will be used to demonstrate confocal slicing. Surfaces S1, S2,...S5 are assumed to be flat and of equal reflectivity. In order to obtain information about the entire specimen, a large number of confocal slices must be taken, about 2 slices per axial resolution distance. Fig. 2.11a shows a cross-sectional view of the test object showing three such slice positions (focal planes 1, 2, and 3) and the axial resolutions associated with the microscope objective being used. If an object is right at the edge of the axial resolution band, the image will appear half as intense as an image taken when the focal plane lies at the surface position. Focal plane 1 is close to S2 such that the image of S2 appears at ~ 85% of its maximum intensity (see Fig. 2.11b). The rest of the image is black since all other objects lie several axial resolutions away from focal plane 1. The corresponding image for the confocal slice at focal plane 2 (not shown) is entirely black since no objects fall within several axial resolutions. Focal plane 3 will generate an image with S4 at about 85% maximum intensity and S5 at 20% maximum intensity (S5 lies just beyond the axial resolution limits) as shown in Fig. 2.11c.

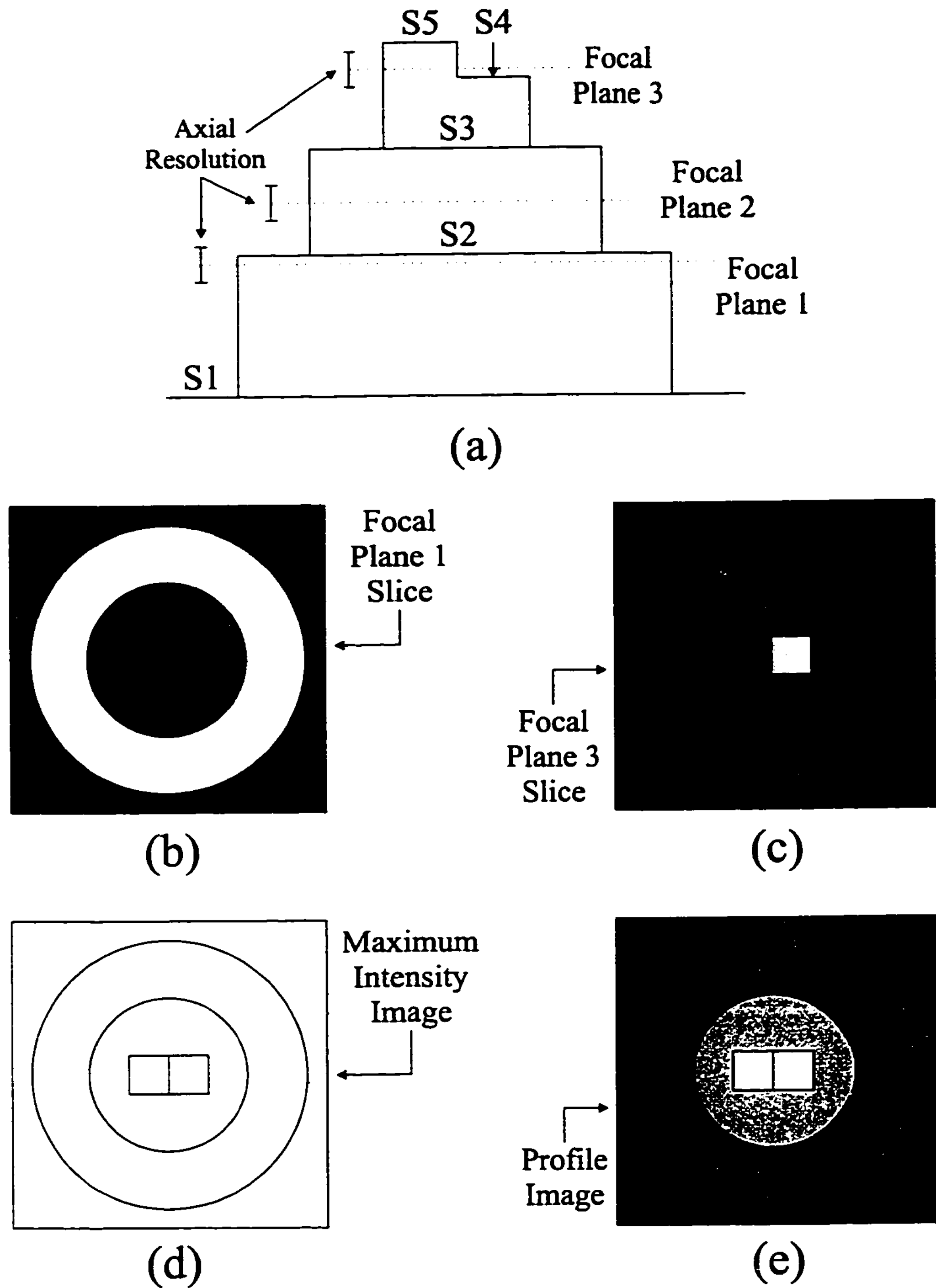

Figure 2.11 (a) A cross-section of the object from Fig. 2.10 showing three focal plane positions where confocal slices will be taken. (b) The image obtained at focal plane 1 will be black everywhere except surface 2 since all other surfaces lie too far away from focal plane 1. (c) The focal plane 3 image includes images of S4 and S5 while the rest is black. (d) The maximum intensity image shows the entire object in high resolution focus. (e) The profile image shows the surfaces as a function of height where white is high and black is low.

Figs. 2.11d and e show the maximum intensity and profile image respectively obtained by combining the data from approximately 20 slices. The maximum intensity image is generated by choosing the maximum intensity pixel among the 20 slices for every pixel position, where it is assumed the object is at best focus. The maximum intensity (MXI) or extended focus image is one in which all parts of the object are in focus and is equivalent to an image taken with a very long depth of field objective lens but with the added bonus of the high lateral resolution obtained with a high NA objective. The MXI image in Fig. 2.11d shows all surfaces in focus but is not terribly interesting since the surfaces were defined to be of equal reflectivity. The profile image is produced by recording the slice position at which the maximum intensity pixel has occurred for each pixel position. Every slice position corresponds to a certain height (z-position) which is converted to a gray scale. Fig. 2.11e shows a profile image where white is high, and black is low. S5 has been assigned pure white while S1 is pure black, and correspondingly S4, S3, and S2 are 11, 30, and 60% black respectively.

2.3 The Confocal Microscope System

Fig. 2.12 shows a block diagram of a typical cslm. The blue lines indicate the light path going toward the objective and the red lines denote the light path returning from the specimen towards the detector arm. The x/y scan part of the microscope will be given extra emphasis in this thesis since it has proven particularly troublesome in both the cslm and MACROscope. Each component in Fig. 2.12 will be discussed briefly in the next sections.

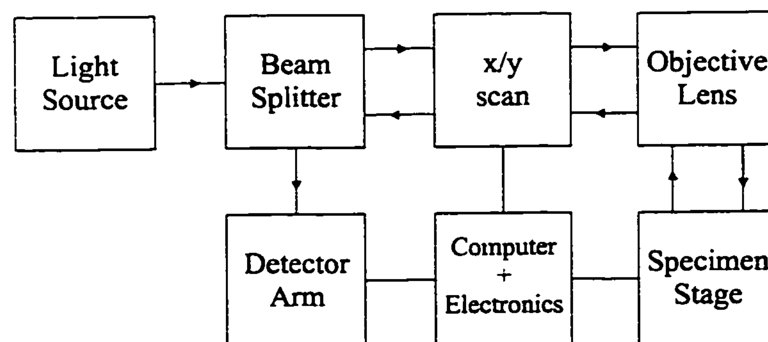

Figure 2.12 Block diagram or flowchart of a generic confocal scanning laser microscope.

2.3.1 Light Sources

Fig. 2.13 shows two types of light sources used in cslms: (a) laser and (b) non-laser. A cslm will typically include a continuous wave (CW) gas laser in the 5-50 mW range. The set of lasers used by UW-CMG are representative of the cslm industry: several HeNe lasers (534, 633 and 1152 nm emission) providing 1-10 mW power, an Ar-ion laser (488 and 514 nm emission) providing 10 mW total power, an Ar-Kr laser (488, 568 and 647 nm emission) with 50 mW total power, and a HeCd laser (325 nm emission) providing ~ 10 mW power. All the above lasers are air-cooled, easy to operate, portable, cost less than $15000, and have a lifetime exceeding 2000 hrs. The large range in emission wavelengths is desirable since it allows a greater amount of flexibility in imaging and short wavelengths such as 325 and 488 nm are especially valuable since they are used in autofluorescence and to excite a variety of fluorophores. Semiconductor lasers have recently begun to replace some gas lasers providing similar performance at a reasonable price. Chapter 5 of the Confocal Handbook[14] gives a thorough review of lasers used in cslms including pulsed lasers which are used in two photon excitation and in fluorescence lifetime measurements.

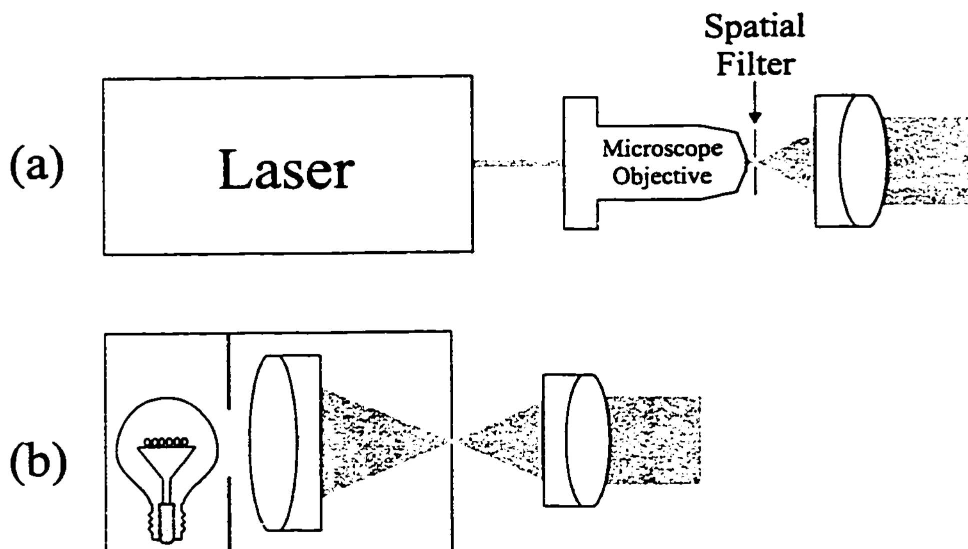

Figure 2.13 (a) Cslms commonly use lasers to illuminate the specimen. The laser beam must be expanded in order to fill the specimen microscope objective (not the one above). A pinhole is sometimes inserted at the focal point of the expander's objective to provide a good beam profile. (b) A simplified setup for a non-laser source such as an arc lamp.

Lasers have properties which in most cases are highly desirable: highly monochromatic light, small divergence, very high brightness, plane polarized emission, and a high degree of spatial and temporal coherence. Fig. 2.13a shows how the laser beam must be expanded to some degree in order to fill the entrance pupil of the microscope objective. A common beam expander consists of a microscope objective followed by an achromatic doublet such that their foci are coincident thus forming a beam-expanding telescope. The microscope objective acts like a very short focal length, nearly aberration-free lens which generates a rapidly expanding beam. The beam expander operates solely on axis such that only spherical and axial chromatic aberrations are present. This type of beam expander is satisfactory in most cases; however, when simultaneous multiwavelength and IR to UV operation is required then a mirror beam expander must be used (see Chapters 5, 6, this thesis). A pinhole is sometimes placed at the focal point of the microscope objective which acts like a spatial filter and 'cleans up' the beam creating an Airy disk beam profile at the achromat. Alignment is critical since an incorrectly placed or mismatched pinhole can decrease the output intensity significantly.

Fig. 2.13b shows a simple schematic of a non-laser light source. Some common non-laser light sources are tungsten-ribbon or quartz halogen lamps, and xenon, mercury, carbon or zirconium arc lamps. The quartz halogen lamp, for example, produces a continuous spectrum approximately following the shape of a blackbody at about 3000K. Arc sources come in a variety of wavelength distributions ranging from continuous to line spectra, and many times, a mix of both. Chapter 6 of the Confocal Handbook[15] gives an excellent review of various non-laser light sources and their operation. There are several features which distinguish non-laser sources from lasers:

1) The radiant energy is distributed over many wavelengths rather than being concentrated in very narrow bands at one or two wavelengths. Lamps therefore operate with hundreds of watts of power rather than milliwatts.
2) They are spatially and temporally incoherent which can be advantageous since this eliminates interference effects due to reflections from optical surfaces.
3) The cost of lamps tends to be less than lasers.

4) Non-laser sources are commonly available and are readily interchangeable as part of a conventional microscope illumination system.

While non-laser light sources have several advantages over laser sources, the majority of commercial cslms utilize lasers. For applications in which an extremely bright monochromatic excitation source is required, such as PL, lasers are the best choice.

2.3.2 Beam Splitter Assembly

Fig. 2.14 shows a photoluminescence set-up for the beam splitter assembly consisting of a short wavelength laser line filter (blue, 488 nm), a dichroic beam splitter which transmits short wavelengths but reflects long wavelengths, and a long pass filter which transmits wavelengths longer than 550 nm (orange).

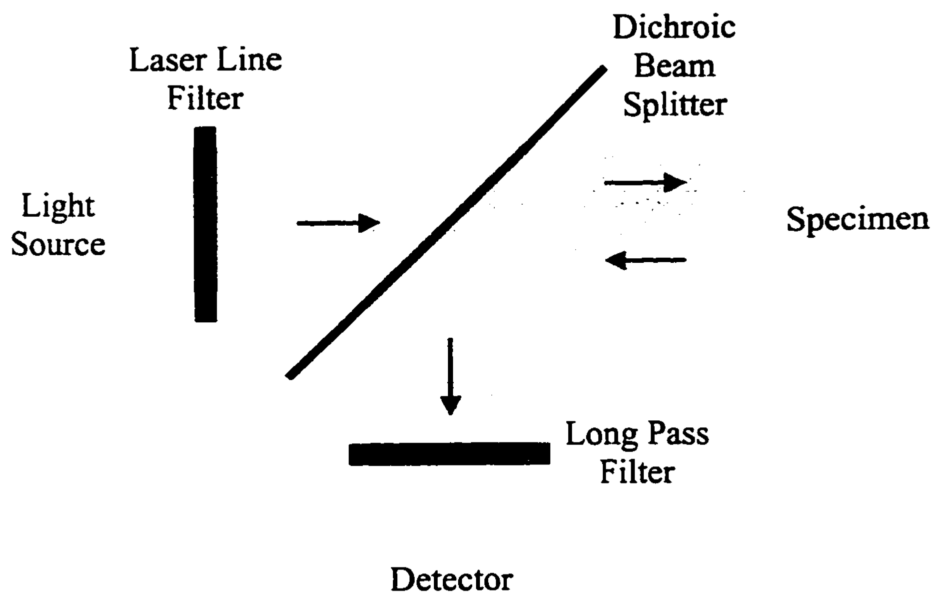

Figure 2.14 An example of a typical beam splitter assembly. The laser line filter isolates one line from the laser source which is transmitted through a dichroic beam splitter. Photoluminesce emissions are reflected by the beam splitter and pass through a long pass filter.

Light source and detector filters can be divided into four categories:

1) Neutral density filters (NDFs)

   NDFs are designed to attenuate light uniformly over the entire spectrum, hence the term neutral. They come in three varieties: metallic films (such as inconel or chrome), absorbing glass, or multilayer thin film dielectric. NDFs are measured in terms of optical density (OD):

   $$\% \text{ light transmitted} = 10^{2-(OD)} \qquad \textbf{(2.15)}$$

2) Polarizers

   In some cases polarizers, ¼, and ½ wave plates are used in various applications.

3) Band Pass Filters

   These multilayer, thin film dielectric filters can be designed to pass a narrow band of wavelengths such as with laser line filters (2 - 10 nm width), a slightly wider band (20 - 40 nm) used with incoherent white light sources, and large bands of practically any size and shape. Laser line filters are particularly useful in photoluminescence imaging where they are used to eliminate unwanted laser lines and plasma lines which in some cases are in a similar wavelength range to the photoluminescence emission. A special type of filter called a notch or laser line blocking filter is designed to pass all wavelengths <u>except</u> a particular laser line. An obvious combination for photoluminescence measurements is a laser line filter transmitting only the laser line filter at the source, plus a laser blocking filter in the detection arm. This combination allows all PL wavelengths to be detected.

4) Short and Long Pass Filters

   These filters are similar to band pass filters in that the pass band includes anything shorter or longer than a given wavelength. Short pass filters are generally made from multilayer thin films. While this is also true of long pass filters, there is also absorbing Schott glass which works very well at blocking the intended wavelengths. Unfortunately many types of absorbing glass photoluminesce and precautions must be taken in order to avoid imaging artifacts.

Beam splitters, which can be considered to be special types of filters, come in three basic varieties:

1) Neutral beam splitters typically consist of a thin metallic layer on a glass substrate so as to achieve the required transmission/reflection ratio. A common 50% reflection / 50% transmission beam splitter falls into this category.
2) Polarizing beam splitters consist of prisms specially made to transmit one polarization and reflect the other.
3) Dichroic beam splitters preferentially transmit a range of wavelengths while reflecting a different range of wavelengths with little or no absorption involved.

2.3.3 x-y Scan Arm

A critical part of a cslm is the x-y scan arm. It is responsible for generating a beam pivoting about a single point coincident with the telecentric plane of the objective. Before describing the four basic types of x-y scanners, the concepts of a telecentric plane and an ideal unitary telescope will be outlined.

Fig. 2.15 shows a collimated beam of light incident upon a simple, positive, thin lens of focal length f. The central ray of the collimated beam passes through the first focal point and must therefore exit parallel to the optic axis after striking the central plane of the lens coming to focus at the focal plane. As long as the collimated beam pivots about the first focal point, such that the central ray always passes through said point, the focusing cone will always be a right angle cone (i.e. with the central ray perpendicular to the focal plane and parallel to the optic axis).

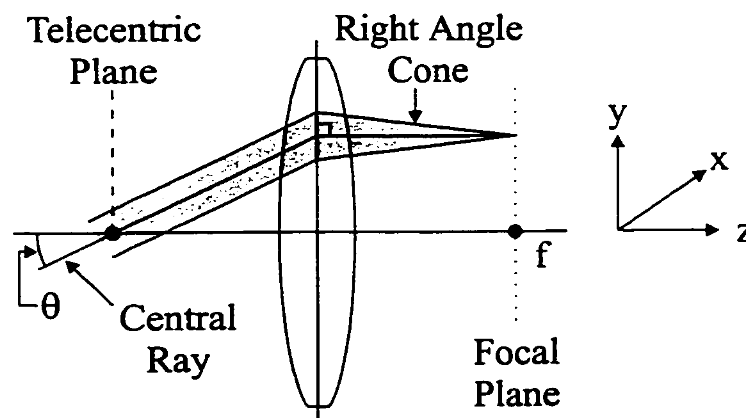

Figure 2.15 A thin lens operated in telecentric mode. When the central ray of a collimated beam passes through the first focal point of a positive lens the resulting cone of light will be a right angle cone.

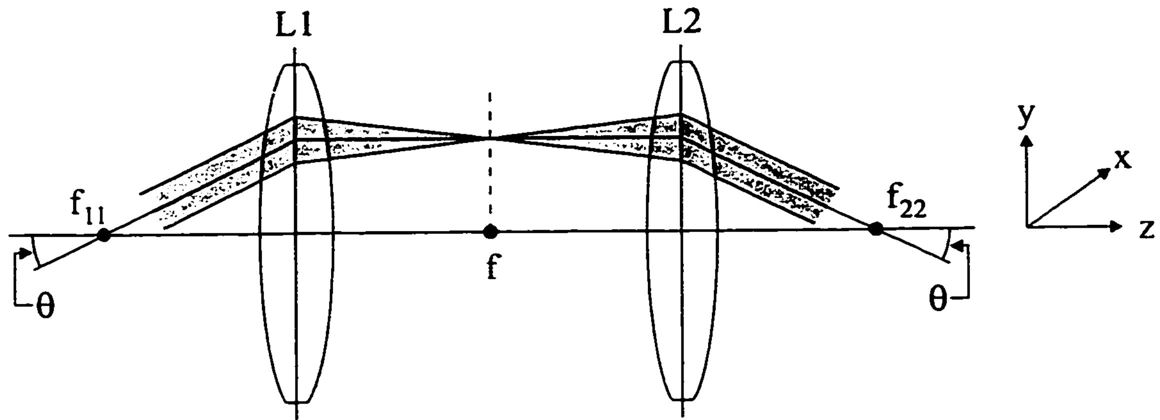

Figure 2.16 A unitary telescope is made up of two identical lenses separated by two focal lengths. A collimated beam pivoted around f_{11} at some angle θ will emerge collimated and with unit magnification pivoting around f_{22} at the same angle.

The lens in Fig. 2.15 is said to be operated in telecentric mode and its telecentric plane is its first focal plane. This lens setup has the interesting property of returning the beam along the exact same path when used as an objective with a plane mirror specimen.

Fig. 2.16 shows a schematic of a unitary telescope made up of two identical simple, positive, thin lenses of focal length f, separated by a distance 2f. Fig. 2.16 is the same as Fig. 2.15 with a mirror image of the system about the second focal point. A collimated beam pivoted at angle θ about the first focal point of lens L1 (f_{11}) will focus telecentrically at the common focal plane, diverge in a right angle cone, and emerge after L2 as a collimated beam at an angle θ with respect to the optic axis passing through the second focal point of lens L2 (f_{22}). This unitary telescope accepts a collimated beam pivoting about f_{11} and generates a collimated beam of equal size pivoting about f_{22}. A continuously pivoting beam can be achieved by inserting a scanning mirror centered at f_{11}. If an objective lens, such as the one in Fig. 2.15, is placed so that its first focal point is coincident with f_{22}, then the pivoting beam will emerge from the objective as a telecentric beam scanning in the y-direction. Inserting a second scanning mirror at f_{22} into the above system, followed by a second unitary telescope, this time scanning the beam in the x-z plane, will result in a telecentric scanning beam in the x-y plane. A 2-D confocal slice can be now obtained by raster scanning the beam in a grid pattern over the entire specimen. In Fig. 2.16, f_{11} and f_{22} are known as conjugate points and the unitary telescope is also called an optical relay.

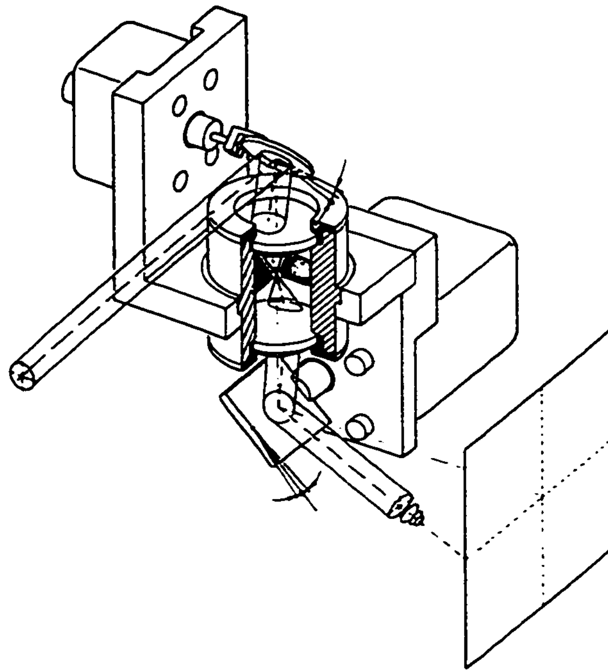

Figure 2.17 An x-y scanner arrangement utilizing a telescope right after the first scanning mirror to bring the beam back to a stationary point on the second scanning mirror. In theory this a perfect telecentric system. In practice the telescope optics must be very well corrected for the system to work properly. Figure modified from Confocal Handbook[16].

Figs. 2.17, 2.18, 2.19 and 2.20 illustrate four different types of x-y scanner arrangements taken from the Confocal Handbook[16]. Fig. 2.17 shows basically the same arrangement as Fig. 2.16. In practice, the relay optics (telescope) must be extremely well-corrected for monochromatic and chromatic aberrations (see chapter 5) in order to ensure diffraction-limited operation. Well corrected relay optics can be very expensive and involve several elements which leads to a compromise in most situations. Fig. 2.18 shows an arrangement where the scanning mirrors are placed as close together as possible with no intermediate optics. The telecentric plane is optimally located at the midpoint between the mirrors. The magnitude and effect of this imperfect telecentric system is further discussed in chapter 3.

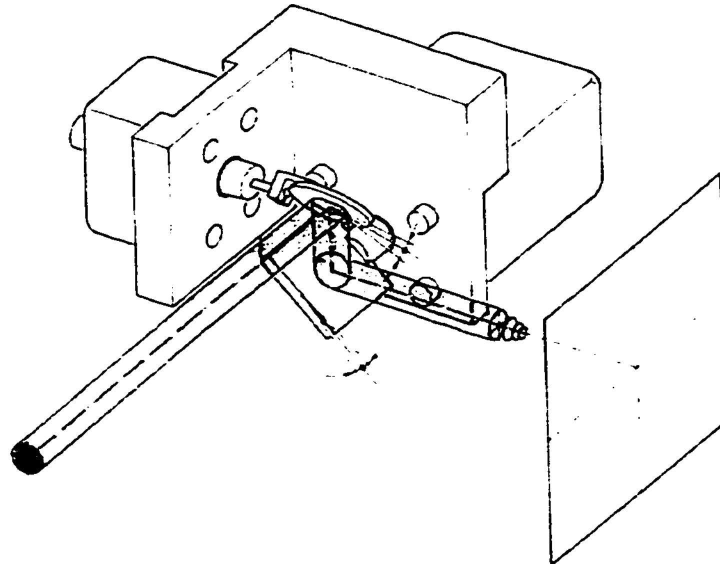

Figure 2.18 An x-y scanner utilizing no intermediary optics. This system is not perfectly telecentric and the error depends upon the distance between the scanning mirrors, the scan angle, and the objective lens. For optimum performance the first two quantities should be kept small. Figure taken from Confocal Handbook[16].

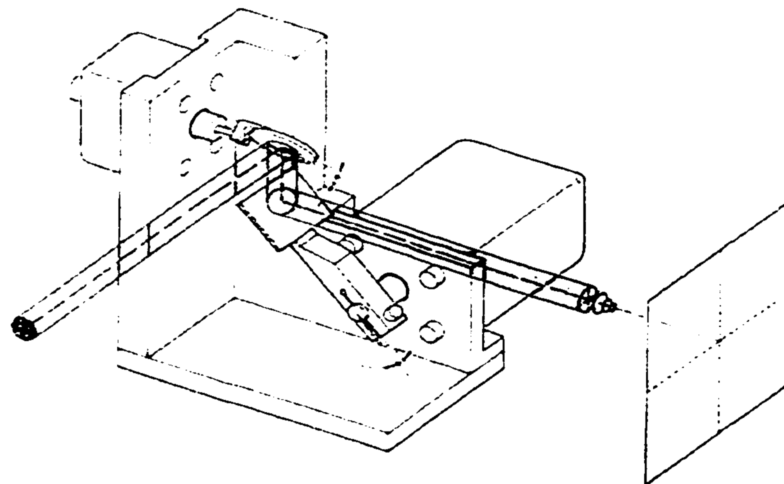

Figure 2.19 The system in Fig. 2.18 is improved by moving the axis of one mirror off the beam axis. In theory this improves the 'telecentricity' by a factor of 25. Figure taken from Confocal Handbook[16].

The system in Fig. 2.18 can be improved by moving the axis of one mirror off the beam axis as shown in Fig. 2.19. The second mirror shifts as it rotates improving the apparent position of the mirror in the telecentric plane by a factor of 25. Unfortunately, this system is only available commercially as a real-time system, utilizing a resonant mirror as the first mirror. The simplest solution is illustrated in Fig. 2.20 which involves a scanning mirror assembly which in turn is rotated by another scan unit such that a single mirror is used to scan along the x and y-directions. Once again, this system is commercially unavailable and it is unclear how accurate and reliable it would be due to the large loads it must rotate.

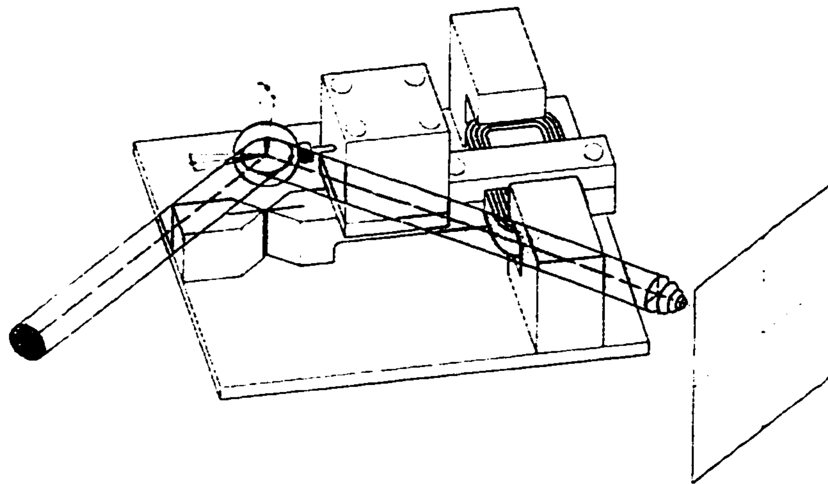

Figure 2.20 The simplest solution to the x-y scanner problem is to pivot one scan mirror in both the x and y directions. This is accomplished by pivoting the entire scan unit about the center of the mirror while scanning the mirror in an orthogonal direction. Figure taken from Confocal Handbook[16].

2.3.4 Microscope Objective and Specimen Stage

The microscope objective on any cslm determines the lateral and axial resolution along with the maximum field of view. It should provide diffraction-limited performance over the entire field of view and over an appropriate range of wavelengths when its entrance pupil is fully filled by a light beam with a good profile. Microscope objectives come in a large variety of types, manufactured to satisfy differing needs.

Below is shown what is written on the barrel of a Mitutoyo microscope objective used by UW-CMG:

M PLAN APO 100

0.70

∞ / 0   f = 200

M PLAN means that it is a metallurgical objective that has been corrected for curvature of field. If no other aberrations are present, this objective will generate a uniform, homogeneous image of a flat mirror test specimen. Curvature of field would cause the image of a flat mirror to be increasingly dark near the edges. APO is short for apochromatic which refers to the amount of colour correction. Achromatic objectives are corrected for two colours chromatically and one colour for spherical aberration. In semi-apochromatic objectives, the crown glass in the achromatic objective is partially or completely replaced with cubic, crystalline calcium fluoride known as fluorite or fluorspar. Semi-apochromats are spherically and chromatically corrected for two colours. Apochromatic objectives go one step further and achieve chromatic correction for three colours and spherical correction for two colours. Fig. 2.21 shows an apochromatic objective focused onto a specimen stage.

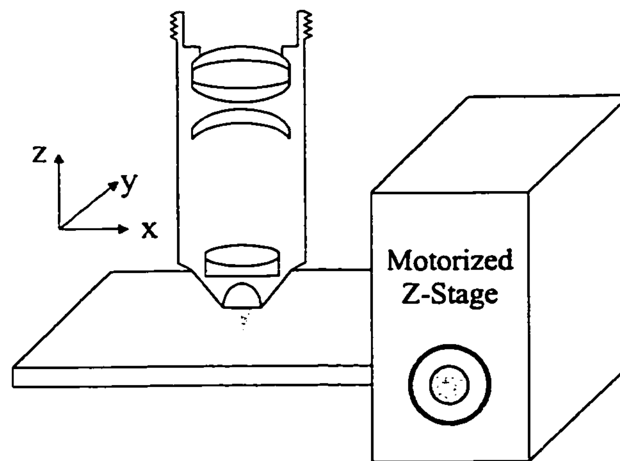

Figure 2.21 A simplified diagram of the specimen stage including a stepping motor to allow computer controlled movement in the z-direction. An apochromatic microscope objective lens is also shown.

'100' refers to the magnification, when used with the appropriate tube lens, and 0.70 is the NA. The symbol ∞ / 0 means that the objective has an infinite tube length, that is, it is infinity-corrected, and that it is designed to operate without a coverslip (it is a metallurgical objective). Since this is an infinity-corrected objective it must be used with a tube lens of focal length f = 200 mm in order to work in a microscope. The combination of tube lens and infinity-corrected objective produce a non-infinity corrected system which can be mated with an eyepiece resulting in a compound microscope. This is briefly treated in Appendix 2. In addition to the above mentioned 'dry' objective, there are water and oil immersion objectives in which the surrounding medium is no longer air and n, in Eqn. 2.10, starts taking on values greater than 1. In addition to improving the NA of the objective, water or oil immersion objectives are designed to reduce or eliminate spherical aberration produced by coverslips and/or the specimen's surrounding medium. There are many other types of objectives such as reflecting, UV, and polarizing objectives to name a few. The reader is, once again, referred to the Confocal Handbook[17] and J. H. Richardson's guide[18] for further information.

The specimen stage usually consists of a standard microscope specimen stage attached to some kind of stepping motor or piezo stage to provide motion in the z-direction. The most important attributes of the z-stage are accuracy, repeatability, and linearity. The smallest step achievable is typically 50 or 100 nm which matches nicely with high NA axial resolutions.

2.3.5 Detector Arm

Fig. 2.22 shows two possible configurations for detector arms in a cslm. Both configurations assume a collimated entrance beam and thus infinity-corrected operation. Fig. 2.22a shows a typical arrangement used by UW-CMG where a collimated beam is focused down to a diffraction-limited spot by an achromat. The confocal pinhole is coincident with the diffraction-limited spot and tends to be 50 - 60% of the spot size in order to achieve a fully optimized confocal effect. Alignment of the pinhole, in many cases to within tenths of microns, is critical for proper operation.

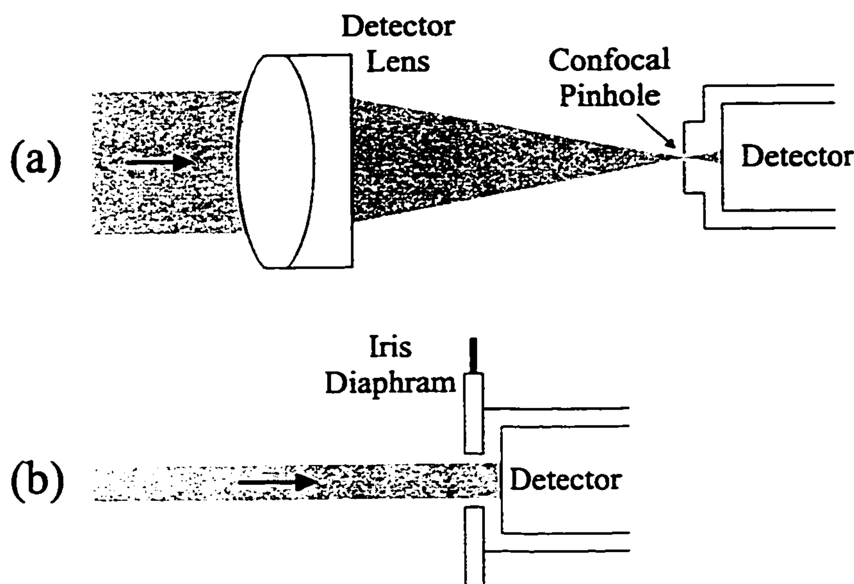

Figure 2.22 Infinity corrected configurations for the detector arm in a cslm. (a) An achromat focuses the beam down to a diffraction-limited point coincident with a pinhole about 50-60% the size of the Airy disk. Confocal operation requires the careful alignment of a properly matched pinhole. (b) Here, the confocal effect relies on the high NA of the microscope objective producing a widely divergent beam at the detector when out of focus. The detector must be placed far from the objective in order to enhance this effect.

Detectors are typically either photoemissive or photovoltaic in nature. Photoemissive detectors such as the photocathode used in photomultiplier tubes (PMTs) are most sensitive to short wavelengths including the UV with photon efficiencies peaking at about 25% in the blue. The main advantage of the PMT is that it provides a large amount (10^5 - 10^7) of nearly noise-free gain, however, beyond 700 nm efficiencies are quite poor (< 5%). Photovoltaic devices such as avalanche photodiodes (APDs) and p-i-n diodes provide enhanced efficiencies (70%+) and broader wavelength response into the IR. Silicon devices typically operate in the ~ 400-1000 nm range. Unfortunately, these devices require better amplification than PMTs in order to measure their signals. The Confocal Handbook[19] provides an in-depth review of detectors in chapter 12. Table 2 on page 188 of the Confocal Handbook is especially useful, listing many types of detectors and their corresponding specifications.

Fig. 2.22b shows a configuration used by Biorad[20] which relies on the objective's high NA for the confocal effect.

The detector is also placed far (1 m+) from the rest of the optics by using a series of fold mirrors such that a diverging or converging beam from the objective will result in 'spot' much larger than the entrance hole on the iris diaphragm. Such a configuration allows for easy alignment, due to the macroscopic nature of the beams, and continuous variability for the confocal iris.

Figure 2.23 Schematic diagram of a Leica confocal microscope taken from their 1996 brochure.

2.3.6 Computer and Electronics

Each pixel position on the specimen will have a certain detector signal associated with it, representing an intensity value. This signal must be amplified, measured, and then recorded digitally for eventual storage in computer memory. UW-CMG utilizes a PMT which feeds a current-to-voltage amplifier, which in turn is linked to a 512 x 512 pixel, 8 bit frame grabber. It accepts a 0-1 V analog signal and outputs a corresponding 0-255 digital number or gray level.

The frame grabber dumps its memory to a computer and thus creates a 512 x 512 pixel, 256 gray level image. In addition to the above analog-to-digital conversion, computer control is utilized to synchronize the mirror motion and hence pixel position on the specimen, with data acquisition. In most cases the z-stage is also computer controlled such that confocal slicing can be done automatically.

Fig. 2.23 shows a schematic diagram of a Leica confocal microscope taken from their brochure. It integrates many of the features discussed in section 2.2. Most notably, the Leica utilizes a single-mirror scanner and an adjustable pinhole.

2.4 Summary and Discussion

The goals for this chapter were as follows:

1) To provide a brief review of elementary, thin lens optics which will be used throughout the thesis to illustrate various concepts.
2) To introduce confocal optics, lateral and axial resolution, and the concept of slicing. Minsky[1] pointed out several advantages derived from confocal optics:
   - increased lateral resolution
   - confocal slicing or optical tomography possible allowing for 3-D imaging
   - electronically controlled magnification
   - reduced blurring from high scattering or photoluminescent specimens due to exclusion of light outside the focal plane
   - complex contrast effects possible
3) To give a brief tour of the components which make up a typical cslm.

This chapter was also intended to link chapter 3, where the present versions of the cslm and MACROscope are characterized, and chapter 6 which suggests improvements and modifications to existing systems in order to facilitate a fully integrated MACROscope/Microscope.

REFERENCES

[1] M. Minsky, U.S. Patent #3013467, 1957.

[2] E. Hecht, Optics, 2nd Edition (Addison-Wesley, Reading Massachusetts, 1987), p142.

[3] E. Hecht, Optics, 2nd Edition (Addison-Wesley, Reading Massachusetts, 1987), p190.

[4] E. Hecht, Optics, 2nd Edition (Addison-Wesley, Reading Massachusetts, 1987), p214, Eqn. 6.8.

[5] E. Hecht, Optics, 2nd Edition (Addison-Wesley, Reading Massachusetts, 1987), p148, Eqns. 5.35, 5.36.

[6] J. B. Pawley (Editor), Handbook of Biological Confocal Microscopy, 2nd Edition, (Plenum, New York, 1995), p2.

[7] E. Hecht, Optics, 2nd Edition (Addison-Wesley, Reading Massachusetts, 1987), p420.

[8] E. Ingelstam, Problems in Contemporary Optics, (Istituo Nazionale di Ottica, Arcetri-Firenze, 1956), p128-143.

[9] J. B. Pawley (Editor), Handbook of Biological Confocal Microscopy, 2nd Edition, (Plenum, New York, 1995), p112, p159.

[10] Personal communication with G.J. Brakenhoff.

[11] C.J.R. Sheppard, Journal of Microscopy, **149** (1988) 73.

[12] J. W. Bowron, Ph.D. Thesis, 1993, Physics Department, University of Waterloo, Waterloo, Canada, p47.

[13] J. B. Pawley (Editor), Handbook of Biological Confocal Microscopy, 2nd Edition, (Plenum, New York, 1995), p58.

[14] J. B. Pawley (Editor), Handbook of Biological Confocal Microscopy, 2nd Edition, (Plenum, New York, 1995), Chap 5.

[15] J. B. Pawley (Editor), Handbook of Biological Confocal Microscopy, 2nd Edition, (Plenum, New York, 1995), Chap 6.

[16] J. B. Pawley (Editor), Handbook of Biological Confocal Microscopy, 2nd Edition, (Plenum, New York, 1995), p147, 148, Figs. 10 - 13.

[17] J. B. Pawley (Editor), Handbook of Biological Confocal Microscopy, 2nd Edition, (Plenum, New York, 1995), Chap 7.

[18] J.H. Richardson, Handbook for the Light Microscope - A User's Guide, (Noyes Publications, Park Ridge, New Jersey, 1991), p77.

[19] J. B. Pawley (Editor), Handbook of Biological Confocal Microscopy, 2nd Edition, (Plenum, New York, 1995), Chap 12.

[20] J. B. Pawley (Editor), Handbook of Biological Confocal Microscopy, 2nd Edition, (Plenum, New York, 1995), p584.

CHAPTER 3

CHARACTERIZATION OF THE CONFOCAL SCANNING LASER MICROSCOPE AND MACROSCOPE

Commercial scanning beam confocal microscopes are typically limited to a field of view less than 5 x 5 mm in size. Scanning stage microscopes have no such field of view limitations; however, they tend to be slow where scan times can reach several minutes for centimeter sized objects, while scan times for scanning beam systems last several seconds. Both these systems are capable of high NA, high resolution operation.

In the early 1990s, The University of Waterloo's Confocal Microscopy Group (UW-CMG) designed a confocal scanning laser MACROscope (cslM) which combined the high scanning speed of a confocal scanning laser microscope (cslm) with the large area scanning ability of a scanning stage microscope (SSM). It provides a relatively high NA, given its low magnification. The MACROscope has evolved through the years to become a distinctly different instrument than the cslm. Efforts have also been made to fuse these two instruments together in order to create a confocal scanning laser MACROscope/Microscope (cslM/m). The first part of the chapter examines the UW-CMG cslm. Each of its components is examined, also the cslm as a whole is characterized with respect to throughput, lateral and axial resolutions, and some of its limitations are examined. The second part of the chapter shows how the MACROscope has naturally evolved from the cslm. The MACROscope is then characterized with respect to throughput, lateral and axial resolution in addition to stating its limitations. The last part of this chapter gives preliminary results from a spectrally resolved MACROscope which is capable of producing images as a function of wavelength in addition to position.

Several new contributions were made: a prototype MACROscope was constructed which lead to subsequent developments and improvements. . PMT linearity for Hamamatsu models R292 and R2228 was measured. The MACROscope and cslm were characterized with respect to throughput, lateral resolution, and axial resolution. This is the first time all this

information has been accumulated in one source. Experimental evidence of aberrations from the unitary telescopes on the cslm was shown. Experimental evidence and analysis of non-telecentric operation was illustrated. Characterization with respect to spectral resolution was shown for a spectrally resolved MACROscope

3.1 The cslm

The UW-CMG cslm was originally constructed in the mid-1980s in order to provide the group with a prototype scanning beam confocal microscope. This cslm readily allowed access to all of its components and facilitated a wide variety of experiments meant to characterize and improve its performance as well as image a large variety of specimens. A notable achievement was the development of the world's first confocal scanning laser transmission microscope[1] which is capable of imaging specimens with transmitted and reflected light from above or below the specimen, or both.

Although the cslm has previously been characterized[2] to some extent, it is important to assess not only its axial resolution as a function of pinhole size, but also the corresponding relative intensity and the extent of the unaberrated field of view. This data is critical in evaluating the performance of the cslm and identifying modifications needed for its improvement. It is clear that if the MACROscope/Microscope is to work properly, then the cslm part of the instrument must meet, and in some cases exceed, the optical standards set by commercial confocal microscopes. A clear understanding of the cslm and its present abilities is a natural step to chapter 6 of this thesis where suggested improvements are analyzed.

3.1.1 cslm Component Breakdown

Fig. 3.1 shows a schematic diagram of the cslm. Light used for excitation originates from the laser source arm which consists of a laser, mirror M1 and M2, a beam expander, and a laser line filter. This part of the cslm sits directly on a vibration isolation table and the rest of the cslm components are mounted on a breadboard which sits vertically on the vibration-isolation table. An expanded beam from the laser source arm passes through the beam splitter and strikes the y-scanning mirror which deflects the beam in the x-y plane.

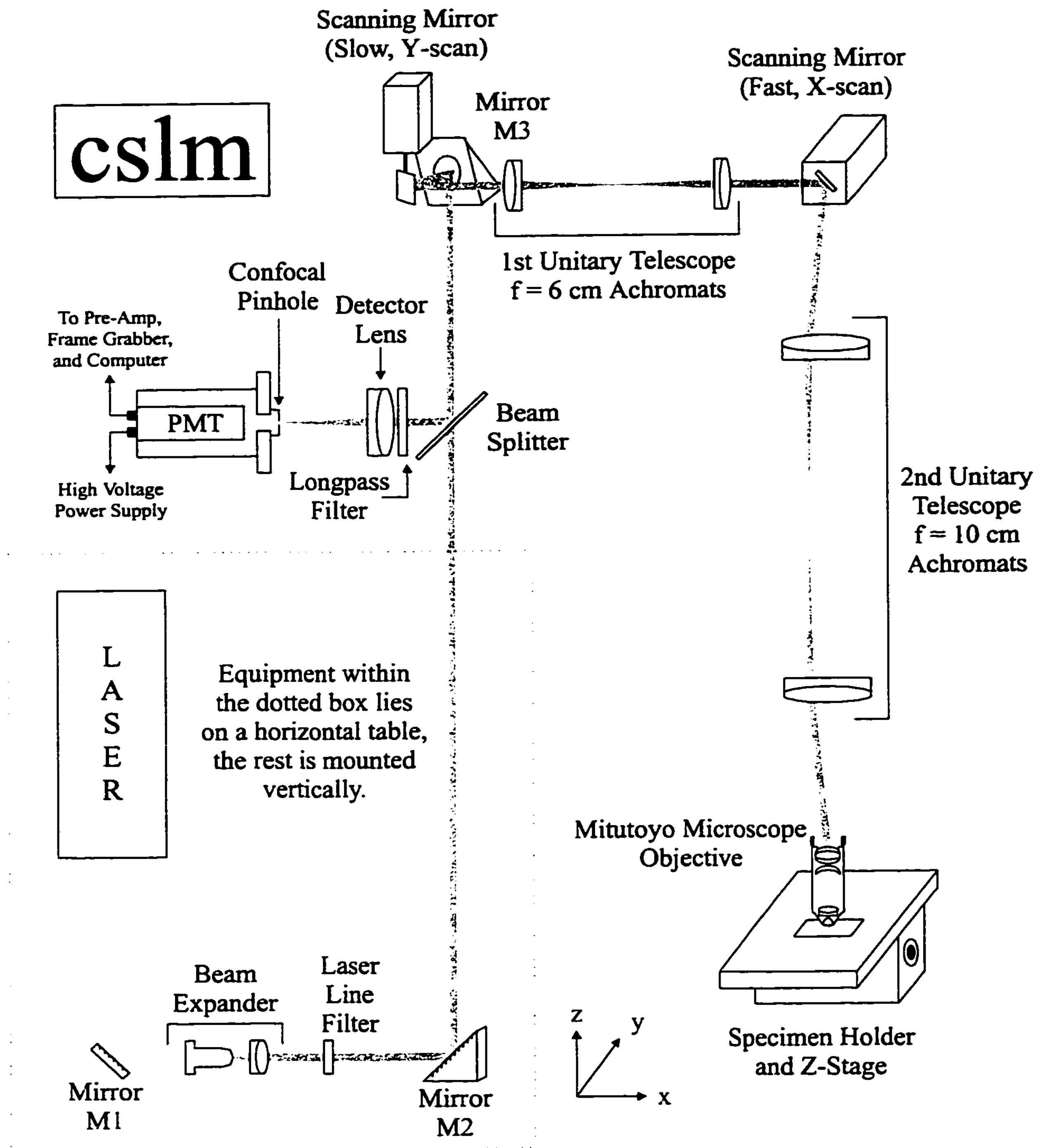

Figure 3.1 Schematic diagram of the confocal scanning laser microscope (cslm).

The first unitary telescope brings the beam back to the x-scanning mirror such that the beam pivots on the center of the x-scanning mirror as the y-scanning mirror scans. The x-scanning mirror deflects the beam in the x-z plane, and the second unitary telescope brings the beam back to the center of the objective lens such that the beam pivots at the telecentric plane of the objective. Light returning from the specimen is collected by the microscope objective, descanned by the system of scanning mirrors and telescopes and is partially reflected by the beam splitter into the rest of the detector arm which consists of the beam splitter, a filter (if needed), an achromatic detector lens, a confocal pinhole, and a PMT detector. The beam is focused by the detector lens to a diffraction-limited spot. The confocal pinhole resides at the focal point of the lens and acts as a spatial filter allowing some of the light from the specimen to strike the PMT detector. The signal generated by the PMT is amplified and converted to a voltage by the pre-amplifier. This voltage signal is then digitized by a frame-grabber and converted to a 0 - 255 gray level which is stored in memory.

The next four sections will examine the cslm components in detail. Particular emphasis will be given to critical components such as the scanning mirrors and unitary telescopes.

3.1.1.1 Laser Source Arm

The purpose of the laser source arm is to provide a highly uniform and intense collimated light beam expanded to an appropriate diameter such that it slightly overfills the entrance pupil of the microscope objective. UW-CMG uses continuous wave, low power gas lasers ranging from 325 to 1152 nm in emission wavelength. Table 3.1 shows a list of lasers used on the cslm with their associated wavelength and power. The beams generated by the lasers in Table 3.1, are from 0.5 to 1 mm in diameter and are stable, with respect to intensity, to within 1%.

Laser Type	Wavelength (nm)	Power (mW)
Omnichrome 3056-15M HeCd	325	18.5
American Laser 60X Ar-Ion	488 514	5 5
Uniphase He-Ne	543	2
American Laser LS300 Ar-Kr	488 568 647	10 20 25
Uniphase He-Ne	633	10
JEA-HN10IR HeNe	1152	2

Table 3.1 A list of lasers used by UW-CMG showing emission wavelengths and their corresponding power output.

The laser beam strikes mirror M1 before entering the beam expander which greatly aids in alignment. As long as the beam strikes M1 at the right height and lateral position, then M1 can be adjusted to correct any angular deviation. This sort of alignment is much more easily accomplished by positioning a mirror than a 5 kg laser.

The beam expander typically consists of a microscope objective followed by an achromat. Since the scanning mirrors ultimately limit the maximum beam diameter to 5 mm, the beam expander factor is about 10X. A shear plate designed to create a unique interference pattern when a collimated beam passes through it is used to calibrate the beam expander. Light within the beam expander is always on-axis such that only spherical and axial chromatic aberrations are present. Spherical aberration is small and the chromatic aberration is avoided since excitation light is almost always monochromatic. Specific excitation wavelengths are isolated with thin film interference laser line filters. Mirror M2 is used to deflect the expanded beam vertically towards M3. The cslm mirrors are typically first-surface, $\lambda/4$ accuracy, SiO-coated aluminum mirrors with reflectivities on the order of 90% depending on their age.

3.1.1.2 Scanning Mirrors and Telescopes

Mirror M3 deflects an expanded beam to the y-scanning mirror. The active area for the scanning mirrors is 7 x 10 mm such that when used at 45° it can accommodate a 5 x 5 mm square beam. The scanners themselves are model G120DT General Scanning galvanometer optical scanners. They are typically operated at < 60 Hz with triangular waveforms which provide a constant angular speed and, in turn, a uniform raster scan speed. The jitter and wobble for these scanners is restricted to 100 and 50 μradians respectively. Scanners jitter as they scan and wobble above and below the scan-line. The wobble specification refers to how well a scanner remains on the scan line while jitter refers to how accurately the scanner returns to a pixel on that line. Noting that there are 512 pixels per 5.4° optical scan (zoom 1) then 100 μradians represents 1 pixel. Even at zoom 8, jitter only represents 8 pixels; however the scanners are 10+ years old and have on occasion exhibited slightly higher jitter and wobble values than the 'maximum' stated above. Unfortunately, aging has significantly affected the scan mirrors reducing them to < 75% reflectivity. The scanners have a step response time of about 1 ms, that is, the time it takes the scanners to 'settle down' when moved abruptly from one position to another.

The purpose of the unitary telescope is to serve as an optical relay as illustrated in section 2.3.3, where basically a scanning beam can be transformed into a beam which pivots about a stationary point. The first unitary telescope is made up of two Melles Griot, 01LAO079, f_{no} 2.00, f = 6 cm, precision optimized achromats separated by 2f with the most curved surfaces facing out so as to minimize spherical aberration. Similarly, the second unitary telescope consists of two f_{no} 2.00, f = 10 cm, Oriel model 42629 achromats. The second unitary telescope was constructed as a unit by mounting the achromats at the ends of a tube such that they were separated by 2f with their optic axes co-linear. Modular construction such as this, as opposed to mounting the achromats individually on the breadboard, was found to greatly simplify alignment of the optical components as a whole.

3.1.1.3 Microscope Objectives

Assuming small aberrations and appropriate diameter beams on the cslm, then the objective lens will determine the resolution and image quality. UW-CMG primarily uses ultra-long

working distance, plan, apochromatic, infinity-corrected Mitutoyo microscope objectives (0.14, 0.42 and 0.70 NA). A 0.9 NA, plan, apochromatic, infinity-corrected, Olympus microscope objective is also used. All of the objectives are designed to be used in air without a coverslip. Fig. 3.2 shows a typical microscope objective with various characteristic distances. The opening on the top flange usually corresponds to the entrance pupil with a diameter equal to the entrance diameter, d_e. The first focal plane, f ', generally lies within the body of the microscope objective at a distance L_A from the top flange. This implies that a unitary telescope must be used to insert the pivoting beam at the f ' plane since placing a scanning mirror at that point is physically impossible. The working distance of an objective, WD, is defined to be the distance between the bottom flange and the second focal plane, f ''. Table 3.2 shows specifications for the 4 microscope objectives mentioned above including theoretical confocal lateral and axial resolution based on Eqns. 2.12 and 2.14, respectively.

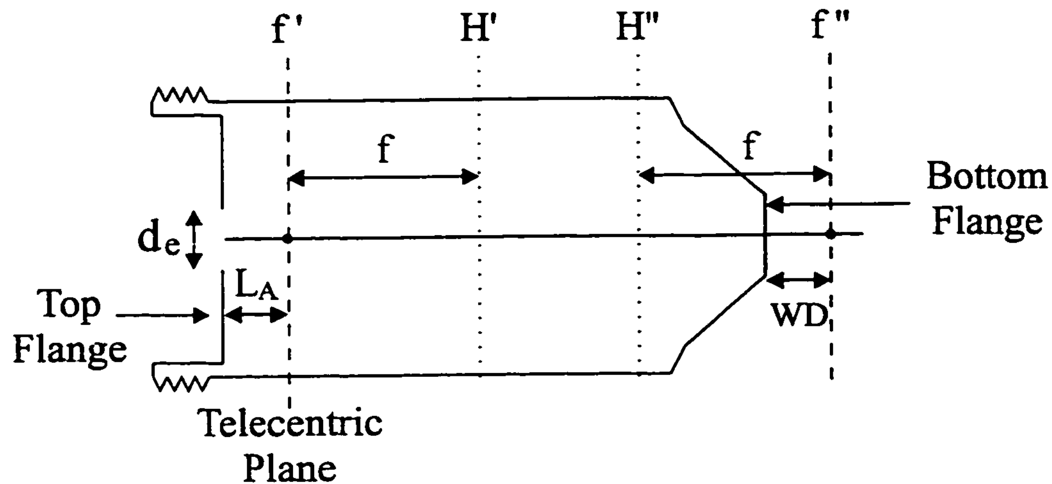

Figure 3.2 A typical microscope objective with defining distances shown.

	Mitutoyo			Olympus
	0.14 NA 5X	0.42 NA 20X	0.70 NA 100X	0.90 NA 100X
d_e (mm)	11.2	8.4	2.8	4
L_A (mm)	8.1	10.3	3.4	N/A
f (mm)	40.1	10.0	2.0	1.8
WD (mm)	34	20	6	0.3
Lateral Res. (μm)	1.52	0.51	0.30	0.24
Axial Res. (μm)	21.8	2.32	0.75	0.38
% Transmission at 633 nm	86	92	74	78
Collection %	0.5	4.5	14.3	28.2
Field of View (mm)	4 x 4	1 x 1	0.2 x 0.2	0.2 x 0.2

Table 3.2 A list of specifications for microscope objectives commonly used on the cslm. The collection percentage refers to the amount of light collected by the objective originating from a point source. Lateral and axial resolution values were calculated assuming 488 nm excitation.

3.1.1.4 Detector Arm

Light from the specimen passes through the objective lens and is descanned by the telescopes and scanning mirrors such that the returning beam is stationary at the beam splitter. The first part of the detector arm consists of a beam splitter which deflects the returning beam towards an achromatic detector lens. A long-pass filter is placed in front of the detector lens, when photoluminescent emissions are being viewed, in order to block out reflected light. The beam is focused down to a diffraction-limited spot at the confocal pinhole which allows some of the light to enter the light-tight PMT case where it is detected by the PMT.

For reflected-light experiments, the beam splitter is generally of the thin film metallic type (50/50) measuring one or two inches in diameter. Assuming ideal efficiency for the rest of the cslm, the 50/50 beam splitter is the most efficient (not counting polarizing beam splitters) for monochromatic light allowing 25% of the light from the laser to pass into the detector assuming a mirror specimen. Other beam splitter ratios are less efficient but are occasionally

used when the specimen is very light sensitive. Photoluminescence imaging requires the use of a dichroic beam-splitter due to its much improved efficiency. For this thesis a general purpose 5 centimeter diameter dichroic beam splitter was used, designed to transmit 488 nm light at > 80% efficiency and reflect wavelengths longer than 550 nm at > 90% efficiency. The combined efficiency is >72% which is almost three times better than a 50/50 beam splitter. In most cases light from a photoluminescent specimen contains mostly reflected light and some photoluminescence. Schott absorbing glass filters were found to be most effective in eliminating reflected light, achieving optical densities greater than 5, unfortunately these filters were found to photoluminesce. Fig. 3.3 shows an 8 x 8 cm photoluminescence MACROscope image of a 550 nm long pass filter held on the specimen stage by four pieces of masking tape. If this filter were to be placed near the detector, then reflected light signals would be detected indirectly via the filter photoluminescence, a highly undesirable situation. This problem is avoided by placing the filter 'far' from the detector as shown in Fig. 3.1 such that photoluminesce emissions from the filter are eliminated due to the confocal effect.

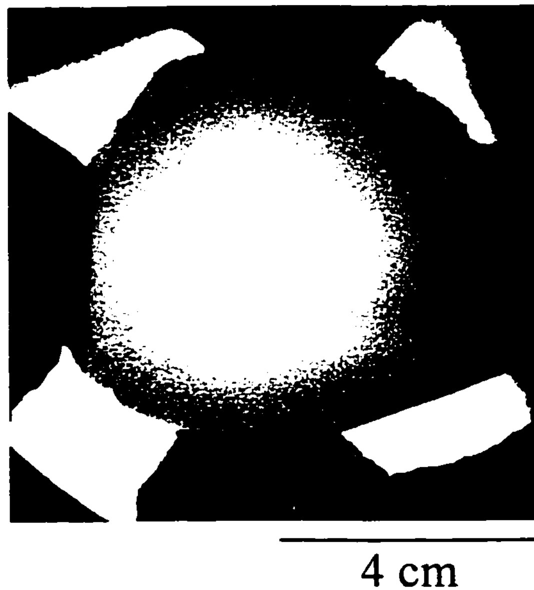

Figure 3.3 An 8x8 cm photoluminescence image, taken on the MACROscope, of a 550 nm longpass absorbing glass filter. The filter clearly photoluminesces and is affixed to the specimen holder by four pieces of masking tape.

Collimated light from the beam splitter passes through and is focused by a 10 cm focal length achromat onto a Newport pinhole (5, 10, 20, 50, 100 or 200 μm diameter), or an iris diaphragm (1 mm minimum diameter).

The ideal pinhole size is not well defined since the emission beam size can range from 3 mm diameter to a 5 x 5 mm square depending on which objective lens is used. Light admitted by the pinhole strikes the PMT face. UW-CMG uses Hamamatsu R292 (blue sensitive) and R2228 (red sensitive) head-on, semi-transparent photocathode PMT tubes. Both types have an active area 25 mm in diameter, are powered by a 1000 V power supply, and have a 100 μA average anode current. Table 3.3 shows specifications for both types of PMT tubes.

Hamamatsu PMT Type	Curve Code	Peak Wavelength (nm)	Current Amplification $\cdot 10^5$	Anode Dark Current (nA)
R292	400 K	420	21	2 - 10
R2228	501 K	650	7.5	8 - 30

Table 3.3 Specifications for two Hamamatsu PMTs used by UW-CMG.

Fig. 3.4 shows photocathode radiant sensitivity as a function of wavelength for various PMTs taken from the Hamamatsu PMT catalog where the R292 and R2228 PMTs correspond to curves 400K and 501K respectively. The radiant sensitivity can be related to the quantum efficiency in the following way:

$$\% \, QE = \frac{S \cdot 1240}{\lambda} \cdot 100 \qquad \textbf{(3.1)}$$

where S is radiant sensitivity in A/W at a given wavelength λ. The R292 PMT has a clear advantage in current amplification and quantum efficiency up to about 600 nm at which point the R2228 dominates as the PMT of choice. An important PMT specification is the range of light levels at which the PMT operates linearly, that is, if the light intensity is doubled then so should the anode current while in linear operation. PMT linearity can be easily measured with a variable intensity laser source such as the Ar-Kr laser.

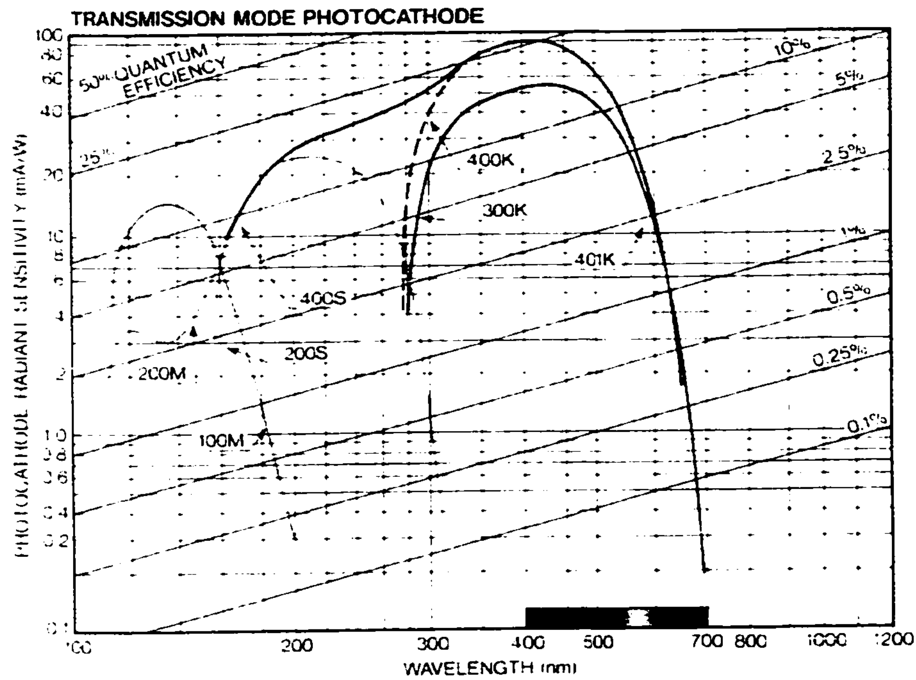

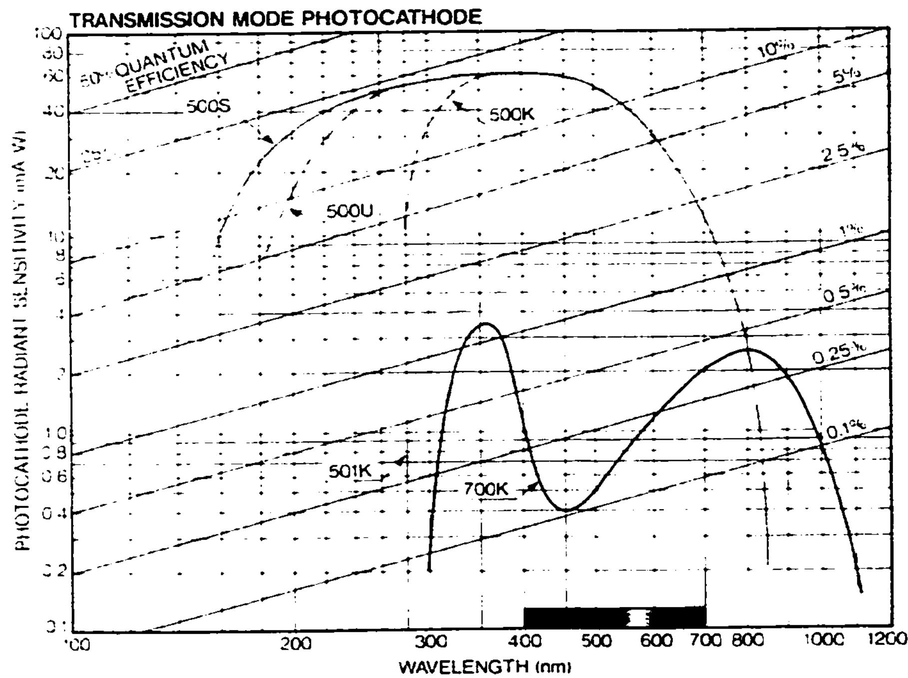

Figure 3.4 Radiant sensitivity vs. wavelength for the R292 (curve 400K) and the R2228 (curve 501K) Hamamatsu PMTs. Curves taken from the Hamamatsu PMT catalog (1996).

Fig. 3.5a shows a plot of silicon detector signal vs. laser power meter reading on the Ar-Kr laser for two laser lines (488 and 647 nm). The laser beam was expanded and attenuated appropriately before feeding it into a calibrated UDT-40X silicon detector with a radiometric filter which outputs 0.1 amps per watt of light energy for wavelengths ranging from 450 to 910 nm. The laser power meter reading was found to be highly linear with respect to relative light intensity yielding linear regression fits exceeding r^2 values of 0.999. The correlation coefficient, r^2, can be interpreted as the fraction of the total variation which is explained by the least-squares regression line. In other words, r^2 measures how well the line fits the data, the closer to 1, the better. Fig. 3.5b shows PMT anode current vs. laser power meter reading using the R292 PMT at 488 nm for two different sets of intensities. For intensities representing less than 200 μA anode current the PMT response is linear while it is clearly non-linear for anode currents exceeding 200 μA. The same behavior can be seen in Fig. 3.5c for the R2228 PMT using 647 nm light. In general, as long as anode currents are kept under 200 μA, both PMTs will respond in a linear fashion.

The PMT anode signal goes into a Stanford Model SR570 current-to-voltage amplifier. The amplifier is limited to a maximum 1 MHz bandwidth but only at its least sensitive setting. Table 3.4 shows the amplifier operating characteristics as a function of bandwidth. In practice, the low noise setting is used for signals greater than ~ 2 μA (2 μA/V setting) and high bandwidth mode is used for signals under 2 μA. Data is typically obtained at a rate of 100 - 300 kHz with no high or low pass filters as well as no biases or DC offsets applied. Low frequency pass filters are applied when the data rate falls below 100 kHz which occurs sometimes with photoluminescence and OBIC imaging. This effectively increases the integration time and reduces high frequency noise. Voltage biases and DC input offsets are applied sometimes with solar cells and detectors in order to enhance and improve their response in OBIC. Flexibility in a pre-amplifier is essential to obtaining high quality images especially in OBIC and photoluminescence. The voltage signal from the Stanford amplifier enters a Data Translation DT2851-50 Hz frame grabber which accepts a 0-1 V signal at a maximum 3.0 MHz rate.

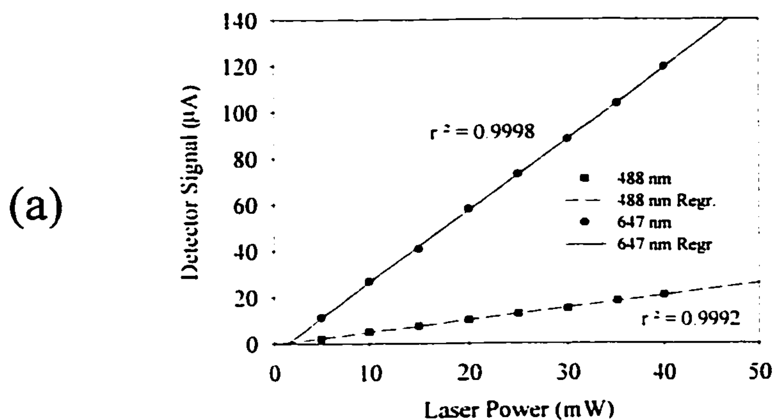

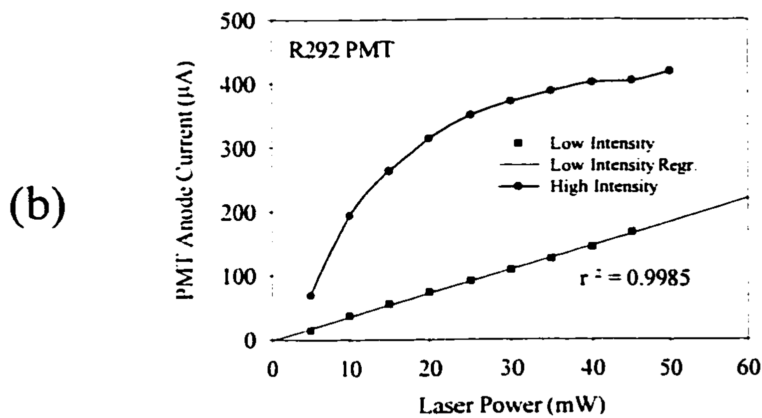

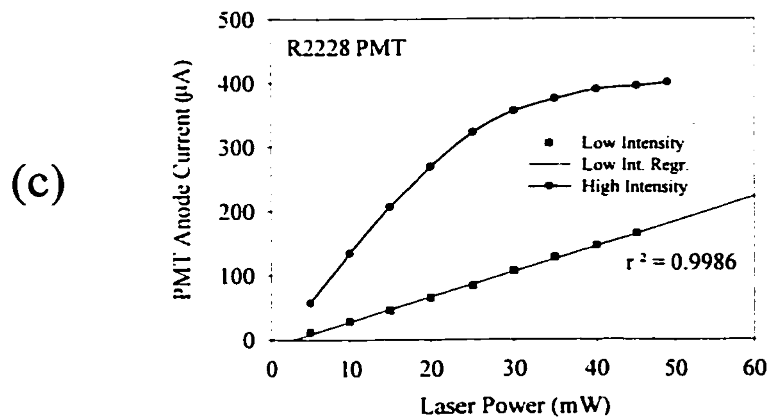

Figure 3.5 (a) Silicon detector signal vs. laser power meter reading for two wavelengths (488 and 647 nm). (b) PMT anode current vs. laser power for the R292 PMT at two different light intensity levels. (c) PMT anode current vs. laser power for the R2228 PMT at two different light intensity levels.

Sensitivity (A/V)	3 dB Bandwidth High BW	3 dB Bandwidth Low Noise	Noise/√Hz High BW	Noise/√Hz Low Noise
10^{-3}	1.0 MHz	1.0 MHz	150 pA	150 pA
10^{-4}	1.0 MHz	500 kHz	100 pA	60 pA
10^{-5}	800 kHz	200 kHz	60 pA	2 pA
10^{-6}	200 kHz	20 kHz	2 pA	600 fA
10^{-7}	20 kHz	2 kHz	600 fA	100 fA
10^{-8}	2 kHz	200 Hz	100 fA	60 fA
10^{-9}	200 Hz	15 Hz	60 fA	10 fA
10^{-10}	100 Hz	10 Hz	10 fA	5 fA
10^{-11}	20 Hz	10 Hz	10 fA	5 fA
10^{-12}	10 Hz	10 Hz	5 fA	5 fA

Table 3.4 Bandwidth and noise as a function of sensitivity for the Stanford current to voltage preamplifier. The High BW (Bandwidth) and the Low Noise settings are commonly used on the preamplifier. As their names imply they give the user the choice between better frequency response or lower noise.

The 0-1 V signal is converted by the frame grabber to an 8-bit digital number (0-255 gray level) with a 10 MHz bandwidth; that is, the integration time is 100 ns. The frame grabber stores images on two 512 x 512 pixel memory boards which transfer the images to a 486-based personal computer.

3.1.2 cslm Characterization

The next four sections will deal with experimentally assessing cslm performance. First, having gone through Fig. 3.1 in great detail it is important to know what photon collection efficiency the system has as a whole. The second section briefly deals with lateral resolution results, while the third section deals with axial resolution as a function of NA and pinhole size in addition to pinhole size dependent intensity. The fourth section examines some of the experimental imaging results due to the primary cslm limitation, the unitary telescopes.

3.1.2.1 cslm Collection Efficiency

Fig. 3.6 shows a schematic diagram of the cslm collection path. Included in the diagram are the percent of light transmitted for each component or set of components, in addition to the total cumulative percentage of light allowed through the system. Transmitted light percentages were all obtained experimentally using a UDT-40X silicon detector with a radiometric filter which outputs 0.1 amps per watt of light energy for wavelengths ranging from 450 to 910 nm. The diagram starts at the top left where a PL emission point is assumed to emit isotropically at 633 nm in all directions. The objective will collect some percentage of the total emission sphere given by the following formula[3]:

$$\text{Collection \%} = \frac{1}{2}\left(1 - \sqrt{1 - \text{NA}^2}\right) \tag{3.2}$$

Table 3.2 shows the collection and transmission percentage for the microscope objectives used on the cslm. Fig. 3.6 uses the 0.7 NA Mitutoyo objective lens as an example which transmits 74% at 633 nm and collects 14.3% of the PL emission sphere. The next set of components are the achromats, one mirror, and two scan mirrors. The achromats each transmit about 96% of the light while the mirror reflects 90% which leaves the scan mirrors which reflect less than 75% each. The poor performance from the scan mirrors is due to 10+ years of aging; they should be replaced or recoated. The dichroic beam splitter is very efficient with 97% reflectivity followed by a 550 nm long pass filter, and an achromatic detector lens with a total transmission of 87%. The total light reaching the PMT varies from 2 to 22% depending on which pinhole is used. The total number of photons detected by the PMT can be calculated by multiplying this total light value by the objective lens collection percentage and the PMT efficiency at 633 nm. For example, assuming the 0.7 NA objective is used with a 50 μm pinhole, then the percentage of photons collected from the specimen is $0.143 \cdot 0.18 \cdot 0.05 \cdot 100 = 0.13\%$; that is, about 1 out of 1000 photons emitted by the photoluminescing specimen are detected which is a typical number for confocal microscopes.

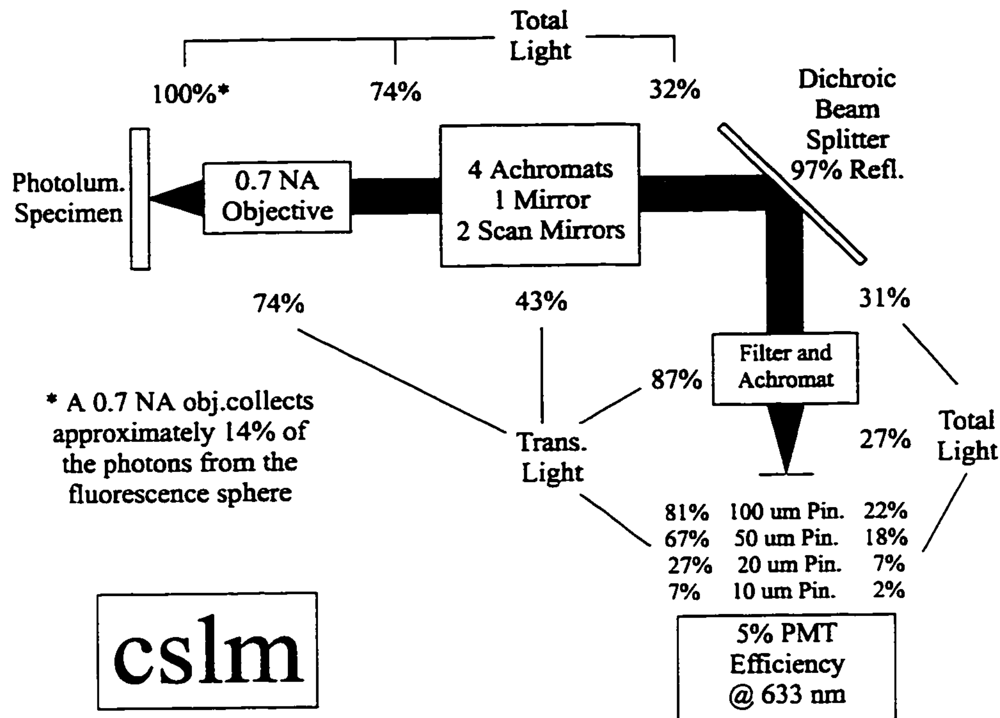

Figure 3.6 Cslm collection efficiency at 633 nm. Transmission percentages for each set of components and the total percentage of light collected by the objective that strikes the PMT as a function of pinhole diameter are shown.

3.1.2.2 cslm Lateral Resolution

The best reflection mode resolution target available to UW-CMG is one with 1, 2, 5 and 10 μm horizontal and vertical lines. Each line is made up of chrome deposited on glass which acts like a mirror and appears white in a reflection image. Fig. 3.7 shows a zoom 1, 200 x 200 μm confocal image of the resolution target taken with the 0.9 NA objective using a green (543.5 nm) HeNe laser, a 50 μm pinhole, and a 10 cm focal length achromatic detector lens. Starting from the bottom left corner the image clearly shows that the 1, 2, 5 and 10 μm lines are extremely well resolved, as expected. The darkening near the top of the image is due to unitary telescope aberrations to be discussed in Section 3.1.2.4. Unfortunately, this target is inadequate for testing lateral resolution for the 0.42, 0.7 and 0.9 NA objectives based on the theoretical predictions in Table 3.2. In practice, both the 0.42 and 0.14 NA objectives are underfilled and effectively have a reduced NA for both illumination and collection.

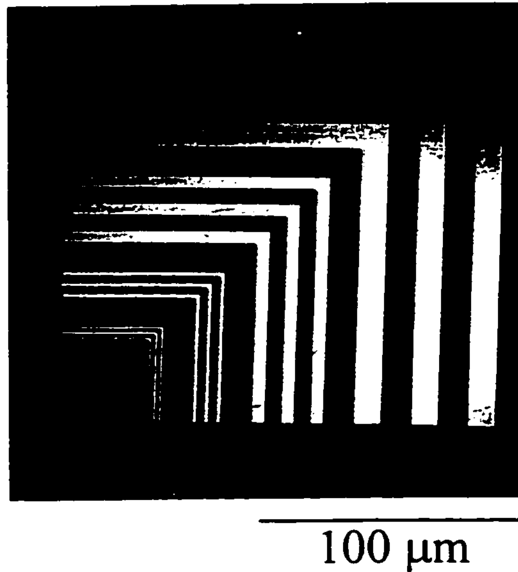

Figure 3.7 Image of a reflecting resolution target showing 1, 2, 5, and 10 μm lines. The confocal image was taken with a 0.9 NA objective at zoom 1 (200x200 μm) using 543.5 nm light.

The effective NA is given by a formula derived in Appendix 3:

$$NA_{EFF} = \left[\left(\frac{d_o}{d_n}\right)^2 \left(NA_{OBJ}^{-2} - 1\right) + 1\right]^{-\frac{1}{2}} \tag{3.3}$$

where d_o is the entrance diameter radius and d_n is the diameter of the incoming beam.

Table 3.5 shows the objective NAs along with their effective NAs and the resulting predicted lateral and axial resolution at 543.5 nm. Reducing the effective NA of an objective has a dramatic effect especially on the axial resolution.

Objective NA	Entrance Pupil Diam. (mm)	Beam Diameter (mm)	Effective NA	Lateral Resolution (μm)	Axial Resolution (μm)
0.42	8.4	5	0.266	0.86	6.64
0.14	11.2	5	0.063	3.76	120

Table 3.5 The 0.14 and 0.42 NA objectives are underfilled on the cslm hence their effective NA, lateral, and axial resolution are changed accordingly.

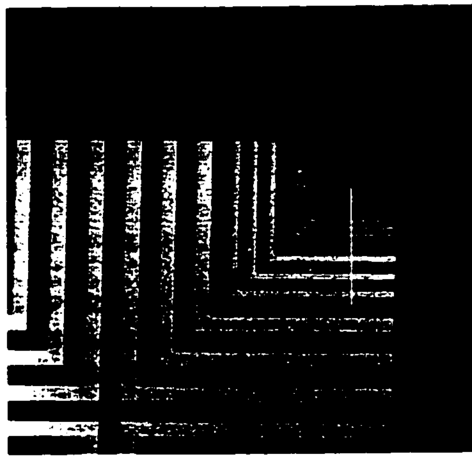

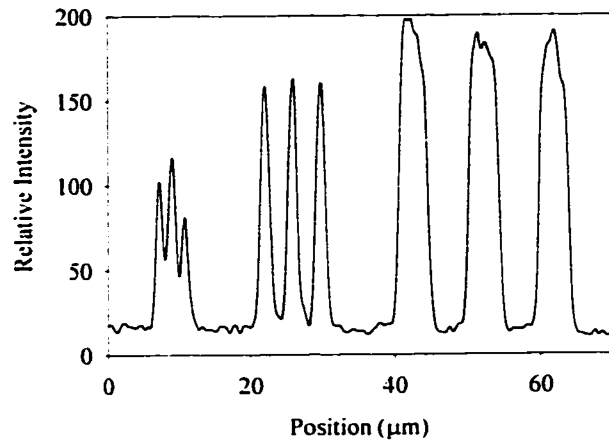

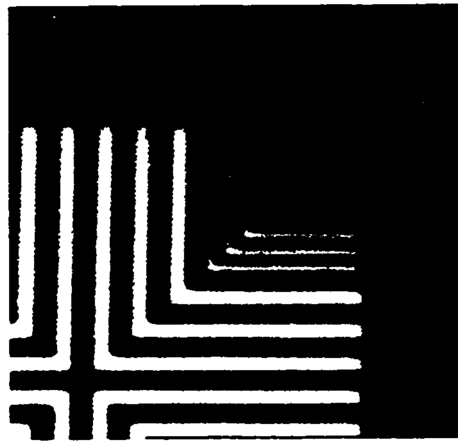

Figure 3.8 (a) Zoom 4 (250x250 μm) confocal image of a reflection resolution target taken with an underfilled 0.42 NA objective and 543.5 nm light. (b) Intensity profile of the white line in a). The 1 μm lines are resolved by the 0.42 NA objective. (c) Zoom 16 (250x250 μm) confocal image of the same resolution target using an underfilled 0.14 NA objective. The 5 μm lines are clearly resolved.

Fig. 3.8a shows a zoom 4, 250 x 250 μm, confocal image of the resolution target taken with the underfilled 0.42 NA objective using a 10 μm pinhole, a 10 cm focal length achromatic detector lens, and 543.5 nm laser light. The 2 μm lines in Fig. 3.8a are clearly resolved, however, the 1 μm lines are difficult to identify. The question of 1 μm resolvability can be answered by plotting an intensity profile along the vertical line shown in Fig. 3.8a. Fig. 3.8b shows such an intensity profile for the 1, 2, and 5 μm lines starting from the left. The 1 μm lines are clearly resolved in this graph. Fig. 3.8c shows a zoom 16, 250 x 250 μm confocal image taken with the underfilled 0.14 NA objective using the same setup as the 0.42 NA objective. The 5 μm lines are resolved as predicted in Table 3.5.

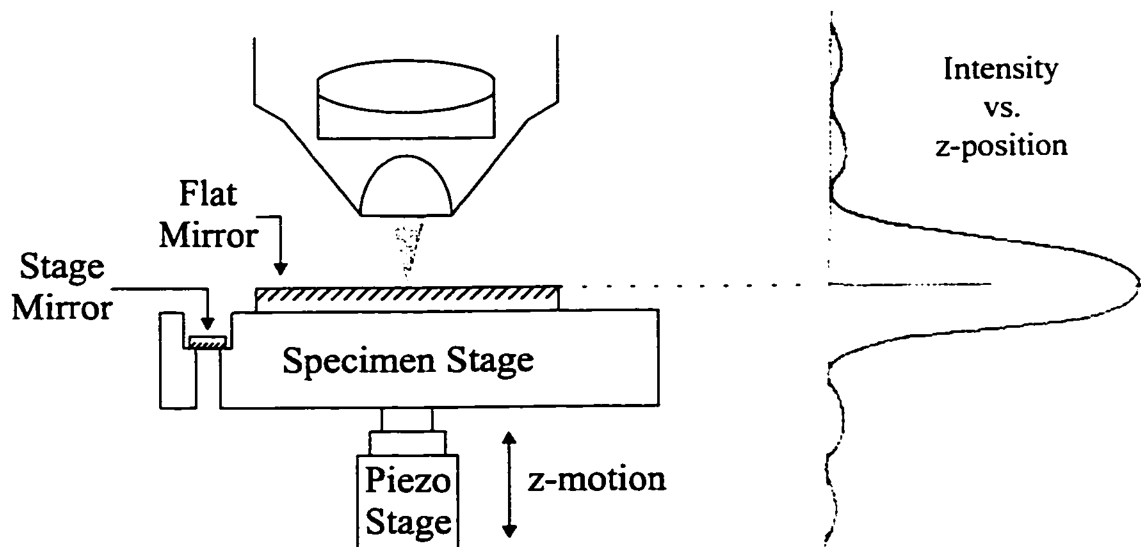

Figure 3.9 Experimental setup used to measure axial resolution on the cslm. As the mirror is moved up and down in the z-direction the detected intensity will vary as shown on the right.

3.1.2.3 cslm Axial Resolution

Axial resolution is the single most important parameter for confocal microscopes. The ideal microscope provides highly confocal operation while maintaining an optimal collection efficiency and generating unaberatted images. Good axial resolution implies improved lateral resolution, improved signal to noise ratio, improved out-of-focus data rejection, etc. The most common method used to measure axial resolution involves measuring the reflected

intensity from an optically flat mirror as a function of z position (distance along optical axis). Fig. 3.9 shows the setup used to measure axial resolution on the cslm. The microscope objective focuses a beam onto a flat mirror mounted on a specimen stage. The specimen stage is supported by a Burleigh piezo stage with a nominal 15 mV/μm z-movement calibration and a maximum 100 μm travel range.

Measuring the axial resolution of the objective in Fig. 3.9 requires several steps starting with the acquisition of an image such as the one shown in Fig. 3.10a. This image was generated by first disconnecting the x and y scanning mirrors so that the beam remained fixed on the optic axis. The signal from the y-scanning mirror was connected to the piezo driver and amplified so as to optimize the z-motion. The image in Fig. 3.10a represents a series of 512 line scans plotting piezo voltage input vertically as a function of intensity represented by gray level. Any horizontal variation in intensity is mainly due to noise. The image in Fig. 3.10a can be converted to an intensity profile plot simply by picking one particular vertical line or by averaging the 512 vertical lines as was done in Fig. 3.10b. When obtaining axial resolution data, the cslm operator must ensure that the background light level is greater than 0 and the maximum peak height is less than 255 (maximum intensity). The axial resolution in Fig. 3.10b is given by the full width at half maximum (FWHM) of the central peak. The peak side lobe intensity represents only about 5% of the central peak intensity which is beneficial since larger side lobes tend to degrade the confocality by making structures at the side lobe peak positions more visible. The z-scan in Fig. 3.10b starts at 512 mV which corresponds to a position where the focal plane is above the mirror's surface. This corresponds to plane 2 in Fig. 2.5 where the beam exiting the objective is slightly converging. Similarly, the right hand lobe pattern in Fig. 3.10b corresponds to mirror positions above the objectives focal plane as illustrated by plane 1 in Fig. 2.5 resulting in a slightly diverging beam. The non-symmetric side lobe pattern illustrated in Fig. 3.10b is typical of confocal microscopes[4]. At this point the voltage values in Fig. 3.10b could not be converted to distances since the piezo stage was thought to exhibit a combination of non-linearity and hysteresis.

(a)

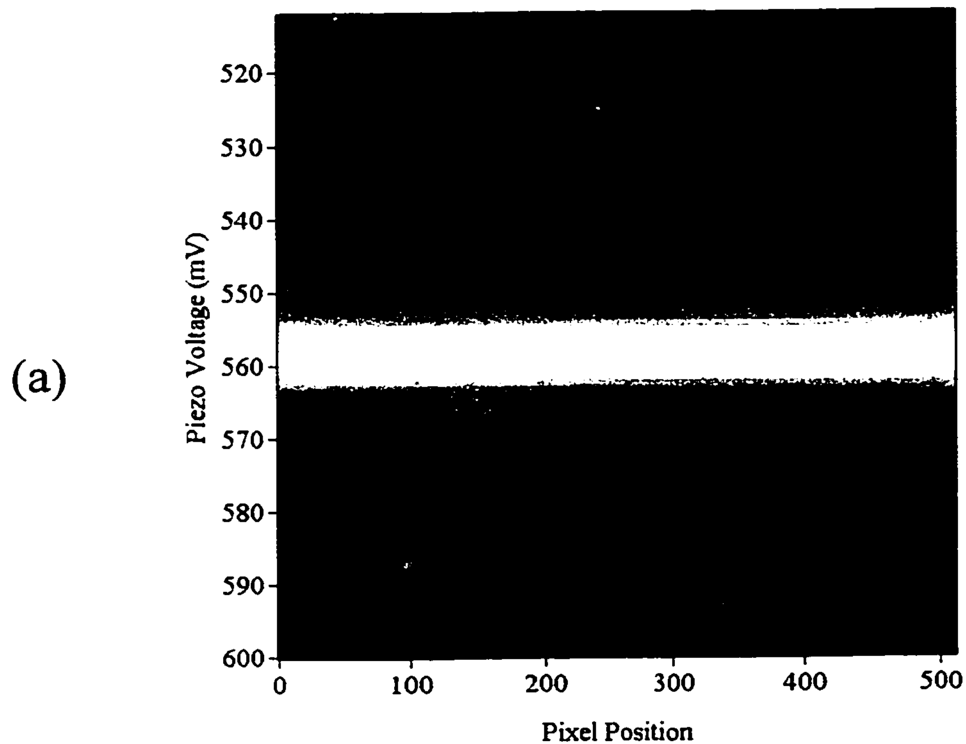

(b)

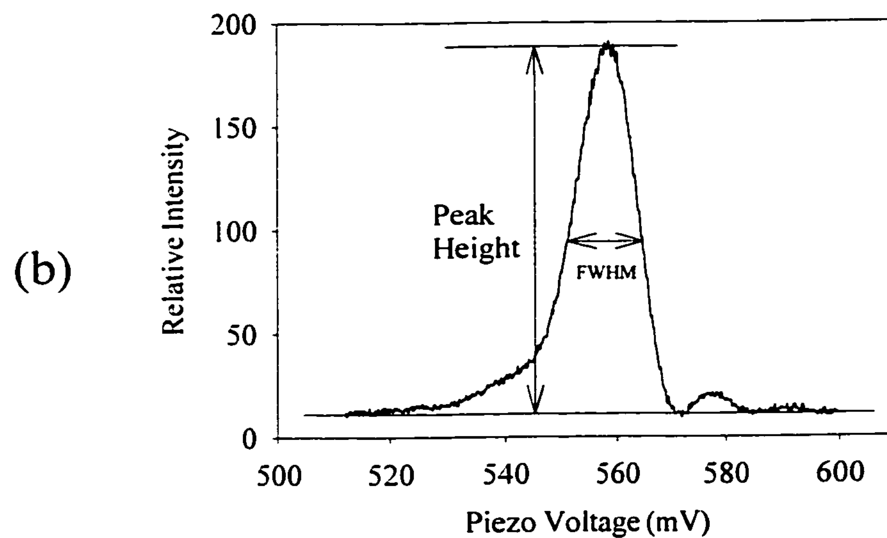

Figure 3.10 (a) A cslm z-scan image of a mirror taken with both x and y scanning mirrors pointing along the optic axis. The y-scanning signal is fed into the piezo z-stage. (b) The average vertical intensity profile of the image in a). The peak height and full-width at half-maximum (FWHM) are measured as shown.

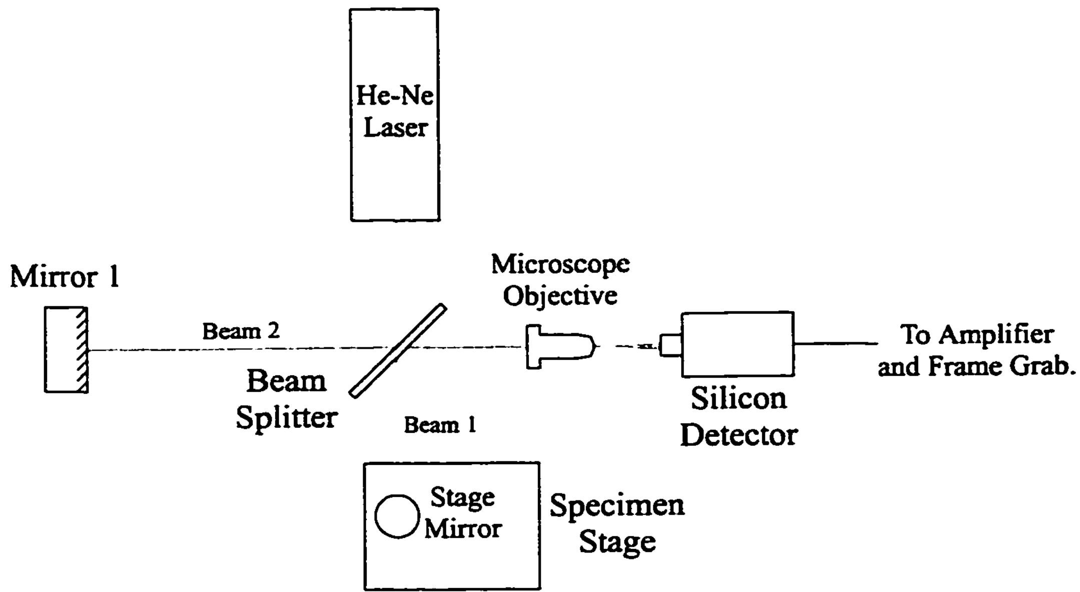

Figure 3.11 Schematic diagram of the Michelson interferometer used to measure specimen stage displacement. Each fringe represents a $\lambda/2$ displacement (316.4 nm).

Fig. 3.11 shows a Michelson interferometer[5] used to measure the true displacement of the specimen stage from which a relationship between piezo input voltage and piezo stage position can be derived. The beam from a HeNe (632.8 nm) laser is split into two by a 50/50 beam splitter. Beam 1 travels to the specimen stage mirror as shown in Figs. 3.9 and 3.11. Beam 2 is reflected by the beam splitter and then is reflected by mirror 1. Both beams combine at the beam splitter, pass through a microscope objective used to expand the beam slightly, and produce an interference pattern on a 3 mm diameter silicon detector. In order to obtain good interference, the beam splitter to mirror 1 distance was adjusted to closely match the beam splitter - stage mirror distance even though the coherence length of the laser was about 10 cm. As the specimen stage is moved, an alternating series of bright and dark fringes is detected by the silicon detector as shown in Fig. 3.12a. Fig. 3.12a is analogous to Fig. 3.10a in that the intensity, in this case of the fringe pattern, is plotted as a function of pixel position or time. Since the fringe pattern changes so slowly with respect to the pixel clock, the pattern appears to change only in the vertical direction hence the pattern in Fig. 3.12a can be reduced to a one dimensional plot by averaging each line.

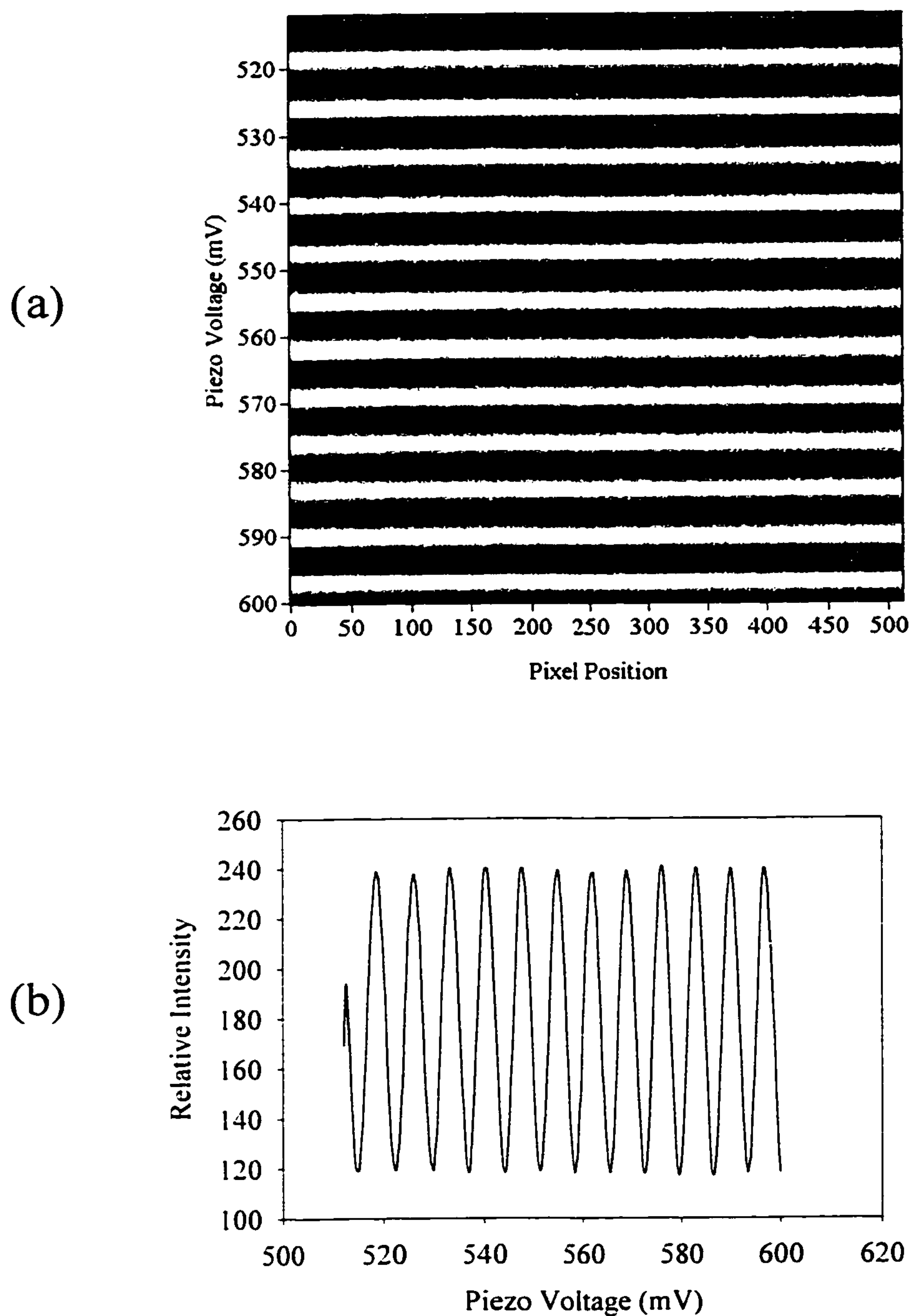

Figure 3.12 (a) Cslm image of what the Michelson interferometer silicon detector 'sees'. The x and y scanning mirrors are immobilized and the y-scanning signal is fed into the piezo stage such that the detector records the fringes as they pass by. (b) Average vertical intensity profile of the image in a). The distance between the peaks is $\lambda/2 = 316.4$ nm.

Fig. 3.12b shows the resulting intensity profile where the distance between the peaks indicates a specimen stage movement of half a wavelength, that is, a distance of 632.8 / 2 = 316.4 nm. The peak positions can be determined as a function of piezo input voltage and a relationship can be found between this voltage and the specimen stage position. When the number of fringes increases to several tens of fringes then the intensity cannot be assumed to remain constant in the horizontal direction as in Fig. 3.12a and the mechanics of how an image is obtained must be examined more closely.

Fig. 3.13 shows how only part of the x-scan input signal is responsible for acquiring an image. A full cycle for the x-scan mirror can be divided into two halves: the rising half of the input signal and the falling half which corresponds to rotation in two different directions. Only the middle half of the rising part of the signal is used for data acquisition in order to allow the scanning mirror to accelerate to a constant speed. The result is that images like Fig. 3.10a and 3.12a are non-continuous samplings of intensity with respect to time. For example, a pixel in the middle of Fig. 3.12a will be separated by one unit of time (this is equivalent to a unit of piezo stage voltage) from its immediate neighbours to the left and right of it on the same line. The pixel directly below this one is separated not by 512 units, which is the case if continuously sampling were in effect , but rather by 2048 time units according to Fig. 3.13. In a sense, 512 x 512 grids are sampled out of a 2048 x 512 grid, and therefore instead of numbering each pixel in Fig. 3.12a sequentially from 0 to 512 x 512 - 1 = 262143, the pixels should be numbered according to Fig. 3.13. The first pixel in Fig. 3.12a will be numbered 255 while the one to the right of it will be numbered 256 and the one below will be 255 + 2048 = 2303. A C^{++} program was written by K.A. Ellis to create intensity profiles such as the one in Fig. 3.12b by averaging sets of pixels taking into account the arrangement in Fig. 3.13. The program was designed to average a set of 64, 128, 256 or 512 pixels. For the special case of a 512 pixel average, where each horizontal line contributes to the generation of one point, the scan layout in Fig. 3.13 is irrelevant since each generated point is separated by a constant amount (2048).

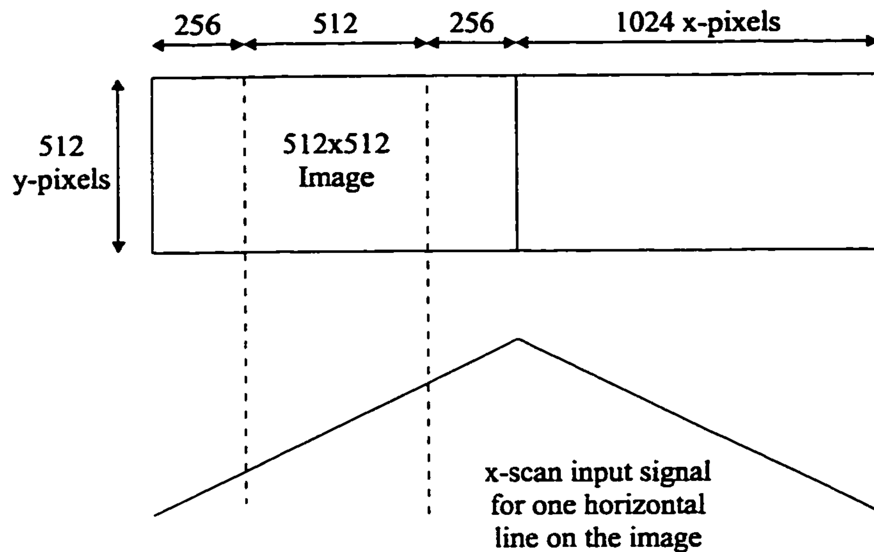

Figure 3.13 Scan layout diagram. The x-scanner receives a triangular signal but data is only taken in the middle half of the rising signal. In essence, the cslm samples a 512x512 pixel square from a possible 2048x512 grid. The pixels in an image are therefore not sampled in a continuous manner when changing lines (horizontal).

If Fig. 3.12b had been generated by a 128 average then the graph would consist of 512 x 4 = 2048 points instead of 512 with the first four points separated by 128 units and point number five separated by 2048 - (3 x 128) = 1664 units from the fourth point. In practice sets other than 512 pixel averages were done very infrequently and only involved interferometer data. Given an interferometer intensity profile showing a series of peaks, their positions as a function of piezo stage voltage can be determined. Since each peak is separated by half a wavelength from its neighbour a relationship between piezo stage voltage and piezo stage displacement can be determined. Fig. 3.14 shows a graph of displacement versus piezo stage input voltage for the set of peaks in Fig. 3.12b. The relationship, in this case, is extremely linear due to the short travel distance, with the slope of the line giving 44 nm piezo stage displacement for each mV of applied piezo voltage.

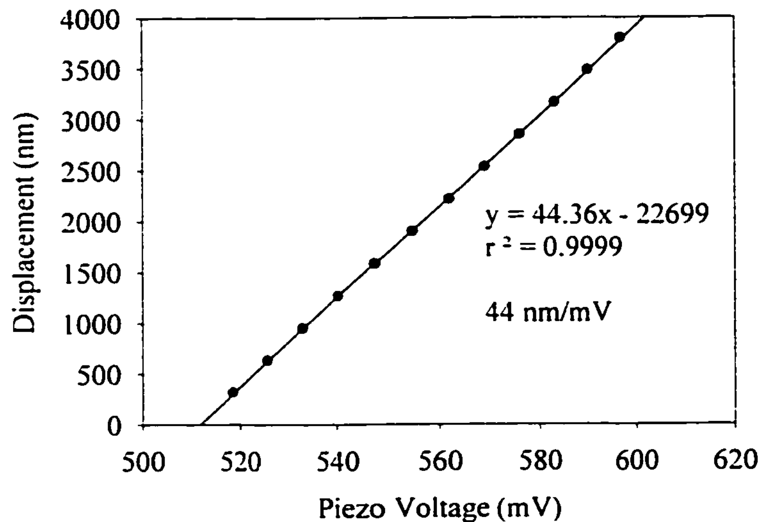

Figure 3.14 Z-stage displacement as a function of piezo voltage. For displacements less than 10 μm the above relationship is extremely linear.

For 17 piezo stage calibrations with total displacements under 10 μm the average calibration value was 47.2 ± 0.5 nm/mV. Each displacement versus piezo voltage plot was very linear. For displacements greater than 10 μm the plots were also linear except at the very start where they were curved as shown in Fig. 3.15, where the total displacement represents a distance of about 100 μm. Also, as the total displacement increased beyond 10 μm the calibration value also increased; in Fig. 3.15 this value was 71 nm/mV. What seems to be happening is that as the piezo stage total displacement is increased the piezo settles into linear operation over most of its range but with an increased sensitivity to changes in voltage.

Having established a reliable measurement technique, a table of FWHM and relative intensity as a function of pinhole size was generated for the 0.42, 0.7 and 0.9 NA objectives. The axial resolution for the underfilled 0.14 NA objective was too large (> 100 μm) to be measured using the piezo stage. All the measurements, unless stated otherwise, were performed with the 543.5 nm HeNe laser, a 10 cm achromatic detector lens and the R292 PMT. Table 3.6 shows relative peak intensity, FWHM, HWHM (half-width at half maximum) and normalized Intensity/FWHM as a function of confocal pinhole diameter for the 0.42 NA objective.

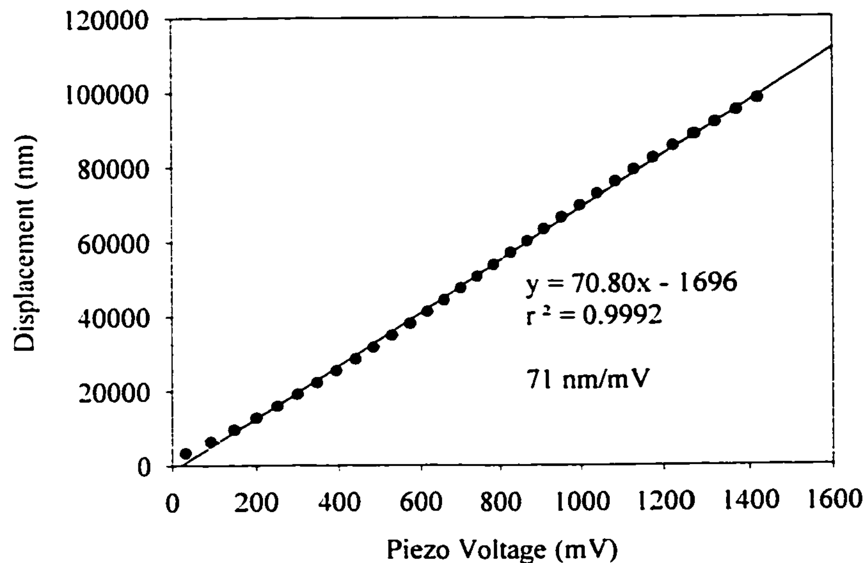

Figure 3.15 Z-stage displacement vs. piezo voltage for a large displacement (~100 μm). The graph is still linear but the slope has increased significantly compared to small displacements.

Some authors[6] use HWHM as the representative measurement for axial resolution, and therefore it has been included in the tables. The relative intensity (see Fig. 3.10b) was measured very carefully, assuring that the same laser intensity was used for all the pinholes. The only thing that varied throughout the measurements was amplifier gain and pinhole size. Fig. 3.16a shows relative intensity plotted as a function of pinhole diameter. When the pinhole is smaller than the Airy disk the intensity should increase very rapidly with pinhole area. As the pinhole reaches the Airy disk size and surpasses it, the intensity should level off since the Airy disk side lobes contribute very little to the total intensity. A more complete discussion of this is given in chapter 5. A spline fit was drawn in Fig. 3.16a showing the general shape of the data set; a fast rise leading into a leveling off of intensity. In theory the Airy disk diameter for a 10 cm focal length with a 5 mm diameter aperture at 543.5 nm is 27 μm which agrees with the data in Fig. 3.16a.

Pinhole (μm)	Relative Intensity	FWHM (μm)	HWHM (μm)	Normalized Int./FWHM
5	0.7	7.3	3.65	1.1
10	30.9	7	3.5	50.6
20	88	10.1	5.05	100
50	100	24.6	12.3	46.7
100	92.4	54.3	27.15	19.5

Table 3.6 Axial resolution and relative intensity measurements for the 0.42 NA Mitutoyo microscope objective. Measurements were done at 543.5 nm.

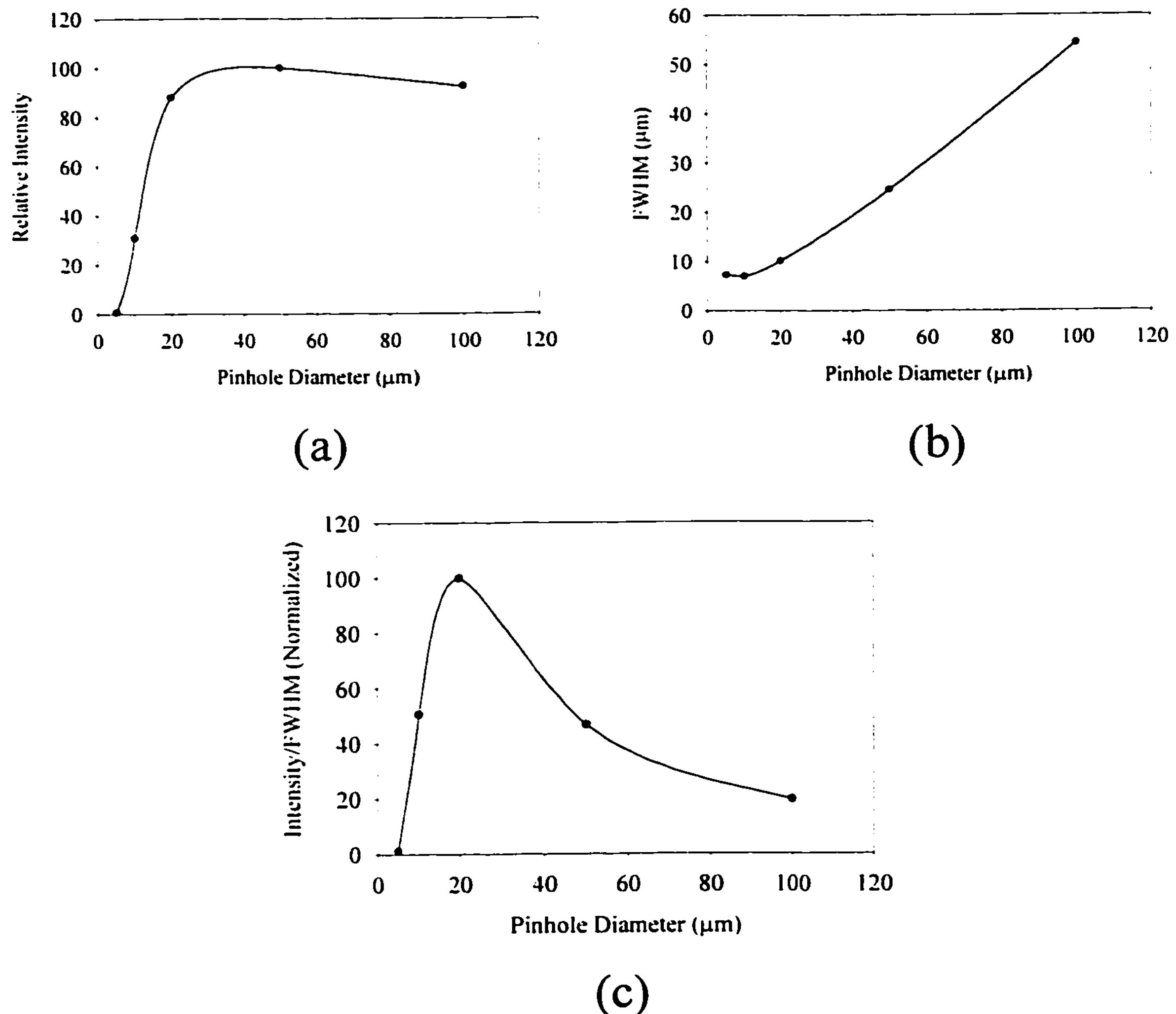

Figure 3.16 Relative intensity, FWHM, and Intensity/FWHM plotted as a function of pinhole diameter in (a), (b), and (c), respectively. Data from Table 3.6 using the 0.42 NA Mitutoyo microscope objective.

The slight decrease in intensity for the 100 μm pinhole is clearly an experimental error due to a fluctuation in laser intensity, a change in PMT supply voltage, a misalignment of the pinhole, etc. Fig. 3.16b shows a FWHM versus pinhole diameter graph with a spline fit. It has been shown[6] both theoretically and experimentally that FWHM decreases approximately linearly with pinhole size until an effective 'zero' size pinhole value is reached at which point the FWHM levels off to a non zero constant. The data recorded with the cslm followed this behaviour. Interestingly enough, the FWHM for the 5 μm pinhole is larger than the 10 μm pinhole FWHM, a trend which repeated itself occasionally. One explanation for this is that the 5 μm pinhole was so difficult to align, due to its size, that is was in an almost constant state of slight misalignment and therefore produced poor results. There are three basic conditions that should be met by an ideal or optimal confocal pinhole: lateral and axial resolution in addition to intensity must be simultaneously maximized and since resolution and intensity are opposing factors, a compromise to maximize both as much as possible must be reached. A plot of Intensity/FWHM versus pinhole diameter should yield a curve whose maximum identifies an optimum pinhole size. Fig. 3.16c shows such a plot for the underfilled 0.42 NA objective where a spline fit has been drawn to show the shape of the data. The optimal pinhole size is generally viewed[7] to be between 50 and 90% of the Airy disk. The data in Fig. 3.16c indicates that the optimal pinhole is about 20 μm in size which corresponds well with the theoretical Airy disk size of 27 μm.

Table 3.7 shows the same data headings as in Table 3.6 for the 0.7 NA objective. Fig. 3.17 a, b and c shows relative intensity, FWHM, and Intensity/FWHM, respectively, plotted as a function of pinhole diameter. All the curves are shaped as expected, for this objective the optimal pinhole is the 50 μm pinhole. This is to be expected since the 0.7 NA entrance pupil is 2.8 mm in diameter resulting in a 47 μm Airy disk at the confocal pinhole.

Table 3.8 shows the same data set as in Tables 3.6 and 3.7 for the 0.9 NA objective. Figs. 3.18a, b and c show relative intensity, FWHM, and Intensity/FWHM, respectively, plotted as a function of pinhole diameter. The FWHM versus pinhole diameter curve were shaped as expected but the intensity versus pinhole diameter curve never leveled off indicating some aberration.

Pinhole (μm)	Relative Intensity	FWHM (μm)	HWHM (μm)	Normalized Int./FWHM
5	0.1	1	0.5	0.1
10	7.5	1	0.5	10.1
20	33.2	0.98	0.49	45.8
50	88.7	1.2	0.6	100
100	100	2.4	1.2	56.4

Table 3.7 Axial resolution and relative intensity measurements for the 0.7 NA Mitutoyo microscope objective. Measurements were done at 543.5 nm.

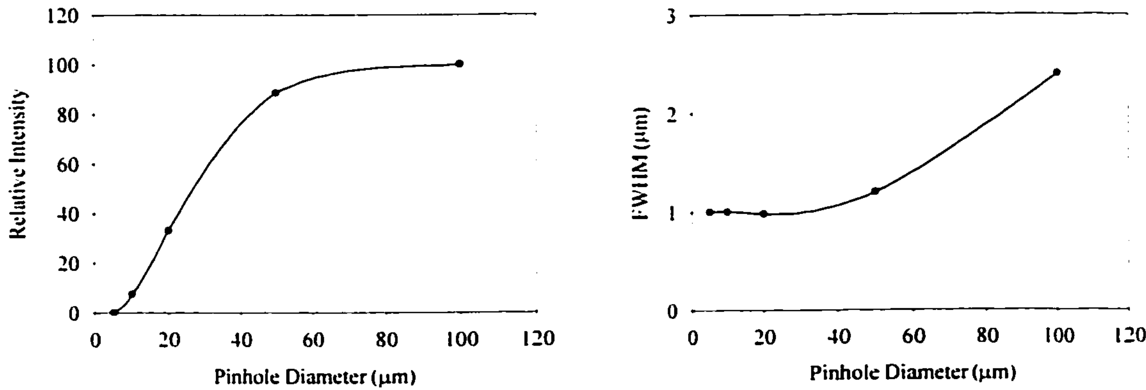

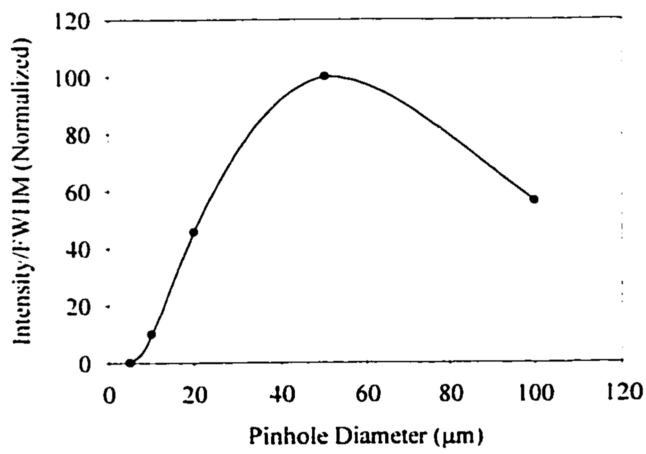

Figure 3.17 Relative intensity, FWHM, and Intensity/FWHM plotted as a function of pinhole diameter in (a), (b), and (c), respectively. Data from Table 3.7 using the 0.7 NA Mitutoyo microscope objective.

Pinhole (μm)	Relative Intensity	FWHM (μm)	HWHM (μm)	Normalized Int./FWHM
5	0.1	0.62	0.31	0.3
10	4.6	0.57	0.285	13.7
20	18.9	0.59	0.295	54.5
50	43	0.81	0.405	90.3
100	100	1.7	0.85	100

Table 3.8 Axial resolution and relative intensity measurements for the 0.9 NA Olympus microscope objective. Measurements were done at 543.5 nm.

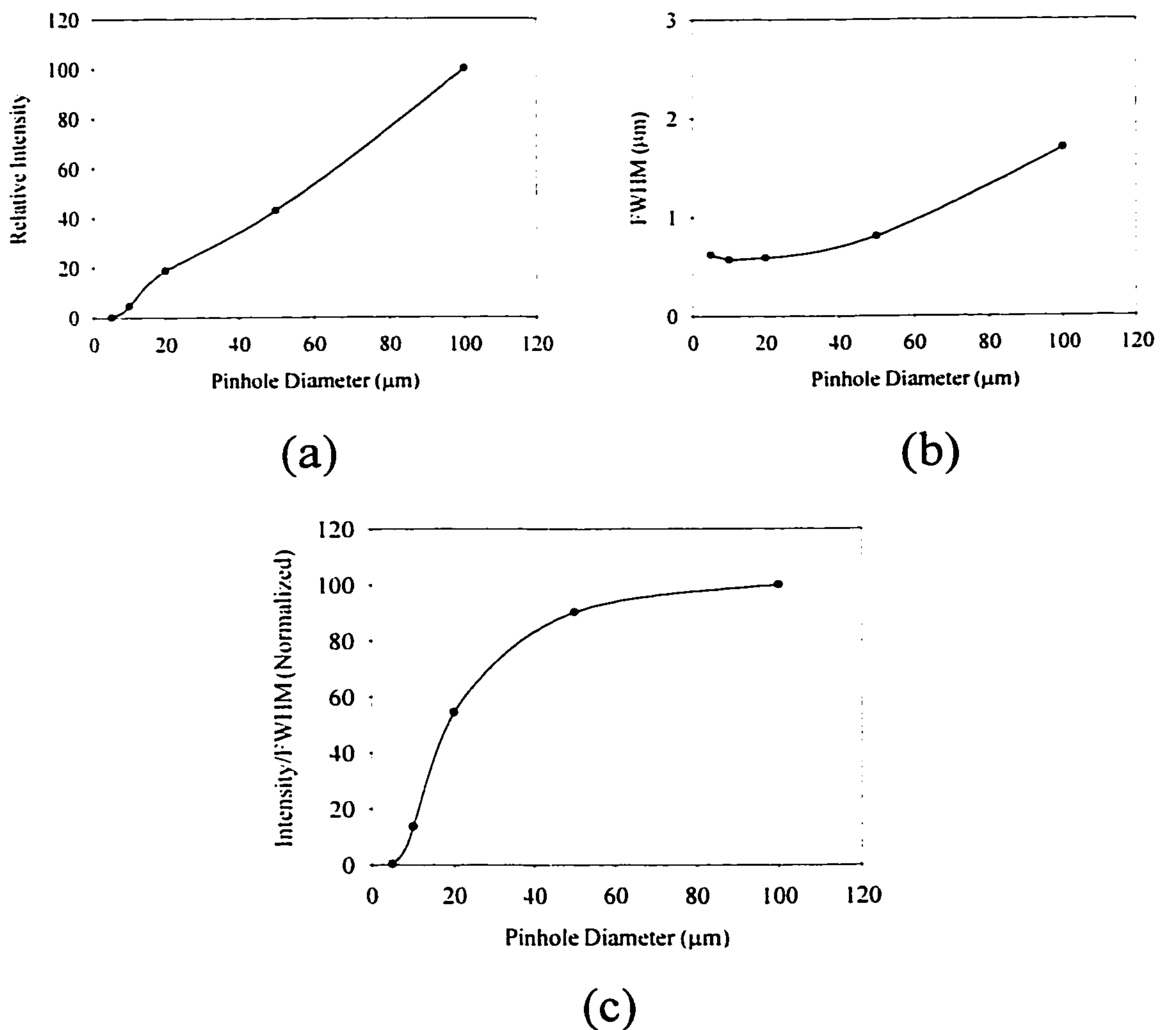

Figure 3.18 Relative intensity, FWHM, and Intensity/FWHM plotted as a function of pinhole diameter in (a), (b), and (c), respectively. Data from Table 3.8 using the 0.9 NA Olympus microscope objective.

One possible reason for this is that the 0.9 NA objective is not even close to being parfocal with the other objectives and has a very small working distance which might lead to a misalignment of the objective when repositioning. Due to the high NA, any mirror tilt would have a significant effect. Pinhole misalignment or a dirty objective might also be a factor. Given a 4 mm diameter entrance pupil the theoretical Airy disk at the confocal pinhole was 33 μm in diameter which would indicate the 20 or 50 μm pinhole as the best choice. The data in Table 3.5 indicates the 50 μm pinhole as the best choice since its Intensity/FWHM is only slightly less than the 100 μm value and its FWHM is half of the 100 μm pinhole FWHM.
Using Tables 3.6 to 3.8, the cslm user can better discriminate what a suitable pinhole might be for a particular imaging task. A 'normal' specimen would probably be best suited to an optimum pinhole with the highest Intensity/FWHM ratio while a specimen that reflects very well might require a smaller pinhole which wastes intensity but ensures good lateral and axial resolution. Tables 3.6 to 3.8 also give the best FWHM values for each of the microscope objectives. Table 3.9 shows the best FWHM values from Tables 3.6 - 3.8 for each of the objectives compared with the theoretical values calculated using Eqn. 2.14.

NA	Experimental FWHM (μm)	Theoretical FWHM (μm)	Percentage Difference
0.42	7.00	6.64*	5.4
0.70	0.98	0.84	17
0.90	0.57	0.42	36

Table 3.9 Experimental and theoretical FWHM values for 3 objectives. The theoretical FWHM for the 0.42 NA objective was calculated using its effective NA of 0.266.

The theoretical values are consistently better than the experimental ones and the difference increases for increasing NA, but there does not seem to be any evidence of systematic aberrations.
The beam expander on the cslm contains no spatial filter. The reason for this was that the image quality did not seem to improve when a spatial filter was added, however the output intensity of the beam expander decreased significantly due to the difficulty in properly matching the pinhole with the Airy disk.

Pinhole (μm)	Relative Intensity	FWHM (μm)	HWHM (μm)	Normalized Int./FWHM
5	0.4	1	0.5	0.52
10	11.7	1	0.5	15.2
20	48.8	1	0.5	63.4
50	100	1.3	0.65	100
100	90.6	2.6	1.3	45.3

Table 3.10 The effect of a spatially filtered beam on axial resolution and intensity as a function of pinhole diameter. Spatial filtering seems to have little effect on cslm performance.

In order to assess the effect of spatial filtering on the beam, a 20 μm pinhole was inserted near the beam expander's point of focus resulting in a very uniform ~1 cm diameter Airy disk. The axial resolution measurements were repeated for the 0.7 NA objective. Table 3.10 shows relative intensity, FWHM, HWHM, and Intensity/FWHM as a function of pinhole size. Comparing Tables 3.7 and 3.10 shows the addition of a spatial filter does not seem to make any difference since the laser produced a high quality beam.

Pinhole (μm)	Relative Intensity	FWHM (μm)	HWHM (μm)	Normalized Int./FWHM
20*	32.8	0.95	0.475	58.3
5	0.8	0.92	0.46	1.5
10	15.1	0.92	0.46	27.7
20	42.6	0.92	0.46	78.2
50	94.7	1.6	0.8	100
100	100	3	1.5	56.3

Table 3.11 The same experimental setup was used as Table 3.10 except that the unitary telescopes were removed. The unitary telescopes, when used on-axis, do not seem to contribute significant monochromatic aberrations. The first measurement was taken with a 20 μm pinhole while the telescopes were still in the system.

The unitary telescopes on the cslm have large off-axis aberrations, as will be seen later in this thesis, but they were not expected to have significant monochromatic on-axis aberrations. In order to verify this, the setup used for Table 3.10 was modified by removing the unitary

telescopes and repeating the axial resolution measurements with the 0.7 NA objective. Table 3.11 shows the results of removing the unitary telescopes where the 20* μm pinhole measurement was taken just before removing the telescopes. Clearly the effects of the telescopes (on-axis) is minimal showing a possible slight decrease in FWHM for the 5, 10 and 20 μm pinholes and a nominal rise in Intensity/FWHM for the 20 μm pinhole.

NA	FWHM (μm) Regular Length Arm	FWHM (μm) Long Detector Arm
0.42	29.5	11.9
0.7	2.4	1.0
0.9	1.7	0.66

Table 3.12 FWHM for three objectives utilizing the 'no detector lens' setup with a 1 mm diameter iris diaphragm. The results from the regular length arm are compared with results from a long detector arm with a 2.5 m extension.

Bowron[8] has shown that detector arm length, that is the distance from the objective lens to the confocal pinhole, is a factor affecting the axial resolution of a confocal microscope in addition to NA and confocal pinhole size. As the detector arm is lengthened apertures at the end of the arm, such as a mirror or a detector lens, will become more and more limiting with respect to non-collimated beams and therefore the axial resolution will improve. The Biorad confocal microscope takes this to an extreme and dispenses with the use of a detector lens altogether relying on the high NA of its microscope objectives and a long detector arm (~ 1 m). This interesting technique was tested on the cslm by removing the 10 cm detector lens and replacing the pinhole with a 1 mm diameter iris diaphragm. FWHMs were measured for the 0.42, 0.7 and the 0.9 NA objectives using the regular detector arm measuring 90 cm from the objective to the beam splitter and 40 cm from the beam splitter to the confocal pinhole. A similar set of measurements was done with an extended detector arm representing a ~ 2.5 m extension using fold mirrors. Table 3.12 shows the results. The long detector arm FWHM values for the 0.7 and 0.9 NA objectives are nearly equal to the best results (zero size pinhole limit) obtained with the detector lens/pinhole combination, while the 0.42 NA FWHM is nearly double the best result. As expected, high NA objectives respond better to a long

detector arm. The regular detector arm setup yielded FWHMs about 2.5 times larger than the long detector arm results for each of the objectives.

3.1.2.4 The Effects of the Unitary Telescopes

The main limitation of the cslm are its unitary telescopes. The fundamental flaw is that a unitary telescope made up of a pair of achromats is reasonably well corrected for all aberrations except astigmatism and curvature of field. A detailed analysis of the aberrations will be given in Chapter 5 of this thesis. Astigmatism is proportional to the square of the angle the beam makes with the optic axis and therefore its effects will be most evident at large scan angles, specifically zoom 1, for all objectives. At zoom 2 the astigmatism is greatly reduced and at zoom 4 virtually non-existent. In practice, the astigmatic aberration has the effect of darkening the periphery of an image. The best test specimen for observing this effect is a flat mirror whose image should be completely uniform. Fig. 3.19a shows a zoom 1, 200 x 200 μm image of a flat mirror using 543.5 nm light, a 10 cm achromatic detector lens, and a 100 μm pinhole with the 0.7 NA objective. This image is in fact quite uniform showing some darkening mostly at the corners. The extent of the uniform region and the degree of darkening can be determined quantitatively by generating an intensity profile along some line of interest as was done in Fig. 3.19a (black line) and shown in Fig. 3.19b. The uniform region in Fig. 3.19b extends about 125 μm while the intensity at the edges dip to between 60-70% of the 'flat' intensity. Fig. 3.19b gives a very good quantitative description for a individual line but not for the image as a whole, while in Fig. 3.19a it is hard to distinguish the subtle variations of intensity represented as gray levels. A compromise between these two forms of representation is shown in Fig. 3.20a. Here, each of the 256 gray levels have been converted to 256 colours ranging from violet to red, with black and white at the extremes, as shown in the colour bar. Fig. 3.20 a, b, c and d shows the effect on the image of a mirror as the pinhole is reduced from 100 to 50, 20 and 10 μm, respectively.

(a)

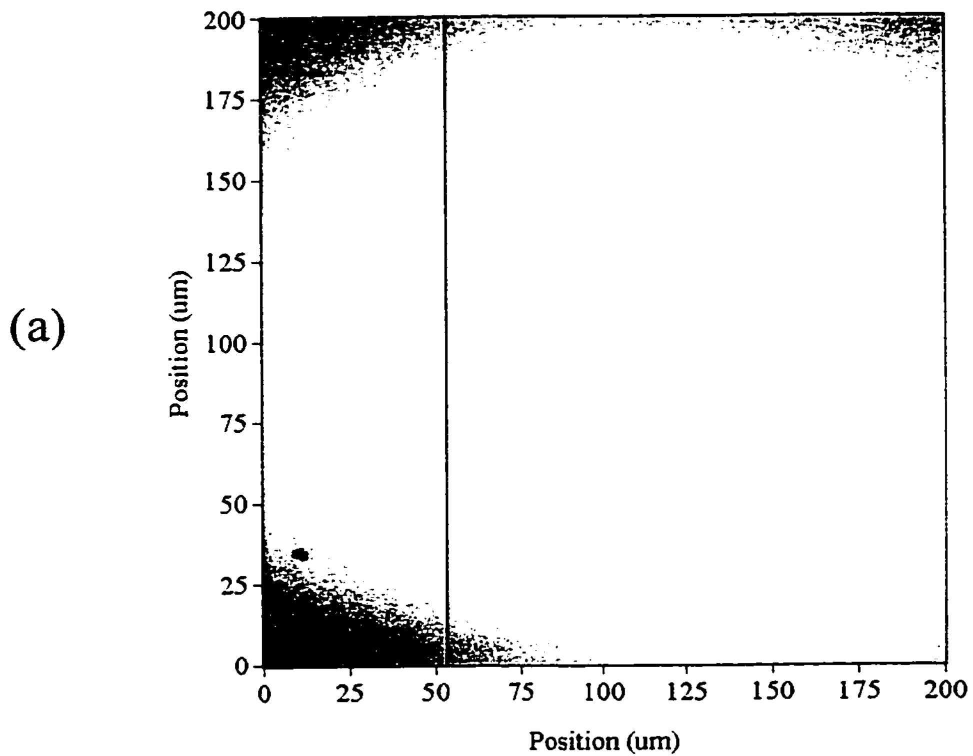

(b)

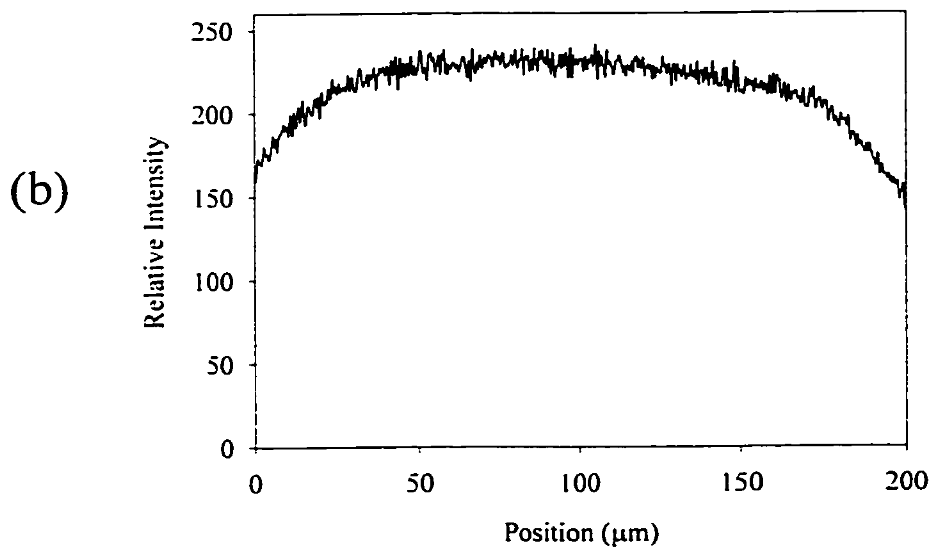

Figure 3.19 (a) A zoom 1 (200x200 μm), 0.7 NA reflected light image of a flat mirror using a 100 μm pinhole with a 10 cm focal length achromatic detector lens. (b) An intensity profile along the black line in a).

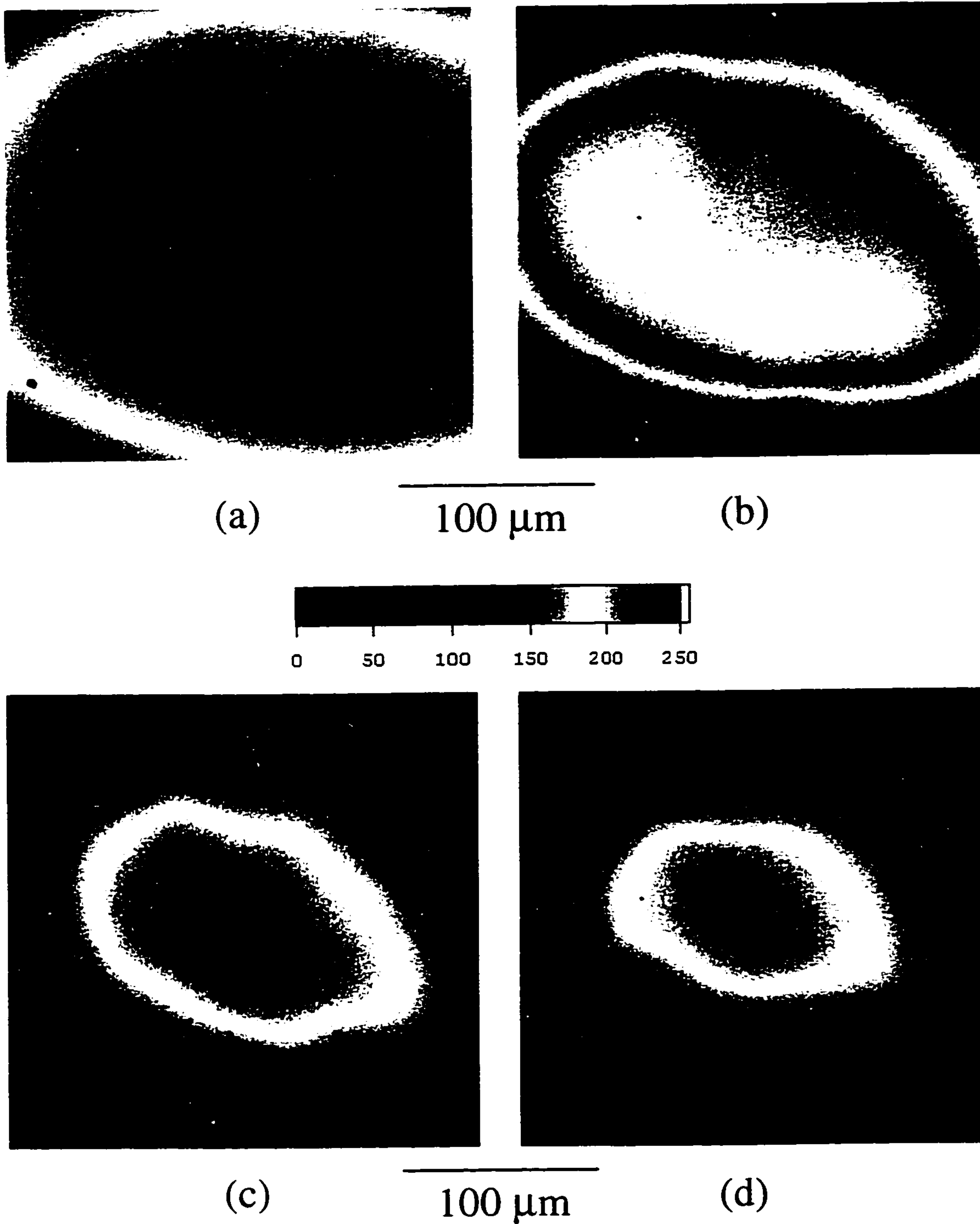

Figure 3.20 False colour images of a flat mirror taken at zoom 1 (200x200 μm) with a 0.7 NA objective and a 10 cm focal length achromatic detector lens. As the pinhole size is decreased from 100, 50, 20, to 10 μm in (a), (b), (c), and (d) respectively, the uniform intensity field of view decreases.

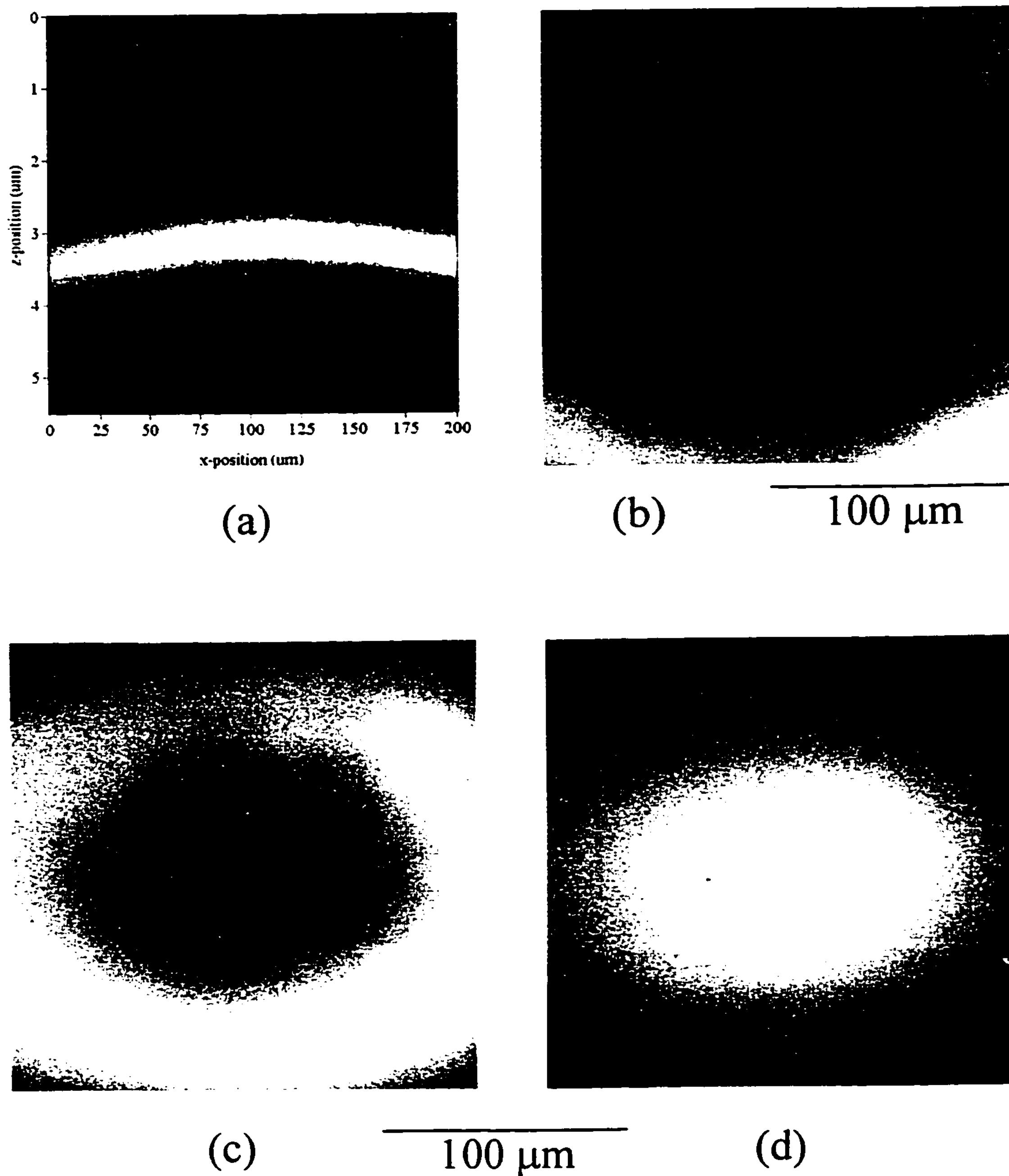

Figure 3.21 Confocal slices of a flat mirror taken at zoom 1 (200x200 μm) with a 0.9 NA objective, a 10 cm focal length achromatic detector lens and a 50 μm pinhole. (a) A x-z image of the flat mirror taken at zoom 1. The curved band indicates that the object being imaged appears to be convex in shape. (b) Slice 9 (0.42 μm from the bottom), which corresponds to the bottom of the band in a). (c) Slice 6 (0.85 μm). (d) Slice 2 (1.41 μm). Notice that the slices of b), c), and d) were obtained over a different range than shown in a).

As the pinhole size is decreased the axial resolution improves which unfortunately reduces the uniform intensity field of view since the cslm becomes more sensitive to curvature of field. In Fig. 3.20b, the 50 μm pinhole image was slightly overexposed so that the actual uniform intensity field of view will be a bit smaller. The end result is that if the optimum pinhole (50 μm) is chosen imaging should be restricted to zoom 2 or 4 while highly confocal imaging (20 μm pinhole) should be restricted to zoom 4. This general theme repeats itself with the other microscope objectives effectively decreasing the field of view when in confocal operation. Further evidence for curvature of field can be found by treating the flat mirror as if it were a curved surface. Fig. 3.21a shows x-z scan of a flat mirror using the 0.9 NA objective with a 50 μm pinhole and a 10 cm achromatic detector lens. This zoom 1, 200 x 200 μm image is similar to Fig. 3.11a except that the x-scanning mirror remained connected while the y-scanning mirror signal is fed to the piezo z-stage. The curved band in Fig. 3.21a clearly indicates a convex surface since the z-value at which best focus occurs (maximum intensity) is higher in the middle than at the sides. Notice how the band is of equal thickness throughout the scan indicating that the dominant monochromatic aberration present is curvature of field/astigmatism. Figs. 3.21b, c and d show three confocal slices from a series of 12 taken of the mirror over a total range of 1.55 μm. Starting from the bottom Figs. 3.21b, c and d are slice 9, 6 and 2, respectively, which corresponds to 0.42, 0.85 and 1.41 μm from the bottom-most slice. The cslm will focus only annular sections of the mirror. As the confocal slices progress the annular region contracts until only the central part of the field comes into focus. A maximum intensity image and a profile image can be generated from these slices as shown in Fig. 3.22. Fig. 3.22a and b shows the resulting maximum intensity image in gray levels and colour, respectively. The uniformity of the maximum intensity image gives an indication of what a mirror should look like with an ideal cslm. The profile image is shown in gray levels in Fig. 3.22c suggesting a convex shape as expected. Fig. 3.22d shows a 3-D representation of the mirror surface which appears as round pyramid-like structure with about seven steps. The image is effectively 'pixelated' in the z-direction since only a small number of slices were taken.

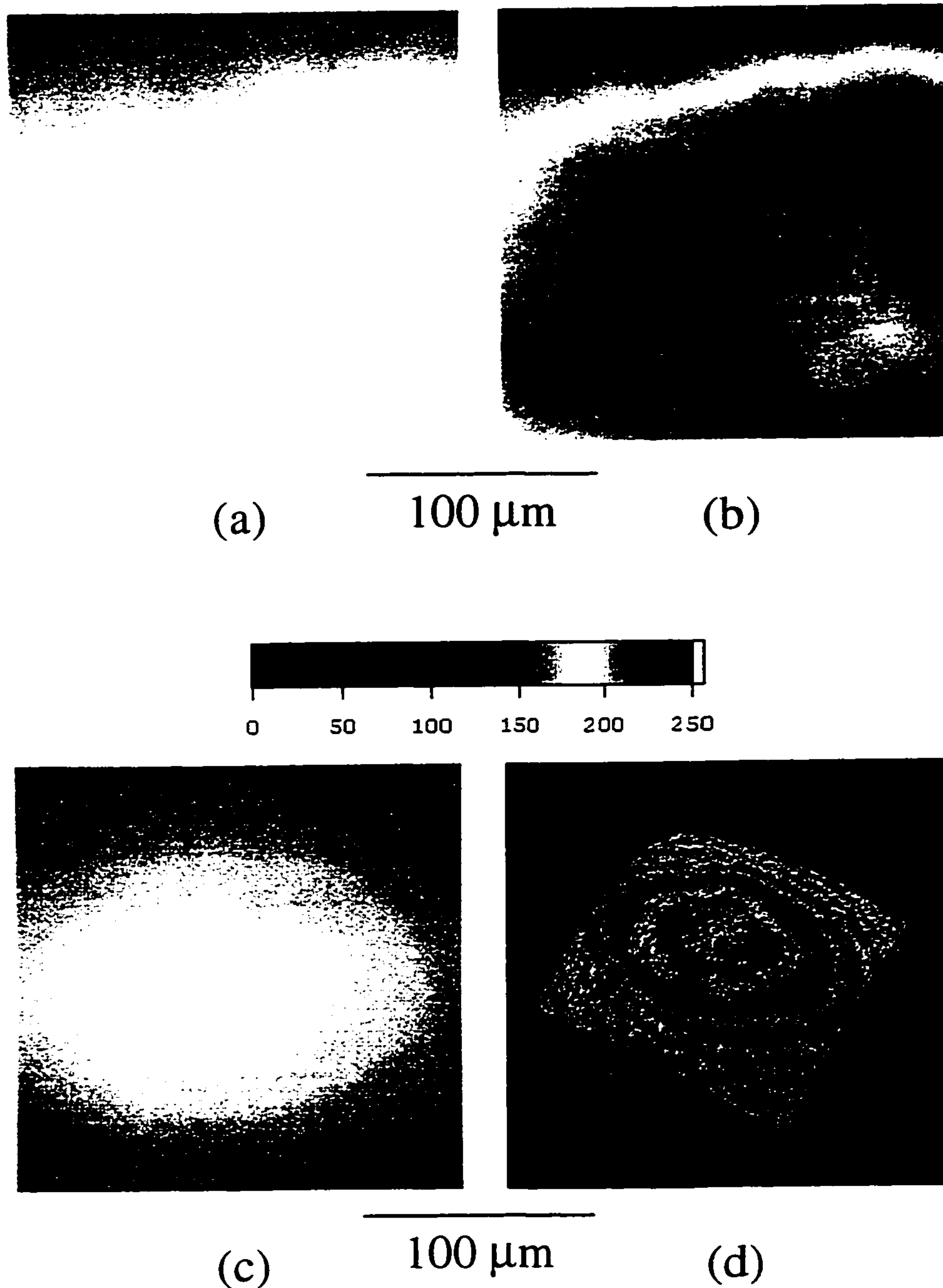

Figure 3.22 The effect of astigmatism and curvature of field on confocal imaging of a flat mirror. Maximum intensity and profile images taken at zoom 1 (200x200 μm) with a 0.9 NA objective, a 10 cm focal length achromatic detector lens and a 50 μm pinhole. (a) Maximum intensity image generated from 12 confocal slices. (b) Maximum intensity false colour image. (c) Profile image with a total depth of 1.55 μm. Black is low and white is high. (d) 3D representation of profile image.

3.2 The MACROscope

The name macroscope intuitively implies a microscope-like device which can look at large objects; large relative to the field of view for a light microscope. The confocal scanning laser MACROscope was therefore envisioned to handle specimens larger than 5 x 5 mm in size. The motivation for the development of a MACROscope was to fuse the abilities of a scanning beam microscope with those of a scanning stage microscope (SSM). Table 3.13 compares various specification from a cslm, SSM and the MACROscope.

	SSM	cslm	MACROscope
Frame Rate	Minutes	< 5 s	< 10 s
Resolution	High (0.95 NA)	Highest (1.4 NA)	Low (0.04 NA)
Field of View	Anything (stage-limited)	< 5 x 5 mm (using low NA)	625 x 625 μm to 7.5 x 7.5 cm
Advantages	- On-axis optics - High resolution - Large area scans	- Fast - Oil immersion	- Fast - Large scan area - Easy to focus
Disadvantages	- Very slow - Moving specimen - Vibrations	- Small scan size	- Lower resolution

Table 3.13 A comparison between scanning stage microscopes (SSMs), confocal scanning laser microscopes (cslms) and the MACROscope.

SSMs provide high resolution, large area scans limited only by the maximum travel distance of the scanning stages. SSMs also have the advantage of utilizing on-axis optics (the beam is always stationary) hence aberrations are greatly reduced. Unfortunately SSMs tend to be slow taking several minutes per scan especially with large (>1 cm) specimens. Also, the fact that the specimen is moving excludes SSMs from imaging most biological specimens, notably specimens suspended in liquids, because of vibrations.

Cslms provide the highest resolution of the three types of microscopes at fast scan rates but they are limited to the field of view of the microscope objective (typically < 5 x 5 mm).

The MACROscope provides 5 μm lateral resolution and an axial resolution equal to ~ 340 μm with a field of view ranging from 625 x 625 μm up to 7.5 x 7.5 cm. Unlike SSMs, acquiring a frame takes less than 10s. The natural beginning for the MACROscope was to use

the cslm in Fig. 3.1 as a template since UW-CMG was familiar with its operation and construction. As discussed previously, the field of view on the cslm is determined by the objective lens which in essence also occurs with the MACROscope. The 'objective lens' used on the MACROscope is a custom made telecentric, f-theta laser scan lens with its telecentric plane sitting several centimeters outside of its housing. It is designed to have a limiting aperture (a scanning mirror at UW-CMG) placed at the telecentric plane. The entrance pupil and telecentric plane are coincident. The laser scan lens also requires a 20 mm diameter input beam as well as a ± 9.5° input angle which are much larger quantities than would be used on conventional microscope objectives (5 mm diameter, ± 3° angle is more typical). The laser scan lens (LSL) basically demands a scaled up version of the cslm. The unitary telescopes in Fig. 3.1 were replaced by telescopes made up of 7.5 cm diameter, 25 cm focal length achromats, and the beam diameter was increased to 18 mm filling a larger set of scan mirrors. It quickly became apparent that the second unitary telescope (Fig. 3.1) that is required in a microscope could be eliminated such that the x-scanning mirror would sit at the telecentric plane of the LSL as shown in Fig. 3.23.

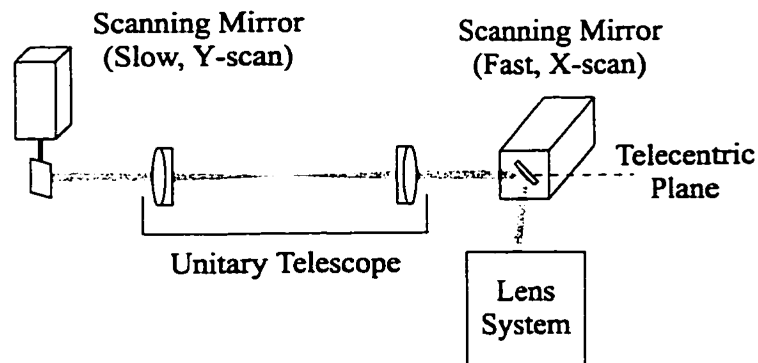

Figure 3.23 Intermediate form of the MACROscope where the second unitary telescope in Fig. 3.1 has been removed since the telecentric plane of the LSL sits several centimeters behind the lens.

Unfortunately, this was not the final form of the MACROscope because the achromats forming the unitary telescope were too small. An 18 mm diameter beam scanned at ± 9.5° requires a 10 cm diameter lens when its focal length is 25 cm in order for beam clipping not to occur. Due to the unavailability of reasonably priced, low f_{no}, large diameter achromats the

unitary telescope was completely removed to allow for the LSL's full field of view to be used.

The final form of the MACROscope is treated component by component in the next section. MACROscope efficiency, lateral and axial resolution as well as the non-telecentric effect of using two closely spaced scan mirrors are examined.

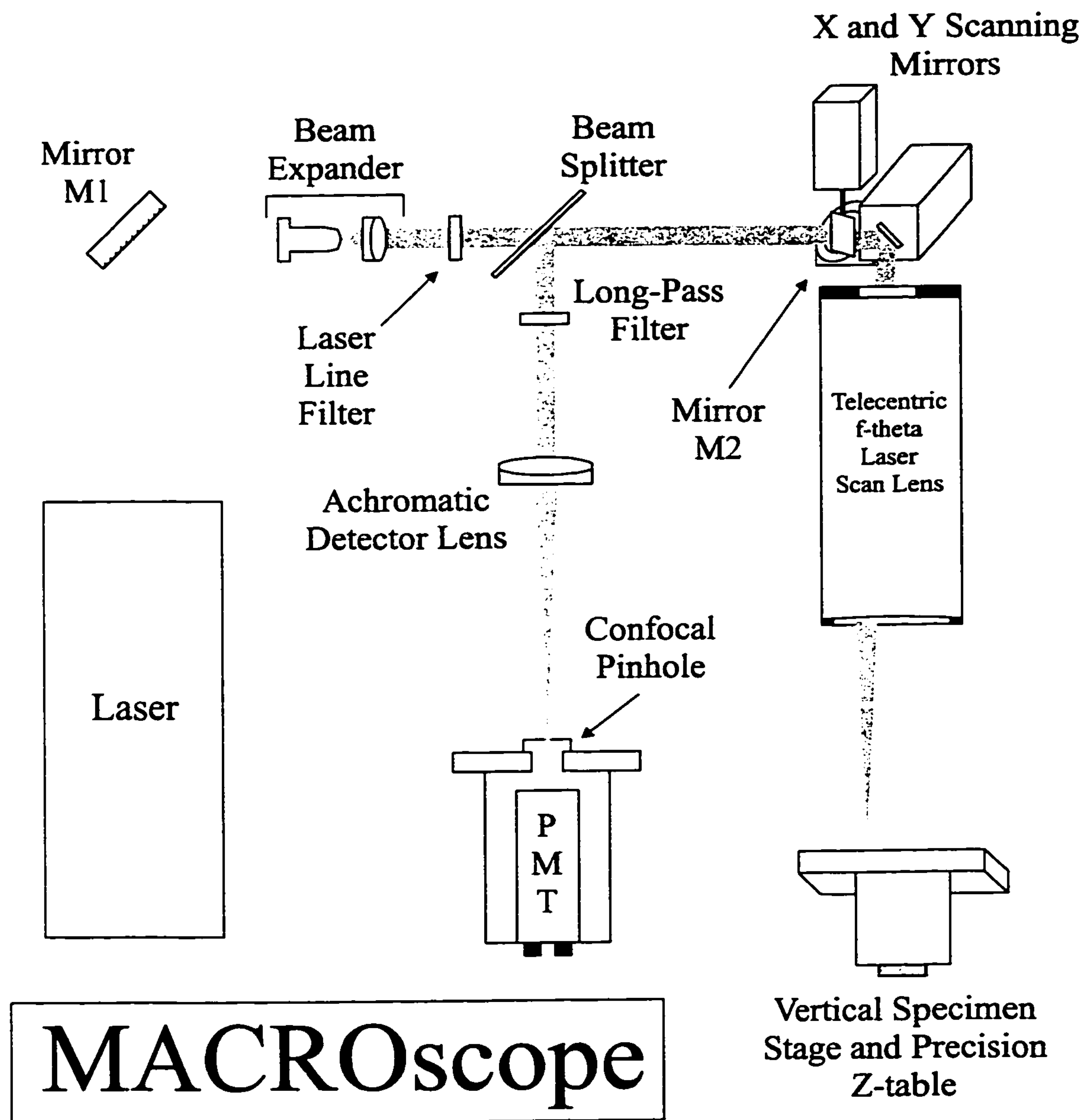

Figure 3.24 The confocal scanning laser MACROscope (cslM)

3.2.1 The MACROscope Components

Fig. 3.24 shows a schematic diagram of the MACROscope. Light from a laser is expanded to an 18 mm diameter. The expanded beam passes through a beam splitter and is scanned by two closely spaced x and y scanning mirrors. The midpoint of these two scanning mirrors corresponds with the telecentric plane of the LSL. Light from the LSL is focused onto the specimen which is mounted vertically on top of a precision z-stage. Light from the specimen passes through the LSL and is descanned and reflected by the beam splitter into the detector arm. Typically a 25 cm focal length achromat is used to focus the returning beam onto the confocal pinhole. An alternative detector arm which is occasionally used is shown in Fig. 3.25 where the achromat is replaced by an 80 cm focal length spherical mirror which allows for larger pinholes to be used while still maintaining confocal operation.

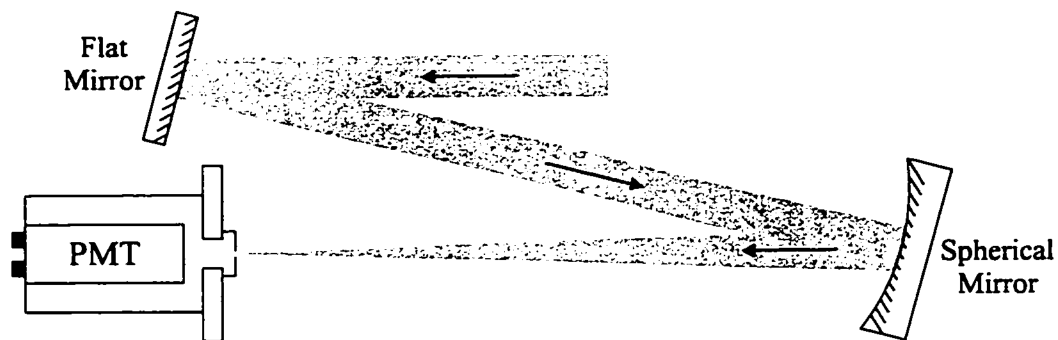

Figure 3.25 Alternate detector arm configuration. The 25 cm focal length achromat is replaced by an 80 cm focal length spherical mirror which allows for larger pinholes to be used since the resulting Airy disk is slightly larger.

The MACROscope and cslm share many components, in fact only the illumination arm consisting of the x and y scan mirrors, the LSL, and the z-stage are unique to the MACROscope.

Both scanners are model 6350 Cambridge Technology optical scanners providing a ±20° excursion angle and a 1.5 ms step response with 15 and 7 μradian jitter and wobble, respectively, which represents 7.6 and 3.8 μm displacement at the specimen. In order to provide the specified LSL input beam diameter, 25 x 25 mm scan mirrors were used which

exceeded the maximum inertial load specification for the scanners, hence a loss in scanner performance was expected.

Fig. 3.26 shows the telecentric, f-theta laser scan lens with a 223 nm (at 633 nm) effective focal length designed for use on the MACROscope. It was designed to accept a 2 cm diameter collimated beam (it is infinity-corrected) with the beam pivoting at the telecentric or first focal plane of the LSL. Telecentricity ensures that the incident and specularly reflected light beams are coincident. This in turn allows the reflected beam to be properly descanned. Telecentric[9] systems also tend to reduce measurement errors caused by defocus, or in other words, magnification is constant with defocus. The LSL was also designed to have the exiting beam move laterally in proportion to $f \cdot \theta$ given an input beam angle of θ. Most microscope objectives are automatically f-theta since θ is small.

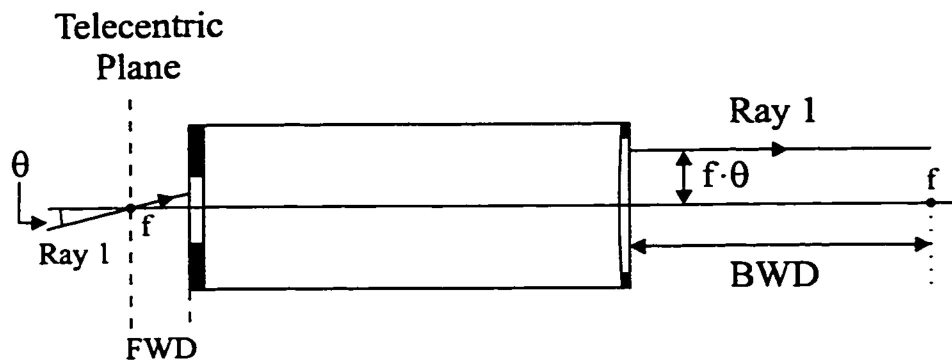

Figure 3.26 The telecentric, f-theta laser scan lens.

The f-theta property ensures a constant linear scan speed at the specimen when the input beam is scanned at a constant angular speed. One early application of the MACROscope was OBIC imaging of semiconductors combined with confocal reflected light imaging. Consequently the LSL was intended to be used with 633 nm (He-Ne laser) light and is therefore not colour corrected, exhibiting large chromatic aberrations. The front working distance (FWD) and the back working distance (BWD) are therefore wavelength dependent. FWD, BWD, NA, the theoretical lateral resolution, and axial resolution are listed for the LSL in Table 3.14 for three commonly used wavelengths.

	Wavelength		
	488 nm	568 nm	647 nm
FWD (mm)	27.5	31.2	34.5
BWD (mm)	209	222	232
NA	0.043	0.041	0.039
Lateral Res. (μm)	4.9	6.0	7.2
Axial Res. (μm)	233	298	375

Table 3.14 Specifications for the LSL. The specifications are wavelength dependent due to chromatic aberration.

The LSL chromatic aberrations makes photoluminescence imaging difficult and confocal PL operation nearly impossible. The effect of the chromatic error on the scanning beam is best understood with the aid of a badly aberrated (chromatically) thin lens as shown in Fig. 3.27. In Fig. 3.27, a collimated blue light beam is pivoted about the blue focal plane such that the beam focuses telecentrically on the specimen. In order to simplify this example, assume that the specimen photoluminesces such that the light returns along the same telecentric cone.

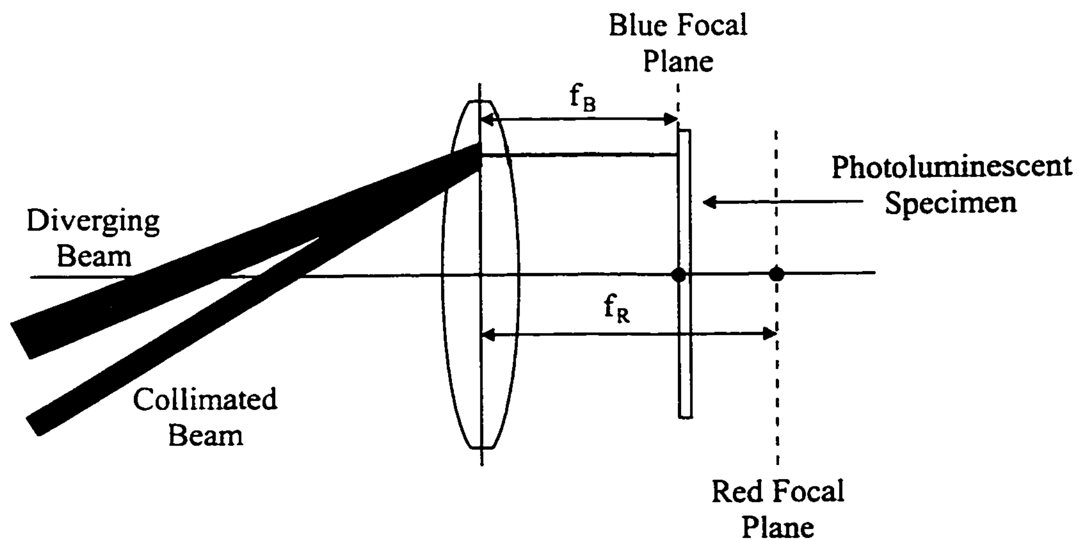

Figure 3.27 The effect of chromatic aberration on the returning luminescence emission. The blue beam enters the lens collimated and pivoting about the blue focal plane while the red beam is divergent and exits pivoting about the red focal plane.

The red photoluminesce beam will emerge from the lens, intersect the red focal plane at the optic axis and emerge with a slight divergence. The divergence can be calculated graphically by noting that it is as if the beam originates from a distance s_o from the lens, where s_o is given by Eqn. 2.1. In the case of Fig. 3.27, $s_i = ¾ f_R$ and therefore $s_o = -3 f_R$; that is, the red beam appears to originate at a distance $3f_R$ to the right of the lens such that its diameter coincides with the diameter of the blue beam at the lens. The arrangement where the LSL is positioned such that the incident excitation beam (blue) is focused on the specimen is typical of photoluminescence imaging on the MACROscope.

The specimen and specimen holder are mounted vertically on a New England Affiliated Technologies RM-400-SM single axis positioning table or z-table. The z-table provides a 0.5 μm resolution with a high degree of linearity and reliability due to its feedback feature which constantly monitors table position.

3.2.2 MACROscope Efficiency

The MACROscope is considerably simpler than the cslm thus an increased transmission efficiency is expected, unfortunately the LSL has a very small NA which leads to a dramatic decrease in collection efficiency. Although not shown in this thesis, the MACROscope can be run in non-confocal mode where a beam splitter is placed between the specimen and LSL. This configuration dramatically increases the collection NA.

Fig. 3.28 shows cumulative efficiency and component transmission values for both illumination (488 nm) and collection (647 nm) arms. The percent transmission values were obtained experimentally using the same methods that were used in section 3.1.2.1. Fig. 3.28a shows the illumination arm using 488 nm light. Unlike the cslm, the scanning mirrors on the MACROscope are in good condition with 92% reflectivity. The LSL is not efficient at 488 nm transmitting only ~ 50% of the light. Most objectives experience a decrease in transmission as wavelengths become shorter, although not to this degree until reaching deep purple or UV. Fig. 3.28b shows the LSL's dramatic increase in transmission, 95%, when using 647 nm light as well as a slight increase in reflectivity for the scan mirrors. More than double the amount of light collected by LSL reaches the pinhole compared to the cslm.

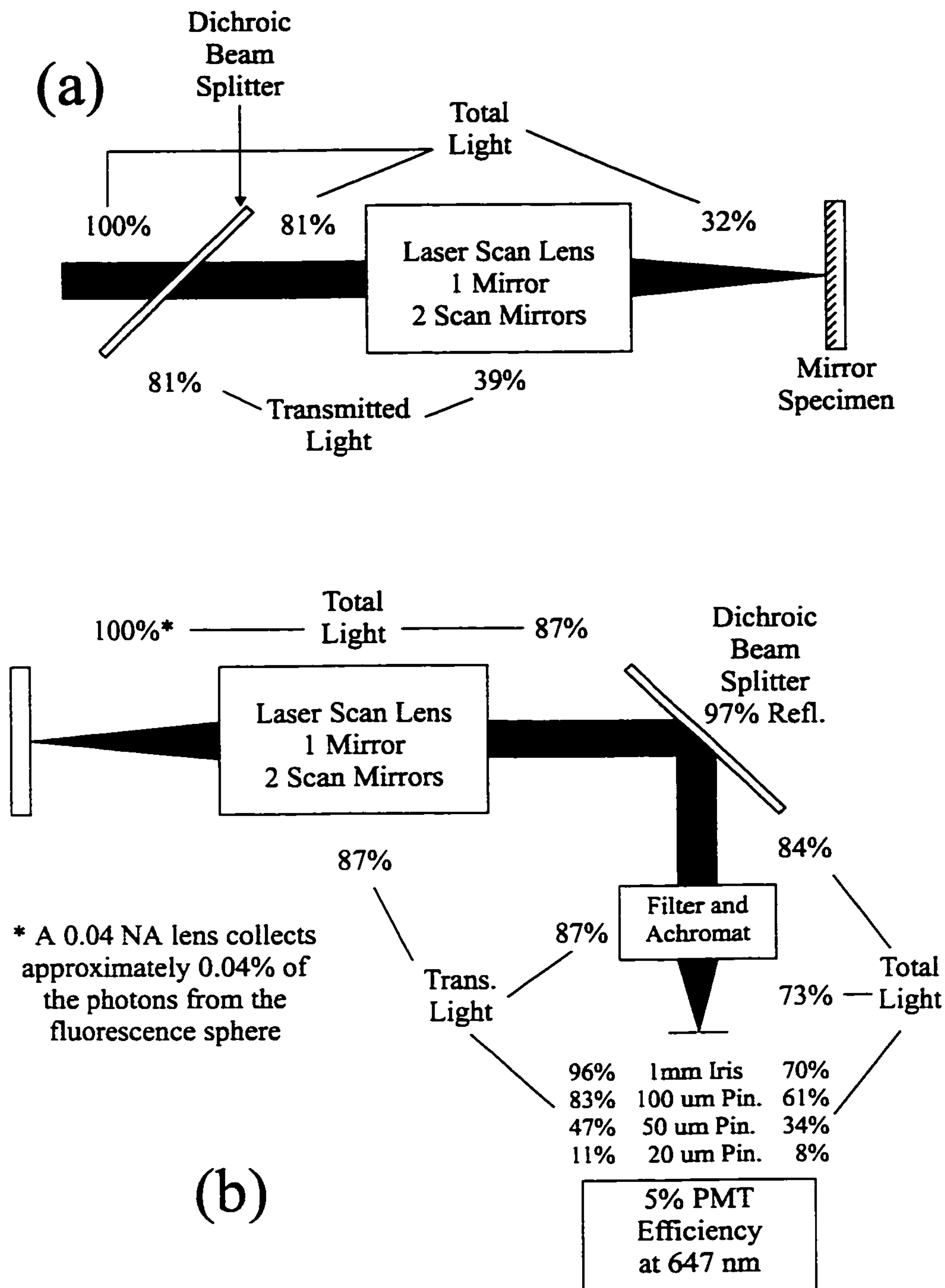

Figure 3.28 Transmission percentage for each component in addition to total cumulative transmission is shown. (a) MACROscope illumination efficiency using the 488 nm Ar-Kr laser line. The LSL transmits approximately 50% of the light at this wavelength. (b) MACROscope collection efficiency using 647 nm light.

When the collection efficiency of the LSL is taken into account, the total MACROscope efficiency drops well below the cslm efficiency. For example, using a 100 μm pinhole, the percentage of photons collected from the PL sphere is $0.0004 \cdot 0.68 \cdot 0.05 \cdot 100 = 0.0014\%$ or about one photon in 100 000, about one hundred times less than the cslm.

3.2.3 MACROscope Lateral Resolution

The lateral resolution on the MACROscope is dictated not so much by the LSL optical resolution but rather the angular resolution and stability of the scanning mirrors. The scanners are overloaded with mirrors many times larger than the rated size and therefore experience scan speed dependent wobble and jitter. The MACROscope user must tune out scanner instabilities by slightly varying the scanning speed.

Fig. 3.29a is a zoom 1, 8 x 8 cm, reflected-light (488 nm) image of a 7.6 x 7.6 cm U.S. Air Force resolution target. A 100 μm pinhole was used along with a 30 cm focal length achromatic detector lens. The slight darkening near the edges of the image will be discussed in the section dealing with the effects of non-telecentric operation. The LSL can be considered an extremely high NA lens given its very low magnification. For conventional objectives, the limits of resolution can be reached with zoom 8 or 16, but with the LSL zoom 128 is needed to reach the resolution limit. Fig. 3.29b shows a zoom 16, 5 x 5 mm image from the center of the air force target with no signs of degrading resolution evident at this point. Fig. 3.29c shows a zoom 128, 625 x 625 μm confocal image of the same resolution target used in Fig. 3.7. This image shows clear signs of scanner instability such as sudden breaks in the image near the top, jittery-looking 10 μm lines, and significant blurring near the bottom. This image was obtained using a 10 μm pinhole with a 30 cm focal length achromatic detector lens at 488 nm. The 5 μm lines are clearly resolved (optically) by the LSL as shown in Fig. 3.29d where an intensity profile was taken along the yellow line shown in Fig. 3.29c.

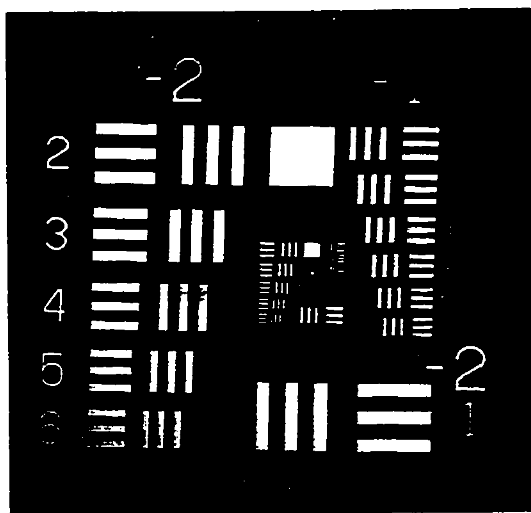

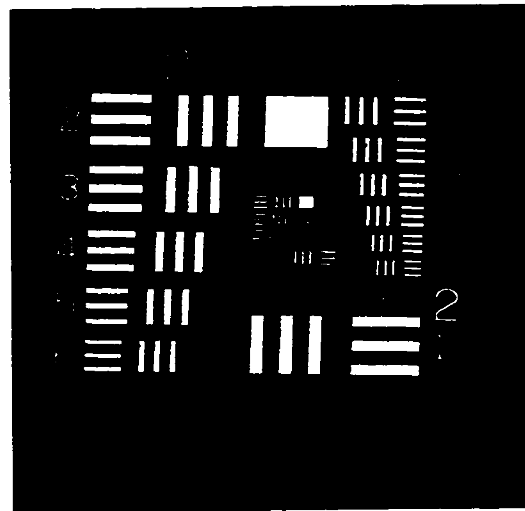

(a) 4 cm (b) 2 mm

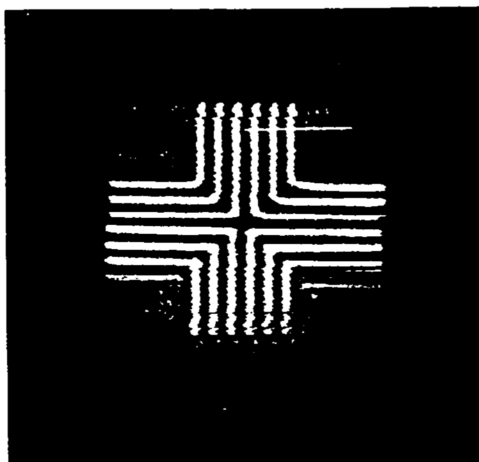

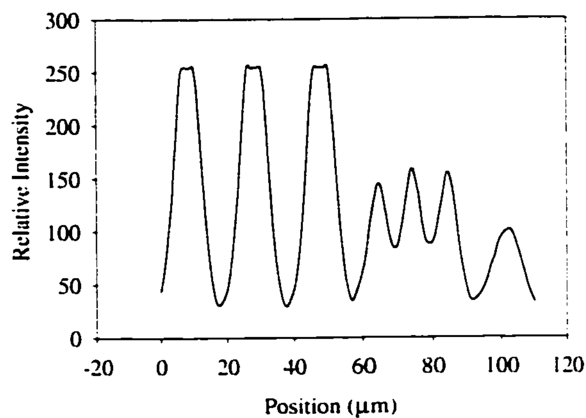

(c) 300 μm (d)

Figure 3.29 (a) Zoom 1 (8x8 cm) image of an Air Force reflection resolution target. (b) Zoom 16 (5x5 mm) image of the same target. No signs of blurring are observed at this point. (c) Zoom 128 (625x625 μm) image of the cslm resolution target. There are signs of scanner related problems, but optically, the 5 μm lines are resolved as seen in (d).

3.2.4 MACROscope Axial Resolution

The MACROscope axial resolution measurements were very similar to the measurements made on the cslm in that they consisted of analyzing z-position vs. intensity and FWHM such as shown in Fig. 3.10a and b. Fortunately, the MACROscope z-stage was of sufficient accuracy and repeatability that a Michelson interferometer calibration was not needed. Measurements such as those in Figs. 3.10a and b were all that was needed to determine FWHM and relative intensity for the MACROscope.

Pinhole (μm)	Relative Intensity	FWHM (μm)	HWHM (μm)	Normalized Int./FWHM
20	0.5	338	169	6.4
50	2.6	410	205	27
100	6.8	724	362	40.3
200	18.7	1149	574.5	70
400	45.3	1946	973	100
1000	82.4	4301	2150.5	82.4
3000	100			

Table 3.15 Axial resolution and relative intensity data as a function of pinhole diameter for the reflective detector arm configuration. The 488 nm laser line was used for this table.

Pinhole (μm)	Relative Intensity	FWHM (μm)	HWHM (μm)	Normalized Int./FWHM
20	0.4	461	230.5	5.1
50	2	476	238	24.9
100	5.3	809	404.5	39.1
200	13.6	1475	737.5	54.4
400	40.5	2396	1198	100
1000	74.7	4915	2457.5	89.9
3000	100			

Table 3.16 Axial resolution and relative intensity data as a function of pinhole diameter for the reflective detector arm configuration. The 647 nm laser line was used for this table.

Tables 3.15 and 3.16 show relative intensity, FWHM, HWHM, and Intensity/FWHM as a function of pinhole size for 488 nm and 647 nm light, respectively.

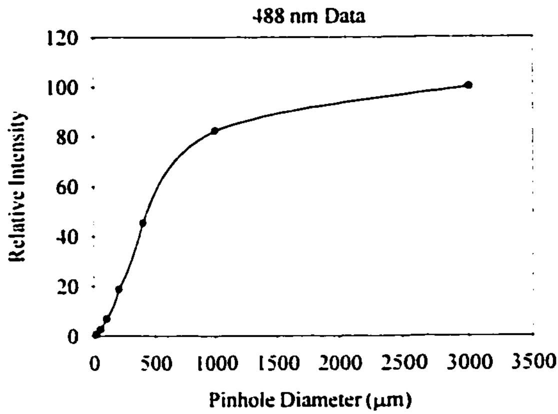

(a)

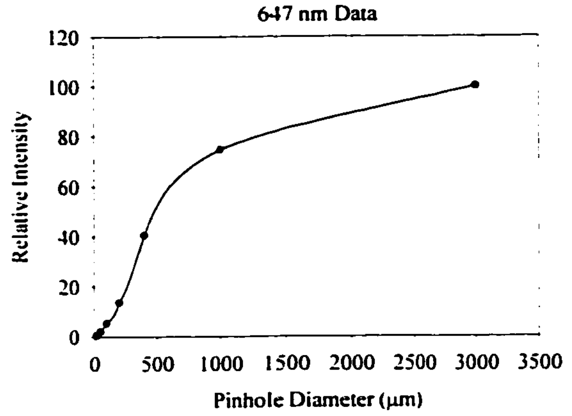

(b)

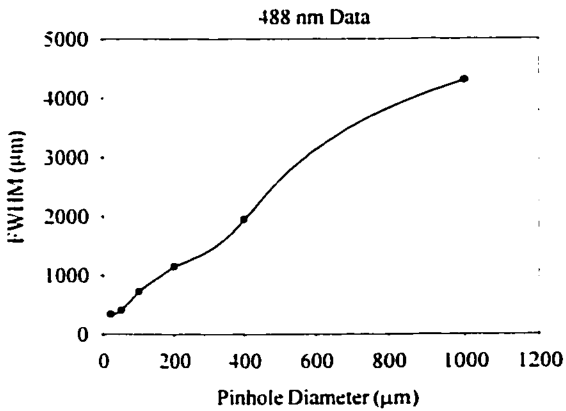

(c)

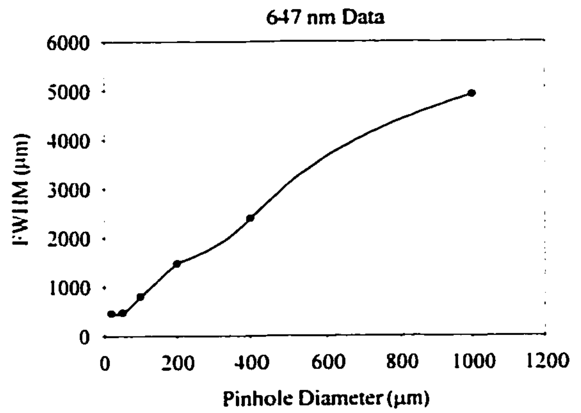

(d)

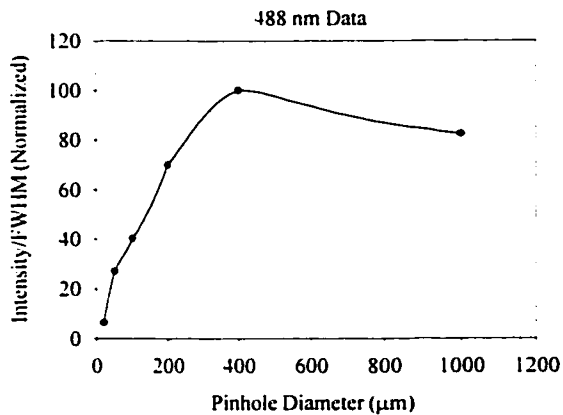

(e)

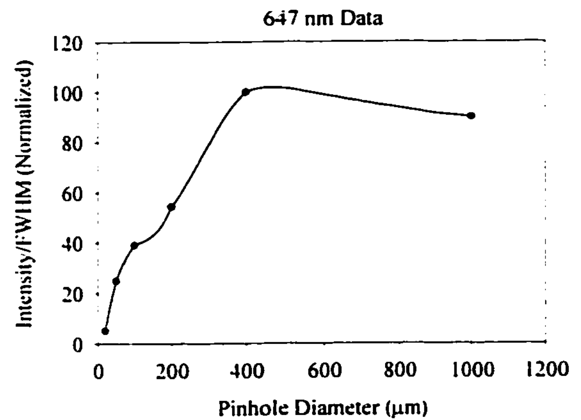

(f)

Figure 3.30 Data from Tables 3.15 and 3.16. Relative intensity, FWHM, and Intensity/FWHM are plotted as a function of pinhole diameter for the 488 nm laser line in (a), (c), and (e) respectively. The equivalent 647 nm laser line data is plotted in (b), (d), and (f).

Axial resolution measurements were performed for these commonly used wavelengths with the reflecting detector arm shown in Fig. 3.25, in order to ensure that the LSL chromatic aberration had no significant effect on axial resolution.

Relative intensity vs. pinhole diameter for 488 and 647 nm wavelengths are plotted in Fig. 3.30a and b. The theoretical Airy disk diameters are 53 and 70 μm for the 488 and 647 nm wavelengths respectively. The curves in Figs. 3.30a and b should level off in intensity at about the 100 μm pinhole mark rather than continuing to increase well beyond the 1000 μm pinhole level. These curves indicate there might have been aberrations present to cause a larger and/or non-circular spot at the confocal pinhole. Figs. 3.30c and d show FWHM plotted as a function of pinhole for 488 and 647 nm wavelengths, respectively. In both cases, the curves are very linear after the 50 μm pinhole level. The minimum FWHM values from Tables 3.15 and 3.16 (338 and 461 μm, respectively) differ by about 100 μm when compared with the theoretical values in Table 3.14, which indicates aberrations once again. Figs. 3.30e and f show Intensity/FWHM vs. pinhole for 488 and 647 nm wavelengths, respectively. These curves represent the combined results of the previous curves in Fig. 3.30 and therefore indicate aberrations. The ideal pinhole for both wavelengths is the 400 μm pinhole which is many times the size of the theoretical Airy disk.

Due to the simplicity of the MACROscope the aberrations can only originate from either the LSL, the beam splitter or the spherical mirror. The LSL is not likely to have a large amount of spherical aberration. The beam splitter is 5 cm in diameter but only ~ 2 mm thick and is therefore prone to deformation at an optical level (several wavelengths). Another explanation is that the spherical mirror caused astigmatism due to its tilt with respect to the light beam (~7°). A fourth explanation is that the 2 cm beam had a poor profile and spatial filtering is needed.

Table 3.17 shows the same type of axial data as Table 3.16 for a refractive detector arm as shown in Fig. 3.24 using 647 nm light and a 25 cm focal length achromatic detector lens. The theoretical Airy disk diameter in this case is 22 μm and therefore the ideal pinhole should be 20 μm or less; unfortunately, it is much larger (100 μm). Once again the relative intensity shows a steady rise well beyond the theoretical Airy disk diameter indicating some aberration. Also the minimum FWHM value was found to be 512 μm which is worse than the

result obtained with the spherical mirror case in Table 3.16. The only plausible explanation for this is wavefront distortion due to the beam splitter or the original beam from the beam expander.

Pinhole (μm)	Relative Intensity	FWHM (μm)	HWHM (μm)	Normalized Int./FWHM
10	1.1	512	256	8.9
20	6.4	568	284	48.1
50	18	983	492	77.9
100	45.1	1920	960	100
1000	100	12083	6042	35.3

Table 3.17 Axial resolution and relative intensity data for the refractive detector arm configuration. The results do not differ dramatically from the reflective detector arm.

3.2.5 MACROscope Telecentricity

The MACROscope scanning beam system consists of two mirrors closely spaced together as shown in Fig. 3.24. This is a telecentrically flawed system since the telecentric plane of the LSL lies between the two scanning mirrors. At best only one mirror can be correctly positioned on the telecentric plane unless an optical relay system is used such as a unitary telescope. The effect of this non-telecentric arrangement can be best illustrated with a single thin lens. Fig. 3.31a shows a collimated beam pivoted about point P which lies a distance x from the first focal point (the telecentric plane). A line parallel to the beam can be drawn, originating from point f, to show where the beam will focus on the specimen. The reflected beam will pass through the lens and emerge parallel to the incident beam, which by symmetry will intersect the optic axis a distance x to the right of point f.

Fig. 3.31b shows how x, θ, t and α relate to each other:

$$t = 2x\sin\theta \qquad \textbf{(3.4)}$$

where t = the perpendicular distance between the incident and reflected beam to the left of the lens and θ = the angle that the incident beam makes with the optic axis to the left of the lens.

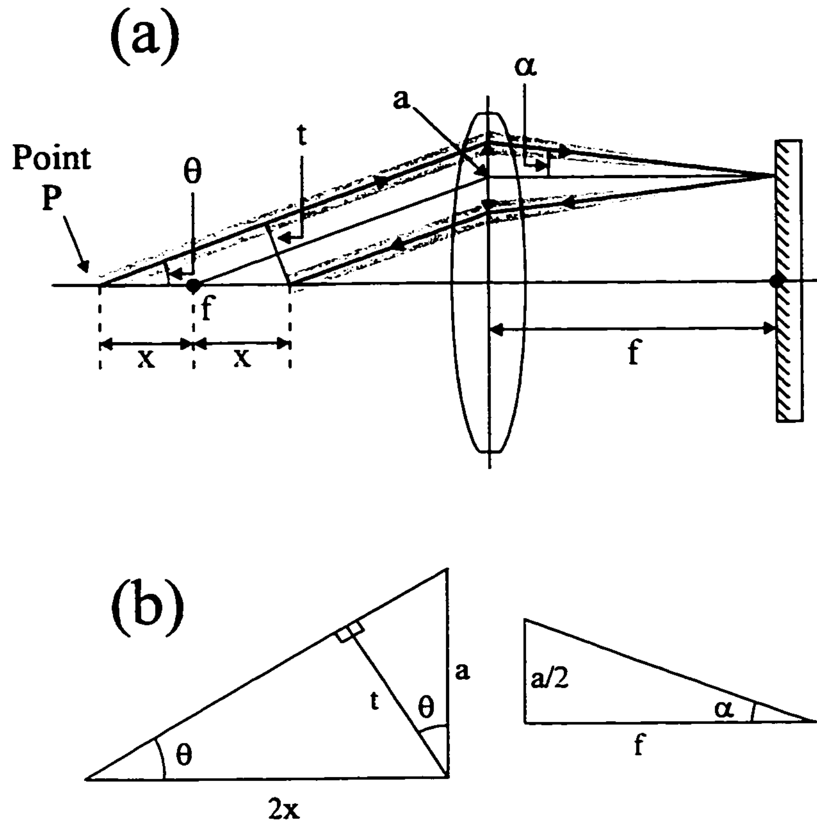

Figure 3.31 (a) The effect of pivoting a beam away from the telecentric plane. The beam deviates from telecentricity by an angle α and the returning beam crosses the optic axis a distance 2x from the incident beam. (b) Diagrams showing various relationships between angles and distances in a).

$$\alpha = \tan^{-1}\left[\frac{x}{f}\tan\theta\right] \qquad \textbf{(3.5)}$$

where α = the angle made by the incident beam with the optic axis to the right of the lens and f = the focal length of the lens. A worst case scenario with the MACROscope might be θ = 10° and x = 2 cm which yields t = 6.9 mm and α = 0.91°, using a 223 mm effective focal length. While the focusing beam is telecentric to within <1°, the beam at the detector lens will move ~ 7 mm to the right, left, up and down as the scan proceeds. In theory as long as the beam entering the detector lens is parallel to the optic axis, it will focus at the same point no matter where it strikes the lens.

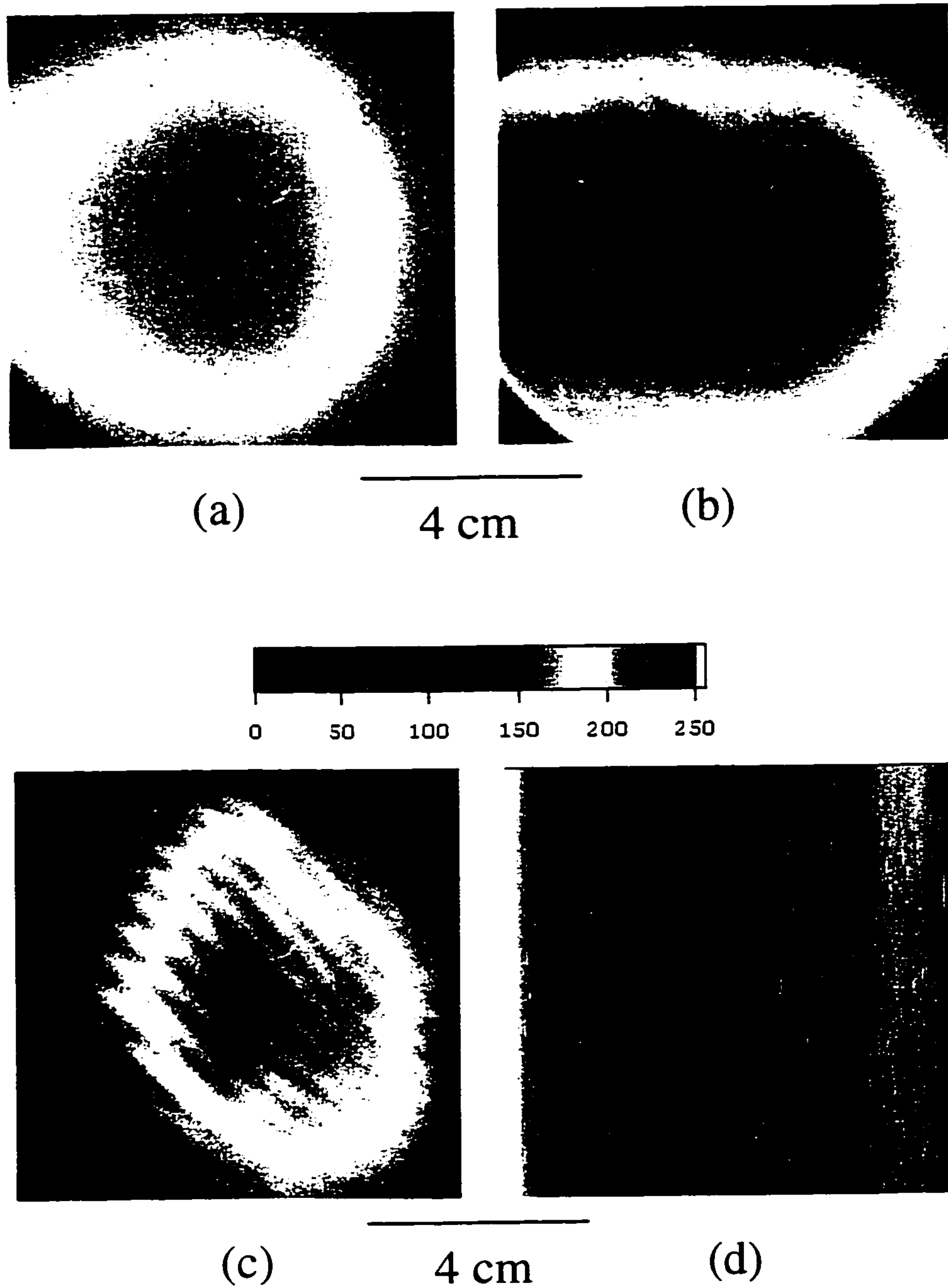

Figure 3.32 False colour images of a flat mirror taken at zoom 1 (8x8 cm) with the reflective detector arm. As the pinhole size is decreased from 1000, 400, to 100 μm in (a), (b), and (c) respectively, the uniform intensity field of view decreases. (d) The x-scanning mirror was placed right at the telecentric plane and the y-scanner was set to zoom 64. The result is no telecentric error and a reasonably uniform image.

In practice. spherical aberration will enlarge the spot at the pinhole as the beam is moved away from the axis. Also, the beam will be stationary only at the focal point such that proper pinhole positioning (axially) is critical in order to avoid a wandering diffraction spot. The moving beam will also cause it to be clipped since the scanning mirrors are almost fully filled by the incident beam. Note that for PL. the specimen emits homogeneously in all directions as a first approximation. If the scan mirror is overfilled then the returning PL light will follow the exact same path as the incident light. Fig. 3.32 illustrates the effect of non-telecentric operation as the pinhole size is decreased from 1 mm in a) to 400 μm in b) and to 100 μm in c). Figs. 3.32 a, b and c show a zoom 1, 8 x 8 cm reflected light images of a flat mirror using 647 nm light and the reflecting detector arm shown in Fig. 3.25. The effects of this aberration closely resemble the effects of the unitary telescopes on the cslm. The banded pattern in Fig. 3.32c is due to interference from the beam splitter. For Fig. 3.32d the LSL was moved such that the x-scanning mirror lay on the telecentric plane. The x-scan was set to zoom 1 and the y-scan to zoom 64 effectively eliminating the non-telecentric problem. Apart from the above mentioned changes. this image was taken using the same setup as in Fig. 3.32c (100 μm pinhole). Fig. 3.32d is clearly more uniform in the x-direction than Fig. 3.32c.

Switching over to the refractive detector arm (Fig. 3.24), did nothing to improve the non-telecentric effect. The images in Fig. 3.33 were produced using the same experimental conditions that were used to generate Table 3.17. Fig. 3.33a shows the non-telecentric effect with a 25 cm focal length achromatic detector lens combined with a 1 mm iris diaphragm. Fig. 3.33a is a zoom 1, 8 x 8 cm reflected light image using 647 nm light. The loss in intensity observed near the edges is mainly due to the scan mirrors clipping the reflected beams. If the beam is reduced from an 18 to a 7 mm diameter, the reflected beam will not be clipped and the image uniformity increases significantly as shown in Fig. 3.33b. Fig. 3.33b is close to the best uniformity available with the MACROscope. The loss in intensity at the top is due to the degradation of the mirror edge where the aluminum has been chipped away near the edge and has decreased in reflectivity. The darkening at the two corners near the bottom are due to the fact that the beams have hit the outer perimeter of the LSL, hence the scan is not perfectly centered in the vertical direction.

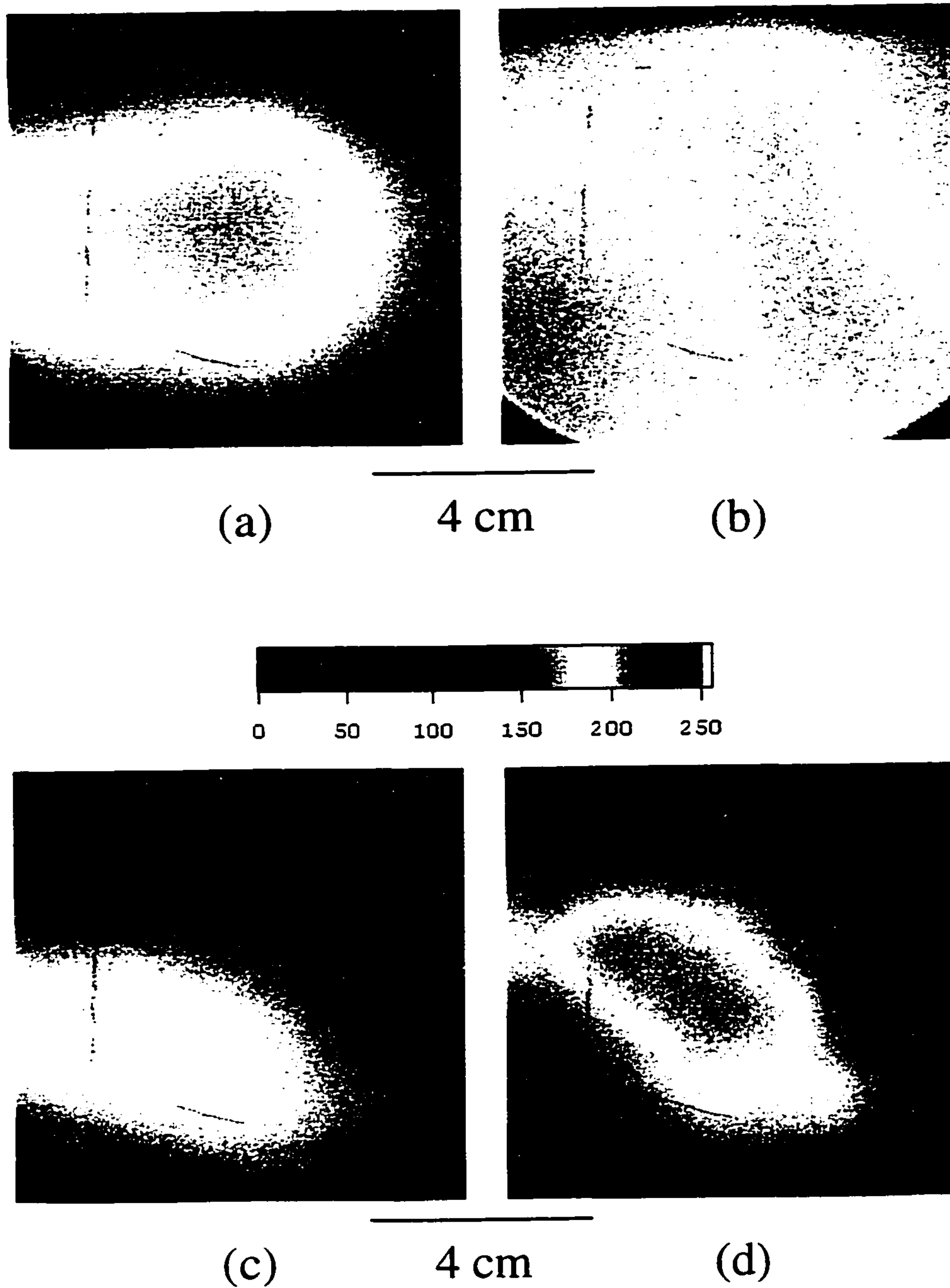

Figure 3.33 False colour images of a flat mirror taken at zoom 1 (8x8 cm) with the refractive detector arm. (a) Using a 1 mm iris diaphragm the image is uniform only near the center. The darkening near the edges is due to the scan mirror clipping the beam as a result of the non-telecentric error. (b) The beam entering the LSL was reduced from 18 mm to 7 mm diameter thereby avoiding the clipping effect, resulting in a very uniform image. As the pinhole size is reduced to 100 and 50 μm, as in (c) and (d), respectively, the clipping effect no longer dominates and the uniform field of view is reduced regardless of entrance beam diameter.

Fig. 3.33b can be used as a benchmark for uniformity measurements on the MACROscope. Figs. 3.33c and d show the effects of using 100 and 50 μm pinholes, respectively. For these pinhole sizes it makes no difference if the beam is 18 or 7 mm in diameter. Other aberrations dominate and are the causes of the non-uniformity. For the ideal pinhole of 100 μm the scan should be limited to zoom 4 or 2, at best, in order to retain a uniform intensity.

3.3 Spectral Characterization on the MACROscope

UW-CMG[10] has done extensive work with confocal spectrally resolved scanning stage microscope imaging. Spectral resolution is achieved on the SSM by scanning a grating situated before the detector lens thereby only allowing a narrow band of wavelengths to enter the detector.

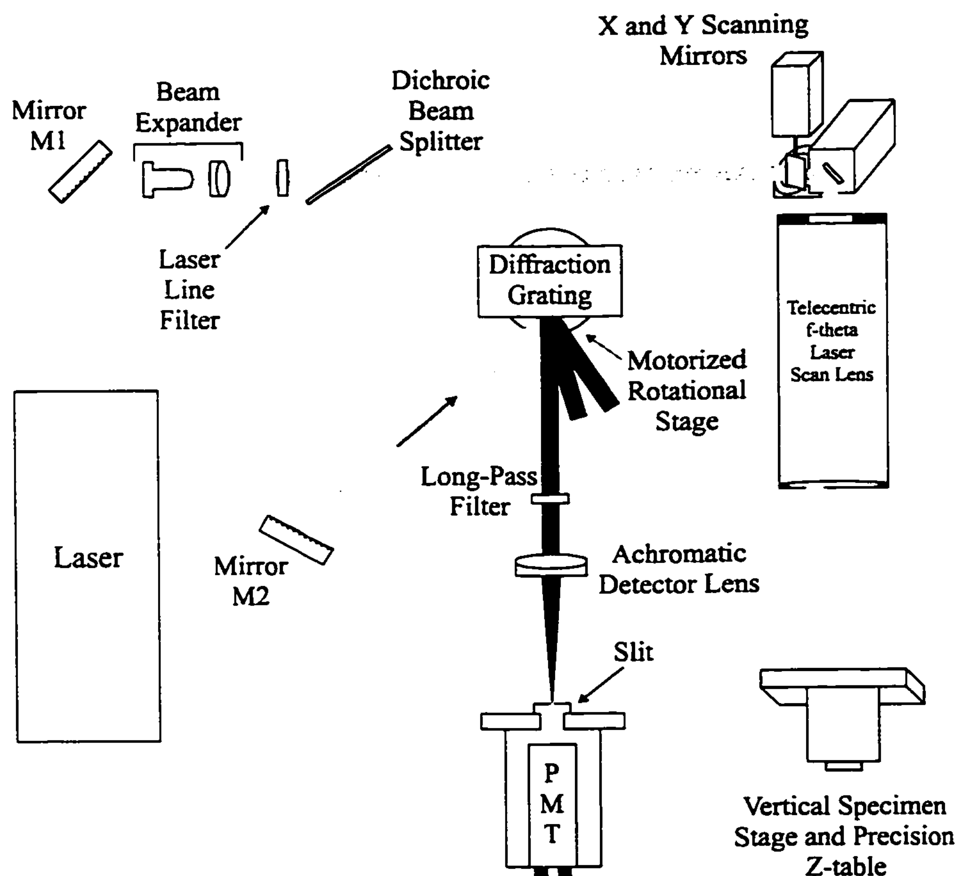

Figure 3.34 Spectrally resolved version of the MACROscope

S. Damaskinos and P. Dube modified the MACROscope, along the lines of the SSM, in order to allow for spectral measurements. Fig. 3.34 shows a schematic diagram of the spectrally resolved MACROscope. This is essentially the 'regular' MACROscope with the addition of a diffraction grating mounted on a precision rotational stage. Instead of a pinhole as the confocal aperture (in this case a spectral aperture), a slit was used. Use of a vertical slit was found to be essential since a pinhole is too sensitive to vertical movements of the diffraction spot which causes large changes in intensity. The slit effectively averages variations in vertical intensity, which has no spectral information, greatly improving the consistency and repeatability. The results in this section are preliminary in nature and are intended to show that it is possible to obtain spectral measurements even with a chromatically aberrated LSL and non-telecentric aberration.

Due to the speed of the rotational stage the MACROscope can only provide two wavelength dependent scans: a λ-scan at a single point, and a x-λ scan along a single horizontal line. The critical parameter, as with any imaging, is resolution. For most photoluminescent specimens excitation can be done with blue (488 nm) and emission occurs somewhere in the red (~650 nm) hence the LSL was focused on the specimen for blue while the achromatic detector lens was adjusted so as to focus red (647 nm) onto the slit. The result was optimum spectral resolution for wavelengths around 647 nm and poor resolution for wavelengths far from 647 nm. Table 3.18 shows spectral FWHMs using a typical slit width for the three Ar-Kr laser wavelengths. As expected, the FWHM is best when using 647 nm light (1.57 nm) and almost three times worse for the 488 nm line (4.80 nm).

Wavelength (nm)	Spectral FWHM (nm)
488	4.80
568	2.46
647	1.57

Table 3.18 Spectral resolution for the MACROscope. The resolution is highly dependent on wavelength due to the chromatic aberration of the LSL.

The non-telecentric aberration had the effect of shifting the diffraction spot left and right at the pinhole when the scan angles were large (zoom 1 and 2). The effect of this shifting can be seen in Fig. 3.35 where wavelength is plotted as a function of position. This zoom 1 image was taken using a mirror specimen and 647 nm light. Instead of a straight band, the image shows a gently sloping band of light which indicates a position dependent shift in wavelength. Fortunately, this wavelength shift error can be corrected by simply applying the inverse wavelength shift.

There are two types of calibration that must be reconciled on this system: wavelength calibration and intensity calibration. Wavelength calibration has to do with finding out what wavelength corresponds to each particular diffraction grating position.

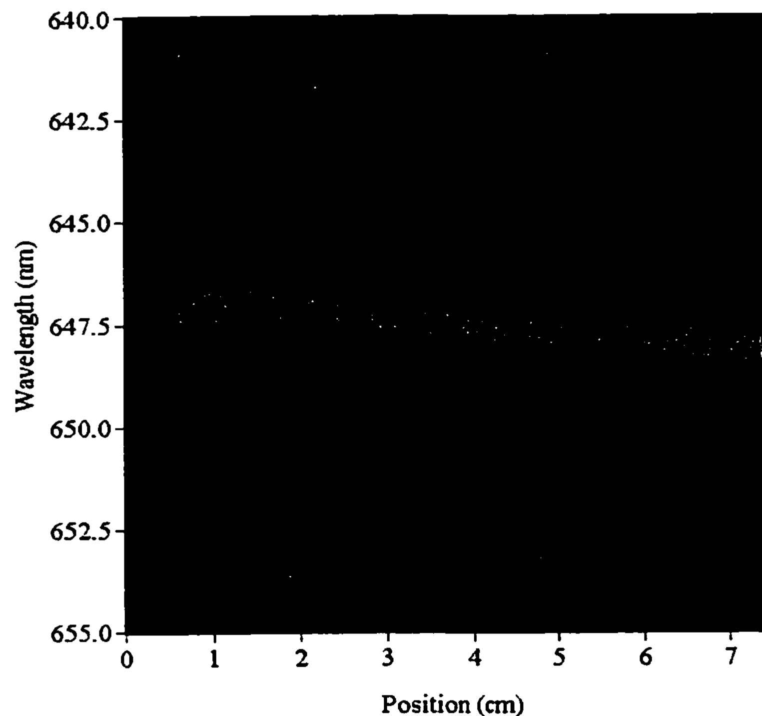

Figure 3.35 MACROscope spectral image of a mirror plotting wavelength vertically and x-position horizontally. The scan was taken at zoom 1 (8x8 cm) in the x-direction with the y scanning mirror disabled.

This relationship can be easily obtained with the Ar-Kr laser since it provides three very narrow, widely spaced laser lines of known wavelength. Intensity calibration has to do with

the response of the entire MACROscope with respect to wavelength. In general this response function should be factored into spectrum measurements such that a true spectrum can be obtained. The best way to obtain the response function is to image a known photoluminescence specimen with a broad, continuous spectrum which is not susceptible to bleaching. The measured and theoretical spectra are compared and a calibration/response curve can be generated and used to correct future spectra. Unfortunately ideal specimens, such as the one described above, are difficult if not impossible to find. The next best specimen is a quasi-black body source as shown in Fig. 3.36. The source in Fig. 3.36 consists of a tungsten halogen 35 W light bulb enclosed in an aluminum box with attached heat sinks and a pinhole mount. The bulb is connected to a regulated voltage power supply and operates at a temperature of ~ 3000 K. The calibration spectrum is generated by measuring the lamp's spectrum with a reliable and properly calibrated spectral radiometer and dividing this by the spectrum measured by the MACROscope. Future MACROscope spectra must be multiplied by this calibration spectrum in order to obtain a 'true' spectrum.

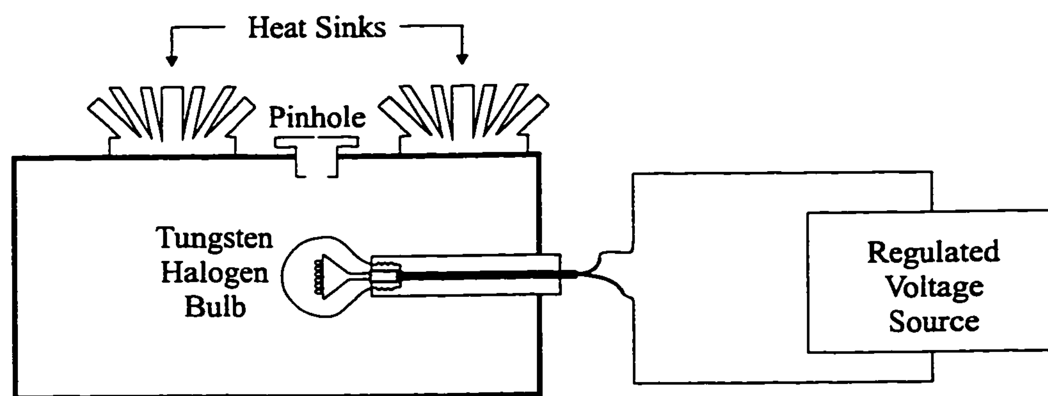

Figure 3.36 Tungsten-halogen light source (~3000 K) used to calibrate spectrally resolved data on the MACROscope.

3.4 Summary and Discussion

This chapter has served to critically evaluate the performance of the UW-CMG cslm and MACROscope. A detailed component by component breakdown of the cslm was given which aided in defining capabilities and operating parameters. The cslm light source consists of a wide range of lasers providing wavelengths from 325 to 1152 nm. The greatest limitation

for the cslm is the scanning arm. The scanning mirrors are too small to accommodate beams larger than 5 mm in diameter and they reflect poorly (<75%) due to aging. The unitary telescopes make alignment very difficult and effectively reduce the unaberrated field of view down to zoom 4 or at best zoom 2. The objectives on the other hand are high quality and range from 0.14 to 0.9 in numerical aperture, providing fields of view ranging from 200 x 200 μm up to 4 x 4 mm.

The collection efficiency for the cslm is mainly limited by the PMT detector (~ 5% efficiency) like most other confocal microscopes. Optically there is need for improvement since only about a third of the light collected by the objective reaches the confocal pinhole. Lateral resolution, as far as can be measured, agrees with theory. The Axial resolution measurements yielded results that were consistently greater than the theoretical values; however graphical data did not indicate any anomalies except with the 0.9 NA objective. While the unitary telescopes cause problems off-axis, they do not seem to affect the system when small scan angles are used. Both lateral and axial resolution were measured using reflected light only, since photoluminescence resolution targets were not available. Although lateral and axial measurements were taken with a 10 cm focal length achromatic detector lens, the resulting curve shapes and best lateral and axial measurements all serve as a benchmark for future measurements regardless of the specifics for the cslm setup.

The MACROscope was designed to combine the fast scanning beam capabilities of the cslm with the large scan area feature of a SSM. The result is a 0.04 NA instrument which can scan areas as large as 7.5 x 7.5 cm in less than 10 s. The heart of the MACROscope is its telecentric, f-theta laser scan lens which is analogous to a microscope objective in the cslm.
The telecentric plane on the LSL is located ~ 3 cm outside of its case. This feature in addition to its long focal length makes it possible to discard unitary telescopes and use two closely spaced scan mirrors as the scan arm. The unitary telescopes work very poorly at large scan angles and beam diameters, however the closely spaced scan mirrors introduce a non-telecentric scan error which results in a reduction in the field of view to about zoom 2 or 4

depending upon the confocality. Due to cost considerations, the LSL was not colour corrected which makes photoluminescence imaging difficult.
Due to the simplicity of the optics the transmission efficiency for the MACROscope is considerably better than the cslm where 2/3 of the light collected by the LSL reaches the pinhole. The most limiting element with respect to total collection efficiency is the LSL itself which only collects 0.04% of the light from an ideal PL sphere. The lateral resolution measurement agree with theory, however, the MACROscope's axial measurements indicate that aberrations are present. The detector arm showed signs of astigmatism due to the beam splitter or the original expanded beam which seems to be distorting the beam profile. In fact the non-telecentric error probably stems from this aberration. The best axial resolution values are significantly higher than the values predicted by theory. Once again these measurements can be used as benchmarks for future experiments involving a modified MACROscope. More importantly, the resolutions calculated in this chapter were the ones in effect for all the imaging results of chapter 4 and therefore should not be dismissed as erroneous or irrelevant.

In addition to the above characterization, a spectrally resolved version of the MACROscope was also examined. Its spectral resolution was on the order of 2 nm. Some preliminary efforts were made to properly calibrate the system.

Several new contributions were made in this chapter:

1) A prototype MACROscope was constructed and subsequently improved.
2) PMT linearity for Hamamatsu models R292 and R2228 was measured.
3) The MACROscope and cslm were characterized with respect to throughput, lateral resolution, and axial resolution.
4) Imaging evidence of aberrations from the unitary telescopes on the cslm was shown.
5) Analysis of non-telecentric operation on the MACROscope and cslm.
6) Spectral resolution measurements on a spectrally resolved MACROscope.

REFERENCES

[1] A.E. Dixon, S. Damaskinos, and M.R. Atkinson, Nature (London), **351** (1991) 551.

[2] J.W. Bowron, Ph.D. Thesis, 1993, Physics Department, University of Waterloo, Waterloo, Canada, Chapter 3.

[3] J.W. Bowron, Ph.D. Thesis, 1993, Physics Department, University of Waterloo, Waterloo, Canada, Appendix 1.

[4] J.B. Pawley (Editor), Handbook of Biological Confocal Microscopy, 2nd Edition, (Plenum, New York, 1995), p130.

[5] E. Hecht, Optics, 2nd Edition, (Addison-Wesley, Reading Massachusetts, 1987), p354.

[6] J.B. Pawley (Editor), Handbook of Biological Confocal Microscopy, 2nd Edition, (Plenum, New York, 1995), Chapter 11.

[7] J.B. Pawley (Editor), Handbook of Biological Confocal Microscopy, 2nd Edition, (Plenum, New York, 1995), p 42, 161, 366, 579.

[8] J.W. Bowron, Ph.D. Thesis, 1993, Physics Department, University of Waterloo, Waterloo, Canada, p61.

[9] W.J. Smith, Modern Optical Engineering, 2nd Edition, (McGraw-Hill, New York, 1990), p 143.

[10] J.W. Bowron, Ph.D. Thesis, 1993, Physics Department, University of Waterloo, Waterloo, Canada, Chapter 2.

CHAPTER 4

MACROSCOPE / CSLM APPLICATIONS AND IMAGING RESULTS

The ultimate value of a new instrument, such as the MACROscope, can be determined by the quantity and quality of its applications. The University of Waterloo's Confocal Microscopy Group (UW-CMG) has applied the confocal scanning laser MACROscope/Microscope (cslM/m) to the imaging of fingerprints[1], DNA gels[2], and various biological specimens[3,4]. This chapter describes two applications related to the characterization of semiconductor materials and devices: solar cells[5,6] and porous silicon[7,8].

Solar cells and some solid state detectors are generally several centimeters in size and therefore lend themselves to imaging on the MACROscope. Reflected-light (RL), photoluminescence (PL) and especially optical beam induced current (OBIC) are used to characterize and identify defects in solar cells. A brief introduction to solar cells and OBIC is given followed by a series of micro and macroscopic images of various silicon and thin-film solar cells. Some limitations of OBIC in addition to a comparison with electron beam induced current (EBIC) are also presented.

The second part of this chapter deals with porous silicon (PSi), a novel material which could possibly lead to the development of all-silicon optoelectronics. A collaboration with P.M. Fauchet's research group in electrical engineering at the University of Rochester has resulted in a wide variety of PSi materials and device images on the cslM/m at virtually all magnifications and modes of operation. The imaging results from PSi materials and devices are presented separately along with a short introduction to PSi.

Applying the cslM/m to real imaging problems is extremely important since without applications it has no purpose. By imaging many different types of specimens, flaws in the cslM/m can be highlighted and corrected. For example, the unitary telescope aberrations were first discovered when imaging highly reflective PSi specimens. Imaging is also very important to the continuing development of the cslM/m.

Several new contributions were made in the field of scanning microscopy: two imaging applications were demonstrated for the MACROscope-Microscope related to porous silicon and solar cells. The MACROscope-Microscope instruments are able to generate confocal PL and RL images, as well as OBIC images both macroscopically and microscopically. Imaging evidence of lateral etching and enhanced PL was shown for two PSi specimens. A PSi solar cell and a PSi device were characterized using RL, PL, and OBIC.

4.1 Solar Cells

A thorough understanding of solar cells requires a good foundation in semiconductor materials and devices which is beyond the scope of this chapter. Although a brief introduction to solar cells is given in this section, the reader is encouraged to consult textbooks such as Streetman[9] and Green[10] for more information on semiconductors and solar cells, respectively.

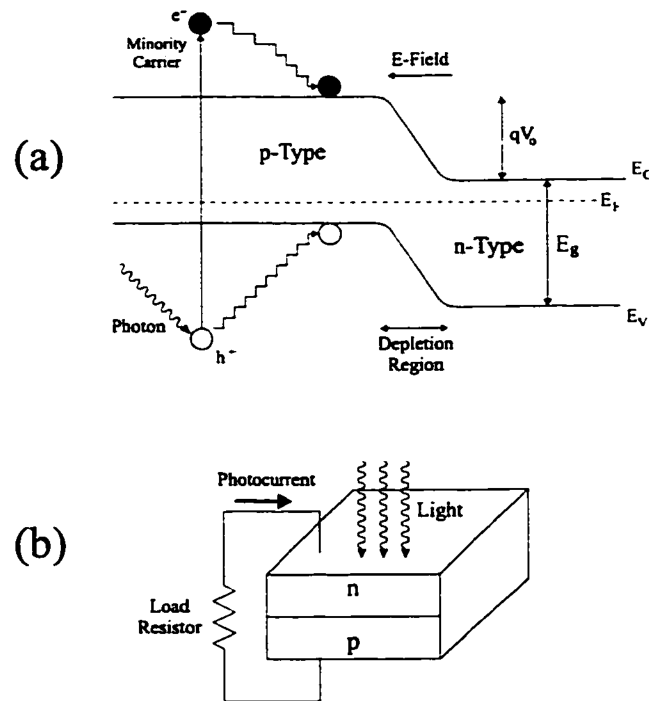

Figure 4.1 (a) A solar cell consisting of a p-n homojunction where electron energy is plotted vertically. Minority carriers created via photon excitation diffuse throughout the semiconductor. Those collected by the junction contribute to the photocurrent. (b) A solar cell connected to a load resistor. The photocurrent flows from n to p-type internally, which is defined to be a negative current.

A basic solar cell consists of a p-n junction, as shown in Fig. 4.1, where electron energy is plotted vertically. Incident photons with energies exceeding the bandgap energy, E_g, create electron-hole pairs which quickly thermalize to the band edges as shown in Fig. 4.1a. Minority carriers (in this case electrons) diffuse throughout the semiconductor and those close enough to the junction are 'swept' by the depletion region electric field into the opposite side. Minority carrier collection by the junction results in the generation of an internal photocurrent from n to p. The current flows from p to n via the load resistor in the external circuit as shown in Fig. 4.1b. A simplified collection probability (no trapping) as a function of electron-hole pair creation position, with respect to the depletion region, is shown in Fig. 4.2 (modified from Green[10], P142) . Practically all electron-hole pairs generated within the depletion region contribute to the photocurrent since the region is assumed to be very thin with a large electric field and few defects to serve as recombination centers. Outside the depletion region, the collection probability decreases exponentially with increasing distance away from the depletion region limits.

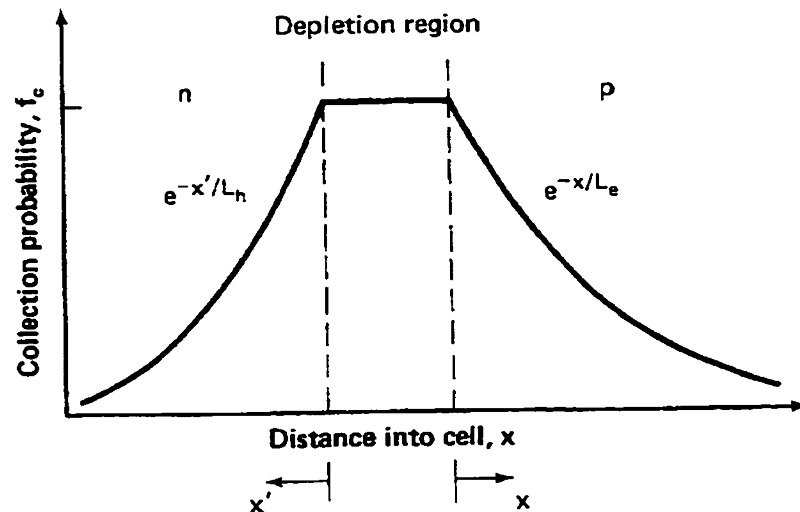

Figure 4.2 Probability of the minority carrier reaching the junction (instead of recombining with a majority carrier) as a function of where the electron-hole pair was created. The collection probability is assumed to be one inside the depletion region while dropping off exponentially at the depletion region borders. Figure modified from Green[10], p142.

The collection probability can be written as follows for the p-side:

$$f_c \cong 1 \quad \text{if inside the depletion region}$$
$$f_c = e^{-x/L_e} \quad \text{if outside the depletion region} \tag{4.1}$$

where L_e = the average distance an electron diffuses before recombining with a hole, and x is the distance to the junction edge (see Fig. 4.2). The electron diffusion length, L_e, depends upon the minority carrier lifetime, τ_e, and the diffusion constant, D_e, in the following way:

$$L_e = \sqrt{D_e \tau_e} \tag{4.2}$$

In the dark, a solar cell will behave like a diode and follow the ideal diode law:

$$I_D = I_o(e^{qV/kT} - 1) \tag{4.3}$$

where I_D = the current flowing through the diode, I_o = the reverse saturation current, q = the charge of an electron, V = the voltage across the diode, k = the Boltzmann constant, and T = the temperature. Under illumination this response is shifted down by the photocurrent, I_L, as shown in Fig. 4.3 (taken from Green[10], P79) . The current-voltage relationship under illumination is given by:

$$I = I_D - I_L \tag{4.4}$$

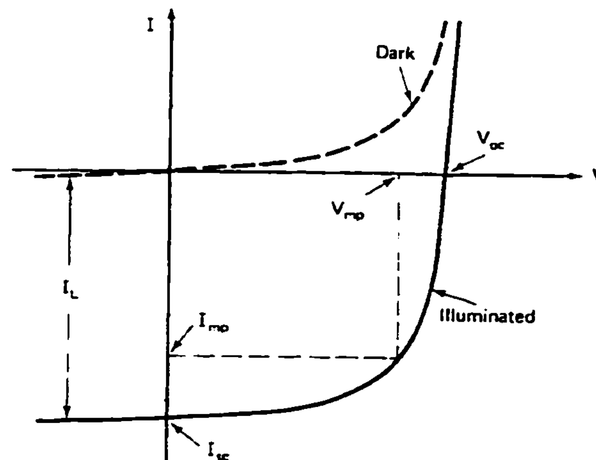

Figure 4.3 Current-voltage (I-V) characteristic curves for a solar cell in the dark and under illumination. The 'dark' curve follows the ideal diode law while the illuminated curve is shifted down by a constant, the photocurrent (I_L). Several key quantities determine the quality of the solar cell such as the open circuit voltage, V_{OC}, the short circuit current, I_{SC}, and the maximum power point (V_{MP}, I_{MP}). Figure taken from Green[10], p79.

Positive voltage is defined to occur when the p-side is positive and the n-side is negative as in Fig. 4.4b. Positive current is defined to flow from p to n internally across the junction, hence the photocurrent is negative. Solar cells therefore operate in the fourth quadrant of an I-V plot as shown in Fig. 4.3. The I-V curve shape and its intercepts are very useful in characterizing solar cells. Three important parameters can be extracted from I-V plots:

1) The short circuit current I_{SC}, which ideally is equal to the light-generated current I_L. The limiting short-circuit current for a silicon solar cell is about 35 mA/cm^2 assuming a standard solar illumination such as AM 1.5 (Green[10], Fig. 5.1, P87). Air mass one (AM1) radiation occurs when the sun is directly overhead. When the sun is at an angle θ to vertical then:

$$\text{Air mass} = \frac{1}{\cos\theta} \qquad \textbf{(4.5)}$$

2) The open circuit voltage, V_{OC}, is dependent upon the reverse saturation current, I_O. For silicon, the maximum V_{OC} is about 700 mV which corresponds to small I_O.

3) The third parameter is the fill factor, FF, which is measure of how 'square' the I-V curve is. The fill factor is calculated as follows:

$$FF = \frac{V_{MP} I_{MP}}{V_{OC} I_{SC}} \qquad \textbf{(4.6)}$$

V_{MP}, I_{MP} indicate the operating point where the output power of the solar cell is maximized as illustrated in Fig. 4.3. High efficiency silicon solar cells have fill-factors as high as 0.85. The efficiency of a solar cell is given by:

$$\eta = \frac{V_{OC} I_{SC} FF}{P_{IN}} = \frac{V_{MP} I_{MP}}{P_{IN}} \qquad \textbf{(4.7)}$$

where P_{IN} is the incident light power. Typical efficiencies for commercial silicon solar cells lie between 12 and 14%.

There are many factors that can affect the above solar cell parameters. I_{SC} losses can result from high surface reflectivity, poor electrical contacts, short minority carrier lifetimes, insufficient cell thickness (loss of light), etc. For high V_{OC}, I_o must be as small as possible which can be achieved by choosing a large bandgap material.

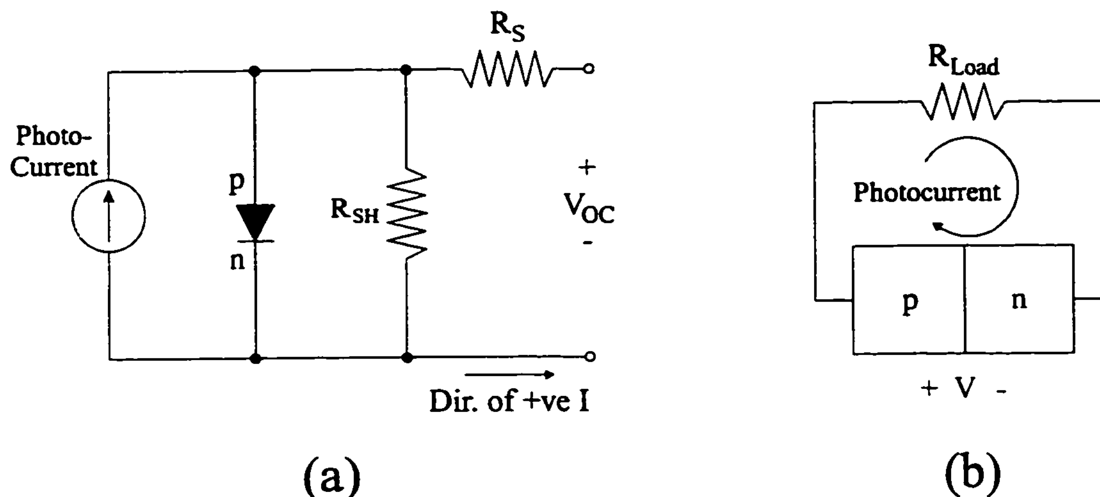

Figure 4.4 (a) Solar cell equivalent circuit. The cell consists of an ideal diode and a current source in addition to parasitic shunt and series resistances. (b) An illuminated solar cell will generate a current that flows in the negative direction. Positive current flows from n to p in the external circuit, while positive voltage is defined to occur when the p-side is positive with respect to the n-side.

Unfortunately as the bandgap increases, I_{SC} decreases. Given a standard solar spectrum (e.g. AM 1.5) the optimum bandgap lies between 1.4 and 1.6 eV which corresponds nicely with gallium arsenide (GaAs) having a bandgap of 1.4 eV. GaAs is costly when compared to silicon and has been restricted mostly to the space industry. Commercial solar cells are almost exclusively (> 95%) made from silicon. Silicon is unfortunately not an ideal material since it has an indirect bandgap equal to 1.1 eV. The indirect nature of the bandgap results in thicknesses on the order of 100 μm (due to weak absorption), at least an order of magnitude thicker than direct-gap semiconductors such as GaAs.

Real solar cells have parasitic shunt, R_{SH}, and series, R_S, resistances associated with them as indicated in the solar cell equivalent circuit of Fig. 4.4a. Ideally $R_S = 0$ and $R_{SH} = \infty$ however the performance of the cell will remain unaffected if $R_S << R_{CH} << R_{SH}$ where the characteristic resistance, $R_{CH} = V_{OC} / I_{SC}$. A large series resistance will cause the I-V plot for the solar cell to look more like a resistor than a diode. Short circuit current is reduced and open circuit voltage remains unaffected. Major contributors to the series resistance are the bulk resistance of the semiconductor material making up the cell, the bulk resistance of the contacts and interconnects, and the contact resistance.

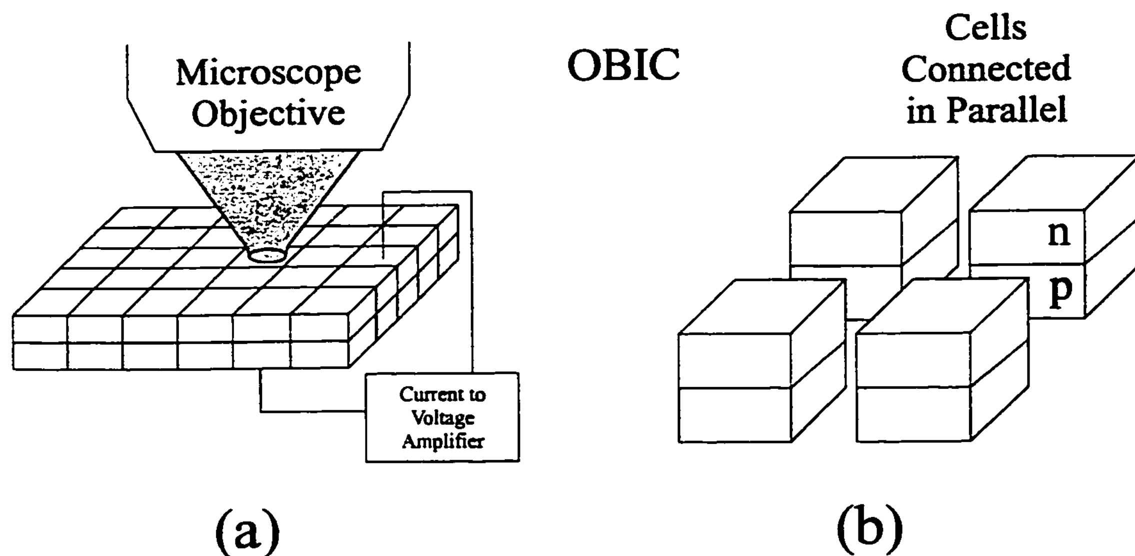

Figure 4.5 (a) Optical beam induced current (OBIC) imaging involves raster scanning a diffraction limited laser spot over a solar cell and recording the photocurrent at every point on an imaginary grid. (b) Each grid square can be treated as a separate cell connected in parallel with all the other 'grid' cells. The photocurrent measured from each grid square can be represented as a gray level pixel forming part of a photocurrent map digital image.

A small shunt resistance will lower V_{OC} while not affecting I_{SC}. R_{SH} is caused by leakage across the p-n junction around the edge of the cell and in regions where defects and impurities have penetrated the junction to produce a short-circuit.

Although I-V plots are an essential part of the characterization of a solar cell, they only give data about the cell as a whole. Information about particular parts of the cell must be obtained with spatially resolved techniques such as optical beam inducted current (OBIC) imaging. OBIC imaging is similar to reflected-light scanning microscopy (Fig. 2.9) except that the specimen is its own detector. An OBIC image is obtained by dividing a cell up into an imaginary grid (Fig. 4.5a) and raster-scanning a diffraction-limited spot at every point on the grid. As the laser spot is raster scanned, the short circuit current from each point on the grid is recorded and displayed as a gray-level pixel. Therefore an OBIC image is simply a high resolution I_{SC} map of a solar cell. Since the laser spot only focuses on one grid element at a time, each grid element can be considered a separate solar cell connected in parallel with the rest of the 'grid element' solar cells as shown in Fig. 4.5b. Any defects within the solar cell will result in grid elements with reduced I_{SC} which will appear dark in an OBIC image, while regions of normal operation will appear white indicating high photocurrents. In principle, it is

possible to also map V_{OC} by adding a large resistor in series with the solar cell and measuring the voltage drop across the resistor. In practice this increases the RC time constant of the circuit such that formation of an image at normal scan rates (10 - 100 μs / pixel) is very difficult. Also, for I = 0, Eqn. 4.4 becomes:

$$V_{OC} = \frac{KT}{q}\ln\left(\frac{I_L}{I_0}+1\right) \qquad \textbf{(4.8)}$$

V_{OC} has a logarithmic voltage response to I_L/I_0 which complicates analysis obtained from the signal. As a first approximation a V_{OC} map would be equivalent to a I_{SC} map with much reduced contrast. OBIC in combination with RL and PL can be used to identify many types of defects such as ones due to impurities, inhomogeneities, point shunts, poor contacts, etc. OBIC imaging can also be useful in identifying poor cells in modules composed of multiple cells. The cslM/m is uniquely suited to do this type of solar cell imaging. Macroscopically it can image cells as large as 7.5 cm in diameter while operating telecentrically and using all imaging modes. Non-telecentric operation allows for even larger fields-of-view while in OBIC mode. Microscopically the Mitutoyo objectives allow for uncomplicated imaging due to their long working distances. In theory, submicron resolution is possible with the 0.9 NA objective although in practice this is only possible with specimens that allow the objective to come within 300 μm of their surface while maintaining electrical contact.

4.1.1 Imaging Results

The MACROscope is ideal for imaging solar cells, allowing for cells as large as 7.5 x 7.5 cm while providing a 10 μm spot size. Fig. 4.6a shows an OBIC (633 nm) image of four ITO coated, $CdS/CuInSe_2$ thin film solar cells. These cells were manufactured by H.F. Tiedje of the Thin Films Group in Physics at the University of Waterloo as part of a Ph.D. project using a combination of sputtering and vacuum evaporation techniques[11]. The cells in Fig. 4.6 were connected in parallel such that they could all be imaged at the same time. This single image technique is extremely useful since it provides quantitative data about all the cells in relation to each other. It avoids the problem of having to ensure conditions are identical if each cell is imaged individually.

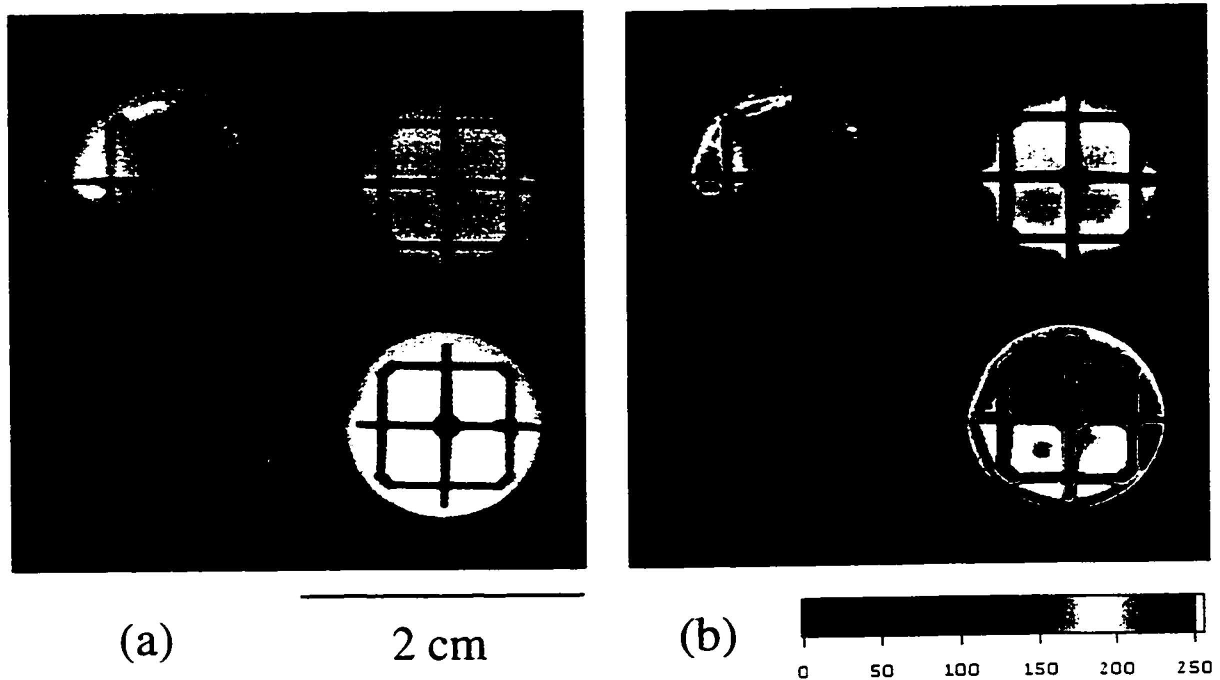

Figure 4.6 (a) OBIC image (632 nm) of four CdS/$CuInSe_2$ thin film solar cells connected in parallel. The cells on the left have gold back contacts while the ones on the right have molybdenum back contacts. (b) The same image represented in false colour which highlights subtle variations in photocurrent. The false colour scale is linear with arbitrary units and represents a set of about 256 photocurrent values.

The single image technique becomes a quality control tool by substituting a cell of known quality into the group of cells to be tested. Cells that do not reach the uniformity or intensity standard of the control cell can be rejected. These techniques are made possible by the MACROscope's large field of view. The scan size in Fig. 4.6a is 4 x 4 cm (zoom 2) where each cell has a diameter of 1.5 cm. The black square pattern on the cells denotes the aluminum contacts which do not produce any photocurrent. The cells on the left have gold back contacts while the ones on the right have molybdenum back contacts. Clearly the cells on the right are superior. In order to better evaluate the photocurrent uniformity, especially for the moly-back contact cells, the images were displayed in false colour in Fig. 4.6b. The subtle variations in photocurrent shown in Fig. 4.6a are readily apparent in Fig. 4.6b.

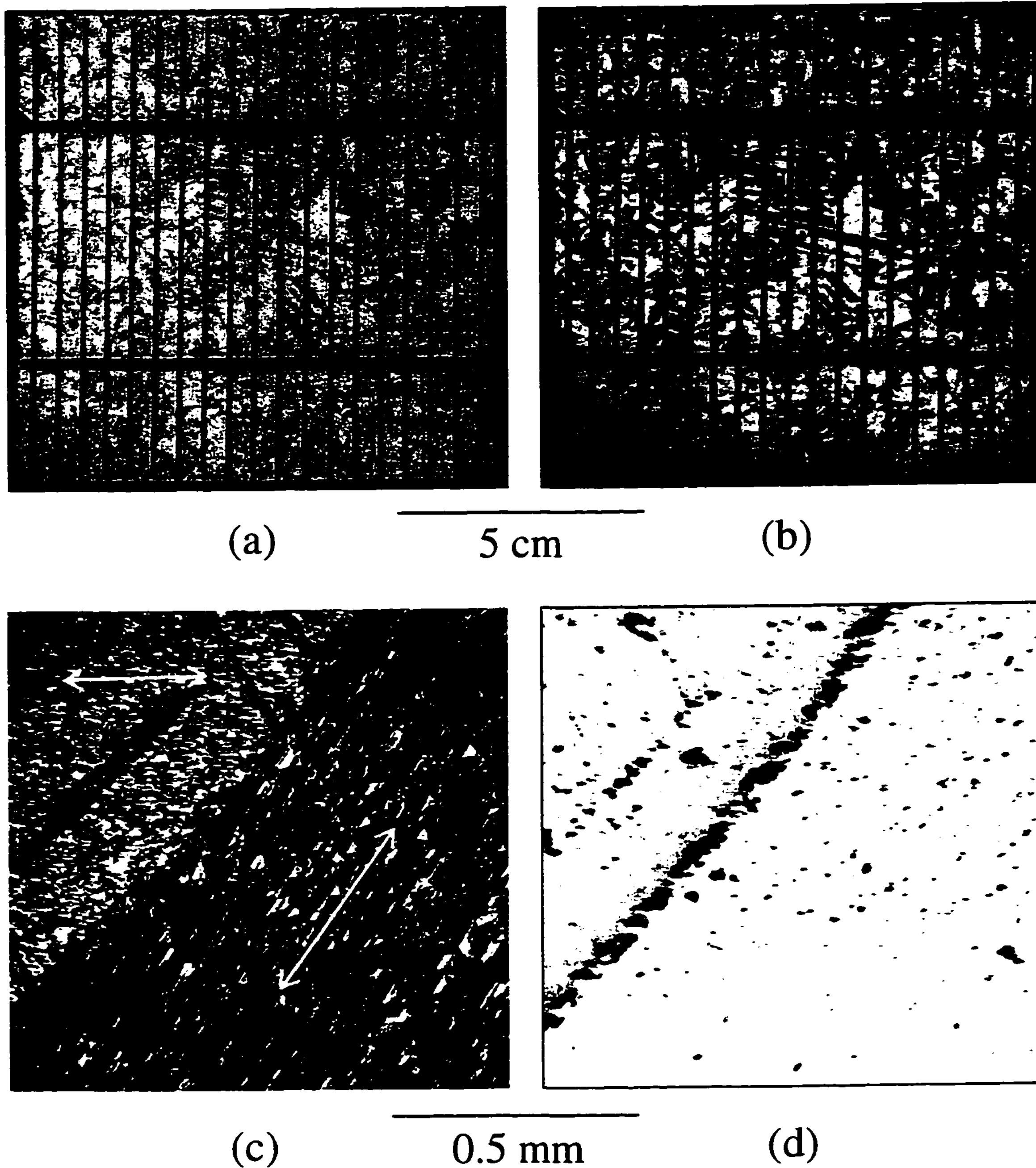

Figure 4.7 (a) OBIC (647 nm) image of a 10x10 cm polycrystalline silicon solar cell obtained using a laser scan lens in non-telecentric mode. (b) The same cell except a DC current offset was added in order to highlight the grain structure. (c) RL image (633 nm) of two grains and their interface using a 0.42 NA objective. The yellow lines indicate the grain directions. (d) OBIC (633 nm) image of the same two grains. The interface appears clearly as a diagonal black line where a great deal of recombination occurs.

Strictly telecentric operation, when imaging in OBIC mode, is not required since there is no beam returning from the specimen. As long as the beam incident on the solar cell does not experience added reflectivity or aberration from the solar cell, the OBIC image will remain undistorted. Non-telecentric operation allows for large fields of view with small lens apertures. Fig. 3.16 shows how the lens diameter can be decreased as the beam's pivot point is moved to the right of the focal point (telecentric plane). Notice the field of view remains constant no matter what pivot point is chosen, assuming the scan angle is kept constant. To scan a large polycrystalline silicon solar cell (10 x 10 cm), a 30 cm focal length f-θ lens was operated non-telecentrically, as described above, in order to generate the OBIC image of Fig. 4.7a. The 647 nm laser line from an Ar-Kr laser was used to generate this image. The polycrystalline nature of the solar cell is clearly evident in Fig. 4.7b where an input offset current has been added by the amplifier in order to highlight the modulated signal caused by the various crystal defects and grain boundaries. A closer examination of the grain boundaries requires the use of the cslm. Fig. 4.7c shows a zoom 1 (1 x 1 mm), RL (633 nm), semiconfocal (f = 10 cm detector lens, 100 μm pinhole) image of two crystal segments taken with a 0.42 NA objective. Fig. 4.7d shows the corresponding OBIC image where the grain boundary running from the bottom left to the top right is clearly visible. The grain orientations are evident in the RL image as indicated by the yellow lines.

A more detailed look at the grain boundary can be obtained with a 0.7 NA objective as shown in Fig. 4.8. Fig. 4.8a shows a zoom 2 (100 x 100 μm) maximum intensity, RL (633 nm) image of two grains taken with a 50 μm pinhole and a 10 cm focal length detector lens. The maximum intensity image was generated from a set of 40 z-slices spanning 18 μm. Fig. 4.8b shows a profile image of the same area where black is low and white is high. The two grain directions are evident in Fig. 4.8a, and it is clear from Fig. 4.8b that the grains sit at different heights with the top left grain resting 7-8 μm below the bottom right grain. The 0.7 NA objectives' small depth of focus (1-2 μm) does not allow both grains to be in focus simultaneously while imaging in OBIC as shown by Fig. 4.8c and d, where the laser spot is focused on the bottom right and the top left grain, respectively. This is effectively the same kind of sectioning observed by wide-field or non-confocal microscopes where out-of-focus areas appear blurry and bright rather than very dark or black as in confocal microscopy.

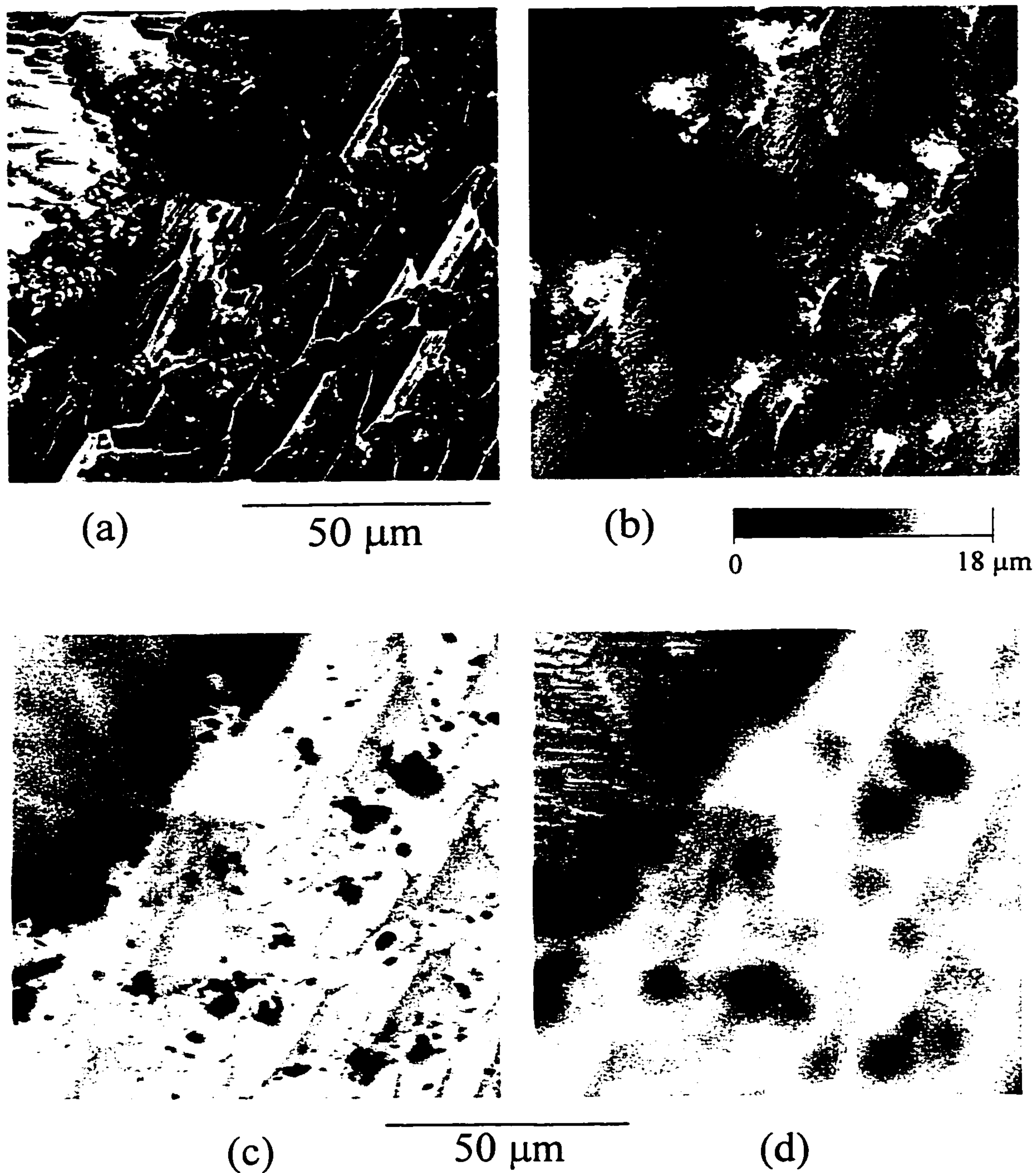

Figure 4.8 (a) RL (633 nm) maximum intensity image of grain interface taken with a 0.7 NA objective. (b) Profile image of the same area. White areas are high while dark areas are low. (c) OBIC (633 nm) image of the same area focused on the bottom right grain. Notice that areas of high recombination, which show up as black in this image, correspond to high areas in b). (d) OBIC image of the same area focused on the top left grain. The grain interface is clearly denoted by a set of large black spots in both c) and d).

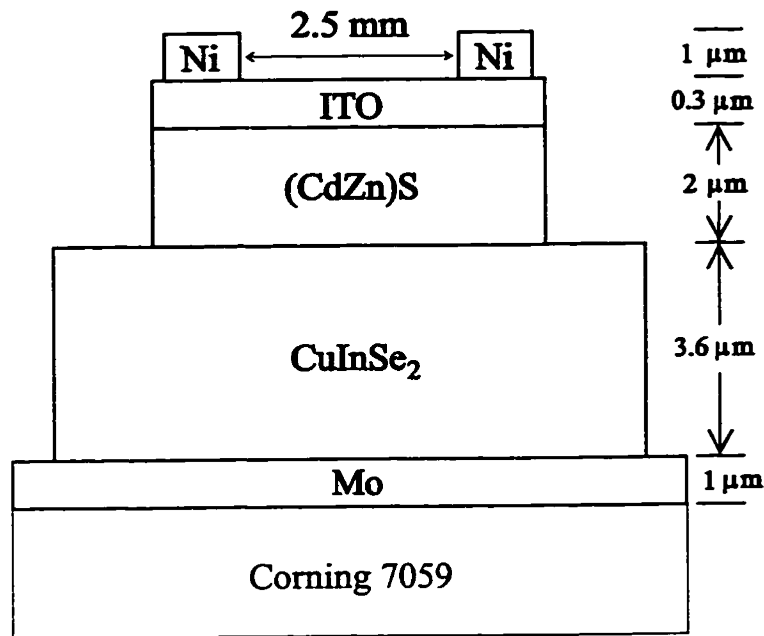

Figure 4.9 Schematic diagram of a $CdZnS/CuInSe_2$ thin film solar cell.

Consequently, deconvolution techniques such as those described in the Confocal Handbook[12] would be needed to produce a topographical OBIC map. It is easy to see a correspondence between all the images in Fig. 4.8. Fig. 4.8a has clusters of very small white dots scattered throughout the right bottom grain, especially at the grain boundary. These clusters correspond to high points in Fig. 4.8b. It is almost as if there is a 'mountain range' of these white clusters separating the grains. These clusters or high points, correspond to recombination sites which appear black in Fig. 4.8c. The cslm, in this case, provided a unique set of images difficult to duplicate with any other microscope system.

Fig. 4.9 shows the structure of an experimental solar cell produced in 1986 (> 10% efficiency) by the Institute of Energy Conversion (IEC)[11] at the University of Delaware. This cell is part of a set of 12 $CdZnS/CuInSe_2$ thin film solar cells, approximately 3 mm high x 3.5 mm wide, deposited on the same substrate using a vacuum evaporation technique. The cells have molybdenum back contacts, Indium-Tin Oxide (ITO) anti-reflective conducting coating, and nickel top contacts.

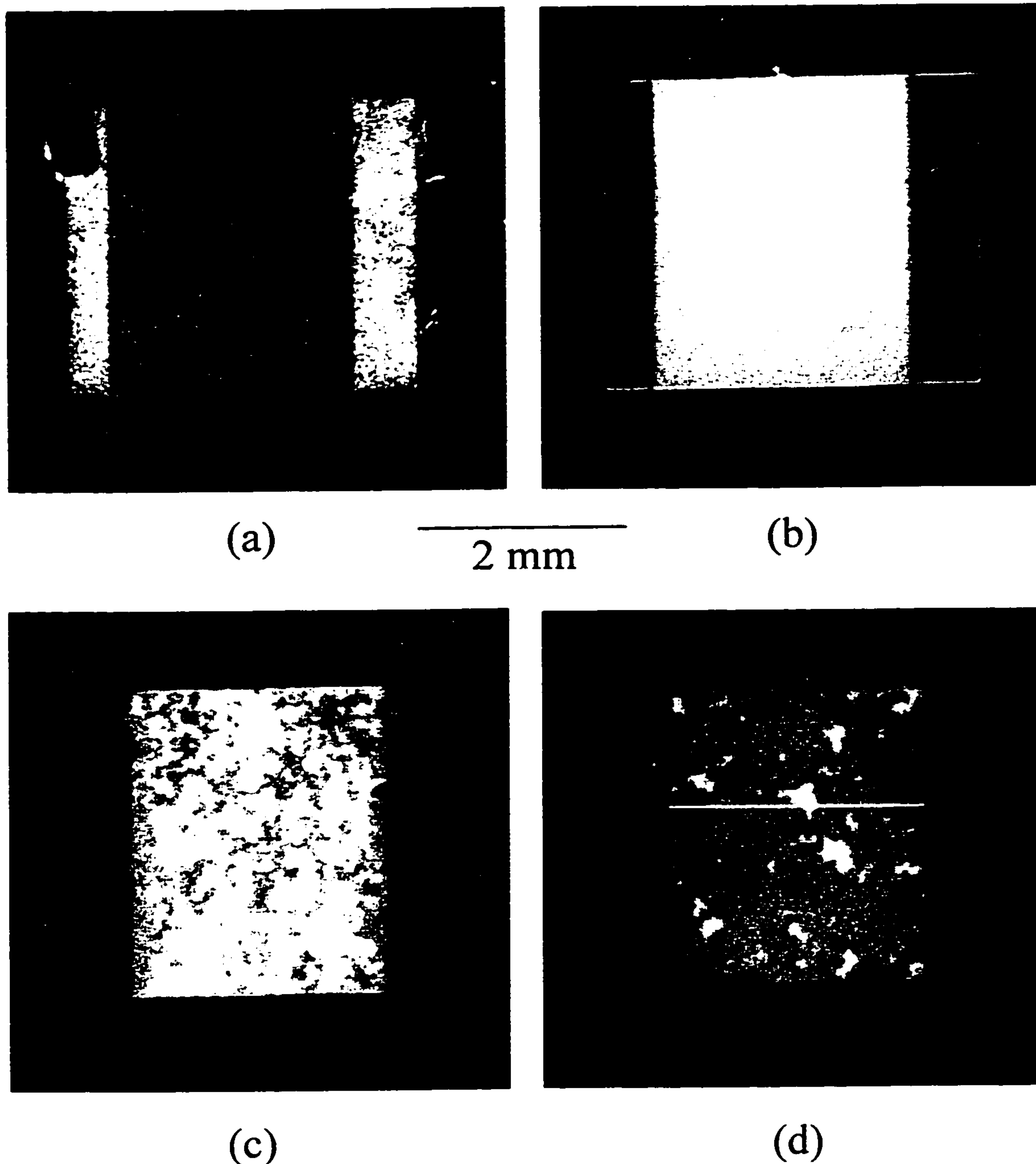

Figure 4.10 (a) RL (633 nm) image of a $CdZnS/CuInSe_2$ thin film solar cell. The contacts show up as vertical bright strips on either side of the cell. (b) PL (488 nm excitation, >515 nm emission) image of the same cell. The CdZnS layer is what photoluminesces. (c) OBIC image (488 nm) of the same cell. Unlike the RL and PL images, the OBIC image indicates structure, showing 10-20% variations in the photocurrent. (d) OBIC image taken at 1152 nm. This image shows a completely different structure compared to c). Notice the dead areas near the contacts.

The images shown in Fig. 4.10 were taken in 1994, 8 years after the cells were produced. During the 8 year interim, the cells were stored in the dark under uncontrolled conditions. Fig. 4.10a shows a zoom 16 (5 x 5 mm) RL image (633 nm) of one of the cells in contact with an electrical probe. The top contacts appear as bright vertical stripes which lie along the left and right edges of the cell while the probe appears black (top left) since it lies outside the focal plane and beyond the axial resolution of the MACROscope. The RL image shows the cell to have a uniformly grainy complexion similar to the one seen by the naked eye. Fig. 4.10b shows the same cell imaged in PL using 488 nm excitation and a 515 nm long-pass filter in between the beam splitter and detector lens. The CdZnS layer is responsible for the PL since the Ni contacts and the surrounding $CuInSe_2$ appears black in the image. Notice a scratch in the top right part of the contact has exposed some CdZnS. The PL emission was roughly centered at 680 nm and the quantum efficiency was estimated to be 1.3% for two excitation wavelengths: 488 and 442 nm (He-Cd laser). The estimate of quantum efficiency is treated in Appendix 4. The solar cell shows no signs of damage when viewed with RL or PL, however this changes when OBIC is used. Fig. 4.10c and 4.10d show the solar cell imaged in OBIC using 488 and 1152 nm light respectively. Defects are clearly evident in Fig. 4.10c representing 10 to 20% variations in photocurrent which contrasts with the very uniform OBIC images obtained 8 years previously by S. Damaskinos[13].

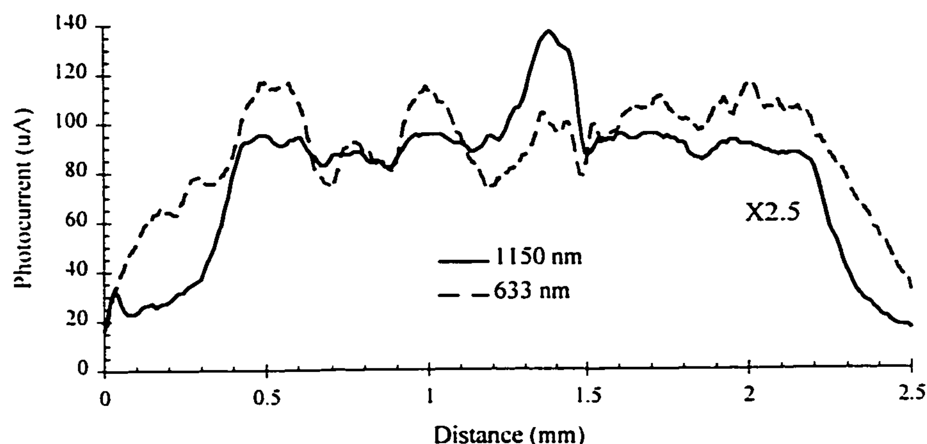

Figure 4.11 Photocurrent profiles along the white line in Fig. 4.10d. The two profiles are distinct and cannot be scaled by any constant to match each other.

Fig. 4.10d is distinct from Fig. 4.10c in that the structure is similar but the contrast is different especially near the Ni contact where the photocurrent decreases significantly. One journal reviewer suggested that Fig. 4.10d could be scaled or multiplied by some constant so as to transform it into Fig. 4.10c which is clearly not the case. This can be best seen by comparing intensity line plots along the white line shown in Fig. 4.10d. Fig. 4.11 shows photocurrent versus position for 633 and 1152 nm wavelengths along this line. The OBIC curves were normalized so as to represent photocurrent output given the same photon flux incident on the specimen for both 633 and 1152 nm excitation. In addition, the 1152 nm profile line was magnified by a factor of 2.5 in order to compare it with the 633 nm line. The 1152 nm line is distinct from the 633 nm line and cannot be scaled by any constant in order to make it match. OBIC profiles for other wavelengths such as 442, 488, 568, and 647 nm (not shown) were nearly identical in shape when compared with the 633 nm profile and differed only in terms of a scaling factor.

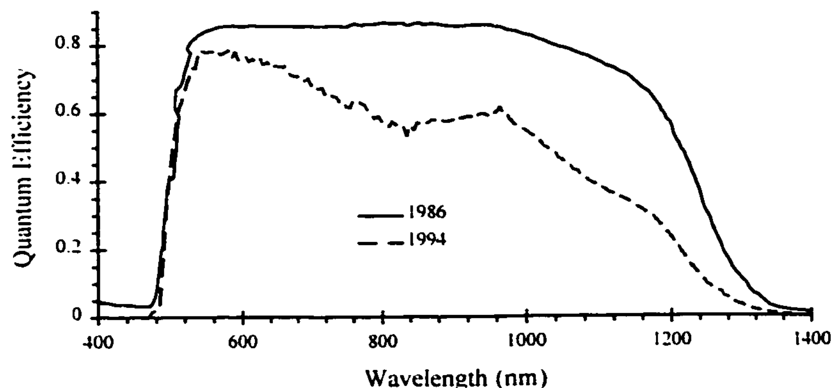

Figure 4.12 Spectral response of the cell in Fig. 4.10 plotting quantum efficiency as a function of wavelength. The response right after manufacturing the cells in 1986 as well as in 1994 are shown.

In order to gain a better understanding of the various wavelength responses, the physical structure must be examined with respect to spectral response. Fig. 4.12 shows spectral response curve (quantum efficiency vs. wavelength) for the cell just after fabrication in 1986, and in 1994. In both cases, wavelengths shorter than ~ 470 nm are absorbed in the 2 μm thick CdZnS (2.55 eV bandgap) layer. The CdZnS layer becomes transparent at longer

wavelengths and light is absorbed in the 3.6 μm thick $CuInSe_2$ (1 eV bandgap) layer. The $CuInSe_2$ layer becomes transparent for wavelengths greater than 1240 nm hence a decreasing number of photons are absorbed in this layer resulting in a smaller quantum efficiency. The 1994 cell had degraded to the point where a significant decline in spectral response starting at about 700 nm was apparent. The spectral response was measured by H.F. Tiedje using a laboratory built instrument[14] which illuminates the entire cell. Assuming small systematic error in the spectral response apparatus the decline in spectral response probably results from a combination of general degradation throughout the entire cell and a complete failure near the contacts at long wavelengths. Due to the undocumented and uncontrolled storage of the cells it is very difficult to determine what caused the cells to degrade. However, it is clear that the dead zones observed in Fig. 4.10d are related to the Ni contacts and not just to the edges because these dead zones do not appear at the top and bottom edges.

Early on in the imaging of this solar cell, it was suggested that the 488 nm OBIC map was due to PL produced in the CdZnS layer. In order to first quantify if any OBIC at all was a result of PL, a 442 nm, 10 mW HeCd laser was used as an excitation source. It was assumed that none of the 442 nm (2.81 eV) light would reach the $CdZnS/CuInSe_2$ junction since it lay well above the CdZnS bandgap (2.55 eV) and should be absorbed within a few tenths of a micron from the surface. It follows that any OBIC signal detected should be solely due to PL. The 442 nm OBIC image turns out to be identical to the 488 nm image of Fig. 4.10c and differs only by a scaling factor, hence PL seems to be responsible for OBIC. This is not surprising once the geometry of the situation is considered. Consider a 10 μm diameter spot (MACROscope) illuminating the top of the cell. The resultant PL spot will expand only slightly upon reaching the junction which is located 2 μm beneath the surface. An increased spot size of up to ~ 20 μm would not affect the OBIC image since sampling occurs every 5000 μm/ 512 = 9.8 μm. The OBIC efficiency at 633 nm was found to be ~ 21%; that is, 21% of the incident photons created electron-hole pairs which were in turn successfully collected by the junction. This efficiency does not agree with the one obtained from Fig. 4.12 which suggests a non-linearity effect discussed in section 4.1.2.

(a)

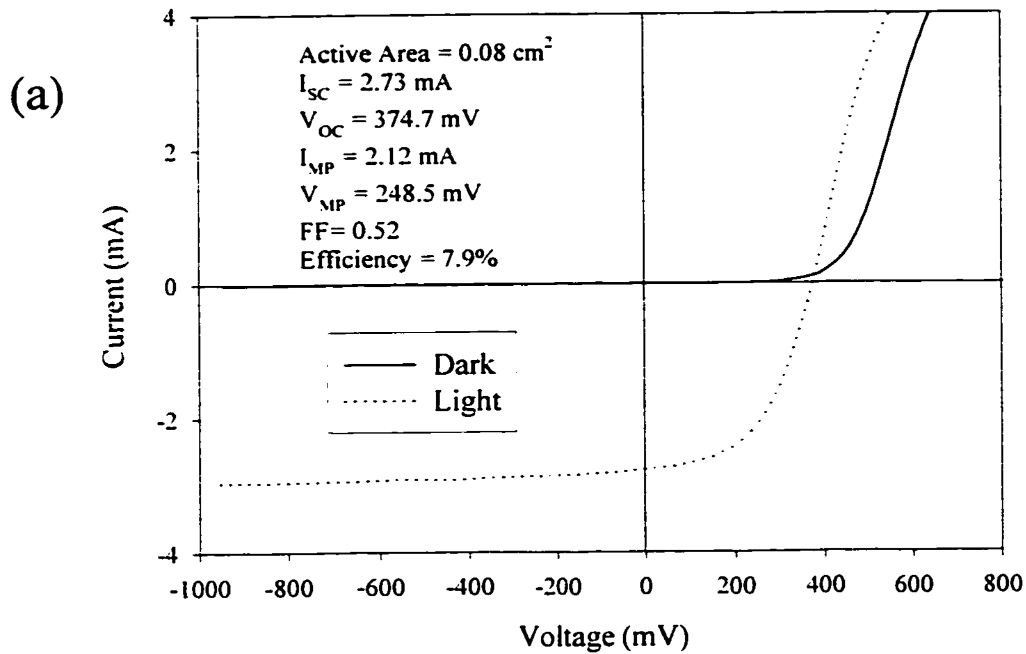

(b)

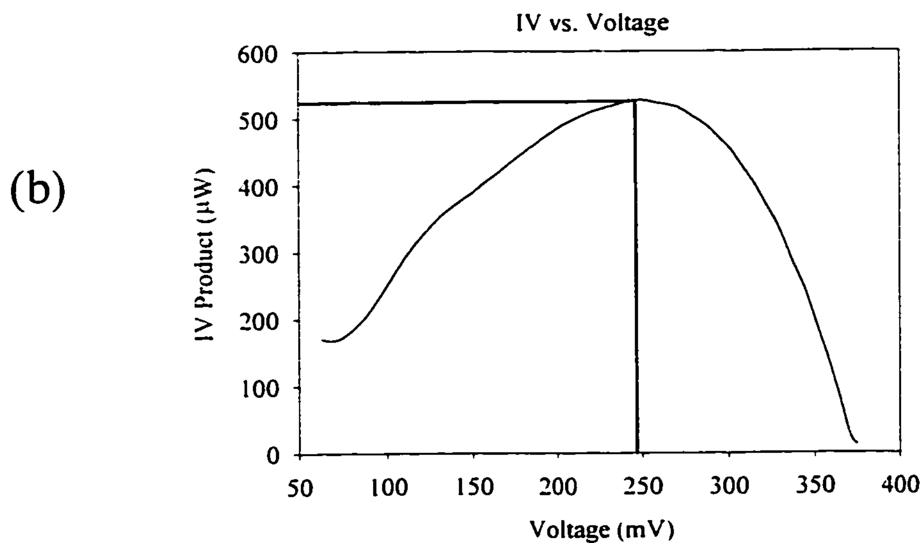

Figure 4.13 (a) I-V plot for the cell in Fig. 4.10 showing dark and illuminated characteristics. (b) IV product vs. voltage plot used to determine the maximum power point.

A rough estimate of the amount of OBIC due to PL in Fig. 4.10c is given by (488 nm photons/s) · (PL efficiency) · (OBIC efficiency) = $3.94 \cdot 10^{15} \cdot 0.0127 \cdot 0.21 = 1.05 \cdot 10^{13} e^-/s$ = 1.7 μA which corresponds to about 10% of the total OBIC signal. An assumption to be made, in order to believe the PL-OBIC effect, is that the hole diffusion length in CdZnS must be only a few tenths of a micron. If this were not true then the OBIC image would be expected to look different for the 442 nm case since it would show the response from the CdZnS layer. Another assumption is that the CdZnS layer has no cracks, microscopic or otherwise. Cracks would allow light to reach the CIS layer and the OBIC image would represent the response from the CIS layer.

Even with all the evidence of degradation the cells still work reasonably well. Fig. 4.13a shows I-V curves for illuminated and dark cases. The illuminated curve was obtained using a tungsten-halogen light. The light was positioned such that uniform illumination resulted at an intensity equivalent to AM 1.5 (83.18 mW/cm^2) although not an equivalent spectrum. The illuminated curve shows a large amount of crossover (i.e. it is not equivalent to a translated dark curve) indicating I_L is a function of voltage. From Fig. 4.13a I_{SC} = 2.73 mA and V_{OC} = 374.7 mV for the 0.08 cm^2 cell. Plotting I·V vs. V for the fourth quadrant in Fig. 4.13a results in the curve shown in Fig. 4.13b. The maximum power point corresponds to (V_{MP}, I_{MP}) = (248.5 mV, 2.12 mA) which gives FF = 0.52. The resulting efficiency is 7.9% in 1994 compared to ~ 10% in 1986.

4.1.2 OBIC Limitations

OBIC is a relatively forgiving imaging technique, however, two effects occur often enough to merit discussion: solar cell bandwidth or time response limitations, and light intensity dependent saturation or OBIC nonlinearity. Fig. 4.14a shows a zoom 1 (8 x 8 cm), OBIC (633 nm) image of a semicrystalline (small crystallites) silicon solar cell. The top and bottom image of the cell is clipped by the unitary telescope in Fig. 3.23. The contacts appear black, as usual, and the cell does not seem to have any defects, however this cell was imaged with a 0.4 V reverse bias voltage applied. Without the reverse bias, the OBIC image exhibits 'ringing' as illustrated in Fig. 4.14b. A large area device, such as the one in Fig. 4.14, will have a large capacitance hence a large RC time constant resulting in a slow response time.

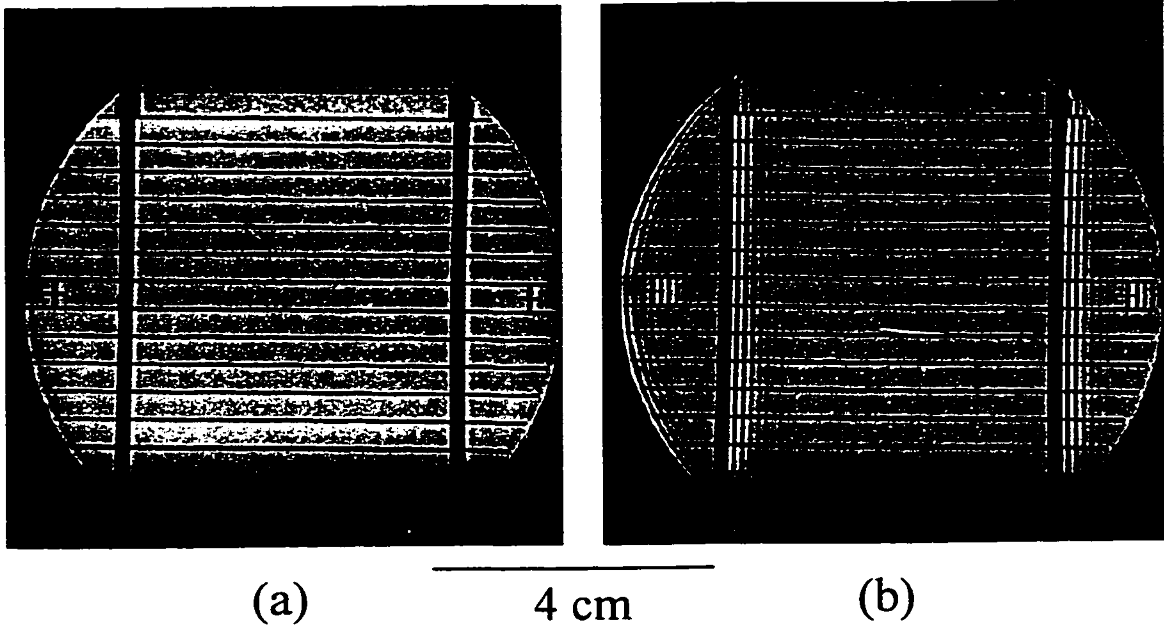

Figure 4.14 (a) OBIC (633 nm) image of a semicrystalline solar cell. A small reverse bias was applied to eliminate the ringing seen in (b) with no bias applied. Large area cells will tend to have higher capacitance, hence a longer RC time constant and therefore a slower response time.

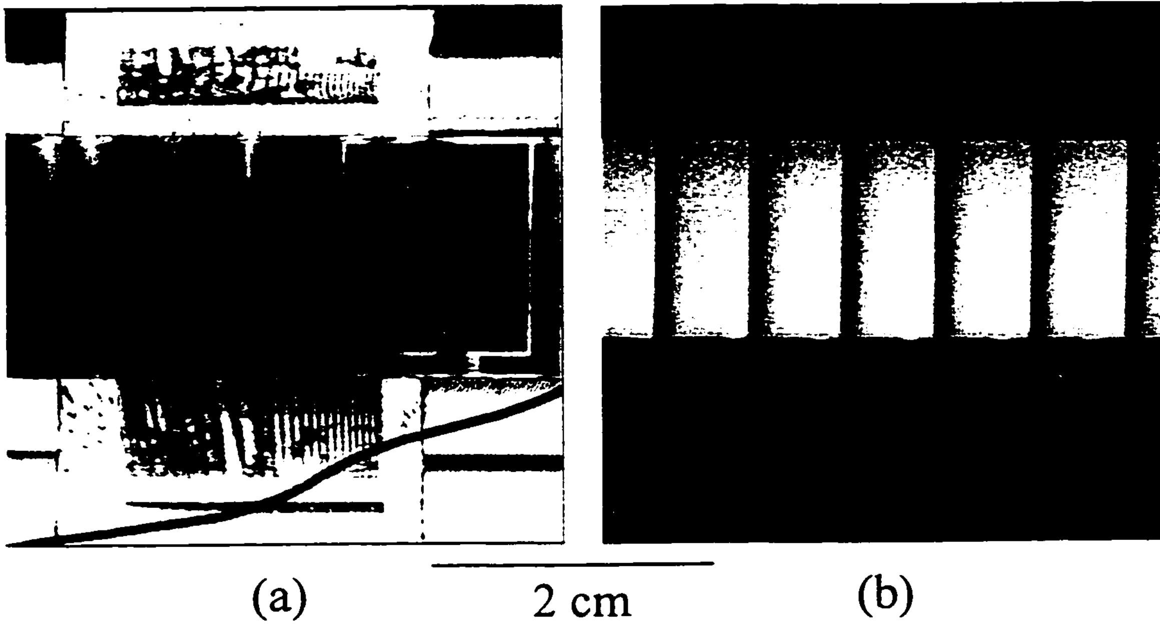

Figure 4.15 (a) RL (633 nm) image of an amorphous silicon solar cell The cell is encapsulated with glass and therefore generates interference fringes. (b) OBIC image of the same cell. The active area does not show any defects or signs of damage.

In some cases inductance will cause 'ringing' to appear due to the inductor-capacitor-resistor circuit formed. The origin of the inductance is unclear but could involve the connecting wires or the current to voltage amplifier. A 'normal' scan time will result in blurring or afterimages, as in this case. Slowing down the scan time is one solution. Another solution is to apply a reverse bias such that the depletion zone is increased and the capacitance decreased.

Fig. 4.15 shows a zoom 2 (4 x 4 cm) image of an amorphous silicon solar cell using a 633 nm He-Ne laser. Fig. 4.15a is a RL image where the solar cell appears as a dark horizontal band with a series of fringes due to interference from the protective glass substrate on top of the cell. The rest of the image appears white, due to its high reflectivity, relative to the cell which appears black to the naked eye. Fig. 4.15b shows the cell imaged in OBIC. The active regions of the cell are uniform and homogeneous with no apparent defects. For low intensities the OBIC signal will increase linearly with increasing intensity. At higher intensities the increase in OBIC starts to lag behind and becomes less sensitive to further increases in intensity. Fig. 4.16 shows a graph plotting OBIC signal as a function of laser power at the cell.

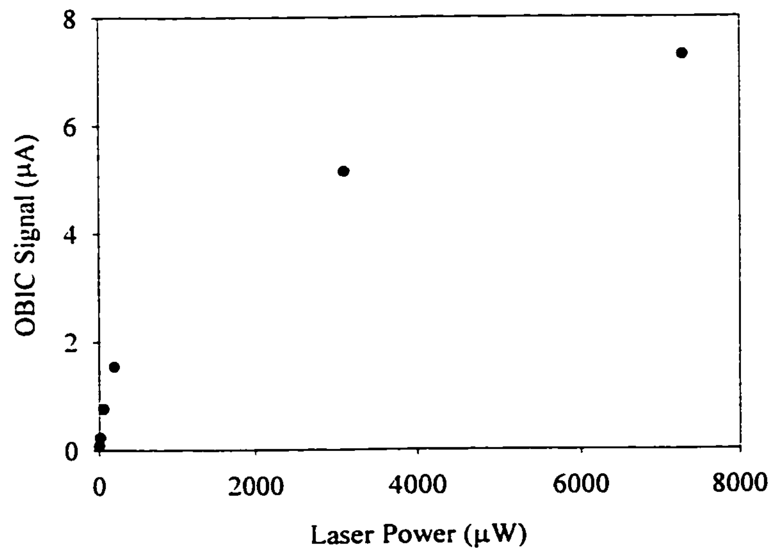

Figure 4.16 OBIC signal (PMT anode current) as a function of laser power at the specimen. The relationship becomes non-linear for large intensities.

The relationship is clearly non-linear. A plausible explanation for this non-linearity is given by Leamy[15]. At high injection rates, a dense cloud of electron hole pairs is formed. Only the electron or holes near the outer edges of the cloud have a chance to diffuse to the junction while the center of the cloud remains shielded and stationary thereby subject to recombination. For OBIC imaging, this effect can be very serious and can significantly affect contrast. If an OBIC image of a multi-gray-level object, such as Fig. 4.7a, is taken in the non-linear regime then a reduced or washed-out contrast would be expected and any quantitative analysis would be difficult. Calculations of diffusion lengths, surface recombination velocity, and carrier lifetimes must all be done in the linear regime.

4.1.3 Comparison of OBIC with EBIC

Electron beam induced current or EBIC is the scanning electron microscope (SEM) version of OBIC. An electron beam, instead of a light beam, is used to generate electron-hole pairs as seen in Fig. 4.17. SEMs will typically generate electrons with 5 to 200 keV energy which enter the solar cell and generate many electron-hole pairs as they traverse the solar cell and loose energy.

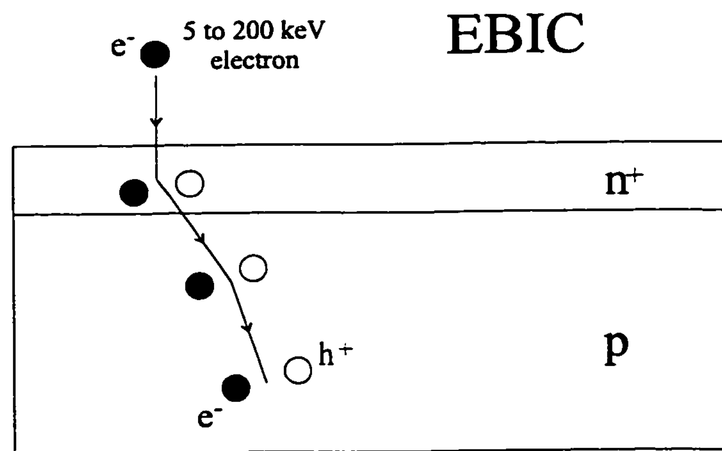

Figure 4.17 Electron beam induced current (EBIC) is the scanning electron microscope equivalent of OBIC. For OBIC, normally one electron-hole pair is created for every incident photon, but with EBIC the energy of the incident electrons is measured in keVs, not eVs, such that thousands of electron-hole pairs are created for every incident electron.

The number of electron-hole pairs generated per second is given by[16]:

$$\Delta N = \frac{G I_b}{q} \qquad (4.9)$$

where I_b = beam current, q = electron charge, G = gain, which in turn is given by:

$$G = \frac{(1 - f) E_b}{e_i} \qquad (4.10)$$

where f = the fraction of electrons lost to backscattering, E_b = electron beam energy, and e_i = ionization charge energy ≅ 3 times the bandgap energy. Typical gains range between 10^3 and 10^4. The resolution in EBIC is never determined by the size of the focused electron beam since electrons scatter inside the specimen as they lose energy and undergo large angular deviations from the original trajectory. The result of this scattering is that the focused electron beam 'mushrooms' within the solid specimen. This generation volume is shown in Fig. 4.18 taken from Leamy[15].

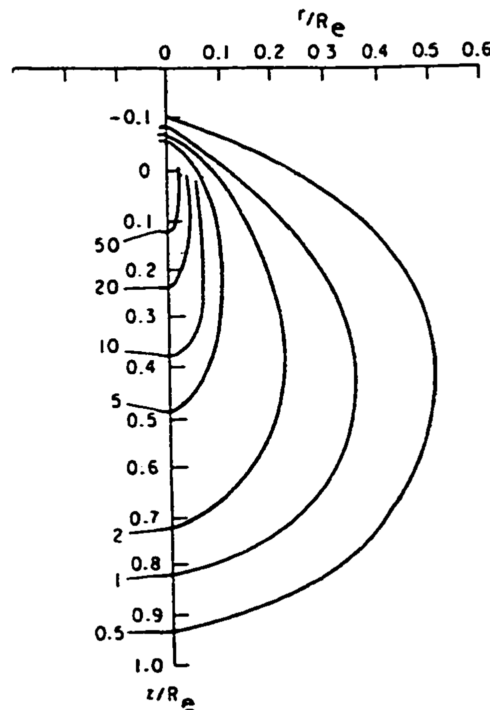

Figure 4.18 Carrier generation by a focused electron beam. The generation rate is shown as contours of equal ionization where the distance scale is normalized to R_e, the average electron range. Figure taken from Leamy[15].

Fig. 4.18 shows several contours of equal ionization or generation rate of electron-hole pairs, where the distance scale has been normalized to the average electron range[16], R_e. R_e is the depth to which an average electron would penetrate if it suffered no large angle scattering:

$$R_e(\mu m) = [(3.98 \cdot 10^{-2}) / \rho (g / cm^3)] \cdot E_b(kV)^{1.75} \quad \textbf{(4.11)}$$

where ρ is the density of the specimen. The generation volume is generally approximated to be a sphere of diameter R_e, hence EBIC resolution is of the same order as R_e. A typical 10^{-10} amp, 15 keV beam will have Re ≅ 2 μm in silicon. From Eqn. 4.9, it is clear that EBIC resolution is proportional to $E_b^{1.75}$. An enhanced resolution requires a reduced beam energy which unfortunately leads to a decreased penetration depth. EBIC can be especially sensitive when the junction lies close to the surface or when 'side-on' measurements of a junction are being made as shown in Fig. 4.19. Except for some special cases EBIC generally gives the same results as OBIC. EBIC implies the use of a SEM which is accepted and well understood as a semiconductor characterization instrument. SEM-based characterization[17] includes secondary electron imaging, backscatter imaging, EBIC, voltage contrast, cathodoluminescence, electron channeling and scanning deep level transient spectroscopy to name a few.

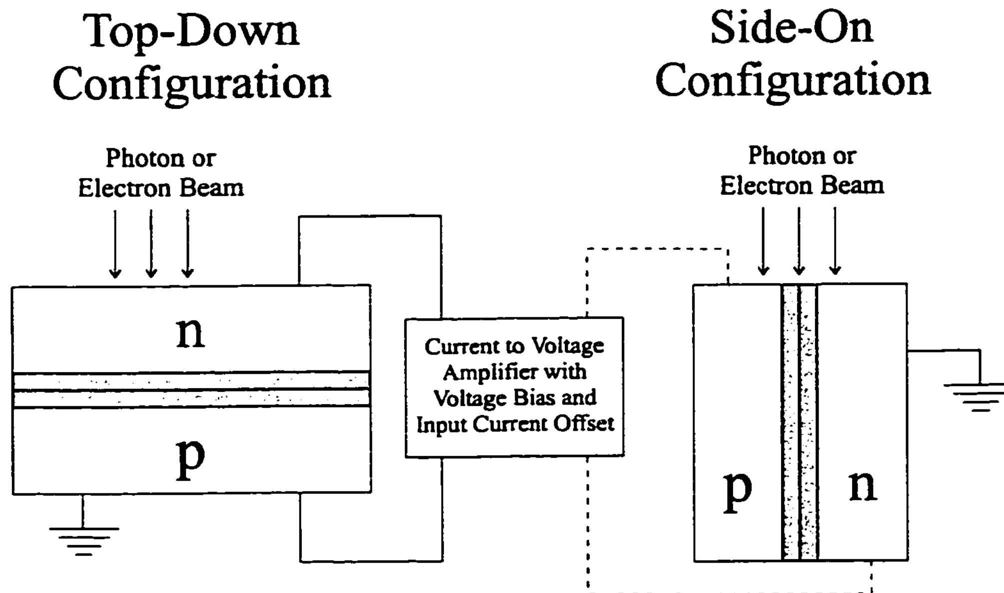

Figure 4.19 Two commonly used configurations in OBIC and EBIC imaging.

The establishment of a well rooted, mature commercial SEM industry and the fact that most institutions have at least one (if not many) SEM has led to a wide use of EBIC. While commercial cslms are available, systems providing macro/microscopic scanning beam imaging capabilities are virtually non-existent. OBIC is therefore not as widely used as EBIC, although it has several advantages over EBIC:

1) EBIC can cause damage especially at high beam energies.
2) EBIC is sensitive to dielectric or non-conducting layers which in some cases can become charged.
3) No specimen preparation is needed with a cslm or MACROscope.
4) Multiwavelength analysis such as shown in Fig. 4.10 is impossible with EBIC.
5) The cost of a simple OBIC system is low (< $20 000).
6) OBIC can be used with encapsulated cells.

4.2 Porous Silicon

Porous silicon (PSi) is a novel form of silicon which luminesces strongly at room temperature, in the visible. Recently a considerable amount of research has been directed towards the development of PSi materials and devices with the eventual goal of all-silicon optoelectronics such as panel displays and optical interconnects.

PSi was first discovered in 1956 by Uhlir[18] when doing work with electrolytic etching. In 1984, Pickering[19] et al. reported visible PL from electrochemically etched PSi at low temperatures but attributed it to amorphous silicon or impurities. It was not until 1990 that Canham[20] produced room temperature light emitting porous silicon (LEPSi) and attributed the PL to a quantum confinement effect. Almost at the same time Lehmann[21] et al. attributed an increased bandgap in PSi to quantum confinement. Since 1990, the number of scientific papers published each year on PSi have increased dramatically from about 100 in 1990, to 700 in 1996.

PSi is commonly produced by anodically etching a silicon wafer in a hydrofluoric acid (HF) solution. A typical setup is shown in Fig. 4.20a where a 1-100 mA/cm^2 current is passed through a 10 Ω-cm, (100), p-type wafer which has one side in contact with the HF/ethanol electrolytic solution. The wafer acts as the anode and etching occurs for several minutes. As shown in Fig. 4.20b (taken from Smith[22]) pore formation occurs at a low current setting when compared with the high currents used in electropolishing. Anodic etching will result in pore formation and consequently a PSi film from 1 to 100 μm thick will be produced. PL quantum efficiency ranges from 1 to 10% and depends upon doping level, wafer type, current density, solution concentration, and duration of etch. This is in contrast with bulk silicon which photoluminesces very weakly (10^{-5} % efficiency) at room temperature, in the IR (1140 nm) due to its indirect bandgap of 1.1 eV. A typical PSi PL spectrum will have a gaussian shape centered at ~ 700 nm with a full width at half maximum on the order of 100 nm. Researchers[23] have been able to create LEPSi with PL ranging from the blue into the IR. Electroluminescent (EL) devices have also been produced but only with efficiencies ranging from 0.01 to 0.1%.

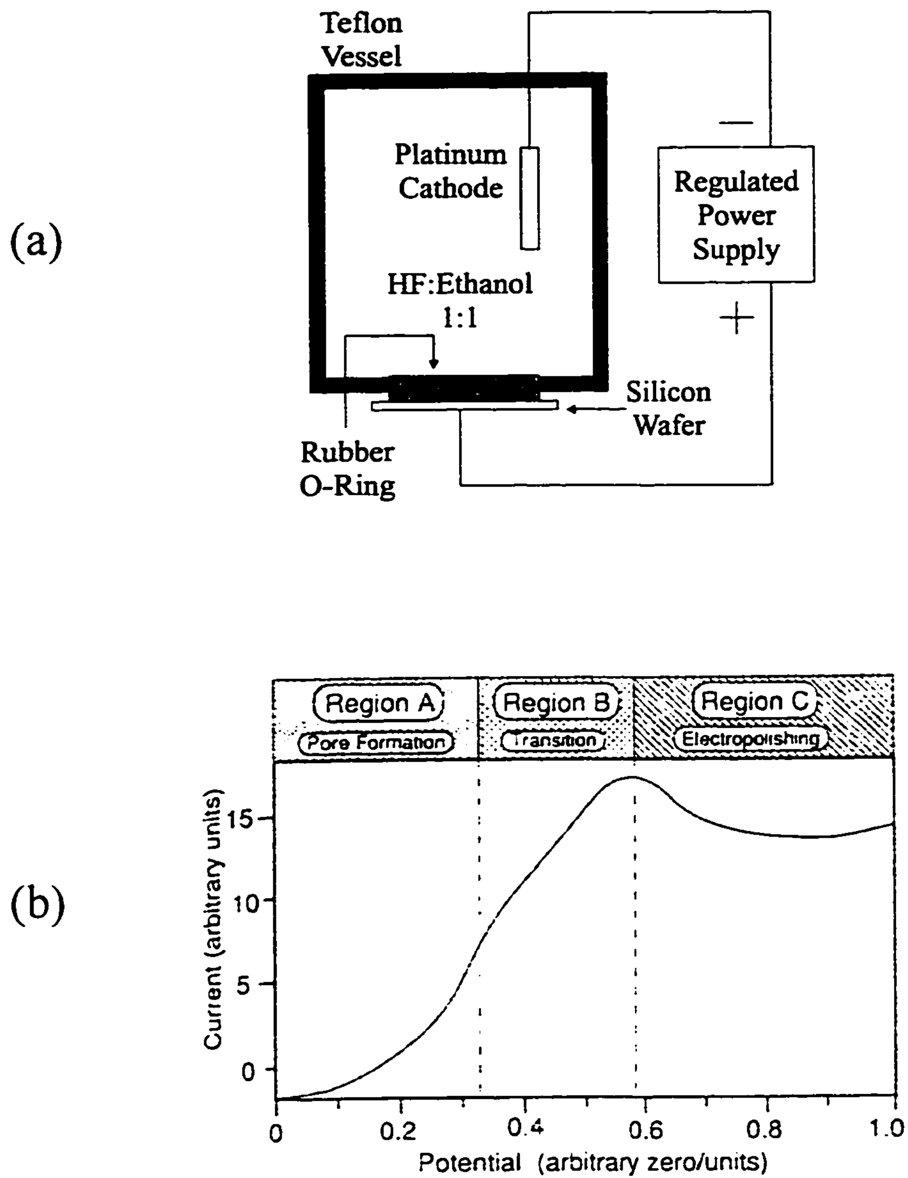

Figure 4.20 (a) A typical electrolytic etching setup used for the creation of porous silicon. (b) Porous silicon is produced using current densities ranging from 1-100 mA/cm^2 while electropolishing occurs at much higher current densities. Figure taken from Smith[22].

The origin of the visible, room temperature photoluminescence is not well understood. Currently there are four theories[24] to explain PL in LEPSi:

1) Quantum confinement. PSi consists of a network of wires making up a sponge-like structure. If the wires become small enough (< 5nm), due to electrolytic dissolution, then electron-hole pairs within the quantum wire will see themselves confined like particles in a box or quantum well[25]. The ground state energy in a square well is non-zero which implies an increased effective bandgap in the crystal resulting in a blueshift for PL emissions. It has been suggested[26] that quantum confinement leads to the relaxation of k-selection rules implying that LEPSi acts like a direct-gap semiconductor and therefore exhibits high PL efficiencies.
2) Radiative decay at surface/interface states partly determined by nanocrystalline particles.
3) PL due to surface molecular species, such as siloxene ($Si_6O_3H_6$ and similar compounds), which coat the silicon skeleton.
4) Hydrogenated amorphous silicon is the product responsible for PL.

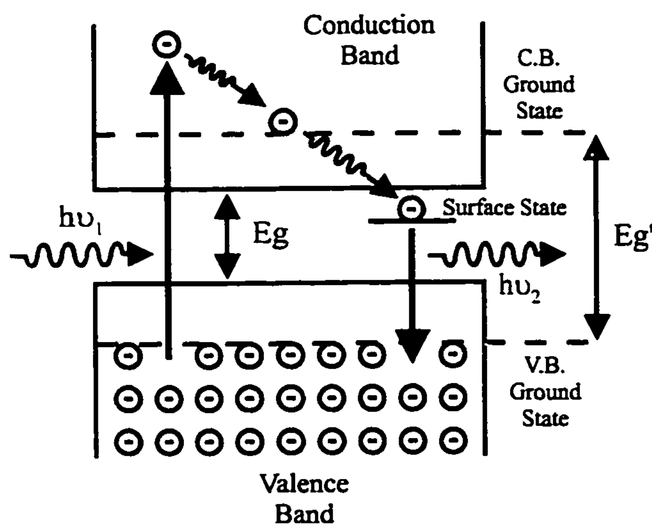

Figure 4.21 As the silicon skeleton in PSi is reduced to < 5 nm diameter, electron-hole pairs will experience quantum confinement. The ground state in a quantum square well has a non-zero energy which translates to an effective increase in the bandgap energy. LEPSi luminescence is also thought to involve surface states. The final result is an overall blueshift in the PL spectrum.

The model[27] receiving the most acceptance (including this author) is a combination of quantum confinement and surface states. As seen in Fig. 4.21 quantum confinement increases the effective bandgap from E_g to E_g' (blueshift). The addition of a surface state results in a redshift but the final effect is an overall blueshift, $h\nu_2 > E_g$.

Fig. 4.22, taken from Kanemitsu[26], shows a model for the pore formation process under anodic etching. The model is based on the fact that holes are necessary for pore formation. Since the bandgap in PSi is increased compared to bulk silicon, holes need an additional energy Eq to penetrate the porous layer. If Eq is larger than the hole energy supplied by the bias, the porous layer becomes depleted of holes and passivated against further dissolution. Pores continue to grow since it is energetically more favorable for a hole to enter the electrolyte directly (solid arrow), than via the porous structure (dotted arrow). Due to the need for holes, n-type silicon requires light assistance in order to produce PSi while p-type silicon can undergo etching in the dark to produce PSi. The dissolution of silicon is thought to be associated with the formation of silicon fluoride molecules which are in turn removed by other chemical reactions. Two silicon dissolution reactions thought to occur simultaneously are shown below[24]:

$$Si + 2HF + nh^{+} \rightarrow SiF_2 + 2H^{+} + (2-n)e^{-} \qquad \textbf{(4.12)}$$

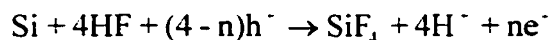

$$Si + 4HF + (4-n)h^{+} \rightarrow SiF_4 + 4H^{+} + ne^{-}$$

PSi can also be fabricated by simple chemical etching of silicon without applying an electrical bias[28]. A typical etchant used is $HF\text{-}HNO_3$ based which produces films similar to those fabricated with conventional anodization. Chemical etching can be considered as a localized eletrochemical process where microscopically, local anode and cathode sites form on the etched surface. In general, anodic etching dominates as a manufacturing method over chemical etching for two reasons:

1) Etching conditions are more easily controlled via anodic etching.
2) The typical PL intensity of chemically etched PSi is weaker than for anodically etched PSi.

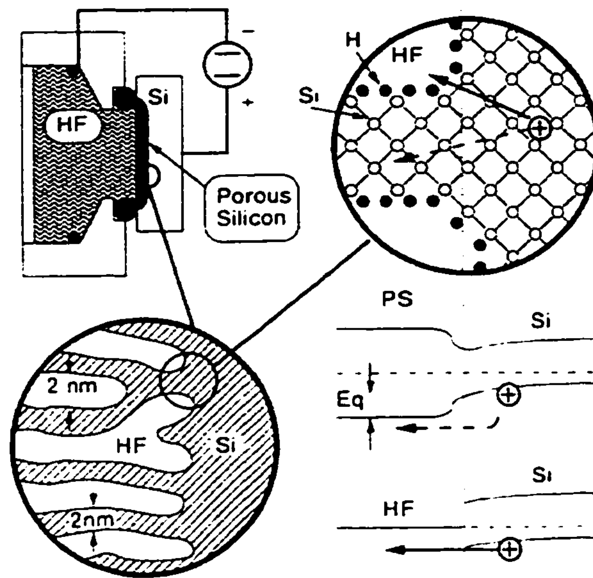

Figure 4.22 A model describing the pore formation process. Pore formation requires holes which are supplied via the applied bias. Pores continue growing since it is energetically more favorable to enter the electrolyte from the bulk Si than through PSi which has an increased bandgap. Figure taken from Kanemitsu[26].

PSi has been traditionally characterized by its pore structure which can be divided into three types:

1) Micro or nanoporous with pores ≤ 2 nm in width. Nanoporous PSi is usually associated with high porosity (80% +), strong PL, poor electrical and mechanical properties.

$$\text{Porosity} = \frac{\rho_{Si} - \rho_{PSi}}{\rho_{Si}} \quad \textbf{(4.13)}$$

   where ρ_{Si} = density of bulk silicon, ρ_{PSi} = density of PSi.

2) Mesoporous PSi has 2-50 nm size pores. It is usually associated with medium porosity (40-60%), weak or no PL, and poor to good electrical properties.

3) Macroporous PSi has > 50 nm size pores. It is associated with low porosity (< 20%), no PL, and good electrical properties.

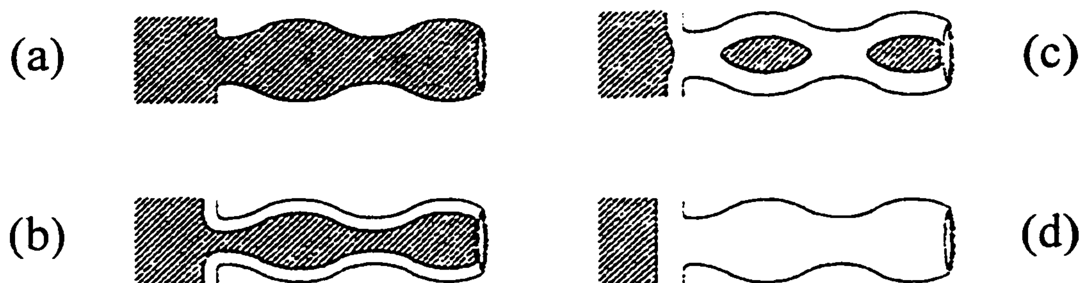

Figure 4.23 (a) A freshly etched PSi quantum wire. Its surface is passivated with hydrogen. (b) Oxidation in air for temperatures <800 °C will create poor oxides at the surface consisting of Si-O and Si-O-H bonds. In some cases this tends to further blueshift the LEPSi PL. (c) Rapid thermal oxidation in dry oxygen at temperatures >1000 °C creates good oxides, Si-O_2. This results in Si quantum dots surrounded by an oxide shell or skeleton. Blue-PL LEPSi is created in this way. (d) Further oxidation results in a completely oxidized specimen, porous glass. Figure modified from Hamilton[24].

Fig. 4.23, modified from Hamilton[24], shows how a quantum wire might look as it is transformed from a freshly etched wire to a completely oxidized specimen (porous glass). Fig. 4.23a shows a freshly etched silicon quantum wire passivated mostly by hydrogen. PSi has in some cases several hundred square meters of surface area per cubic centimeter and therefore requires a high order of passivation to support efficient PL. Hydride passivation tends to be unstable especially when the specimen is heated or exposed to UV light. Specimens will show degradation in PL efficiency as time passes but in most cases can be restored by dipping them in HF. In addition to passivation, surface chemistry plays an active role in PL emission. Vacuum annealing of PSi has produced LEPSi with PL centered at 1250 nm (Fauchet[23]). Oxidation at room temperature or oxidation at temperatures less than 800°C tends to blueshift the PL spectrum as far as the green. In this case, surface species go from Si-H to Si-O-H. The cases in Fig. 4.23a and b represent the LEPSi visible-IR PL band exhibiting μs decay times. The blue PL band exhibits ns decay times and can be obtained by rapid thermal oxidation. LEPSi heated to ≥ 800 °C, in dry O_2, for several seconds (~ 30 - 100) will create a thick oxide shell resulting in silicon dots as shown in Fig. 4.23c. Very good oxides are produced at these temperature (Si-O_2) and form a skeleton to support the silicon quantum

dots. Blue-band LEPSi is thought to be direct gap due to its short decay time while the state of IR-visible band LEPSi is still unclear.

After several years of intensive research efforts, PSi is not completely understood. This is not surprising since porous silicon is a complex material requiring a truly interdisciplinary effort involving spectroscopy, structural and chemical microscopy, surface science, and electrochemistry. The rest of this section aims to show imaging results obtained with the cslM/m of various LEPSi materials and devices. Early in this thesis, a collaboration was formed between UW-CMG and P.M. Fauchet's group at the University of Rochester. C. Peng and S.P. Duttagupta were responsible for manufacturing all of the specimens imaged in this section.

4.2.1 PSi Materials

Fig. 4.24a and b show RL and PL images, respectively, of one of the first LEPSi specimens received from the Rochester group. The images were taken on the MACROscope at zoom 8 (1 x 1 cm) using 488 nm light in non-confocal mode. The specimen consists of three regions:

1) Unetched silicon which appears white in RL due to its high reflectivity and appears black in PL.
2) Partially etched silicon where LEPSi failed to be created. This appears black in both RL and PL.
3) LEPSi which reflects poorly in RL, thus appearing black while appearing white in PL.

The specimen was etched from a p-type, 12 Ω cm silicon wafer using 30% HF in H_2O for 5 minutes at 10 mA/cm^2 followed by 6 h in 49% HF solution. To the naked eye, the etched region appears as a dull yellow residue and is clearly inhomogeneous at a macroscopic level. The specimen is also non-homogeneous at a microscopic level as can be seen in Fig. 4.24c. Fig. 4.24c shows a confocal RL (488 nm), zoom 1 (200 x 200 μm) image, taken on the cslm with a 0.9 NA objective consisting of a series of LEPSi islands sitting on a silicon substrate. Each island can be considered a flat plateau sitting approximately 10 μm above the substrate. This type of 'dry riverbed' structure is typical of early attempts to make highly porous or nanoporous LEPSi.

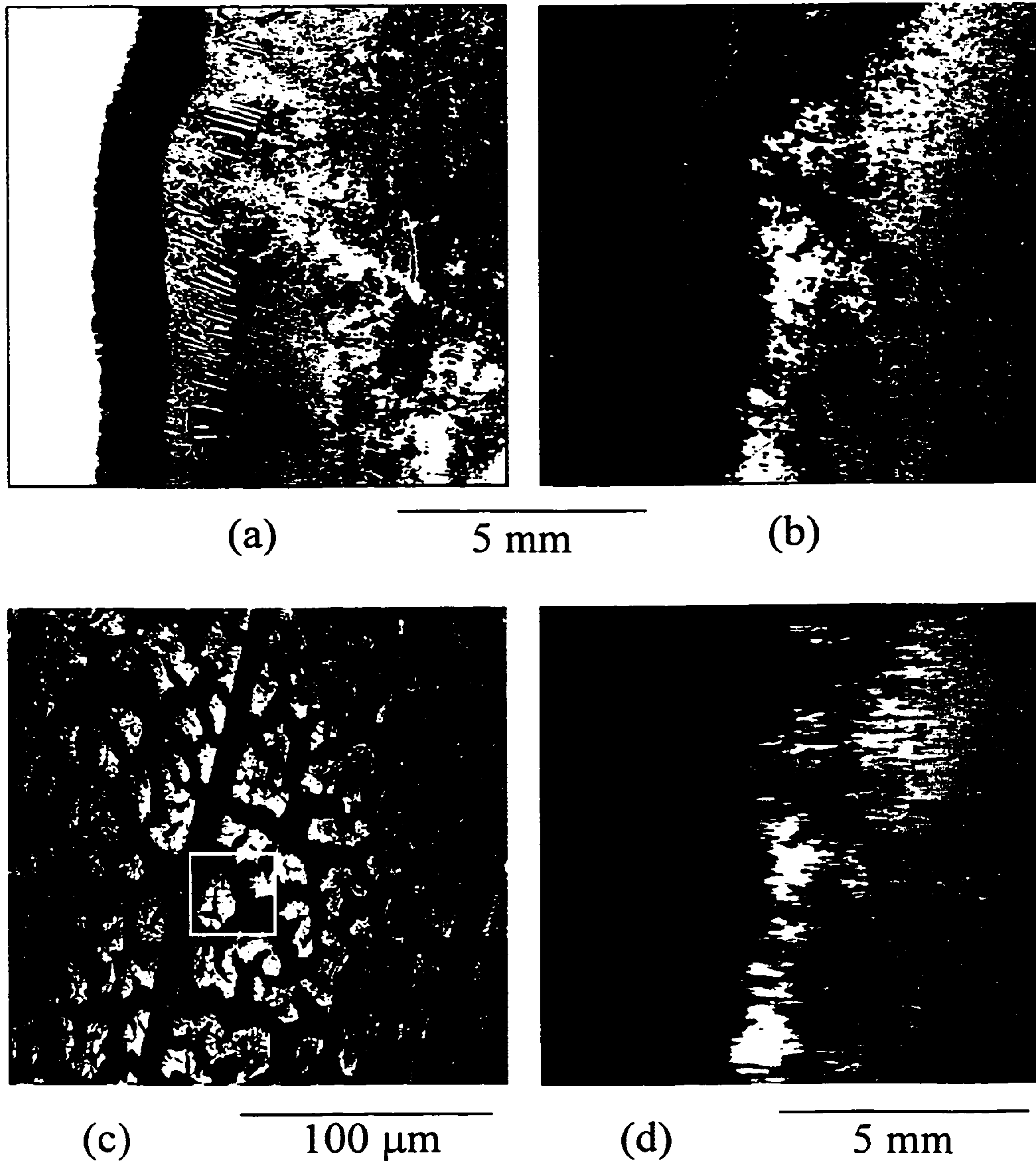

Figure 4.24 (a) RL (488 nm) MACROscope image of an early LEPSi specimen. The etching is clearly non-homogeneous at a macroscopic level. (b) The same specimen imaged in PL (488 nm excitation, > 550 nm emission). LEPSi areas appear bright in this image while appearing dark in the RL image. (c) Confocal RL image (488 nm) of a set of 'islands' forming part of the LEPSi structure in b). (d) PL image of the same area in b) taken at 'normal' scan speed (5 s). The PL lifetime for this specimen is on the order of several µs such that the dwell time at each pixel must be tens of µs resulting in scan times lasting 30-100 s, otherwise streaking or blurring occurs.

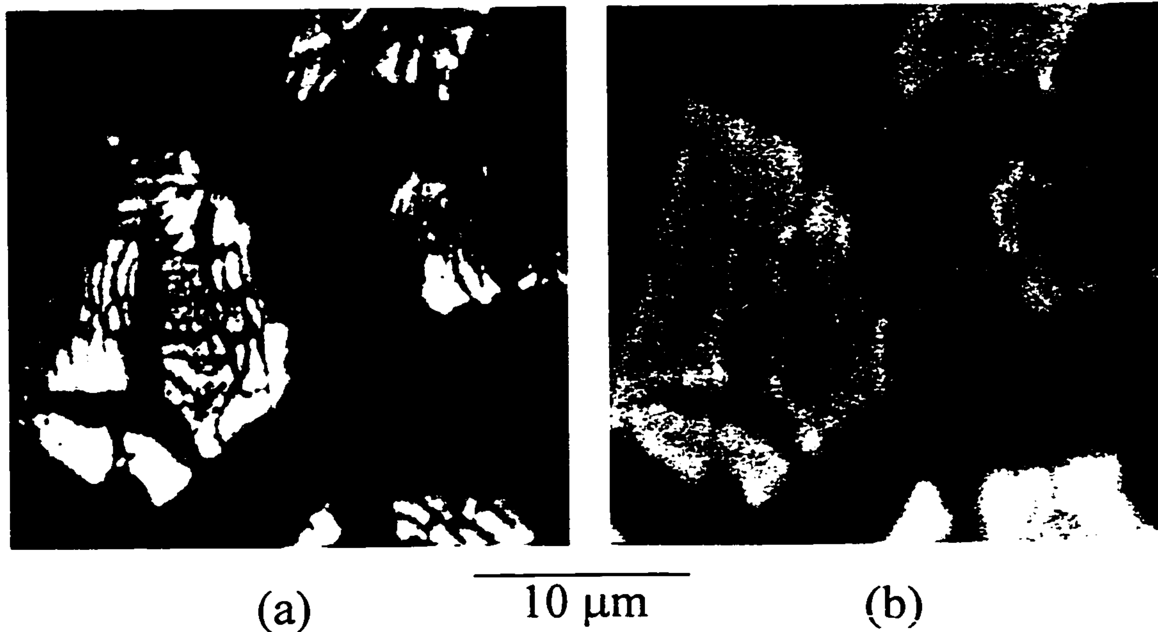

Figure 4.25 (a) Confocal RL (488 nm) image of the top part of one of the islands from the boxed section of Fig. 4.24c. The island itself consists of a series of smaller islands suggesting a fractal-like structure which supposedly repeats itself at the nm level. (b) Confocal PL image (488 nm excitation, > 550 nm emission) of the same area.

The PL decay time for this specimen is on the order of several μs or tens of μs. The scanning speed was reduced by a factor of ~ 10 in order to obtain the image in Fig. 4.24b. Variable scanning speed is essential with this kind of imaging since without it, the resulting PL image is blurred as seen in Fig. 4.24d. Fig. 4.25a and b show RL and PL images, respectively, of the boxed-in area in Fig. 4.24c. The images were obtained with a 0.9 NA objective using 488 nm light, at zoom 8 (25 x 25 μm) in confocal mode using a 50 μm pinhole and 10 cm focal length detector lens. At this zoom, many cracks can be seen running throughout each of the 10-20 μm size islands suggesting a fractal structure which supposedly repeats itself at the nm level. Once again these images show one confocal slice focused at the top of the island or plateau.

One of the most interesting LEPSi specimens requiring the full microscopic and macroscopic capabilities of the cslM/m is shown in Fig. 4.26. Fig. 4.26a shows a zoom 1 (8 x 8 cm), RL (488 nm) image of a 9 cm diameter silicon wafer with a square LEPSi pattern etched into its

center. The LEPSi squares reflect poorly hence they appear black in contrast with the surrounding partially etched, pitted silicon which acts like a mirror. The X mark on the top left is made with masking tape and was put there for calibration and identification purposes. Masking tape luminesces very strongly compared to PSi which makes it serve as a good marker both in RL and PL. Fig. 4.26b shows the same wafer imaged in PL (488 nm excitation, > 550 nm emission). The LEPSi squares are unevenly etched which leads to an inhomogeneous PL pattern. The top part of the wafer labeled 'blue back', due to its bluish appearance to the naked eye, was treated with a low energy/dose reactive ion etch (RIE)[29], before anodization, while the bottom half labeled 'gray back' went untreated. The purpose, at a macroscopic level, was to assess the effects of low energy/dose RIE on the PL quality of LEPSi. The top RIE treated part of the wafer shows a clear enhancement of PL over the untreated part. Fig. 4.26c and d show RL and PL images, respectively, of the center area in Fig. 4.26a. Once again the top part of the wafer shows a clear enhancement of PL compared to the bottom. At this zoom (zoom 2) each of these squares appears to be made up of about 20 LEPSi lines. Fig. 4.27a and b show RL and PL images, respectively, of the boxed LEPSi square in Fig. 4.26d. At this magnification it is evident that the squares are made up of about 80 lines rather than 20. The discrepancy between the two images can be attributed to an aliasing[30] effect caused by undersampling in the lower magnification images. Fig. 4.26c and d are zoom 2 images while Fig. 4.27a and b are zoom 8 images, a zoom difference of 4. Therefore, sampling occurs once every 4 lines for Fig. 4.26d in relation to Fig. 4.27b such than $80 / 4 \cong 20$ lines are visible in Fig. 4.26d. In Fig. 4.27b, PL homogeneity and defects within the LEPSi square can be quantified. A better view of the lines can be achieved with the 0.42 NA objective on the cslm as shown in Fig. 4.27c and d. Fig. 4.27c shows the 'gray back' lines imaged in PL at zoom 2 (500 x 500 μm). Fig. 4.27d shows the 'blue back' lines imaged in PL using the same zoom. Both sets of lines have a considerable amount of structure associated with them which can be studied closer with the 0.9 NA objective.

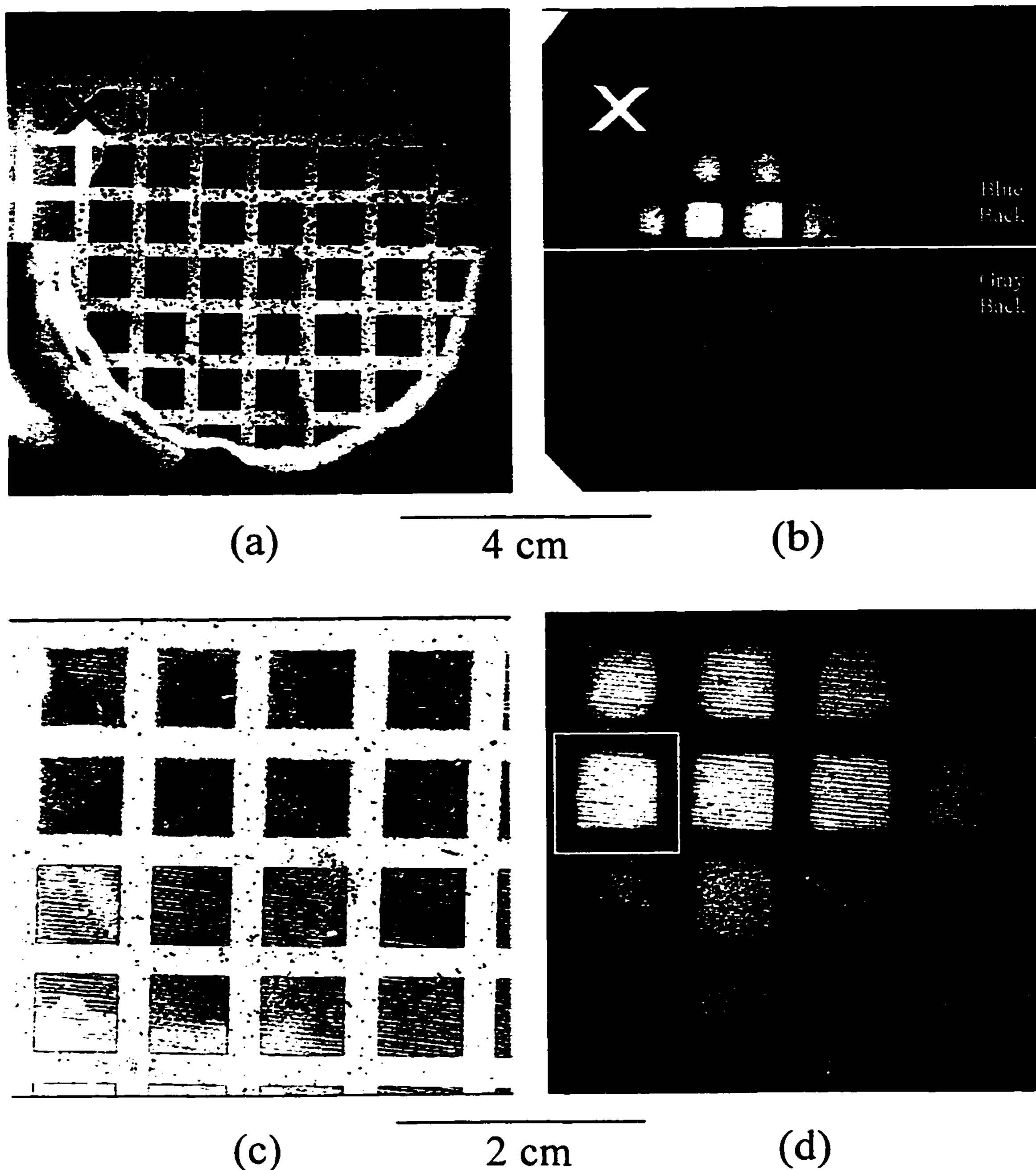

Figure 4.26 (a) MACROscope RL (488 nm) image of a set of LEPSi squares etched into a 9 cm diameter silicon wafer. (b) The same area imaged in PL (488 nm excitation, > 550 nm emission). The X on the top left is made from masking tape and serves as a good marker in PL and RL. The top part of the wafer was exposed to a RIE treatment which enhanced the PL. (c) RL image of the center part of a). (d) PL image of the same area. At this magnification each square seems to be made up of about 20 LEPSi lines.

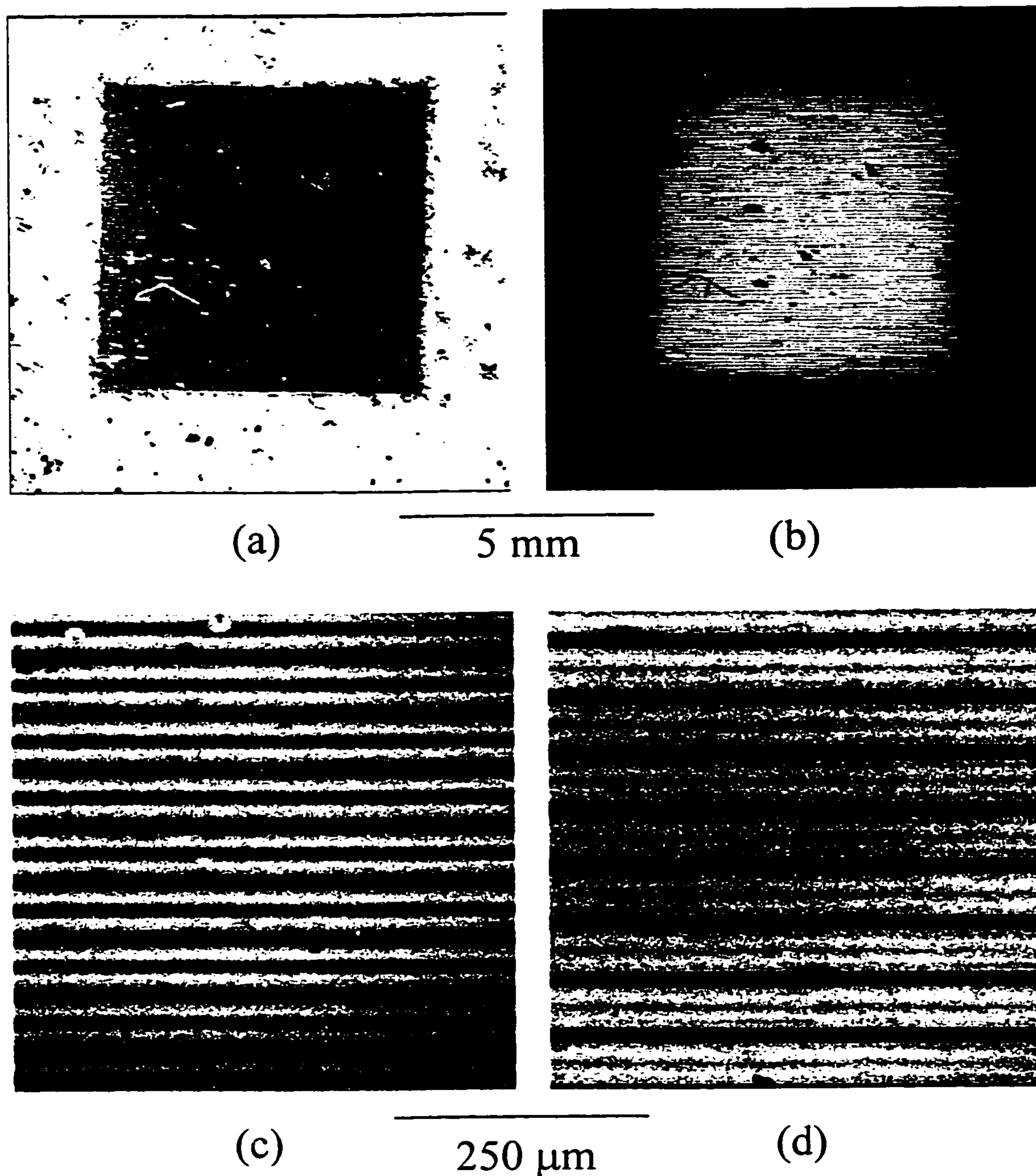

Figure 4.27 (a) MACROscope RL (488 nm) image of the LEPSi square in the white box of Fig. 4.26d. At this magnification, the LEPSi square is made up of about 80 lines. The discrepancy between this image and Fig. 4.26d is due to an aliasing effect caused by undersampling in Fig. 4.26d. (b) PL image (488 nm excitation, > 550 nm emission) of the same area. (c) PL image of the LEPSi lines located in the 'gray back' part of the wafer. (d) PL image of the LEPSi lines located in the 'blue back' part of the wafer.

Fig. 4.28a shows a zoom 2 (100 x 100 μm), maximum intensity, RL image (488 nm) of a set of 'gray back' LEPSi lines generated from 7 confocal slices using a 0.9 NA objective. A 10 μm pinhole was used in combination with a 10 cm focal length achromatic detector lens to achieve confocality. Fig. 4.28b shows the same set of lines imaged in PL with a 50 μm pinhole. Fig. 4.28c shows a 3-D rendition of the lines, generated from the profile data, which provides height information in combination with the maximum intensity data giving contrast information. The creation of these lines had two purposes: to evaluate the resistance to etching of amorphized regions and to investigate the mechanism and rate of undercutting with a silicon nitride (Si_3N_4) protective layer. The structures in Fig. 4.28 were created as follows: a p-type silicon wafer was first exposed to a high energy/dose[29] ion implantation preceded by a Si implant to guarantee complete amorphization. The amorphized lines were nominally 15 μm wide. The rest of the wafer was coated with silicon nitride applied via chemical vapor deposition CVD. The wafer was then anodized in HF:ethanol (1:1) with a current density of 10 mA/cm^2. The bright 15 μm wide lines at the top and bottom of Fig. 4.28a are the amorphized regions, which appear as horizontal black lines in Fig. 4.28b. The amorphized lines resisted etching and therefore no LEPSi was created in these regions, as expected. While it is clear that no LEPSi was created in the amorphized region, the 3-D image of Fig. 4.28c shows that lateral etching did occur. The amorphized lines in Fig. 4.28c are the tall structures with triangular crossections. Had the amorphized lines been completely impervious to etching, a square or rectangular crossection would be expected. What happened instead was that as the etching ate away several microns of silicon, the top of the amorphized lines spent a long time in the etching solution and experienced quite a bit of etching while the bottom were etched for a short time. The tops of the amorphized lines in Fig. 4.28c lie ~ 1.8 μm above the rest of the structures. In Fig. 4.28a the structures in between the amorphized lines consist of a bright central band surrounded by two dark bands. In Fig. 4.28b, the central band appears dimmer than the surrounding bands. The three band region was covered with silicon nitride right before the etching procedure. As the anodization proceeded, the silicon was etched due to undercutting of the silicon nitride at the top and bottom of the bands.

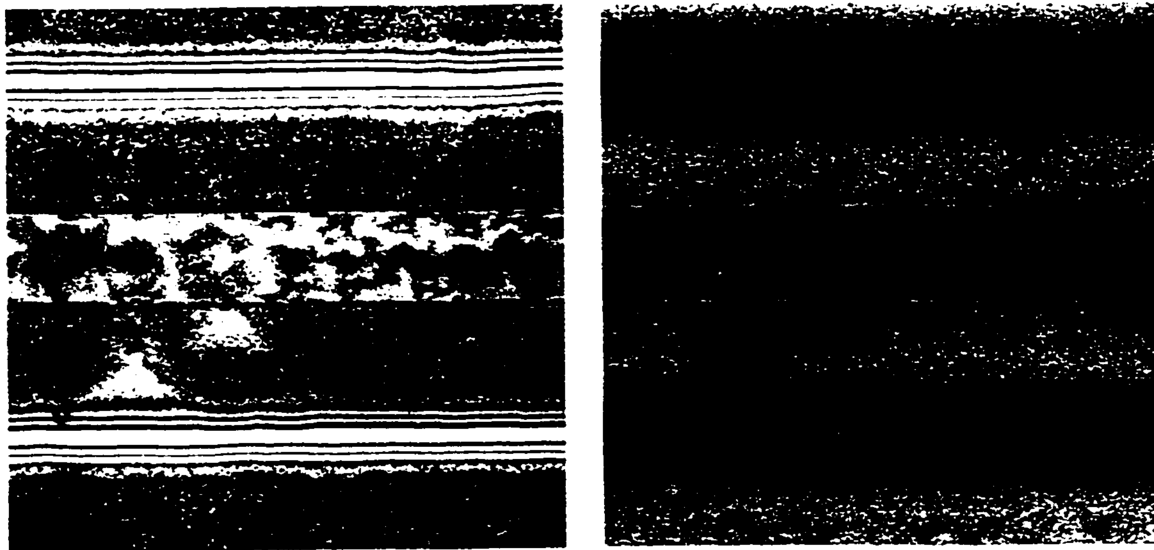

(a) 50 μm (b)

(c)

Figure 4.28 (a) Confocal RL (488 nm) maximum intensity image of a set of LEPSi lines from the 'gray back' part of the wafer. (b) Confocal PL image (488 nm excitation, > 550 nm emission) of the same area. The black horizontal lines correspond to amorphized regions. The central, dim band corresponds to partially etched LEPSi while the surrounding bright bands are fully etched LEPSi. (c) 3-D image of the lines where the maximum intensity image has been incorporated with height data. The amorphized lines, which lie 1.8 μm above the rest of the structures, show clear signs of lateral etching due to their triangular cross-section.

Good LEPSi was created in the regions where complete liftoff of the silicon nitride occurred. The etching was stopped before complete liftoff could occur along the central band and as a consequence poor LEPSi was created in this band.

Fig. 4.29a shows a zoom 2 (100 x 100 μm), maximum intensity, RL (488 nm) image of a set of 'blue back' LEPSi lines generated from 8 confocal slices using the same setup as was used in Fig. 4.28a. Fig. 4.29b shows the same set of lines imaged in PL with a 50 μm pinhole. These set of lines were created via lithographic processes[29] for the purpose of evaluating pre-anodization low dose/energy RIE treatments on LEPSi PL quality. The structures were manufactured by depositing a set of ~ 15 μm wide photoresist lines separated by ~ 45 μm spaces. The wafer was then exposed to a low energy/dose RIE. The photoresist, which protected the silicon during RIE, was removed and the wafer was anodized in HF:ethanol (1:1), with a 10 mA/cm^2 current density. The center RIE treated LEPSi line of Fig. 4.29b shows clear signs of PL enhancement with respect to the surrounding untreated lines. Data from the confocal slices was used to generate a 3-D image shown in Fig. 4.29c. The 3-D image does not include maximum intensity information but does show that the RIE treated band is higher (~ 1.5 μm) than the untreated bands. While the reasons for this is not clear, the RIE treated regions formed LEPSi faster than the untreated bands. Fig. 4.29d was taken under the same conditions as Fig. 4.29b except that the 50 μm confocal pinhole was removed and a 1 mm iris diaphragm was inserted in its place effectively making this image a non-confocal one. The confocal PL image is clearly superior to the non-confocal image. Micron-sized features are resolved in Fig. 4.29b while the same features in Fig. 4.29d appear as a blur. Notice that the use of a 50 μm pinhole implies a negligible or non-existent gain in lateral resolution based on the 1.4 factor effect described in section 2.2.2. In practice the effective lateral resolution improves due to the exclusion of out-of-focus light which tends to blur features as shown in Fig. 4.29d.

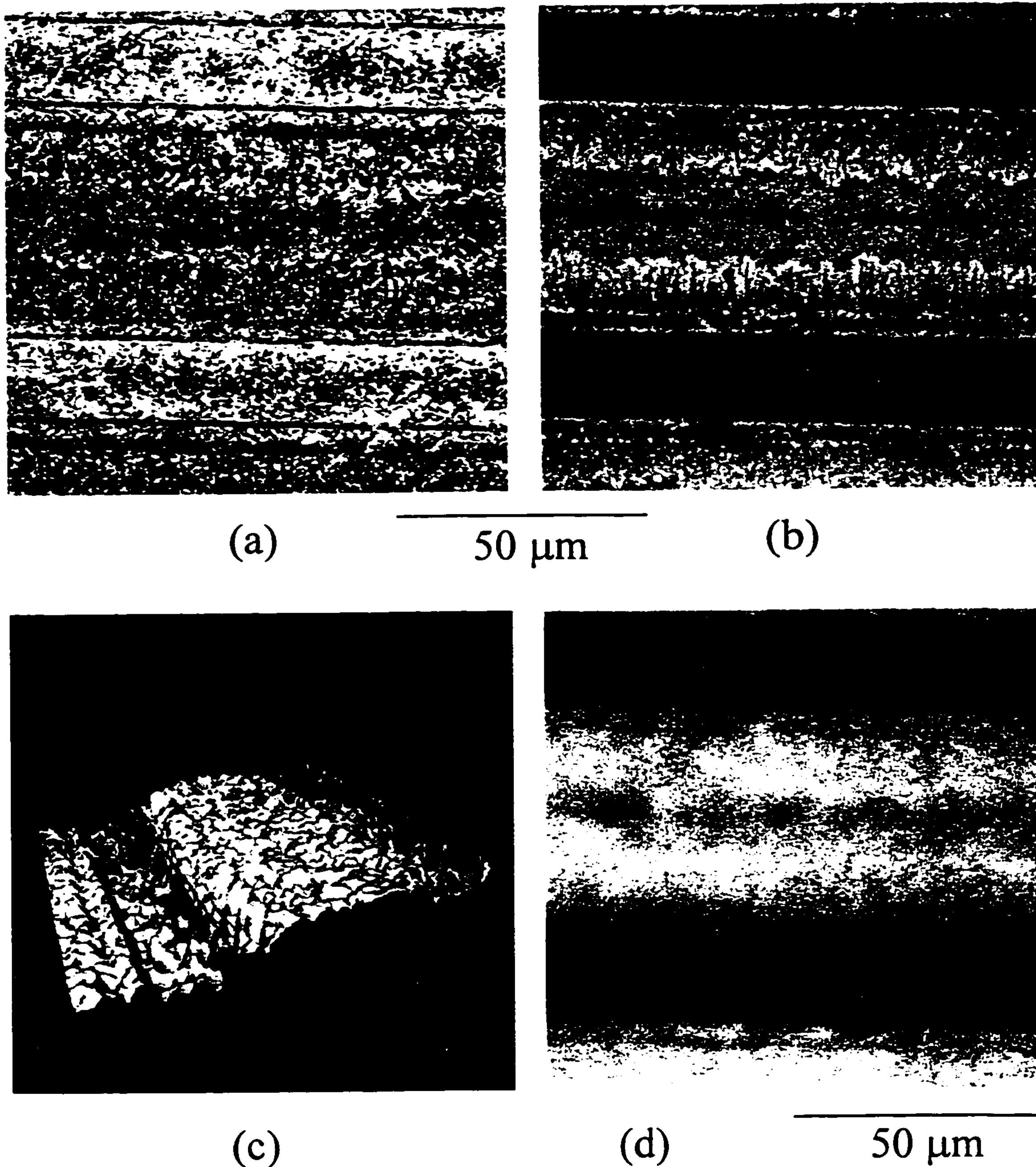

Figure 4.29 (a) Confocal RL (488 nm) maximum intensity image of a set of LEPSi lines from the 'blue back' part of the wafer. (b) Confocal PL image (488 nm excitation, > 550 nm emission) of the same area. The central band corresponds to RIE treated LEPSi. The black horizontal lines correspond to untreated regions which clearly show less PL. (c) 3-D image of the lines. The central RIE treated line underwent enhanced etching and lies about 1.5 μm above the other lines. (d) Non-confocal PL image of the same area as b). The resolution in this image is substantially inferior when compared with the confocal image where submicron resolution is possible.

Fig. 4.30a shows a RL (488 nm) zoom 2 (4 x 4 cm), MACROscope image of a LEPSi specimen. The circular area in the center is LEPSi, while the surrounding white area is unetched silicon. The PSi specimen was created from a 0.1 Ω-cm, n-type silicon wafer etched in 1:1, HF:ethanol with a 25 mA/cm^2 current density using light assistance. The specimen is affixed to a glass slide with scotch tape. Fig. 4.30b shows the same specimen imaged in PL (488 nm excitation, > 550 nm emission). This high quality specimen is basically the successor to the specimen shown in Fig. 4.24. The RL and especially the PL uniformity in this specimen allowed for spectrally-resolved and bleaching data to be obtained. Fig. 4.30c shows a PL image of the boxed area in Fig. 4.30b taken with a scanning stage microscope[31] using a 5 cm focal length fused-silica singlet as an objective. Excitation occurred at 325 nm and PL was collected for wavelengths longer than 385 nm. Fig. 4.30d shows the same part of the specimen imaged in PL with 633 nm excitation and > 695 nm emission. A series of white spots are clearly evident in Fig. 4.30d which appear very faintly in Fig. 4.30c. The 633 nm light seems to be penetrating deeper into the specimen than UV or blue, as expected, which results in a 'deep PL' image. Fig. 4.30d suggests the formation of hydrogen bubbles which is common in the anodization procedure. Multiwavelength excitation PL can give additional information especially for materials with broad PL spectra. Fig. 4.31a shows a PL spectrum taken with the MACROscope at a point near the middle of the specimen. The spectrum was not calibrated and the secondary peaks to the left of the central peak are highly suspect, however, the general shape of the spectrum is typical of LEPSi. Fig. 4.31b shows an x-λ PL scan taken along the line shown in Fig. 4.30b. Wavelength is plotted vertically while distance is plotted horizontally. The peak wavelength is centered between 650 and 700 nm. The three lines that extend beyond the LEPSi in Fig. 4.31b are clearly artifacts since no PL should emanate from the unetched silicon. x-λ plots provide useful spectral information on the specimen as a whole. Unfortunately the image in Fig. 4.31b took several hours to acquire which suggests a smaller number of pixels (less than 512 x 512) might be appropriate in both directions.

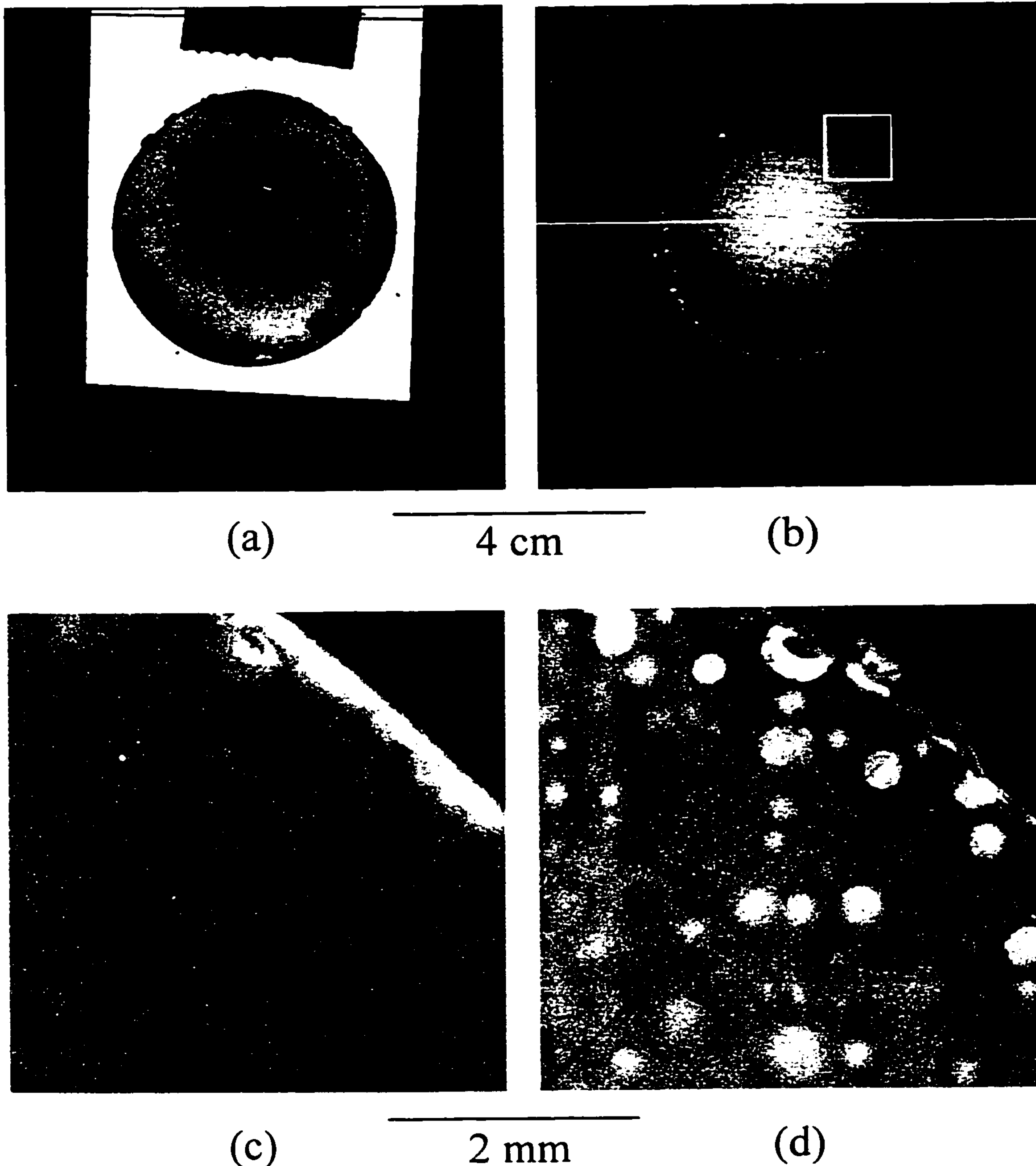

Figure 4.30 (a) RL image (488 nm) of a LEPSi specimen. The LEPSi circle is surrounded by unetched silicon which acts like a mirror. (b) PL image (488 nm excitation, > 550 nm emission) of the same area. The PL is reasonably uniform at all magnifications down to the resolution limit of the cslm. (c) PL image of the boxed section in b) taken with a scanning stage microscope using 325 nm excitation and > 385 nm emission. The image looks fairly uniform except for some extremely faint spots. (d) PL image taken with the same microscope but using 633 nm as excitation and > 695 nm emission. The spots in this case are very apparent. The PL seems to originate deep within the specimen.

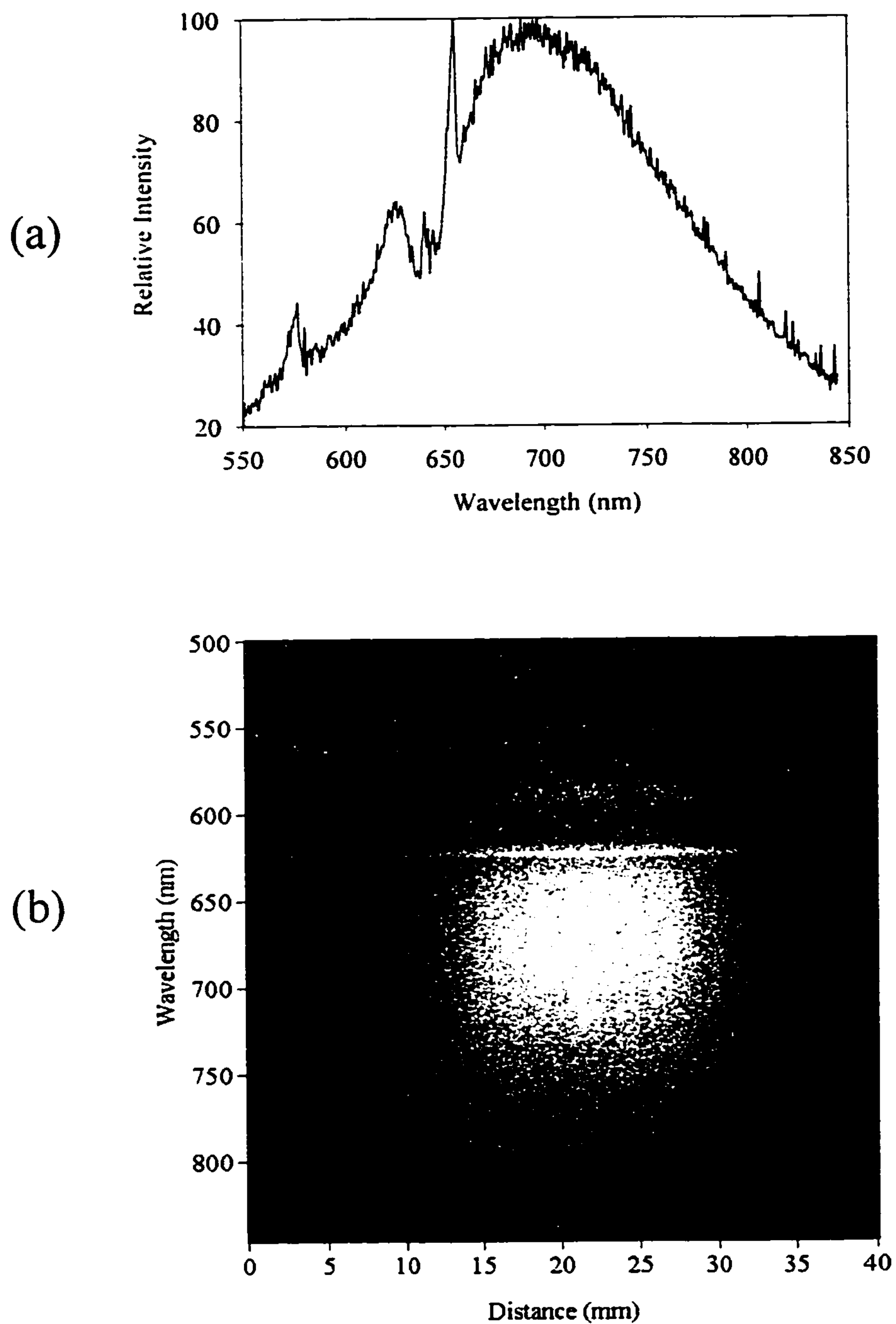

Figure 4.31 (a) PL (488 nm excitation) spectrum of a single point in the center of the Fig. 4.30b specimen. (b) X-lambda PL image plotting wavelength vertically and distance along the white line of Fig. 4.30b horizontally. Any signals not originating from the LEPSi are clearly artifacts.

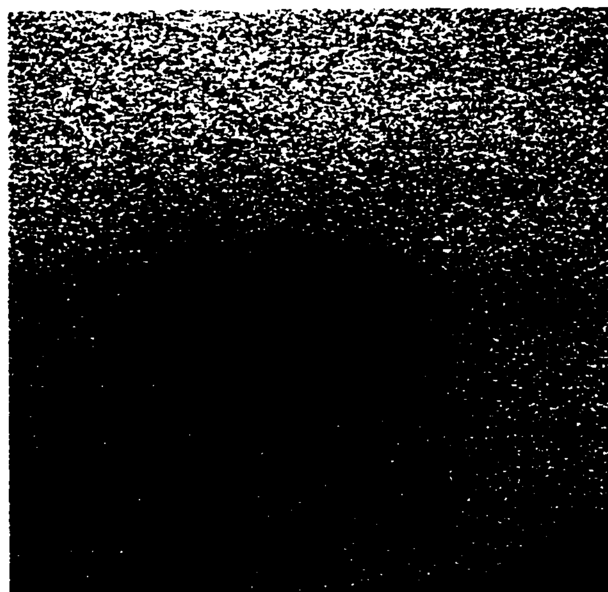

Figure 4.32 Clear evidence of bleaching. This is a zoom 1 image of the Fig. 4.30 specimen taken with a 0.9 NA objective. The dark rectangles indicate bleaching caused by excessive intensities at zooms 2, 4, and 8.

The scanning stage microscope used to take the image in Fig. 4.30 achieved optimal focus by scanning along a diagonal line running from the bottom left to the top right. In some cases, continual scanning along the same line can cause bleaching. When a molecule or fluorophore is placed into an excited state it tends to react more readily especially when in a triplet state[32]. Such a reaction has the possibility of creating a non-photoluminescing species, at which point the fluorophore is said to have been bleached. In practical terms, an area on the specimen can only be exposed to so much light before it bleaches or darkens in PL with respect to the unlit part of the specimen. The faint, dark, diagonal line running from bottom left to the top right in Fig. 4.30d is evidence of bleaching. Better evidence can be obtained by using a high NA objective, as shown in Fig. 4.32. Fig. 4.32 shows a zoom 1 (200 x 200 μm), PL (488 nm excitation, > 550 nm emission) confocal image of the specimen in Fig. 4.30. Previous to taking this image, zoom 2, 4, and 8 images were taken which resulted in bleaching wherever the laser was scanned. The scan areas are rectangular in shape due to the scan requirements discussed in section 3.1.2.3.

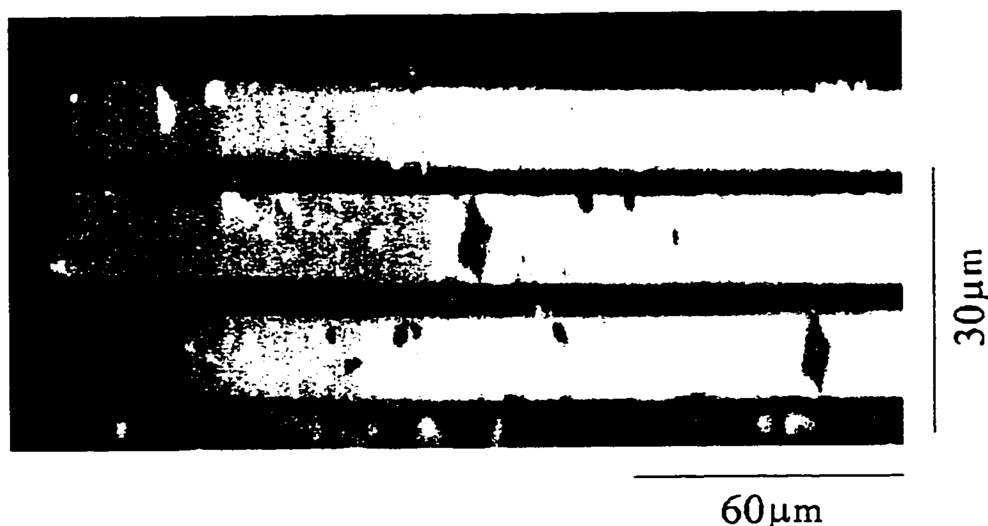

Figure 4.33 Evidence of photon induced passivation in a PL (325 nm excitation, > 385 nm emission) image taken on the scanning stage microscope. The scanning stage microscope's focusing mechanism involves continually scanning about a particular line over and over. In this case the focus line ran vertically. Evidence of passivation, hence PL enhancement, can be seen in the bright vertical lines on the right of the three laser facets (horizontal bands). Also, the right hand side of the image shows signs of PL enhancement since it was scanned many times previous to taking this image.

This type of severe bleaching is not usually observed on the MACROscope due to its larger spot size. For the MACROscope, intensities typically range from hundreds of W/cm^2 to kilowatts/cm^2 while on the cslm, with a 0.9 NA objective, intensities range from tens to hundreds of kW/cm^2. Consult Appendix 5 for a table showing intensities at the specimen for various NAs.

In some cases intense light will passivate the specimen thereby <u>increasing</u> its PL output. An example of this is shown in Fig. 4.33 where 3 semiconductor laser facets were imaged on the scanning stage microscope using a reflecting objective and 325 nm light as an excitation source. The laser facets appear as ~ 10 µm wide horizontal bars. The white vertical lines on the right of the laser facets are enhanced regions due to continual scanning from the focusing mechanism. Several images were taken (previous to this image) to the right of center. A slight but noticeable increase in the PL signal can be seen for the right of center parts of the facets when compared to the left parts.

4.2.2 PSi Devices

Fig. 4.34a shows a RL (633 nm), zoom 8 (1 x 1 cm), MACROscope image of one of the first PSi solar cells created by the Rochester group, unfortunately the cell turned out to be somewhat of a failure. The MACROscope was used in identifying some of the cell characteristics. The cell was created by first taking a p-type silicon wafer and ion-implanting it to create a n^+p junction. The n^+ side of the wafer was anodically etched to create PSi. Due to the high resistance of PSi, a 50% transmitting Au window was deposited onto the cell to serve as a conducting window. The large, bright spot in Fig. 4.34a corresponds to the transparent window while the small even brighter dot corresponds to a thick opaque gold layer serving as a top contact. The energy efficiency of the cell had been previously measured by the Rochester Group to be ~ 5% with the assumption that all of the photocurrent originated from the area enclosed by the 50% transmitting gold dot. The OBIC image shown in Fig. 4.34b tells a totally different story. The strongest photocurrents originate from the areas surrounding the gold dots which suggests that the PSi film was a good conductor or that it had been improperly manufactured. Consequently, the transparent gold dot only serves to reduce the amount of light reaching the junction thereby reducing the photocurrent. The I-V curve in Fig. 4.34c clearly shows that this is indeed a very poor solar cell.

The next attempt at creating a PSi solar cell occurred several years after the first try resulting in a much superior device. There are several reasons[33] for using PSi in solar cells:

1) PSi has a textured surface which reduces reflection losses and therefore serves as an anti-reflection layer.
2) PSi offers a tunable bandgap which in turn allows sunlight absorption optimization. PSi can therefore serve as a window layer or the top part of a tandem cell.
3) PSi can be used as a sandwich layer matching Si with GaAs due to its increased flexibility.
4) PSi is appealing for solar cell fabrication due to the ease of scaling manufacturing processes up to large areas.

There are also disadvantages to using PSi such as chemical instability, high resistivity, mechanical fragility, and poor thermal conductivity.

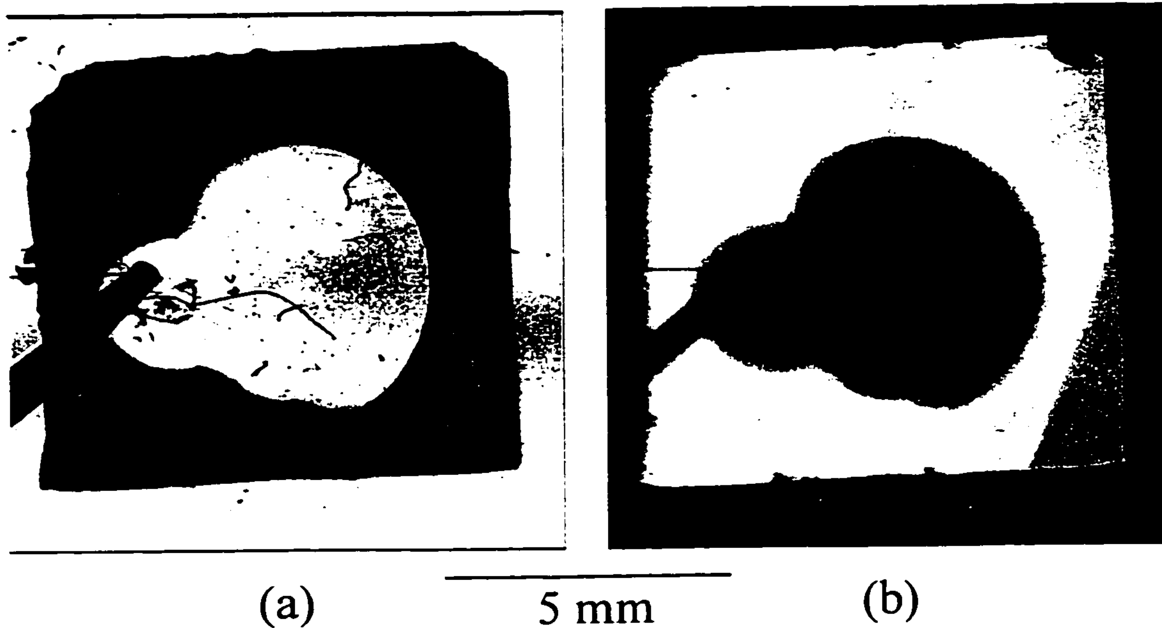

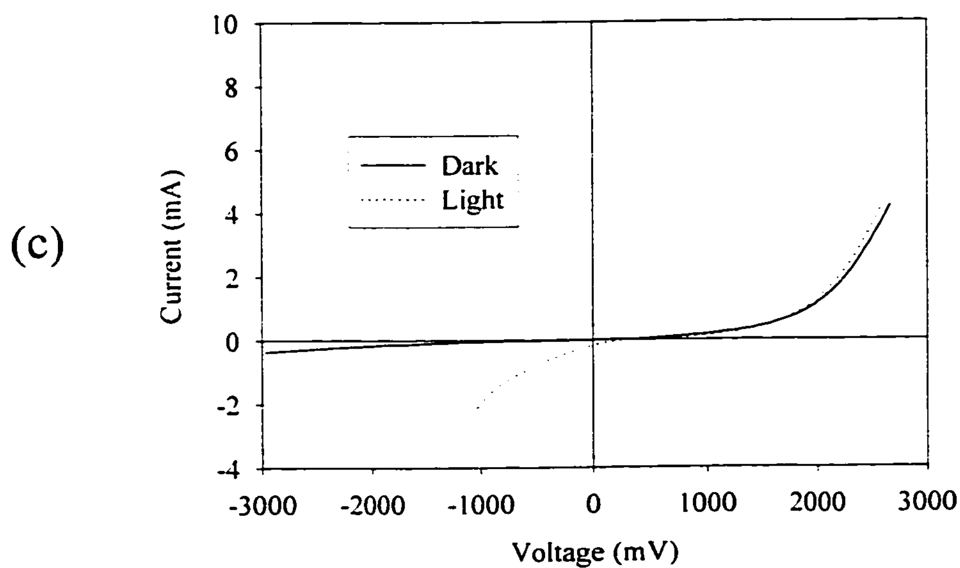

Figure 4.34 (a) RL image (633 nm) of a PSi solar cell. The small bright circle is a gold contact while the larger circle is a transparent, conducting gold window. Only the large circle is supposed to be active. (b) OBIC image of the same area. The entire square seems to be active and the transparent gold layer only seems to reduce the number of photons reaching the junction. (c) The I-V plots for dark and illuminated response indicate a very poor 'solar cell'.

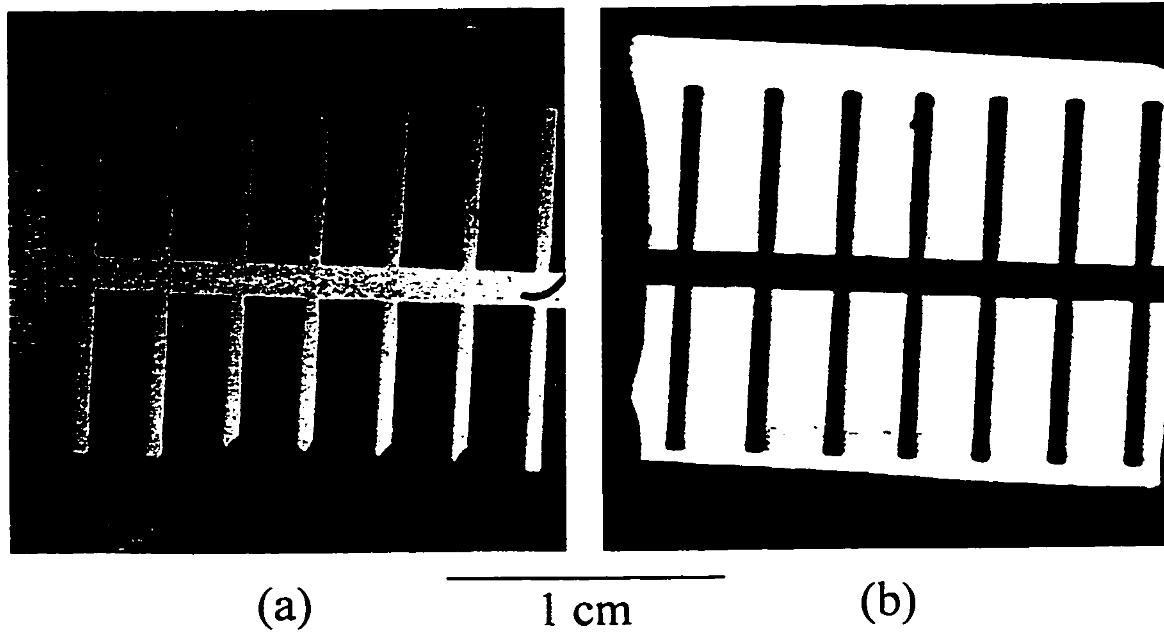

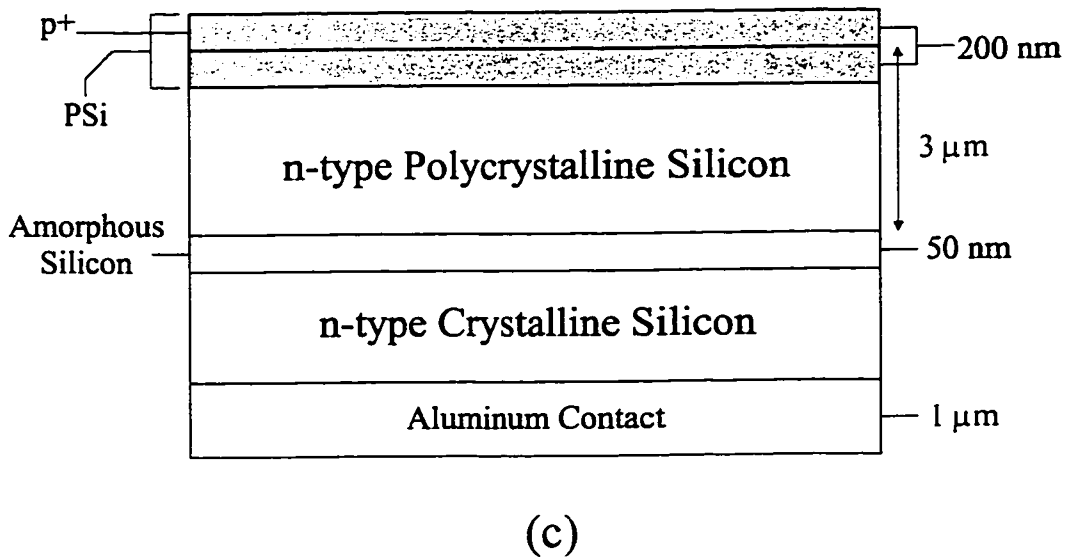

Figure 4.35 (a) RL image (633 nm) of a PSi solar cell taken on the MACROscope. (b) OBIC image of the same area. Both RL and OBIC images show no indication of defects or damage. (c) Solar cell structure where the gray area indicates PSi. The top p^+ layer becomes mesoporous PSi while the n-type layer etches to nanoporous PSi.

Fig. 4.35a shows a RL (633 nm), zoom 4 (2 x 2 cm), MACROscope image of a PSi solar cell. Fig. 4.35b shows the same cell imaged in OBIC (633 nm). Both the RL and OBIC images show no apparent defects; at this level the cell seems good. Fig. 4.35c shows the structure of PSi solar cell; several steps were employed in its production. The first step involved depositing 50 nm of amorphous silicon via CVD onto an n-type silicon wafer. The purpose of this layer was to isolate the wafer from the rest of the cell. Next, approximately 3.5 μm of n-type polycrystalline silicon was deposited on the substrate via CVD followed by boron implantation to make the top 0.2 μm p^{+}-type. The next step was to anodically etch the polycrystalline silicon side of the wafer so as to produce mesoporous and nanoporous PSi. Using a 10 mA/cm^2 current density and a 1:1, HF:ethanol etching solution, p^{+}-type silicon naturally becomes mesoporous PSi while p-type silicon becomes nanoporous PSi. The idea was to create a thin nanoporous PSi layer with excellent optical properties (highly absorbing, large bandgap) sandwiched between a top mesoporous PSi layer with good electrical properties and the bottom n-type polycrystalline silicon layer. Fig. 4.36 shows a spectral response curve[14] for the entire cell plotting quantum efficiency as a function of wavelength.

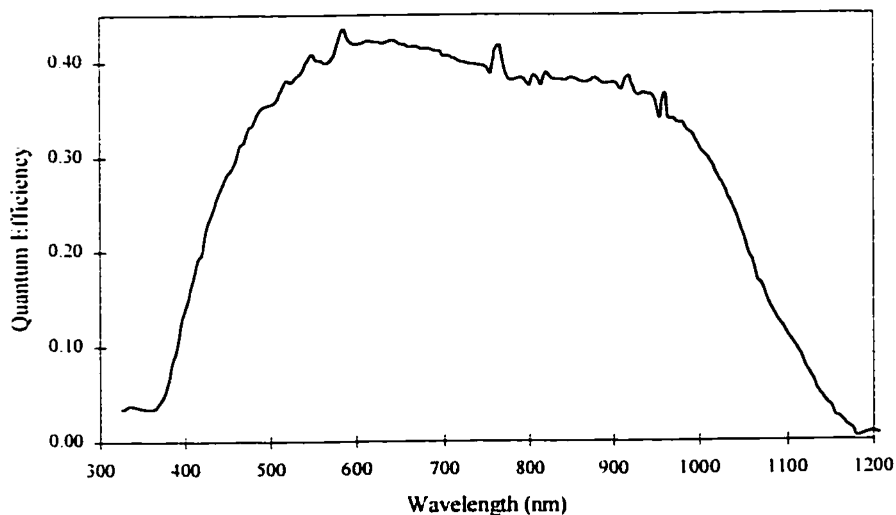

Figure 4.36 Spectral response curve plotting quantum efficiency as a function of wavelength for the PSi solar cell of Fig. 4.35.

The response is reasonably flat between 500 and 1000 nm and drops off at 450 and 1150 nm which is not atypical for a polycrystalline silicon solar cell. The big question is what portion of the response is due to the PSi junction, if any? In other words, is this truly a thin film silicon solar cell or is the crystalline silicon substrate playing some role? In silicon, wavelengths shorter than ~ 650 nm are absorbed within the first 3 μm and therefore the image in Fig. 4.35b can be attributed to the PSi junction. Just to be sure, a similar OBIC image (not shown) was taken with 488 nm, which has a penetration depth of several tenths of microns. The signal strength for blue OBIC image was similar to the red OBIC image of Fig. 4.35b, showing the existence of the PSi junction. Beyond ~ 650 nm the question of photocurrent originating from the crystalline substrate is unclear. A side-on OBIC scan might yield data about a crystalline junction. Making the cell on a substrate such as a heat-resistant glass instead of a silicon wafer would be ideal. Regardless of the mechanism, this cell shows a clear improvement over the cell in Fig. 4.34. Fig. 4.37 shows an I-V curve for the cell.

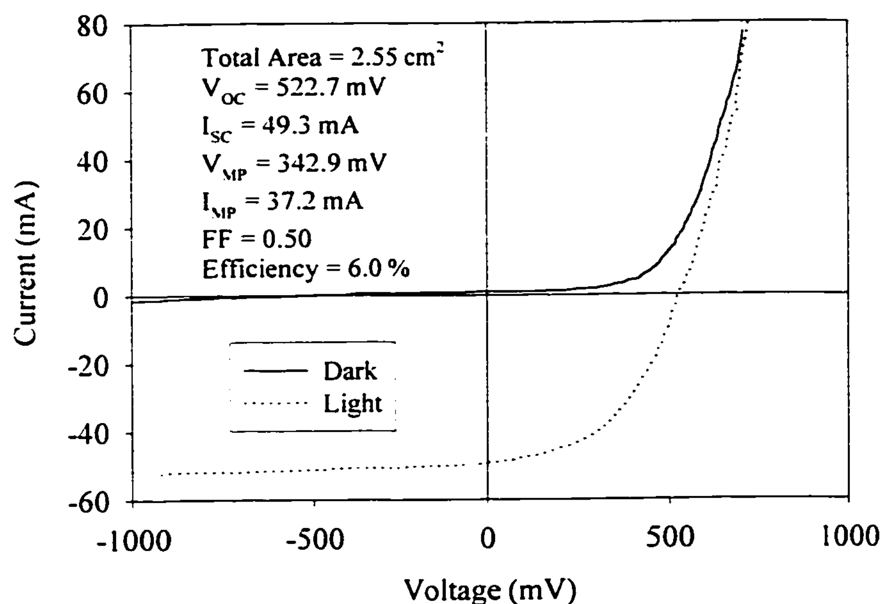

Figure 4.37 I-V characteristic curves showing dark and illuminated responses for the cell from Fig. 4.35. The illuminated response is quite good showing some crossover and an efficiency of 6%, and 8% efficiency considering only the active area.

The 'light' curve shows some signs of crossover and also indicates a series resistance of ~ 2.5 Ω. The open circuit voltage was 522.7 mV and the short circuit current was 49.3 mA, while the maximum power point was (V_{mp}, I_{mp}) = (342.9 mV, 37.2 mA) measured using the spectrum from a tungsten-halogen light bulb calibrated to give AM 1.5 power (83.18 mW/cm^2). The fill factor was calculated to be 0.50 while the solar cell efficiency was calculated to be 6.0% for the entire 1.7 x 1.5 cm cell, and 8.0% considering only the active area. These are very promising results which merit further research.

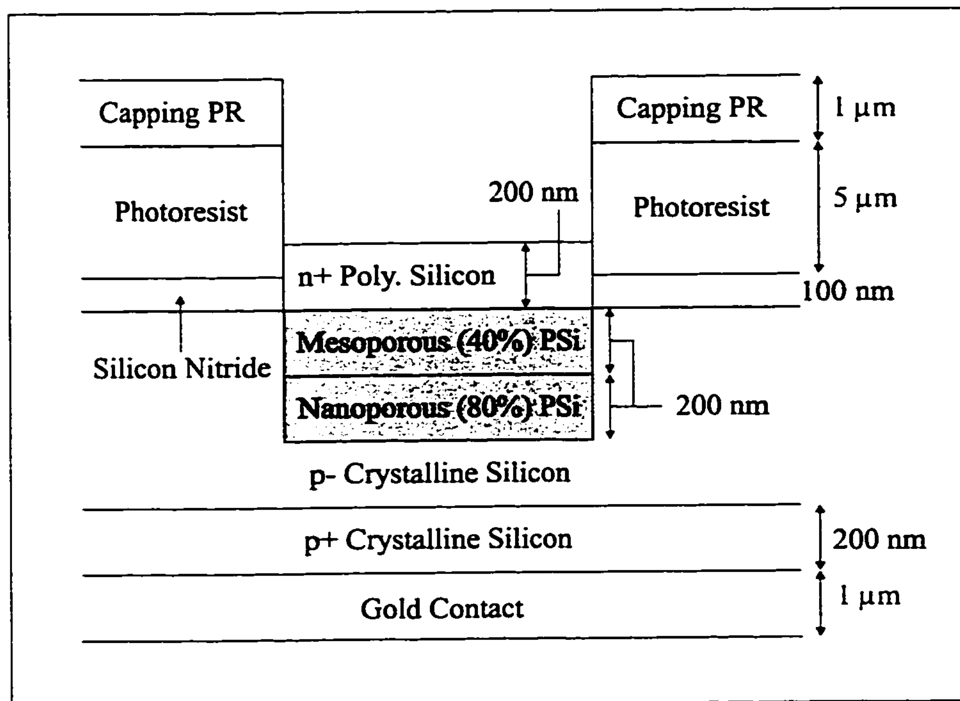

Figure 4.38 Structure of 'Dot' devices. This kind of structure is eventually intended to yield PSi LEDs.

Fig. 4.38 shows a schematic diagram of one 'dot', among many, forming part of a series of devices. While similar in construction to the solar cell of Fig. 4.35 its purpose was quite different. The 'dot' structure was produced using the techniques described by S.P. Duttagupta[29] and consists of several layers: a top n^- polycrystalline silicon layer which acts as a good top contact, a mesoporous (40% porosity) and a nanoporous (80% porosity) PSi layer to give a combination of good electrical and optical properties, a p^- silicon substrate, and a

thin p^- layer (back surface field) followed by a gold back contact. Starting with a p^- silicon wafer a trilayer mask consisting of silicon nitride, photoresist, and capping photoresist was deposited using standard photolithographic methods[29]. The trilayer mask was found to produce an optimum isolation barrier to the anodization process. The exposed regions were subjected to ion implantation to produce a 0.2 μm thick p^- layer. The back side of the wafer was also ion implanted to produce p^- which was followed by a 1 μm thick gold contact. The mask side of the wafer was then anodically etched in HF:ethanol (1:1) with a 10 mA/cm^2 current density for several minutes in order to create a ~ 0.5 μm layer of PSi. The p^- layer became mesoporous while the p^- layer became nanoporous PSi. The last step in creating the 'dot' was to deposit 0.2 μm of n^- polycrystalline silicon via CVD. The imaging goal in this case was to prove the 'dots' contained nanoporous silicon, and that the dots were indeed devices, hence PL and OBIC imaging respectively. From the Rochester group's point of view, achieving this goal was one of the steps necessary for the eventual production of PSi LEDs. Efficient (> 0.1%) PSi LEDs are difficult to make. Some reasons for this are[23]:

1) The mechanisms of carrier injection are possibly inefficient and not well understood.
2) The semitransparent metal contacts absorb part of the luminescence.
3) The most important reason is that it is extremely difficult to make a good contact over a large microscopic surface area. While light can come in 'contact' with all of a PSi specimen, this is not true of a physical contact.

Fig. 4.39a shows a RL (488 nm), zoom 1 (4 x 4 mm), non-confocal image taken with a 0.14 NA microscope objective. The black rectangle enclosing a series of black dots have the structure described in Fig. 4.38 <u>without</u> the n^- polycrystalline silicon layer. Removing the top polycrystalline silicon layer allows the PSi layers to be imaged, which appears black in RL. Fig. 4.39b shows the same specimen imaged in non-confocal PL (488 nm excitation, > 550 nm emission). This image conclusively shows that the 'dot' devices contain nanoporous LEPSi. Fig. 4.39c shows a RL (647 nm), zoom 1 (4 x 4 mm), non-confocal image taken with a 0.14 NA objective. The rectangle and dots in this case have the same structure described in Fig. 4.38. The top polycrystalline silicon layer is highly reflective and appears white with RL in relation to the surrounding photoresist.

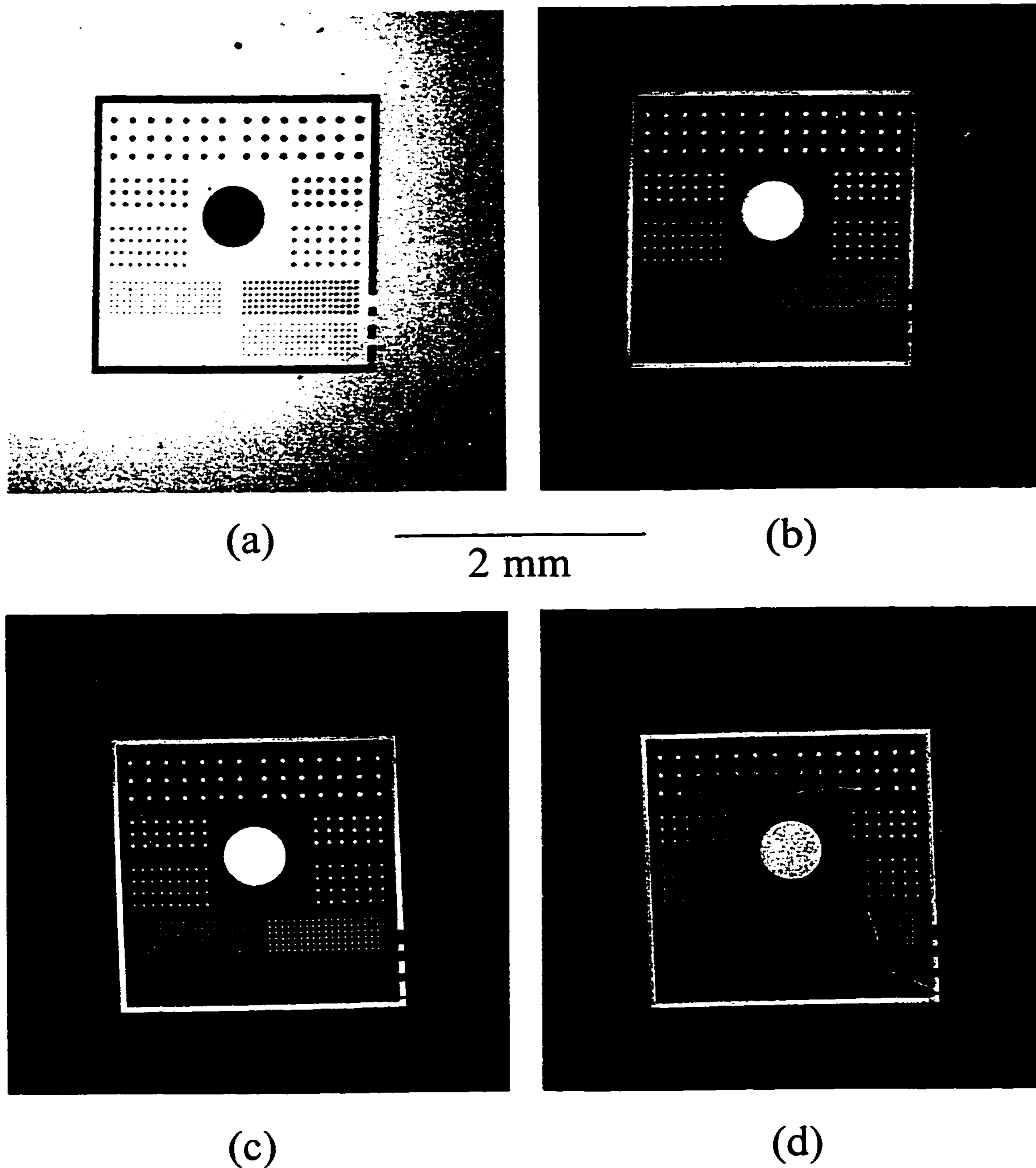

Figure 4.39 (a) RL image (488 nm) of a series of 'Dot' devices. The top polycrystalline silicon layer of Fig. 4.38 has been removed to expose the PSi layers hence the dots appear black in RL. (b) PL image (488 nm excitation, > 550 nm emission) of the same area. The existence of PL proves that there is a nanoporous layer in the devices. (c) RL image (647 nm) of the devices as shown in Fig. 4.38. The top polycrystalline layer reflects strongly with respect to the photoresist and therefore the dots appear white. (d) OBIC image of the same devices proving that they are indeed viable devices.

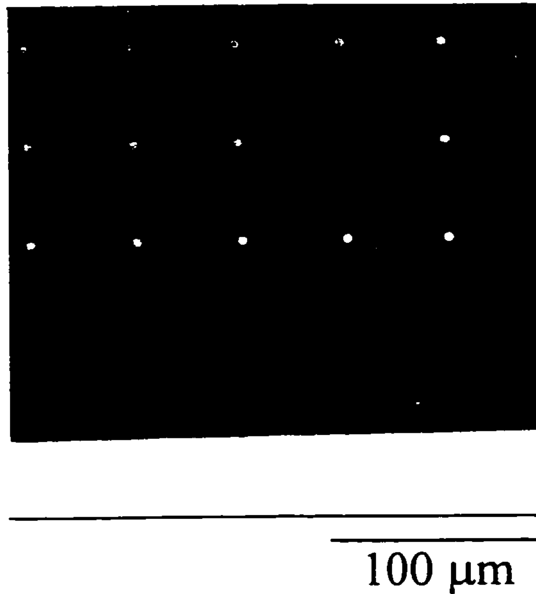

Figure 4.40 OBIC (647 nm) image of the 5 μm diameter devices from Fig. 4.38.

Fig. 4.39d shows the same specimen imaged in OBIC (647 nm) where a very thin layer of gold was sputtered over the devices in order to create a common, semitransparent contact such that all the devices were connected in parallel. The gold layer was not of optimum quality and in general caused a large amount of scattering. Scratches on the gold surface caused so much scattering that they appeared in the OBIC image due to light collection by the devices. This, in addition to pickup and imaging problems, required the use of a small reverse bias and a DC current offset. Fig. 4.39d clearly shows the dots and rectangle structures to be devices producing a measurable photocurrent. The smallest dots, hence the smallest devices in the structures of Fig. 4.39 were 5 μm in diameter. At the time of their production these represented the smallest PSi devices manufactured to date. Fig. 4.40 shows an OBIC (647 nm) image taken at zoom 4 (250 x 250 μm) with a 0.42 NA objective. The 5 μm dots are clearly resolved verifying the successful production of 5 μm PSi devices in addition to demonstrating 5 μm OBIC resolution on the cslm.

4.3 Summary and Discussion

This chapter has focused on two materials research applications: solar cells and a novel material, porous silicon (PSi). In general, a large part of UW-CMG research efforts have been dedicated to the development of applications for the MACROscope and cslM/m. It is clear that without applications the cslM/m stagnates as a useful instrument. Focusing on real applications is crucial to determining the faults and attributes of the cslM/m. Many of the ideas for current and future developments of the cslM/m came about solving problems encountered during the imaging of many specimens. For example, the unitary telescope problem was discovered, in part, due to the inability to image a highly reflective PSi specimen.

The first part of this chapter deals with solar cells. A brief introduction is given to solar cells and their characterization in addition to an introduction to OBIC imaging. A series of RL, PL and OBIC are used to highlight the various capabilities of the cslM/m:

1) An OBIC image of four $CdS/CuInSe_2$ thin film solar cells connected in parallel demonstrated the macroscopic capability (up to 7.5 x 7.5 cm scans) of the cslM/m as well as showing how the cslM/m can be used as a quality control instrument by comparing simultaneously imaged solar cells to a standard or control.
2) In OBIC, the telecentric condition can be somewhat relaxed to accommodate small lens aperture, wide angle, and large field of view imaging. Images from a 10x10 cm polycrystalline silicon solar cell illustrate this. The combined confocal RL and OBIC capabilities of the cslm were illustrated by showing a profile image and an OBIC image of two grains and their interface.
3) The MACROscope's full capabilities were explored with a $CdZnS/CuInSe_2$ thin film solar cell from the Institute of Energy Conversion in Delaware. RL, PL, and multiwavelength OBIC images were shown as well as an I-V and a spectral response curve.

Two limitations in OBIC were investigated:

1) Solar cell time response. This is easily spotted and avoided by slowing the scan speed or applying a small reverse bias.

2) OBIC nonlinear response to beam intensity. This can be a very serious problem which causes a decrease in contrast. Minimizing beam power is a good start but the only way to completely avoid this is to plot OBIC signal vs. beam power for <u>every</u> cell or groups of cells. Testing every cell is of course impractical, however, at least a database for a wide variety of cells should be generated.

The last part of the first section deals with EBIC and its advantage and disadvantages with respect to OBIC. Both systems have equal resolving power except in special situations such as shallow junctions and side-on imaging where EBIC proves superior. OBIC offers several advantages and techniques such as multiwavelength analysis not available to EBIC.

The second part of this chapter is dedicated to PSi, a luminescent form of silicon which, if successfully developed, will revolutionize the optoelectronics industry. Solar cells in the first part of this chapter were used primarily to define the cslM/m's capabilities, limitations, future improvements, etc., and in a sense characterize the cslM/m. While this is also true of PSi, the collaboration with P.M. Fauchet's research group at the University of Rochester also allowed the cslM/m and UW-CMG to participate in the characterization of many interesting PSi materials and devices. After a brief introduction to PSi a series of macroscopic and microscopic, RL and PL, confocal and non-confocal images of various LEPSi materials were shown. Uniformity and morphology at various magnifications were studied. Low energy/dose RIE pre-anodization treatments were found to enhance PL in LEPSi. Lateral etching on 'protected' amorphized regions was found to occur. This was determined by studying 3-D confocal RL reconstructions in combination with PL images. A point spectrum as well as a x-λ image of a LEPSi specimen was shown as well as evidence of bleaching and optically induced passivation.

In the device section of this part of the chapter OBIC was used to show the true nature of a first attempt at making a PSi solar cell. The second set of attempts at making a solar cell by

the Rochester group resulted in a 6.0% efficiency polycrystalline silicon/PSi solar cell. OBIC imaging showed the cell to be uniform. While the PSi junction is responsible for photocurrents when the wavelength of incident light is shorter than ~ 650 nm, the contribution beyond 650 nm by the PSi junction is unclear. The last device to be imaged consisted of a series of lithographically created dots with a silicon-PSi, n-p junction structure. PL and OBIC imaging on the cslm successfully proved that the devices contained nanoporous LEPSi in addition to generating a photocurrent.

This thesis has limited the cslM/m to semiconductor applications. UW-CMG has used the cslM/m to image a much wider variety of specimens such as DNA gels, protein gels, fingerprints, and large insects to name a few.

Several new contributions were made in the field of scanning microscopy, solar cell imaging, and porous silicon imaging:

1) The MACROscope-Microscope instruments were shown to provide macroscopic and microscopic confocal images of various solar and PSi specimens using RL, PL, and OBIC.
2) The first confocal images of LEPSi were obtained concurrent with Nassiopoulos[34].
3) Imaging evidence of lateral etching and PL was shown for two PSi specimens.
4) A PSi solar cell and a PSi device were characterized using RL, PL, and OBIC.

REFERENCES

[1] K.M. Beesley, S. Damaskinos, and A.E. Dixon, J. Forensic Sciences **40** (1995) 10.

[2] E.K. Seto, S. Damaskinos, A.E. Dixon, W.L. Diehl-Jones, and C.A. Mandato, Electrophoresis **16** (1995) 934.

[3] S. Damaskinos, A.E. Dixon, K.A. Ellis, and W.L. Diehl-Jones, Micron, **26** (1995) 493.

[4] A.E. Dixon, S. Damaskinos, A.C. Ribes, and K.M. Beesley, J. Microscopy **3** (1995) 178.

[5] A.C. Ribes, S. Damaskinos, H.F. Tiedje, A.E. Dixon, D.E. Brodie, S.P. Duttagupta, and P.M. Fauchet, Material Research Society Symposium Proceedings, **426** (1996) 581.

[6] A.C. Ribes, H.F. Tiedje, S. Damaskinos, A.E. Dixon, and D.E. Brodie, Solar Energy Materials and Solar Cells **44** (1996) 439.

[7] A.C. Ribes, S. Damaskinos, A.E. Dixon, K.A. Ellis, S.P. Duttagupta, and P.M. Fauchet, Progress in Surface Science, **50** (1995) 295.

[8] A.C. Ribes, S. Damaskinos, A.E. Dixon, G.E. Carver, C. Peng, P.M. Fauchet, T.K. Sham, and I. Coulthard, Applied Physics Letters, **66** (1995) 2321.

[9] B.G. Streetman, Solid State Electronic Devices, 3rd Edition, (Prentice-Hall, Englewood Cliffs, New Jersey, 1990).

[10] M.A. Green, Solar Cells, (Prentice-Hall, Englewood Cliffs, New Jersey, 1982).

[11] R.W. Birkmire, L.C. DiNetta, P.G. Lasswell, J.D. Meakin, and J.E. Phillips, Solar Cells **16** (1986) 419.

[12] J.W. Pawley (Editor), Handbook of Biological Confocal Microscopy, 2nd Edition, (Plenum, New York, 1995), Chapters 23, 24.

[13] S. Damaskinos, Solar Cells **26** (1989) 151.

[14] H.F. Tiedje, Ph.D. Thesis, 1997, Physics Department, University of Waterloo, Waterloo, Canada.

[15] H.J. Leamy, Journal of Applied Physics, **53** (1983) R51.

[16] R.J. Matson, Scanning Microscopy Supplement 7, Pages 243 - 251, 1993.

[17] D.B. Holt and D.C. Joy (Editors), SEM Microcharacterization of Semiconductors, (Academic Press, New York, 1989).

[18] A. Uhlir, The Bell System Technical Journal, **35** (1956) 333.

[19] C. Pickering, M.I.J. Beale, D.J. Robbins, P.J. Pearson, and R. Greef, Journal of Physics C **17** (1984) 6535.

[20] L.T. Canham, Applied Physics Letters, **57** (1990) 1046.

[21] R.J. Matson, Scanning Microscopy Supplement 7, Pages 243 - 251, 1993.

[22] R.L. Smith and S.P. Collins, Journal of Applied Physics, **71** (1992) R1.

[23] P.M. Fauchet, L. Tsybeskov, C. Peng, S.P. Duttagupta, J. von Behren, Y. Kostoulas, J.M. Vandyshev, and K.D. Hirschman, IEEE Journal of Selected Topics in Quantum Electronics, **1** (1995) 1126.

[24] B. Hamilton, Semicond. Sci. Technol., **10** (1995) 1187.

[25] R.A. Serway, C.J. Moses, C.A. Moyer, Modern Physics, (Saunders College Publishing, New York, 1989), Chapter 5.

[26] Y. Kanemitsu, Physics Reports, **263** (1995) 1.

[27] J. Kocka, I. Pelant, and A. Fejfar, Journal of Non-Crystalline Solids **198** (1996) 857.

[28] K.H. Jung, S. Shih, and D.L. Kwong, Journal of the Electrochemical Society, **140** (1993) 3046.

[29] S.P. Duttagupta, C. Peng, P.M. Fauchet, S.K. Kurinec, T.N. Blanton, J.Vac. Sci. Technol. B. **13** (1995) 1.

[30] J.W. Pawley (Editor), Handbook of Biological Confocal Microscopy, 2nd Edition, (Plenum, New York, 1995), Chapter 4.

[31] J.W. Bowron, Ph.D. Thesis, 1993, Physics Department, University of Waterloo, Waterloo, Canada, Chapter 2.

[32] J.W. Pawley (Editor), Handbook of Biological Confocal Microscopy, 2nd Edition, (Plenum, New York, 1995), Chapter 3.

[33] P. Menna, G. DiFrancia, V. LaFerrara, Solar Energy Materials and Solar Cells, **37** (1995) 13.

[34] A.G. Nassiopoulos, S. Grigoropoulos, L.T. Canham, A. Halimaoui, I. Berbezier, E. Godolides, D. Papadimitrious, Thin Solid Films, **255**(1995)329.

CHAPTER 5

QUANTITATIVE LENS ANALYSIS AND DESIGN WITH CODE V

Optical systems can be characterized by determining their total aberrations and the consequent effects on image quality. This can be done by analyzing the optical system as a whole by determining optical aberrations for each individual component via geometrical ray tracing and diffraction analysis. Such analysis is very calculation intensive hence the use of a computer is essential. UW-CMG has employed CODE V (version 8.10A by Optical Research Associates), a comprehensive program for the design and analysis of optical systems. In the past, CODE V's complexity required the use of VAX or SUN workstations but recently it has been possible to run CODE V on 486 or Pentium based microcomputers which has made lens analysis and design accessible to a much broader population.

CODE V was used to analyze the quality of the unitary telescopes on the cslm. CODE V was also used to aid in the design of an all-reflecting (mirrors instead of lenses) telescope. This telescope will be shown to be superior to the existing refracting telescope. An innovative optical relay consisting of telescope eyepieces is also analyzed and, in most respects, is shown to be superior to the above two telescopes. A series of low-cost ultraviolet (UV) objectives with a 2 x 2 cm field of view were designed. In addition, an all-reflecting detector arm and a 30X beam expander were designed and analyzed on CODE V. The ultimate goal of all the above designs/analyses was to suggest possible ways to improve the cslM/m. A push towards all-reflective optics was initiated in order to make the cslM/m as wavelength insensitive and UV/IR compatible as possible.

Before presenting analyses and designs for the various optical components, a review of the primary chromatic and Seidel aberrations is given. A clear understanding of lens aberrations is essential before embarking upon lens analysis and design. A brief set of diagrams and definitions will be given to illustrate how CODE V deals with optical systems. The first lens

analyzed will be a simple achromatic doublet where CODE V analysis options such as the point spread function and astigmatic and spherical aberration field curves are introduced.

Several new contributions were made in this chapter: the effects of small tilts in spherical mirrors was studied with respect to beam expanders and detector arm optics. An analysis of aberrations was made of the existing unitary telescope consisting of achromats, and a reflecting telescope made up of off-axis parabolic mirrors. An optical relay made up of telescope eyepieces was also analyzed.

5.1 Seidel Aberrations

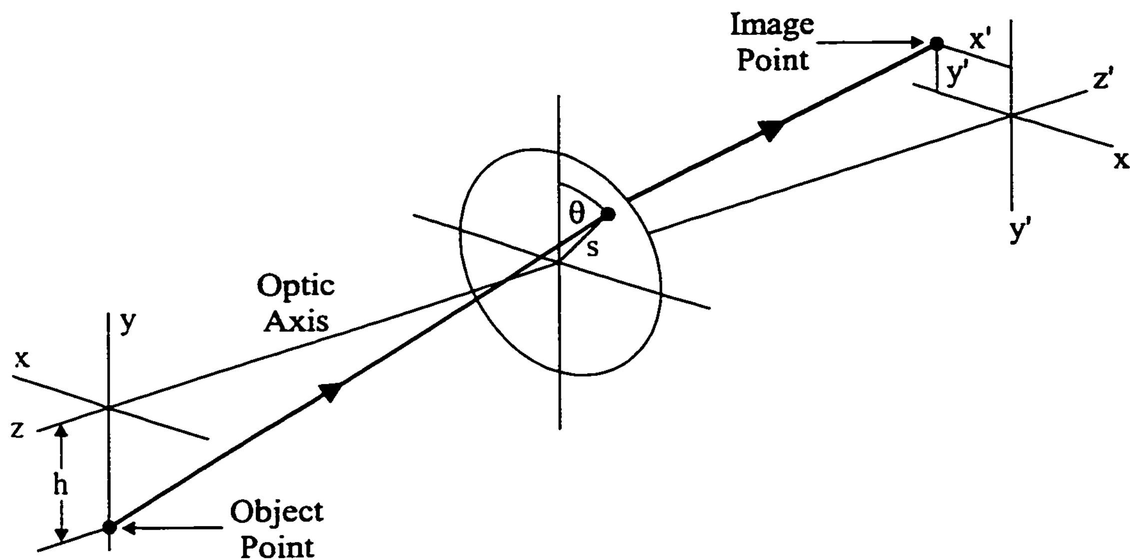

Figure 5.1 Schematic diagram illustrating the coordinate system used in equations 5.1 and 5.2. A ray from the object point y = h passes through the aperture at (s, θ) and intersects the image surface at (x′, y′). Figure taken from Smith[1].

The optical system in Fig. 5.1 (taken from Smith[1]) has symmetry about the optical axis. A ray that starts from an object point at $y = h$ will pass through the system aperture at a point (s,θ) and will intersect the image plane at (x',y').

It can be shown[2] that the coordinates x′ and y′ can be written as follows:

$$
\begin{aligned}
y' = {} & A_1 s\cos\theta + A_2 h \\
& + B_1 s^3\cos\theta + B_2 s^2 h(2+\cos 2\theta) + (3B_3 + B_4)sh^2\cos\theta + B_5 h^3 \\
& + C_1 s^5\cos\theta + \cdots
\end{aligned}
\qquad (5.1)
$$

$$
\begin{aligned}
x' = {} & A_1 s\sin\theta \\
& + B_1 s^3\sin\theta + B_2 s^2 h\sin 2\theta + (B_3 + B_4)sh^2\sin\theta \\
& + C_1 s^5\sin\theta + \cdots
\end{aligned}
\qquad (5.2)
$$

where A_n, B_n, etc. are constants.

For the B terms, the exponents total 3, as in s^3, s^2h, etc. They are therefore referred to as third order terms. Similarly, the A and C terms are referred to as first and fifth order terms respectively. The A terms are related to paraxial or small angle theory[3]. All angles made by rays in this approximation can be set equal to their sines and tangents. A_2 is the magnification and A_1 is a measure of the distance from the paraxial focus to the image plane. All the other terms in Equations 5.1 and 5.2 represent the distances by which the ray misses the ideal image point, as described by paraxial imaging theory, and are called transverse aberrations. The B terms are called the third-order, or primary, or Seidel aberrations. B_1 is spherical aberration, B_2 is coma, B_3 is astigmatism, B_4 is Petzval field curvature, and B_5 is distortion. Each of these monochromatic or Seidel aberrations will be defined in the sections that follow. Their characteristics and effects on the appearance of the image will also be discussed.

5.1.1 Paraxial Image - The Airy Disk

If a collimated beam of light enters an ideal lens with no aberrations, then geometrical ray tracing predicts a dimensionless point image at the paraxial focal plane. When diffraction is included, the result is the familiar Airy disk shown in Fig. 5.2a (modified from Hecht[4]). In order to see the outer rings, the central spot in Fig. 5.2a has been overexposed. Fig. 5.2b shows a 3-D intensity profile of the Airy disk where height represents intensity. The peak intensity for the first ring represents 1.75% the peak intensity of the central spot. A real lens with aberrations will distort and enlarge the Airy disk pattern.

Figure 5.2 (a) The Airy disk. The central spot has been overexposed in order to make visible the surrounding disks. (b) The Airy disk pattern shown in 3D where height represents intensity. The maximum intensity on the first ring represents only 1.75% the intensity for the central peak. Figures modified from Hecht[4].

5.1.2 Spherical Aberration

Spherical aberration is the change of focus with aperture. Fig. 5.3 shows an example of undercorrected spherical aberration in which the focal power of the lens increases with increasing distance from the optic axis. The central rays, which are very close to the optic axis (paraxial rays), will focus onto the paraxial image plane while rays at height y will focus closer to the lens. The distance between the paraxial focus point and the axial intersection for ray R is called longitudinal spherical aberration (L·SA). Spherical aberration increases rapidly with aperture where L·SA, for example, is proportional to y^2. Transverse spherical aberration (T·SA) is the distance from the paraxial focal point to the intersection of ray R with the paraxial image plane. It is related to L·SA via the following formula:

$$T \cdot SA = -(L \cdot SA) \cdot TAN(U'_R) \quad \textbf{(5.3)}$$

Spherical aberration with a negative sign is called undercorrected spherical and is generally associated with positive lens elements while a positive sign indicates overcorrected spherical which is associated with diverging elements.

Fig. 5.4 (modified from Born and Wolf[5]) shows the effect that varying degrees of spherical aberration has on the Airy disk.

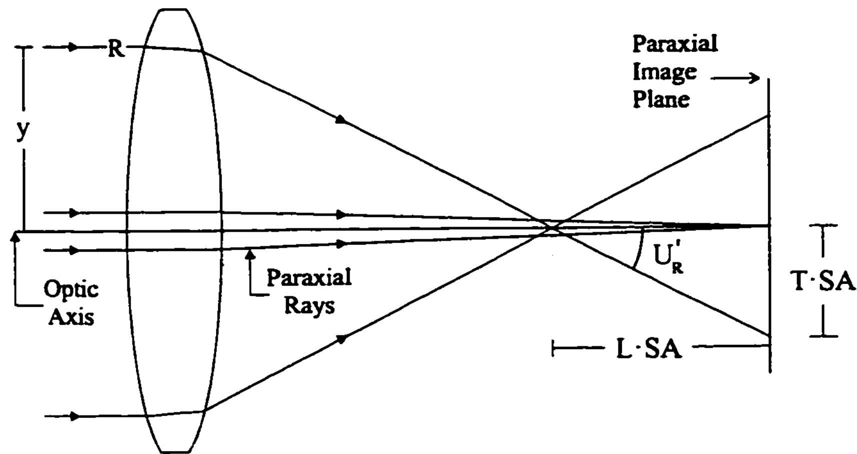

Figure 5.3 Undercorrected or negative spherical aberration. The focal power of the lens increases for rays far from the optic axis.

Figure 5.4 The effect of spherical aberration on the Airy disk. As spherical aberration increases the outer rings grow in number and intensity, while the central spot decreases in intensity. Figure modified from Born and Wolf[5].

As spherical aberration increases the rings surrounding the central spot in the Airy disk increase in number and intensity, while the central spot decreases in intensity. Note that spherical aberration is an axial aberration. It is the only Seidel aberration which does not go to zero when the field angle (the angle ray R makes with the optic axis before entering the lens) approaches zero. For a given f-number, the amount of spherical aberration in a simple lens is a function of object position and lens shape. It is also important to distinguish between potential and actual spherical aberration. The lens in Fig. 5.3 has a large amount of negative spherical aberration when its full aperture is used. If, however, a thin laser beam is used (a common situation in this thesis) then the effective aperture is reduced along with the actual spherical aberration.

5.1.3 Coma

Coma is the change of magnification with aperture. When a series of rays are incident on a lens with coma, the rays passing through the edge portions of the lens are imaged at a different height than those passing through the central portion. In Fig. 5.5, the vertical distance from ray P to the intersection of ray A and B is called the tangential coma (TCO). Fig. 5.6 shows the relationship between the position at which rays pass through the lens aperture (a) and the resultant locations occupied on the coma patch (b). Fig. 5.6a shows a head-on view of the lens aperture with the ray positions indicated by the letters.

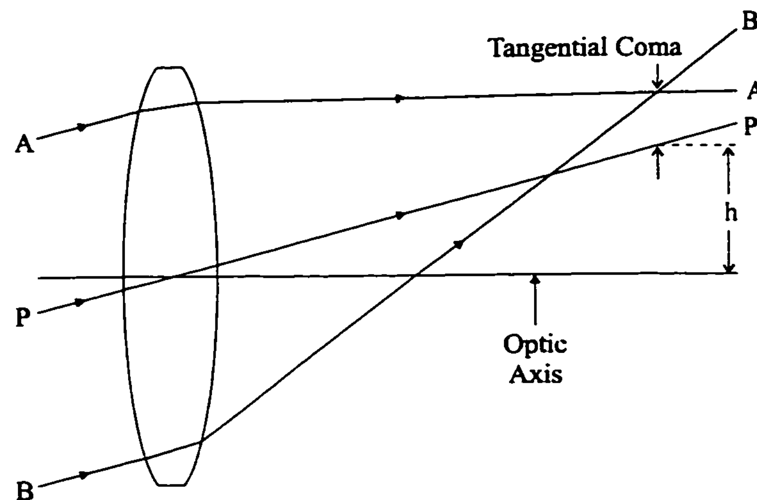

Figure 5.5 Coma is the variation of magnification with aperture. The vertical distance between the intersection of rays A and B, and the chief ray P is called the tangential coma.

The resultant image is shown in Fig. 5.6b (Smith[1], p64). Note the rays that formed a circle in the aperture also form a circle in the coma patch but with rays going around the image circle twice. The comatic image can be viewed as being made up of a series of different sized circles arranged tangent to a 60° angle with the size of the image circle proportional to the square of the diameter of the aperture circle. In Fig. 5.6b, the distance from P to AB is the tangential coma while the distance from P to CD is called the sagittal coma which is one third of TCO. Coma varies with the shape of the lens and with the position of any limiting apertures. Fig. 5.7 (modified from Born and Wolf[6]) shows the effect coma has on the Airy disk. As coma increases, the image appears more and more comet shaped.

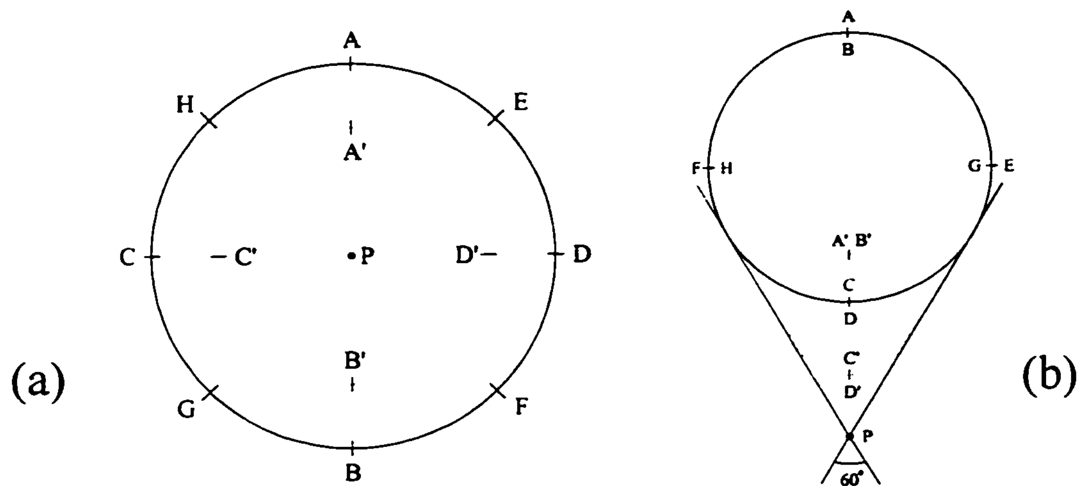

Figure 5.6 (a) The relationship between the positions of rays in the lens aperture and (b) their positions in the coma patch. The diameters of the circles in the image are proportional to the square of the diameters in the aperture.

Figure 5.7 The effect of coma on the Airy disk. Figure modified from Born and Wolf[6].

5.1.4 Astigmatism and Petzval Field Curvature

In order to understand astigmatism, the tangential and sagittal planes must be defined. When a lens system is represented by a drawing of its axial sections, rays which lie in the plane of the drawing are called meridional or tangential rays. Rays A, B and P in Fig. 5.5 are tangential rays. The plane through the optic axis containing the principal or chief ray P (the oblique ray through the center of the aperture) is called the tangential or meridional plane. The plane passing through the chief ray and perpendicular to the meridional plan is called the sagittal plane. In Fig. 5.6, rays A, A′ , B and B′ are tangential rays while rays C, C′, D and D′ are sagittal rays.

Astigmatism occurs when the tangential and sagittal images do not coincide. When astigmatism is present, the image of a point will take the form of two separate lines as shown in Fig. 5.8 (taken from Hecht[7]). The image of a point source formed by a fan of rays in the tangential plane will be a line lying in the sagittal plane. Thus the lens has a tangential focal length F_T. Similarly, rays of the sagittal fan will form a line image at F_S in the tangential plane. The image between the astigmatic foci will be elliptical or circular in shape.

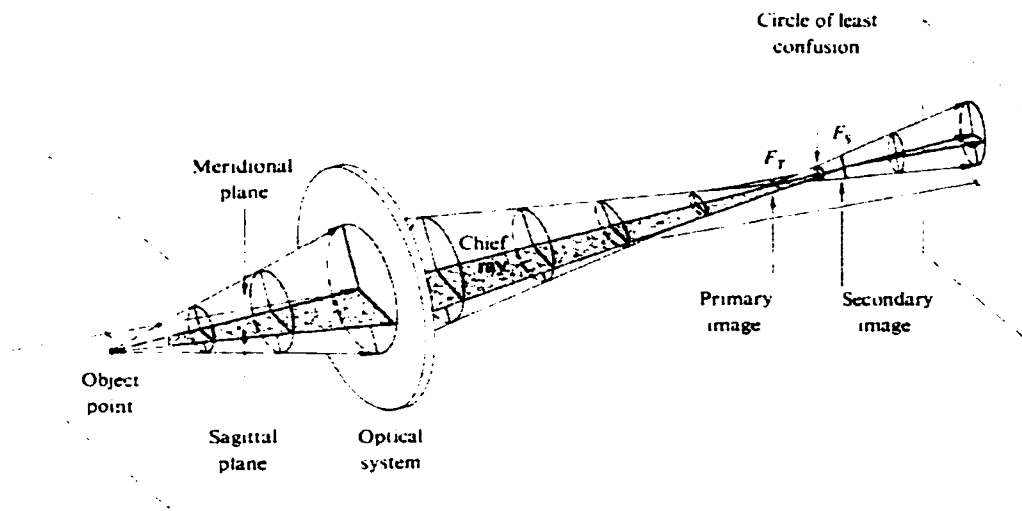

Figure 5.8 A lens with astigmatism will produce two line images of an off-axis point object at the tangential (F_T) and sagittal (F_S) focal surfaces. Figure taken from Hecht[7].

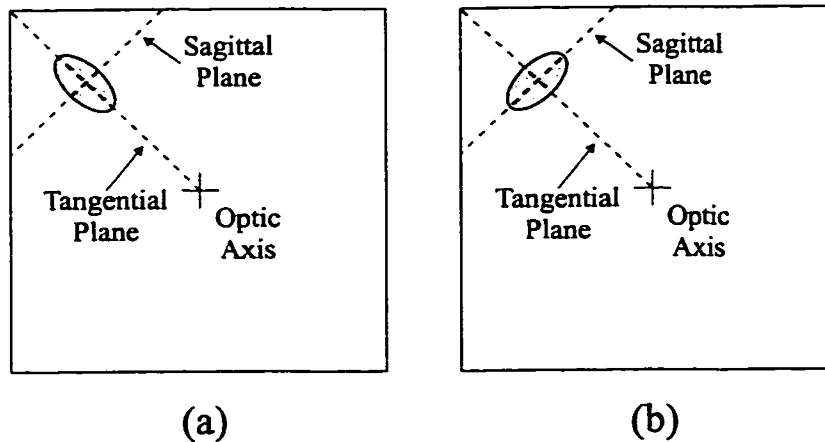

Figure 5.9 (a) The image spot is elongated radially when the image screen is placed in between the circle of least confusion and F_S in Fig. 5.8. (b) Similarly the image spot is elongated tangential to the radial direction when the image screen is placed in between the circle of least confusion and F_T.

The least aberrated image of the object point can be obtained at the location where the image is a circular blur, known as the circle of least confusion, which is found in between F_T and F_S. As the object is moved further off-axis the astigmatic difference increases which causes the circle of least confusion to increase in size. If an image screen is placed at the circle of least confusion, in Fig. 5.8, and is moved towards the secondary image plane (F_S) the image spot will become elliptical with the major axis in the tangential plane as shown by Fig. 5.9a. Notice that as the image screen reaches F_S, the image deforms into a line which always points radially regardless of the object point position. With the image screen at the paraxial image position the image spot will appear radially elongated as in Fig. 5.9a. Fig. 5.9b shows how the image spot becomes elliptical with the major axis in the sagittal plane when the image screen is in between the circle of least confusion and F_T. The line at F_T is always perpendicular to the radial line at F_S.

Most simple lenses have associated with them a basic field curvature called the Petzval curvature dependent upon the index of refraction and the surface curvatures of the lens. If no astigmatism is present then the sagittal and tangential image surfaces will coincide with the Petzval surface. When primary astigmatism is present then the tangential image surface lies three times as far from the Petzval surface as the sagittal surface as shown in Fig. 5.10.

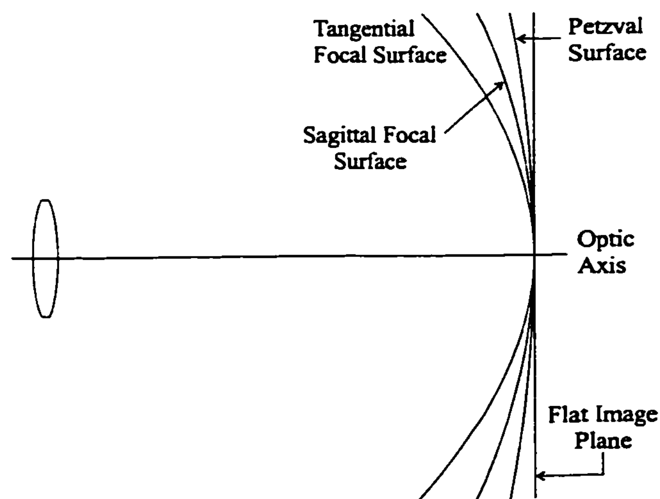

Figure 5.10 Field curvatures associated with a simple positive lens. A lens with no astigmatism will have the tangential and sagittal surfaces coinciding on the Petzval surface.

All of these surfaces are parabolic in shape, however, small field curvatures can be approximated by using circular sections. Fig. 5.11 shows several ways of quantifying astigmatism or field curvature. As mentioned above, the field curvature can be approximated by a circular shape hence it will have a radius of curvature, r, associated with it. CODE V expresses Petzval field curvature as PTZ = 1/r. Longitudinal astigmatism is the horizontal distance from the flat image plane to the astigmatic image plane. In CODE V, the 3rd order transverse astigmatism is related to the longitudinal astigmatism by a quantity known as the image space f-number or just f_{no}:

$$(f_{no})_I = \frac{1}{2U'_R} \quad \textbf{(5.4)}$$

where U'_R is the same angle found in Fig. 5.3. From Fig. 5.11, it can be seen that

Transverse Astigmatism = TAN(U'_R) [Longitudinal Astigmatism] **(5.5)**

When U'_R is small (which CODE V assumes for 3rd order aberrations), then TAN(U'_R) is approximately equal to U'_R and therefore

Longitudinal Astigmatism = 2 $(f_{no})_I$ [Transverse Astigmatism] **(5.6)**

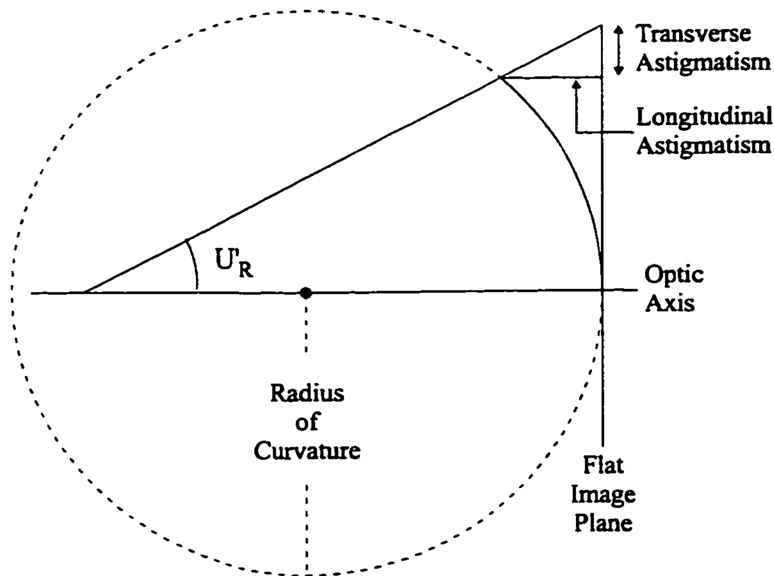

Figure 5.11 Field curvatures can be approximated by a circular section of radius r. Both astigmatism and Petzval can be measured as longitudinal or transverse deviations from a flat or paraxial image plane.

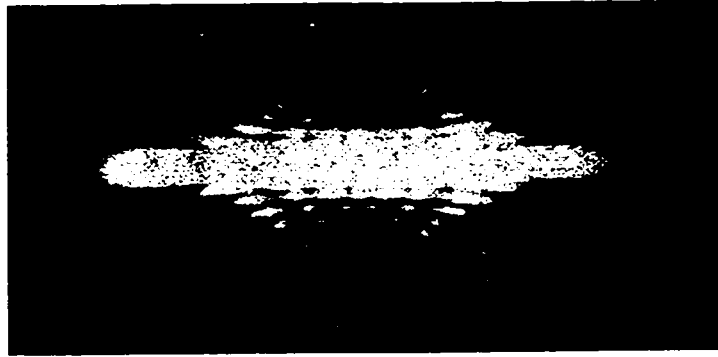

Figure 5.12 The effect of astigmatism on the Airy disk. Elliptical, elongated, and in some cases square-shaped images are classical signs of astigmatism. Figure modified from Born and Wolf[6].

Equation 5.6 applies equally well to tangential, sagittal and Petzval 3rd order quantities found in CODE V. Fig. 5.12 (modified from Born and Wolf[6]) shows the effect of astigmatism on the Airy disk. The pattern is elliptical in nature and in severe cases will exhibit a square or rectangular shape. For a simple lens with a fixed aperture the astigmatism is proportional to the image height squared divided by the focal length. When the tangential image is to the left of the sagittal image the astigmatism is negative or undercorrected as in Fig. 5.10. When the order is reversed, the astigmatism is positive or overcorrected. Positive lenses typically introduce negative astigmatism while diverging lenses introduce positive astigmatism.

5.1.5 Distortion

A lens is said to have distortion when the image of an off-axis point is formed farther or closer from the optic axis than the paraxial image height. Its effects can best be illustrated with a square object as shown in Fig. 5.13. When the image is displaced outwards from the correct position, this is called pincushion (positive) distortion. When the image is displaced inwards, this is barrel or negative distortion. The amount of distortion is the displacement of the image from the paraxial position which is expressed directly or as a percentage of the paraxial image height. Distortion usually increases as the cube of the image height hence the sides of the squares in Fig. 5.13 will experience less distortion (a factor of $2^{3/2}$) than the corners.

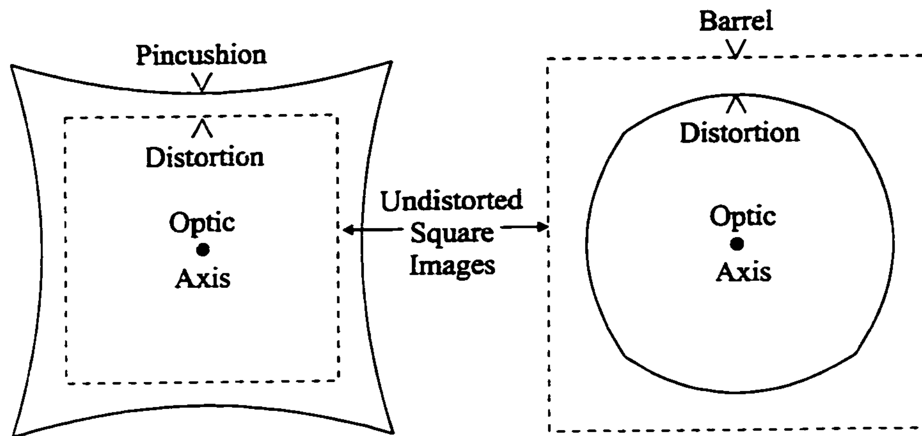

Figure 5.13 The amount of distortion varies with the cube of the distance from the axis, hence the sides of the images are curved.

5.2 Chromatic Aberrations

Chromatic aberrations exist because, for most materials, the index of refraction varies with wavelength. It is as if each wavelength 'sees' a different lens with its own particular focal length and magnification. Axial chromatic aberration is the longitudinal variation of focus with wavelength. In general, the index of refraction decreases as wavelength increases hence blue light will be focused more strongly than red light for a simple positive lens as shown in Fig. 5.14.

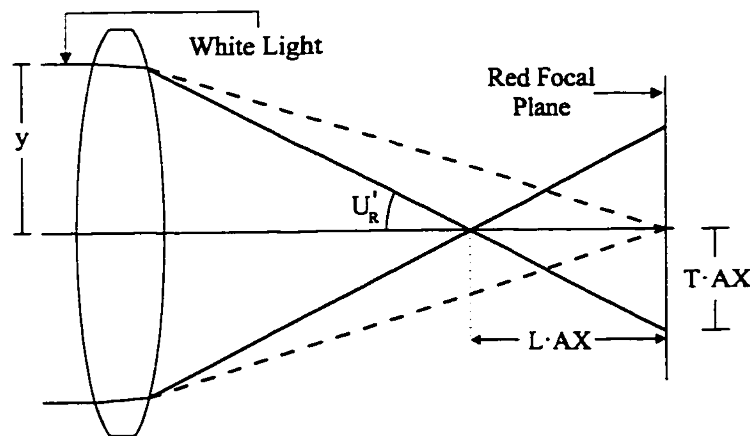

Figure 5.14 A simple positive lens will in general tend to have negative or undercorrected axial chromatic aberration. The solid blue ray will undergo a greater amount of refraction than the dashed red ray.

The distance along the axis between the two foci is the longitudinal axial chromatic aberration (L·AX) which in this case is negative or undercorrected. The transverse axial chromatic aberration is calculated the same way as with spherical aberration:

$$T{\cdot}AX = TAN(U'_R)[\, L{\cdot}AX] \qquad (5.7)$$

where U'_R is the angle between the reference wavelength marginal ray (in this case the outermost blue ray) and the optic axis. The image of an axial point in the presence of chromatic aberration is a central bright dot surrounded by a halo. For example, a focused red dot will have a yellowish halo surrounded, in turn, by a blue halo.

If a lens forms different size images for different wavelengths or spreads the image of an off-axis point into a rainbow, the difference between the image heights for different colours is called lateral colour aberration or chromatic difference in magnification. Fig. 5.15 shows a white light chief ray experiencing lateral colour aberration where the blue ray is refracted more than the red ray hence the blue image size is smaller than the red. Since each wavelength 'sees' a different lens, the Seidel aberrations will be slightly different for each wavelength.

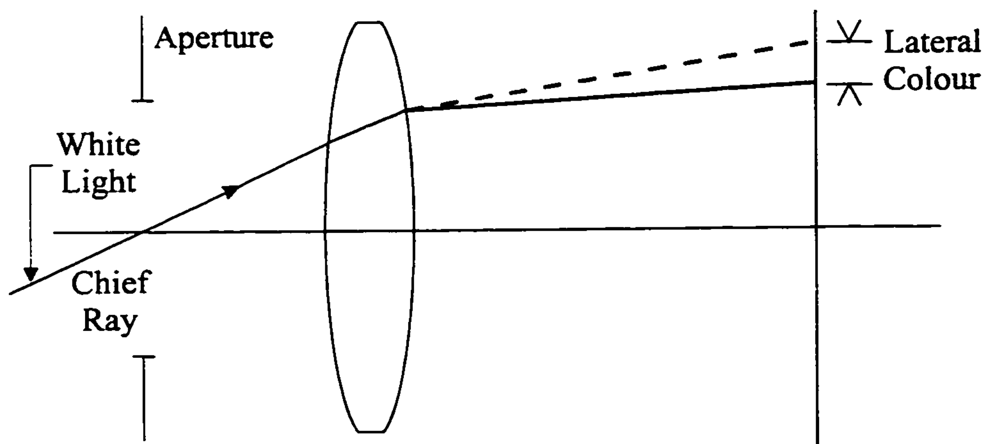

Figure 5.15 Lateral colour aberration occurs when a lens system forms images of different sizes for different wavelengths. The solid blue ray will experience more refraction than the dashed red ray.

5.3 Aberrations in Lens Systems

Two fundamental quantities encountered in CODE V are the entrance pupil diameter and the field angle. These quantities are equivalent to aperture size y and image height h. Table 5.1 (Smith[1], p74) shows the variations of the primary monochromatic and chromatic aberrations with y and h.

Aberration	vs. Aperture	vs. Field Size or Angle
Spherical (longitudinal)	y^2	—
Spherical (transverse)	y^3	—
Coma	y^2	h
Astigmatism and field curvature (long.)	—	h^2
Astigmatism and field curvature (transverse)	y	h^2
Distortion (linear)	—	h^3
Distortion (in percent)	—	h^2
Axial chromatic (transverse)	y	—
Lateral chromatic	—	h

Table 5.1 Primary aberrations as a function of aperture and field size. Table modified from Smith[1], p74.

For a confocal microscope to operate properly its optics must be well corrected for all aberrations. This is especially true for the objective lens. A microscope objective consists of many lens elements of different size, shape, and refractive index. Each lens in the system has been chosen to minimize all aberrations when in combination with the other components. An example of a simple lens design or optimization problem is the achromatic doublet as shown in Fig. 5.16. A cemented achromat consists of a low index positive lens (negative spherical and axial chromatic aberration) and a high index negative lens (positive spherical and axial chromatic). It can be shown[8] that this lens system has three independent variables which can be used to correct for spherical aberration, coma, and axial chromatic aberration. Unfortunately, very little can be done to correct for astigmatism and field curvature. More elements must be added to correct these aberrations. Although it is beyond the scope of this thesis to delve into the world of lens design, one lens design principle is worth mentioning, the symmetrical principle.

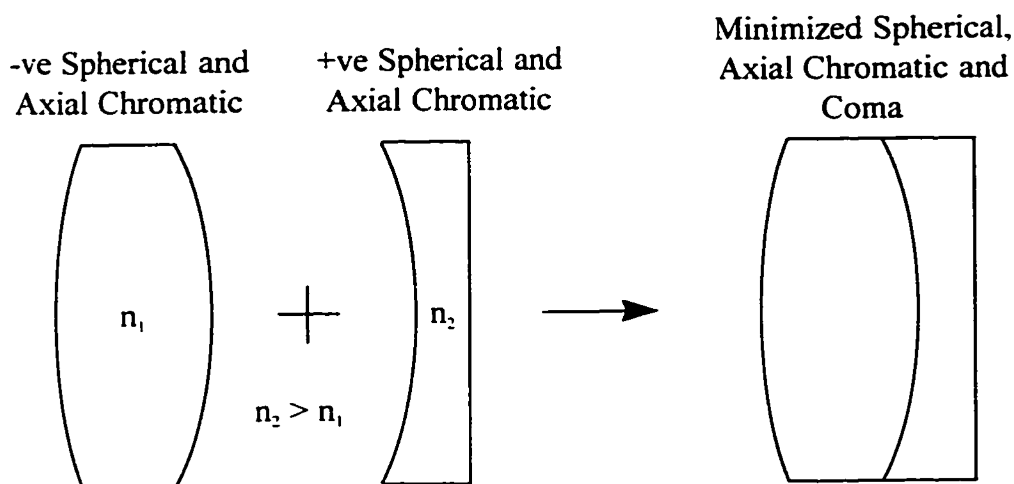

Figure 5.16 An achromat is constructed by combining positive and negative lens elements. By choosing the appropriate curvatures and materials, aberrations such as spherical, axial chromatic and coma can be minimized.

Simply stated, an optical system which is completely symmetrical will have coma, distortion, and lateral colour equal to zero. Complete symmetry implies unit magnification in addition to mirror images of the elements about the stop. Even systems that are nearly symmetric will exhibit some of these advantages. The unitary telescopes, which form part of the confocal scanning laser microscope, are clearly symmetrical systems.

5.4 CODE V Results Part I—Analysis and Design

CODE V was used to evaluate existing optical systems such as the unitary telescopes on the confocal scanning laser microscope (cslm). CODE V was also used to help design and evaluate an all-mirror telescope as well as low-cost UV objectives, a reflecting beam expander, and a reflecting detector arm. Before the results are given, some basic definitions of various quantities used in CODE V will be presented.

Fig. 5.17a depicts a typical thick lens. The lens contains two principal planes from which the various focal lengths can be determined. The front focal length (FFL) is the distance from the object focal point F_o to the first vertex V_1. Similarly, the back focal length (BFL) is the distance from V_2 to the image focal point F_i.

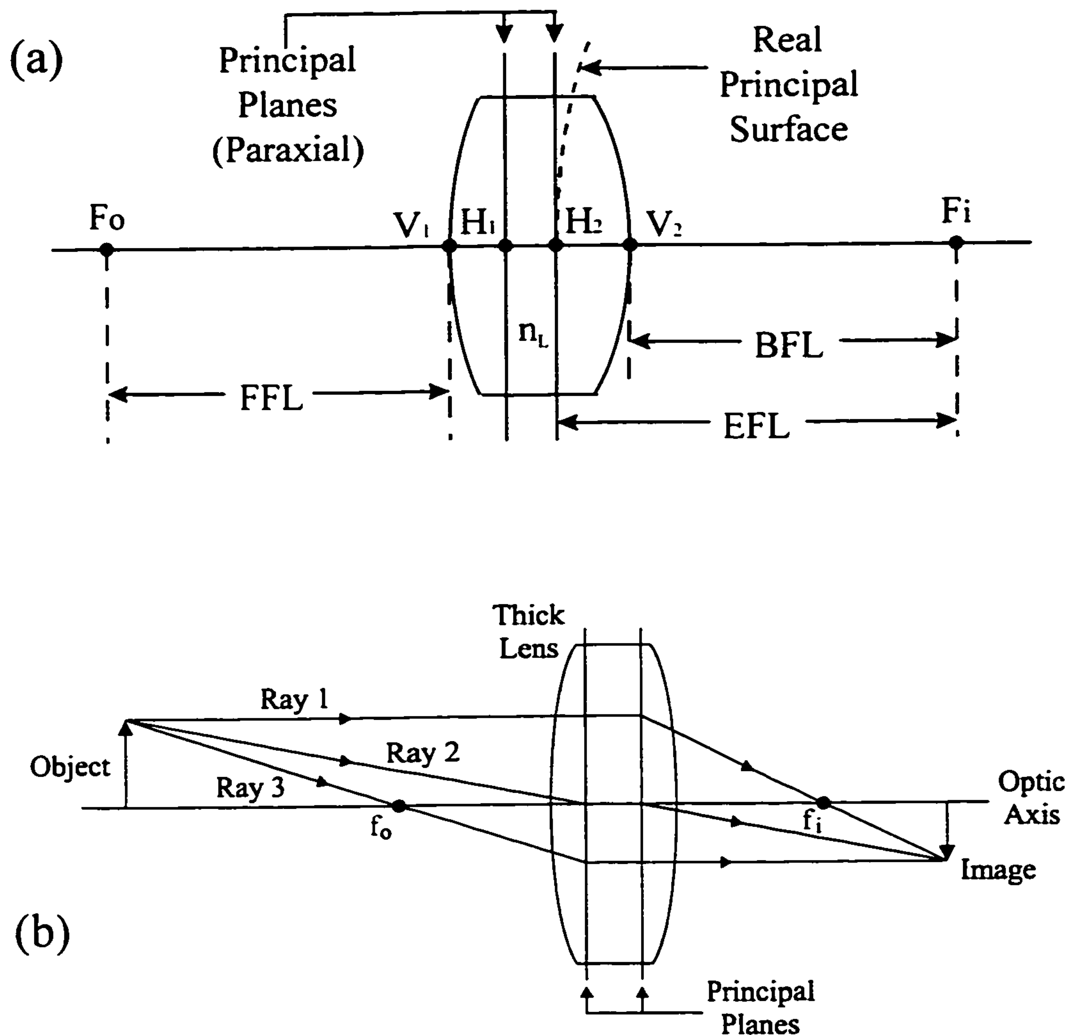

Figure 5.17 (a) Schematic diagram of a typical thick lens. Front, back, and effective focal length are key quantities in CODE V. (b) Graphical ray tracing is done the same as in Fig. 2.1a except a horizontal line is used to connect a ray from the first to the second principal plane.

The effective focal length (EFL) for the lens is the distance from any of the foci to its corresponding principal plane. EFL can be expressed by the following formula:

$$\frac{1}{EFL} = (n_L - 1)\left[\frac{1}{R_1} - \frac{1}{R_2} + \frac{(n_L - 1)d}{n_L R_1 R_2}\right] \qquad \textbf{(5.8)}$$

where n_L = index of refraction of the lens, d = distance from V_1 to V_2 , and R_1 = radius of curvature for the surface containing V_1 (positive in Fig. 5.17), and similarly R_2 = radius of curvature for the surface containing V_2.

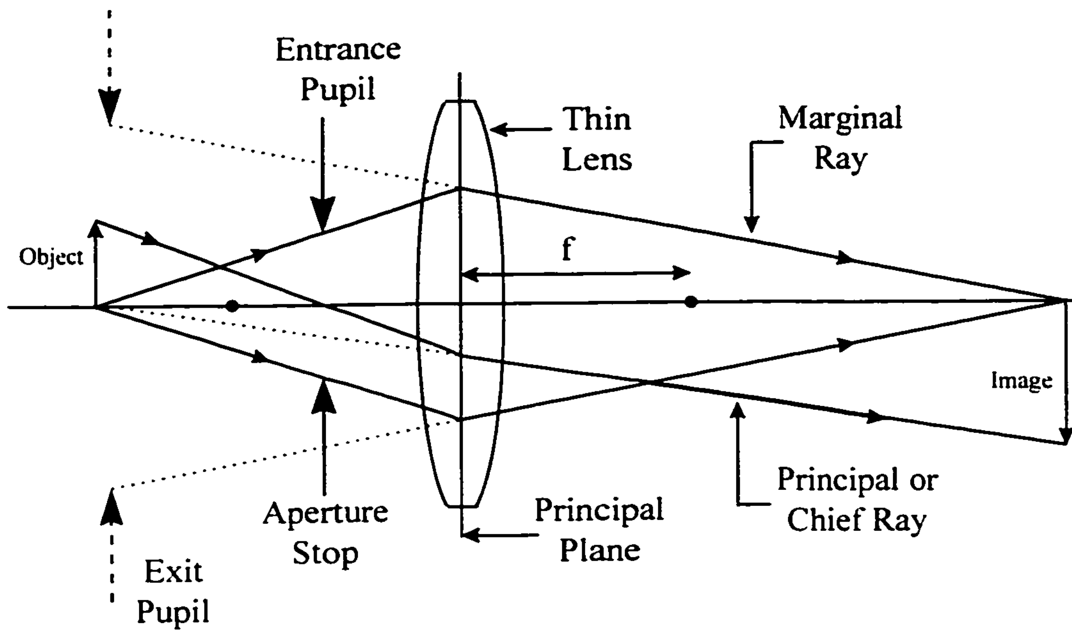

Figure 5.18 The entrance and the exit pupils are the images of the limiting aperture as seen from the object and image respectively.

H_1 and H_2, in Fig. 5.17a, are sometimes called unitary planes because graphical ray tracing requires that rays located between H_1 and H_2 always be parallel to the optic axis. Fig. 5.17b shows a graphical ray tracing example with a thick lens. Note that all the formulas and examples shown in this thesis relating to thin lenses can be interpreted for thick lenses by defining distances with respect to the appropriate principal plane instead of a single central plane. Fig. 5.18 shows the relationship between aperture stop, entrance pupil, and exit pupil. The aperture stop or limiting aperture of the system is the aperture which limits the size of the axial cone of light from the object. The entrance and exit pupils are the images of the aperture stop as seen from object and image space, respectively. When the aperture stop is moved to the focal position of a lens, it becomes a telecentric stop. If the stop in Fig. 5.18 were to be moved back to the first focal position, then the exit pupil would be located at infinity (to the left) and would have an infinite diameter. Telecentric stops will be a common situation with most of the optics discussed in this chapter. Fig. 5.19 shows a diagram of a Melles Griot, LAO138, 12 cm focal length achromat. In CODE V, the lens is defined by various quantities. The three lens surfaces will each have a specific radius of curvature where a center of curvature lying to the right indicates a positive radius. Surface 1 thickness is the

distance from surface 1 to surface 2 which is occupied by SK11 glass. In Fig. 5.19 the aperture stop is located on surface 1 which makes this also the entrance pupil. The entrance pupil diameter as well as the field angle are two key quantities in CODE V. Note the coordinate system. The optic axis is in the z-direction while the page is in the y-z plane. The x-direction is into the page. The angle which moves a ray in the y-z plane is the y-field angle, while the angle that moves a ray in the x-z plane is a x-field angle. All field angles mentioned hereafter are y-field angles unless otherwise noted.

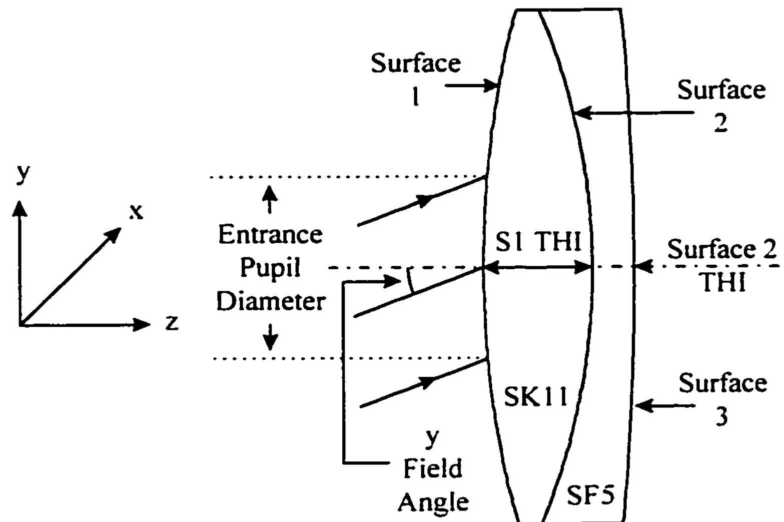

Figure 5.19 A Melles Griot LAO138 achromat as defined by CODE V.

5.4.1 Achromat

Fig. 5.20 shows the same achromatic doublet as in Fig. 5.19 as drawn by CODE V. This 12 cm focal length lens is representative of what would be used as a detector lens for the cslm. The diagram is drawn with a scale bar and shows a 7 mm entrance pupil diameter and two field angles: 0° and 5°. This very simple optical system will be used to illustrate some of CODE V's analysis options which will be used throughout this chapter as well as showing some of the chromatic problems associated with this detector lens. An important step in understanding an optical system is to fully list all the system parameters. Shown on the next page is an abbreviated lens data list, with comments and explanations, generated by CODE V for the achromat in Fig. 5.20.

	RDY	THI	GLA
OBJ:	INFINITY	INFINITY	
STO:	77.21000	8.200000	SK11_SCHOTT
2:	-54.09000	3.000000	SF5_SCHOTT
3:	-216.10000	114.353368	
IMG:	INFINITY	0.000000	

The first column lists the surface numbers and special surfaces such as the object (OBJ), image(IMG), and aperture stop (STO). The radii for each surface is then listed where positive radii have their centers of curvature to the right of the surface. Column three shows the thickness or distance to the next surface. The last column shows the type of glass used.

SPECIFICATION DATA

EPD	7.00000	*entrance pupil diameter*			
DIM	MM	*dimensions - mm*			
WL	725.00	647.10	568.20	488.00	*wavelength (nm)*
REF	2	*reference wavelength (647.1 nm)*			
WTW	1	1	1	1	*relative weight*
XAN	0.00000	0.00000	*x field angle*		
YAN	0.00000	5.00000	*y field angle*		

APERTURE DATA/EDGE DEFINITIONS

CA

CIR S1	EDG	20.000000	
CIR S2	EDG	20.000000	*size of actual surface (radii)*
CIR S3	EDG	20.000000	

REFRACTIVE INDICES

GLASS CODE	725.00	647.10	568.20	488.00
SK11_SCHOTT	1.558870	1.561341	1.564814	1.570128
SF5_SCHOTT	1.662215	1.667307	1.674856	1.687123

refractive indices for each type of glass at each of the wavelengths in use

SOLVES

PIM *paraxial image plane calculation in use*

INFINITE CONJUGATES

EFL	120.1032	*effective focal length*
BFL	114.3534	*back focal length*
FFL	-118.7170	*front focal length*
FNO	17.1576	*f-number*
IMG DIS	114.3534	*image distance*
OAL	11.2000	*overall length of optic system*
PARAXIAL IMAGE		
HT	10.5077	*height*
ANG	5.0000	*field angle*
ENTRANCE PUPIL		
DIA	7.0000	*diameter*
THI	0.0000	*first surface to entrance pupil distance*
EXIT PUPIL		
DIA	7.0817	*diameter*
THI	-7.1523	*last surface to exit pupil distance*

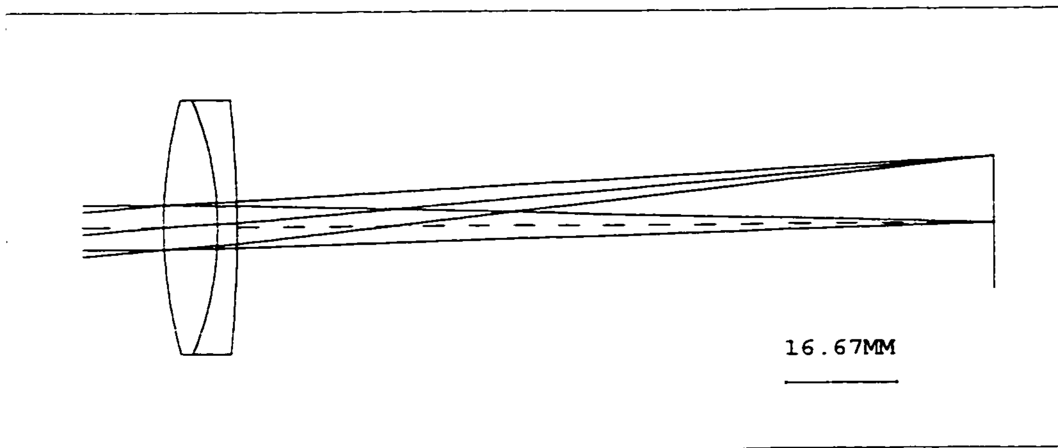

Figure 5.20 Schematic of LAO138 achromat drawn by CODE V with zero and five degree field angles shown. The aperture stop is at surface 1 with the entrance pupil diameter equal to 7 mm.

In Fig. 5.20, the central 0° field angle ray is expected to produce a nearly diffraction-limited spot since no off-axis aberrations are present and the aperture is small, thereby minimizing spherical and axial chromatic aberrations. Figs. 5.21a and 5.21b show the point spread function for the 0° and 5° field angles respectively. The point spread function (PSF) plots intensity of the image spot as a function of position on the image plane. In this case, CODE V has represented the PSF as a contour plot with a total of 10 contour lines spaced at 9.09% intervals. The peak intensity is normalized to 100 such that the most central contour line will trace out intensities that are 100 - 9.09 = 90.91% of the peak intensity. The second contour will be at 81.82% of the peak intensity and so on until the 10th and final contour, which represents 9.1% of the peak intensity. Another way to represent the PSF is to plot encircled energy. Fig. 5.22 shows a graph plotting encircled energy as a function of circle diameter for 0° and 5° field angles. The 9.1% contour (the outermost) in Fig. 5.21a corresponds to 80.9% encircled energy. The 80% encircled energy diameters for the 0° and 5° field angles are 21 and 72 μm respectively. Fig. 5.23 (taken from Born and Wolf[9]) shows the fraction of total energy as a function of circle radius x in an Airy disk pattern.

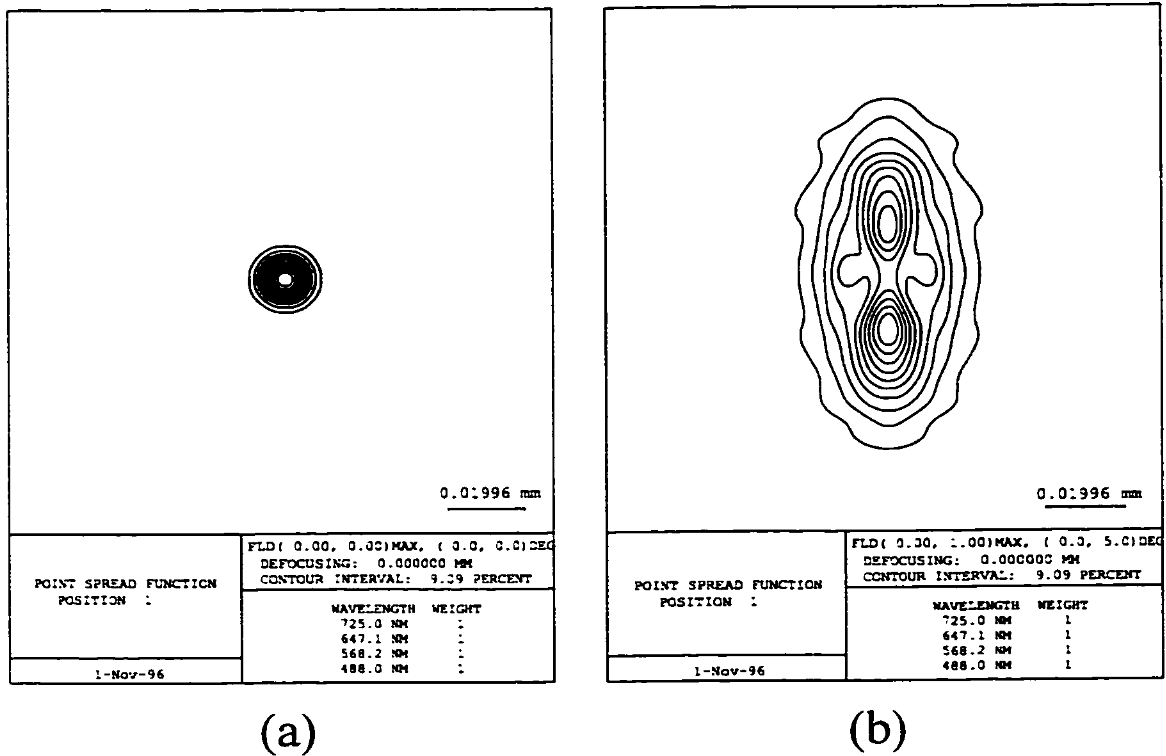

Figure 5.21 (a) Point spread function for the LAO138 achromat at a 0 degree field angle and at (b) 5 degree field angle.

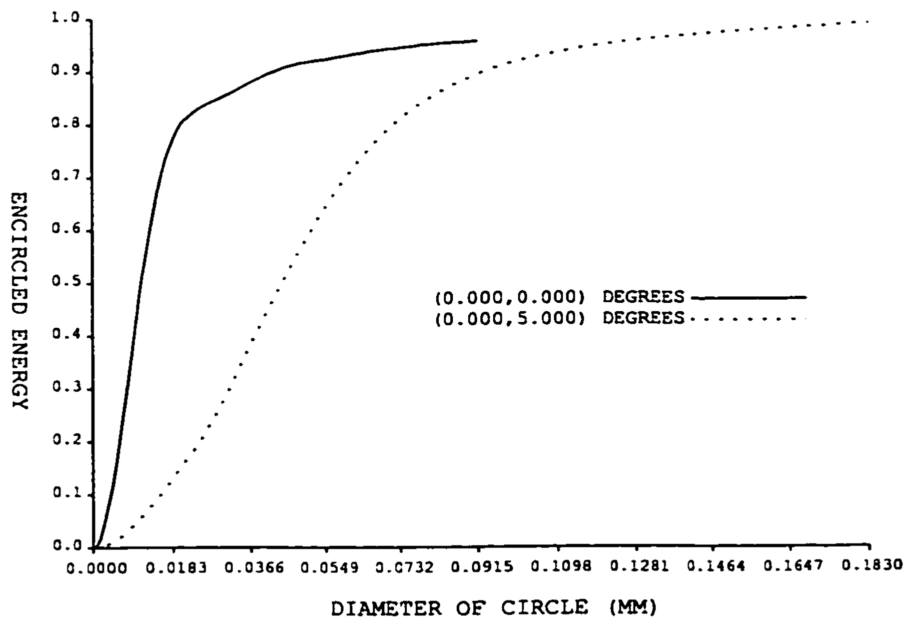

Figure 5.22 Encircled energy as a function of circle diameter for the LAO138 achromat at 0 and 5 degree field angles.

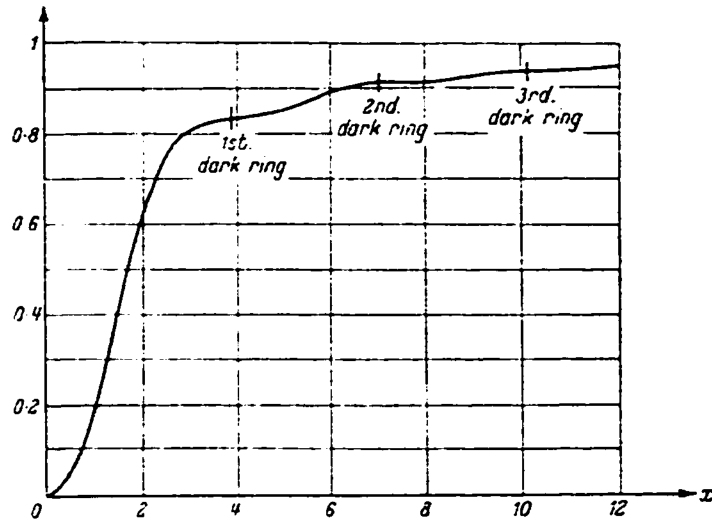

Figure 5.23 The fraction of total energy as a function of circle radius in an Airy disk pattern using monochromatic light. The Airy radius (1st dark ring) encircles about 84% of the energy. Figure taken from Born and Wolf[9].

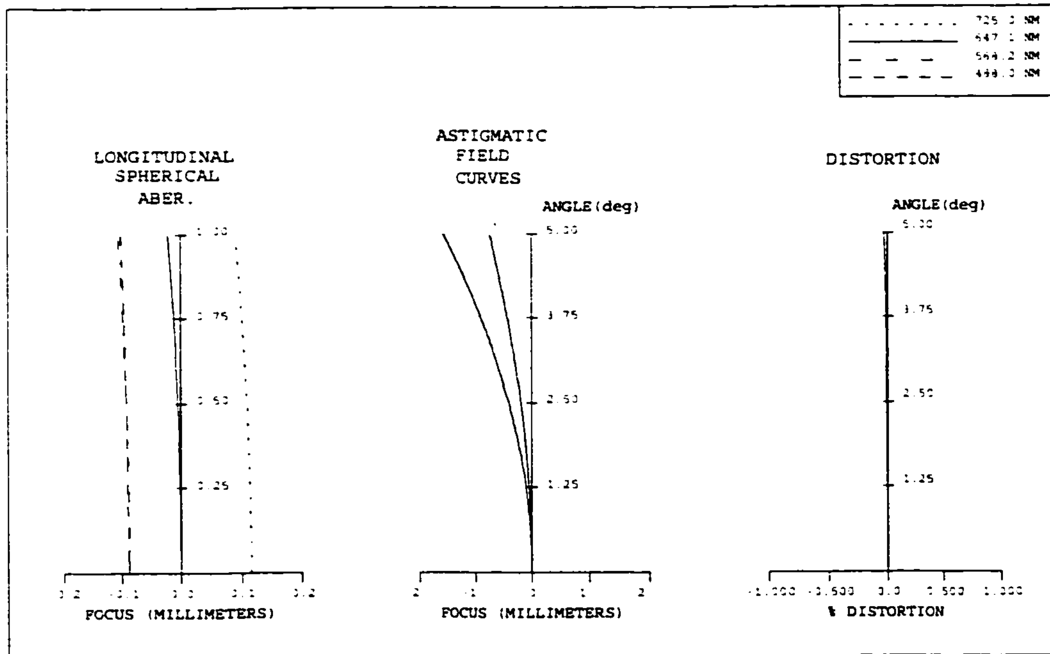

Figure 5.24 A CODE V field plot showing longitudinal spherical aberration, astigmatism and distortion for the LAO138 achromat.

The fraction of total energy is represented by the following function:

$$\text{Fraction Of Encircled Energy} = 1 - J_0^2(x) - J_1^2(x) \quad (5.9)$$

where J(x) is a Bessel function. Four wavelengths (all equally weighted) were chosen to simulate reflected-light and photoluminescence imaging. These wavelengths corresponded to Ar-Kr laser lines (488.0, 568.2, 647.1 nm) and porous silicon photoluminescence emission (approximately 725 nm). The 7 mm entrance pupil corresponded to a typical beam diameter for the cslm. The resulting image spot for the 5° field angle case is several times larger than the ideal diffraction limited spot. The spot has two peaks and is elongated in the y-direction exhibiting classical signs of astigmatism.

Fig. 5.24 shows another CODE V analysis option, a field plot, where three graphs are plotted: longitudinal spherical aberration as a function of pupil fraction (1.00 indicates a full entrance pupil of 7 mm in this case), tangential and sagittal astigmatic field curvature and percent distortion both as a function of field angle. In addition to showing the longitudinal spherical aberration, which is small in this case, this graph gives the longitudinal axial chromatic aberration to be approximately 200 μm between the 488 and 725 nm wavelengths. The LAO138 achromat was designed to work in the 480-650 nm wavelength range. 725 nm is well beyond the design range and therefore the achromat is significantly aberrated at this wavelength. This kind of chromatic problem can be avoided by using reflecting instead of refracting optics. As expected, the astigmatic field curve indicates a large amount of astigmatism at 5 degrees while distortion is almost negligible in comparison.

5.4.2 Reflecting Detector Mirror

There are several good reasons for using reflecting optics instead of refracting optics in the detector arm. A mirror will immediately eliminate any chromatic aberration which might prove especially troublesome in photoluminescence. However, the Airy disk diameter will still be dependent on the incident wavelength due to diffraction. Mirrors also facilitate the use of UV and infra-red (IR) with which refractive optics have problems, especially in combination. The spot size for the achromat in Fig. 5.21a is about 21 μm (this represents approximately 95% of the Airy disk diameter) so that the appropriate confocal pinhole might have a 10 or 20 μm diameter.

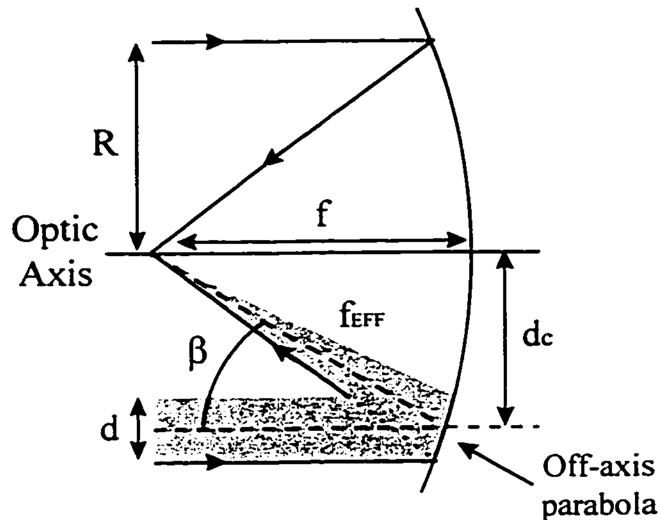

Figure 5.25 A collimated beam of light parallel to the optic axis of a parabolic mirror will produce a diffraction limited spot at f. Only part of a full mirror need be used to do this.

While this size pinhole is workable, it is always preferable to use a larger pinhole than a small one. Large pinholes are easier to position and will maintain proper alignment through time. An easy way to increase the spot size is to go to a longer focal length lens. Long focal length, small diameter achromats are both expensive and hard to find. On the other hand high f-number concave mirrors are abundant and less expensive.

Once reflective optics has been decided upon, the best solution is to use an off-axis parabolic mirror. A parabolic mirror with half-aperture R is shown in Fig. 5.25. It has the property of producing a diffraction-limited image at f for any aperture when the beam enters parallel to the optic axis of the parabola. A spherical mirror will not produce a diffraction-limited image for large apertures since it introduces spherical aberration into the image. Unfortunately the large beam of radius R in Fig. 5.25 is on-axis and therefore not very useful in a real system. If the beam size is reduced to a small diameter, d, then only a part of the parabolic mirror need be used. The useful section of the parabola could be 'cut out' and the rest discarded at which point an off-axis parabola has been created. Since the small diameter beam is contained within the larger beam, a diffraction-limited spot will appear at f. The focused beam exits at some angle with respect to the incoming collimated beam thus optics for both incoming and outgoing beams will not interfere with each other. For a spherical mirror the focal point is

always located a distance f from its surface which is not the case for a parabolic mirror. Fig. 5.26 (modified from Spiegel[10]) shows the relationship between the primary or parent focal length, f, and the effective focal length, f_{EFF}. The effective focal length[10] is given by:

$$f_{EFF} = \frac{2f}{1-\cos\theta} \tag{5.10}$$

Given a beam with known angle β, as in Fig. 5.25, the decenter, d_c, is given by:

$$d_c = f_{EFF}\sin\beta = \frac{2f\sin\beta}{1+\cos\beta} \tag{5.11}$$

where $\beta = \pi - \theta$. The telecentric plane for an off-axis parabola lies at f_{EFF} with respect to the center of the beam. In CODE V this distance must be defined with respect to the parabola's apex (at the optic axis). This distance is given by:

$$\text{Apex to Tel. Plane Distance} = f_{EFF} + (f - f_{EFF}\cos\beta) = \frac{f(3-\cos\beta)}{1+\cos\beta} \tag{5.12}$$

$\cos\beta$ can be obtained in terms of d_c and f by noting that:

$$\sin\beta = k(1+\cos\beta) \tag{5.13}$$

where $k = d_c/2f$. With some manipulation:

$$\cos\beta = \frac{1-k^2}{1+k^2} \tag{5.14}$$

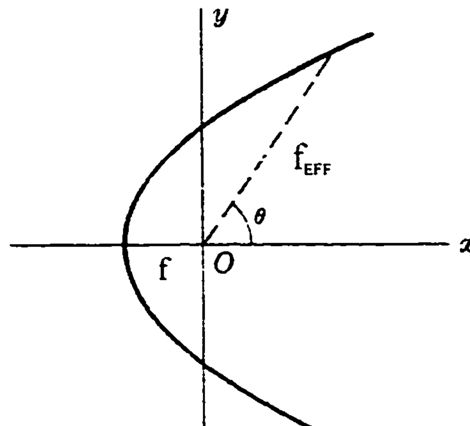

Figure 5.26 Parabola with various defining quantities. Figure modified from Spiegel[10].

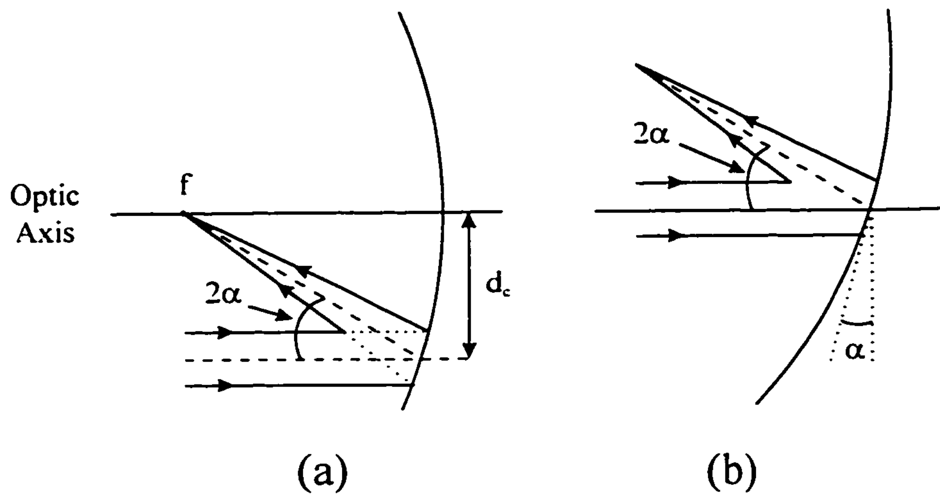

Figure 5.27 Decenter-tilt equivalence for spherical mirrors. (a) A decentered collimated beam strikes a spherical mirror, is deflected by a total angle 2α and focused at f. (b) The decenter in part a) is equivalent to a mirror tilt of α.

Off-axis parabolic mirrors are usually referred to as 30°, 45°, 60° and 90° off-axis parabolic mirrors where the angle refers to β in Fig. 5.25.

Although off-axis parabolic mirrors will be used later, in this case, long focal length off-axis parabolas are hard to come by. An alternate solution is to use a spherical mirror which provides good performance under small aperture and small field angle conditions. Fig. 5.27a shows a collimated beam of light parallel to the optic axis striking a spherical mirror at some distance d_c from the optic axis. The angle at which the beam is deflected towards the focal point is given by:

$$2\alpha = \tan^{-1}\left(\frac{d_c}{f}\right) \cong \frac{d_c}{f} \tag{5.15}$$

where f = focal length of the mirror, and α is assumed to be small. On a spherical mirror the decenter, d_c, shown in Fig. 5.27a is equivalent to tilting the mirror by an angle α at the optic axis as shown in Fig. 5.27b. The question is how far can the mirror be tilted for a given f-number without causing significant aberrations?

Edmund Scientific sells a 1016 mm focal length, 50.8 mm diameter spherical mirror for under $100 which serves as a good example. To simulate this detector mirror in CODE V the beam was rotated about the mirror instead of rotating the mirror itself, i.e. the aperture stop was located at the surface of the mirror while the field angle was varied.

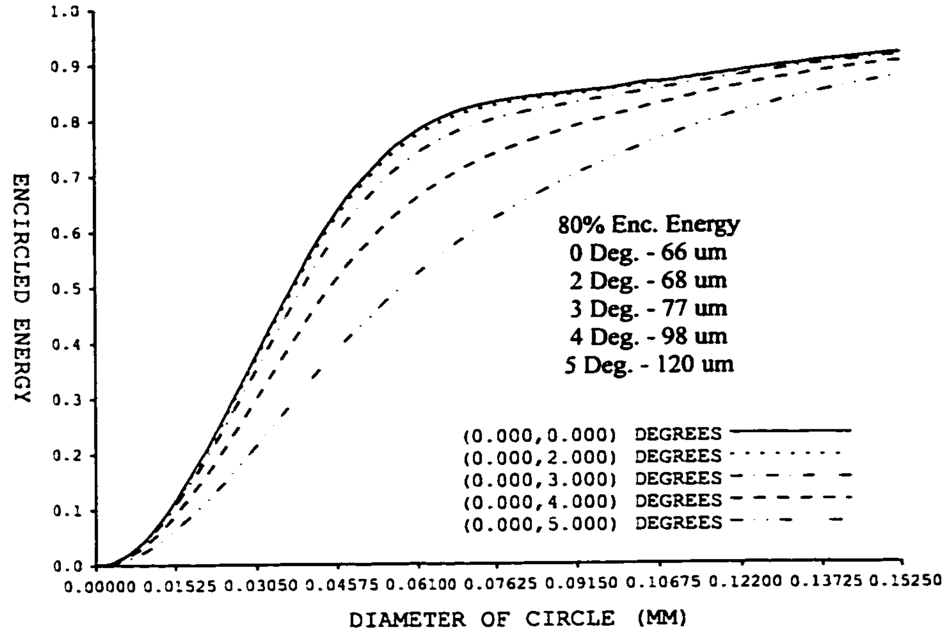

Figure 5.28 Encircled energy plot for the detector mirror (f=1016 mm) at various field angels with an 18 mm diameter entrance beam.

Fig. 5.28 shows an encircled energy plot for an 18 mm diameter beam with 0°, 2°, 3°, 4°, and 5° field angles incident on the 1016 mm focal length spherical mirror. Aberrations, especially astigmatism, enlarge the spot for tilt angles greater than 3°. Notice that spherical aberration is negligible due to the large effective f_{no} (1016/18 = 56). The choice of 'maximum' tilt angle of 3 degrees is clearly a conservative one which yields virtually no aberration. The spot size at 80% encircled energy is 77 μm hence a 50 or 100 μm pinhole would be appropriate. In most microscope systems, the beam would have to be folded with mirrors to accommodate a 1 m focal length while maintaining the tilt angle to less than 3 degrees. Another quick way to obtain the 'maximum' angle value is to generate a modulation transfer function (MTF) graph as shown in Fig. 5.29. The MTF is related to the PSF in the following way[11]:

$$F\{PSF\} = OTF = MTF\, e^{i\,PTF} \qquad \textbf{(5.16)}$$

where OTF = the optical transfer function, PTF = the phase transfer function, and F{} is the Fourier transform. Also PSF = $F^{-1}\{OTF\}=(F^{-1}\{G\})^2$, where G = the pupil function[12]. The MTF plots image modulation or contrast as a function of spatial frequency for an object with sinusoidal intensity modulation.

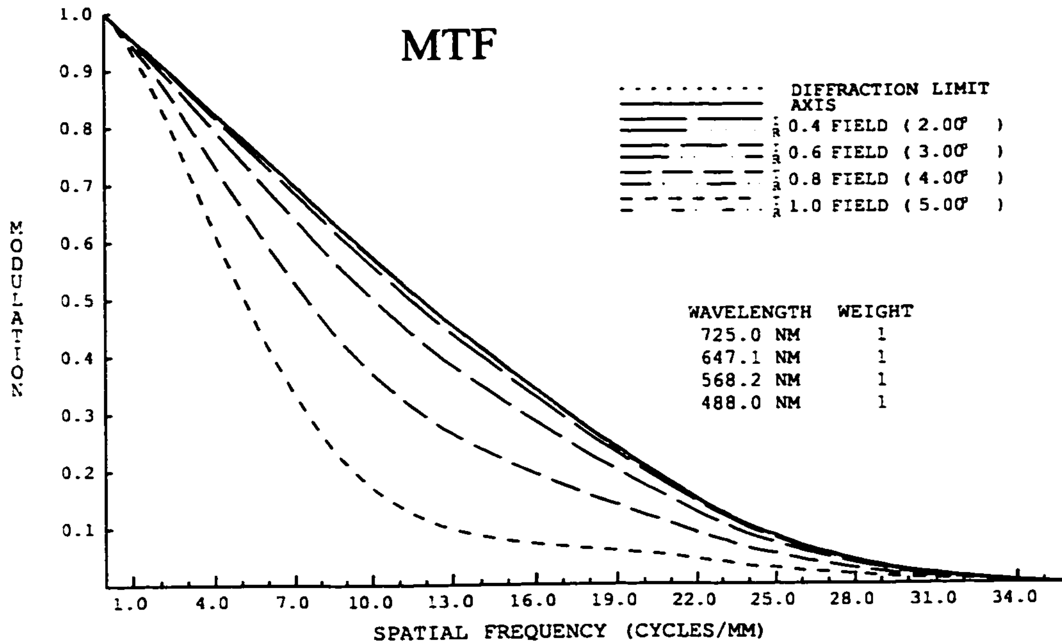

Figure 5.29 Modulation transfer function (MTF) for the detector mirror (f = 1016 mm) at various field angles, with an 18 mm diameter entrance pupil. T and R refer to the transverse and radial (sagittal) planes.

Fig. 5.29 shows that even in the diffraction limit the contrast will decrease as the spatial frequency increases. In addition to plotting the diffraction limited response, the MTF is plotted for the optic axis and the tangential and radial (sagittal) planes at each field angle. Fig. 5.29 shows MTFs for 2°, 3°, 4° and 5° field angles. The three degree value gives a curve which closely follows the diffraction limit curve, while the five degree curve clearly shows signs of significant aberrations. Notice that all the sagittal plane lines are nearly coincident with the diffraction limit axis since the spot elongation occurs only in the tangential plane, i.e. the spot is elongated radially (see Fig. 5.9).

A beam diameter of 7 mm is typically found on the cslm which allows the detector mirror tilt angle to increase while maintaining a nearly perfect image spot as shown in Fig. 5.30. Recall, from Table 5.1, that transverse astigmatism is proportional to aperture size. The spot size has increased to a 178 μm diameter (6° optimum field angle) representing approximately an eight-fold increase when compared to the achromat from section 5.4.1, allowing for a larger confocal pinhole.

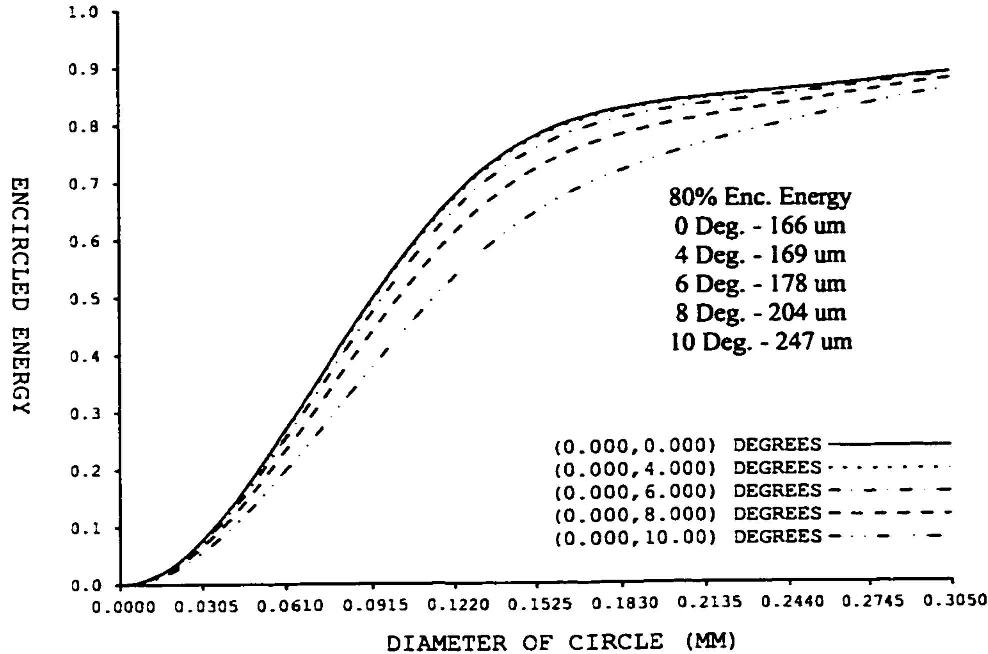

Figure 5.30 Encircled energy plot for the detector mirror (f = 1016 mm) with a 7 mm diameter entrance beam. The spot sizes have increased considerably when compared to the spot size in Fig. 5.28. As the entrance beam diameter is decreased, so will astigmatism decrease and the maximum allowable tilt angle will increase.

5.4.3 30X Reflecting Beam Expander

A common setup for a laser beam expander consists of a microscope objective followed by an achromat. This works well for one wavelength at a time since it is an on-axis system. If, however, multiwavelength operation is required, especially when the UV and IR are included, then all-reflecting optics are essential. The optimum all-mirror beam expander consists of two off-axis parabolic mirrors with focal lengths f_1 and f_2 where the expansion ratio is determined by the ratio of f_1 and f_2. A 0.68 mm diameter He-Ne laser beam (632.8 nm) needs to be expanded by a factor of about 30 to produce a 2 cm diameter collimated beam. The smallest off-axis parabolic mirror which JANOS provides is a 25.4 mm parent focal length, therefore the second element must have at least a 762 mm focal length. As was discussed in section 5.4.2, a tilted spherical mirror will work here as long as the tilt angle is kept small.

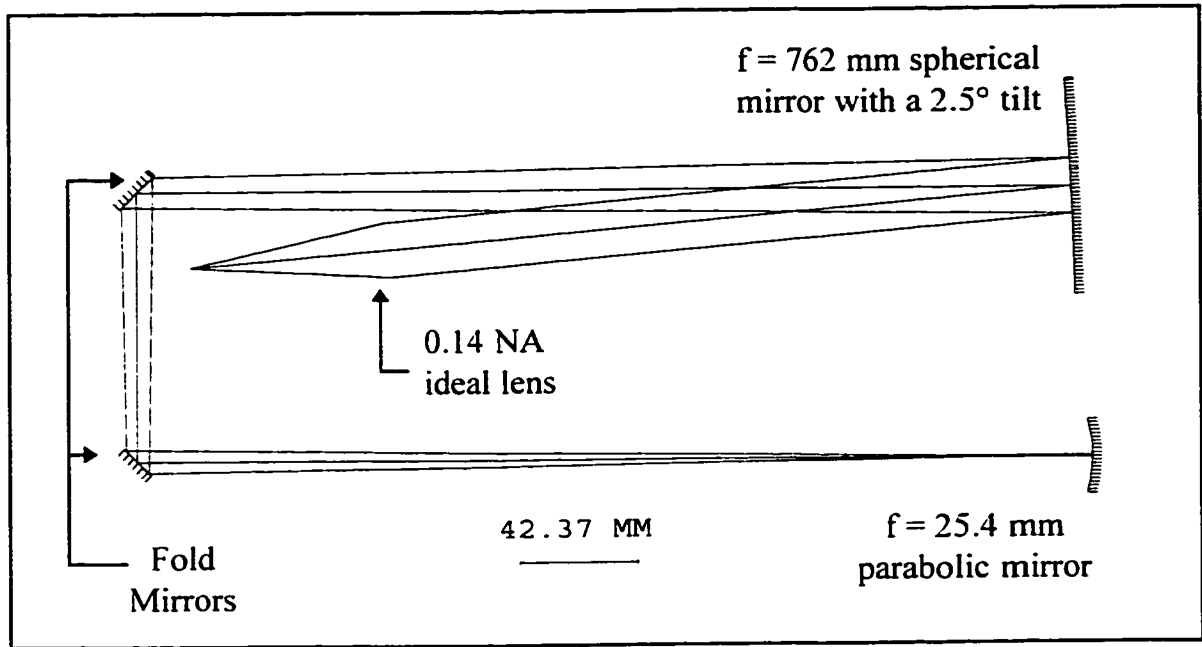

Figure 5.31 A 30X all-reflecting beam expander. Off-axis parabolic mirrors can be replaced with spherical mirrors when the tilt angle is small and f-number is large.

Edmund Scientific sells a 762 mm focal length, 76.2 mm diameter spherical mirror which is used as the second component in the beam expander while the first component is a 25.4 mm diameter, 25.4 mm parent focal length parabolic mirror. In the CODE V simulation of an on-axis parabola was used since it would yield the same results as an off-axis parabola with respect to aberrations. Fig. 5.31 shows a schematic of the 30X beam expander where fold mirrors have been added to make the system more compact and easily viewed. Notice that the 0.68 mm diameter incoming beam is incident from the left and strikes the small parabolic mirror first. The incoming beam does not appear in Fig. 5.31 because it is obscured by the reflected beam. The 30X beam expander is an afocal system, meaning that its effective focal length is infinite. In order to analyze and work with such a system CODE V must convert it to a focal system. CODE V does this by inserting an ideal thin lens, with no aberrations, of any desired focal length at the end of the afocal system. Throughout the rest of this chapter, the focal length will be chosen such that the numerical aperture (NA) of the ideal lens is equal to 0.14. This is a convenient quantity since it allows direct comparison with the data from a real 0.14 NA Mitutoyo microscope objective. Choosing a 0.42 NA ideal objective was found to give unreliable results and CODE V recommended an ideal lens no smaller than

0.05 NA. It was found that the maximum allowable tilt angle for the spherical mirror was 2.5° (total reflection angle of 5°). Fig. 5.32 shows a PSF for the 30X beam expander with a 2.5° tilt angle on the spherical mirror compared to the PSF when a parabolic mirror with no tilt is used.

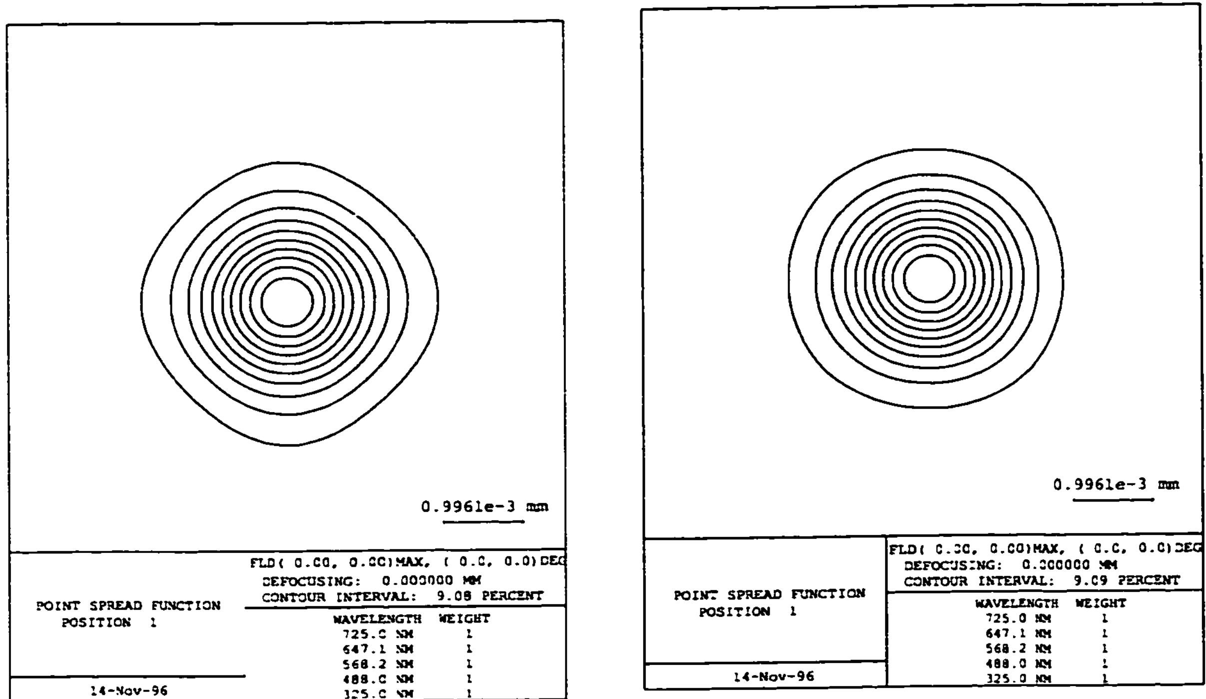

Figure 5.32 PSFs for the 30X all-mirror beam expander. (a) Spherical mirror tilted at 2.5 degrees. (b) Ideal case where spherical mirror is replaced by a parabolic mirror with no tilt.

5.5 CODE V Results Part II—Telescopes and UV Objective

One of the main reasons for using CODE V was to determine how an all-reflecting unitary telescope compared to the refracting telescopes presently in use on the cslm. A detailed and direct comparison will be made between these two types of telescopes. Several designs will be presented in this section for a very low-cost UV objective with a 2 x 2 cm field of view.

5.5.1 Refracting and Reflecting Telescopes

The cslm has employed refracting unitary telescopes in its configuration for many years which has limited its performance especially when used at low zoom in combination with small pinholes (section 3.1.2.4).

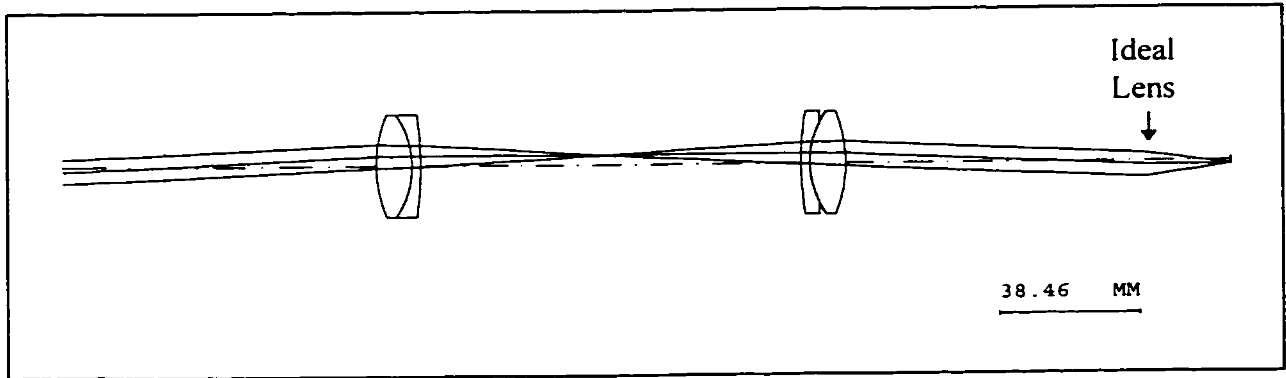

Figure 5.33 Schematic diagram of the refracting telescope made up of two LAO079 achromats. A 2.7° field angle is shown as well as a 0.14 NA ideal lens to the right of the telescopes.

The telescopes perform an essential task: to bring the scanning beam back to the center of the next optical component. A CODE V schematic for one of the refracting telescopes is shown in Fig. 5.33. The telescope consists of two Melles Griot, 6 cm focal length, LAO079 achromats oriented such that the most curved surface faces the collimated beams in order to reduce spherical aberration. CODE V allows the user to choose the LAO079 lens from its Melles Griot catalog and then duplicate and flip the lens to create a telescope. The system is then optimized to produce an infinite focal length combined with an infinite size exit pupil. Fig. 5.33 shows a 7 mm diameter beam entering at a 2.7° field angle with the rotation of the beam occurring a focal distance away from the first lens (telecentric stop). The ± 2.7° sweep angle is enough to scan the entire field of view for all the Mitutoyo microscope objectives. The afocal option in CODE V introduces an ideal lens with a focal length equal to 24.75 mm after the second achromat such that the system is equivalent to 0.14 NA. The entire CODE V lens data for the refracting telescope can be found in Appendix 6.

Spherical Aberration	0.003779	Distortion	0.000000
Tangential Coma	0.000000	Axial Colour	0.011138
Tangential Astigmatism	0.029806	Lateral Colour	0.000000
Sagittal Astigmatism	0.012916	Petzval Curvature	-0.023211
Petzval Blur	0.004472		

Table 5.2 Third order transverse aberrations for the refracting telescope in units of mm. The symmetry principle requires coma, distortion, and lateral colour be equal to zero. Astigmatism is clearly the dominant aberration at the maximum field angle.

Table 5.2 shows transverse 3rd order aberrations, in mm units, for this telescope at the reference wavelength (647.1nm), and 2.7° field angle. These values give a good indication of the aberrations for this telescope since higher order aberrations are small due to the small field angle and aperture size values. As expected, coma, distortion, and lateral colour aberration are identically zero due to the symmetry principle. The largest aberrations are axial chromatic and astigmatism. These aberrations can best be visualized by referring to Fig. 5.34 where a field plot is shown. These plots are generated using real rays hence they include all higher order aberrations. Longitudinal spherical aberration is about 25 μm for each of the wavelengths while the longitudinal axial chromatic aberration is 73 μm between the 725 and 488 nm lines. Considering the axial resolution is on the order of 30 μm for a 0.14 NA lens at 600 nm, these aberrations are significant. The worst aberration is longitudinal tangential astigmatism which has a value of 107 μm at the full field angle.

An all-reflecting unitary telescope can be constructed by taking two identical parabolic mirrors and placing them opposite each other with a common focal point as shown in Fig. 5.35. If full on-axis parabolas were used then the incoming and outgoing beams would be blocked assuming no fold mirrors were used. A real telescope is constructed by shifting the beam off-axis by some amount and using only as much of the parabola as is needed. As shown in Fig. 5.35, the two off-axis parabolas must be identical and diametrically opposed for the telescope to be unitary and function properly.

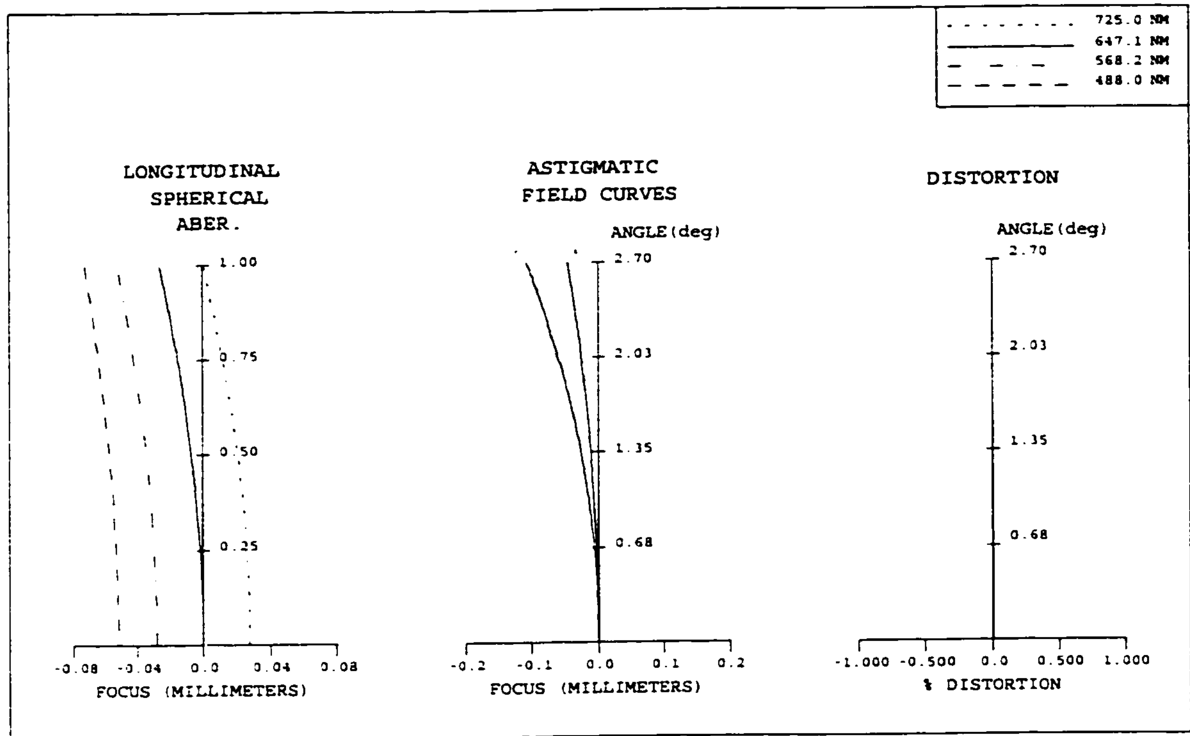

Figure 5.34 Field plot for the refracting telescope. There is a significant amount of axial chromatic aberration but the dominant aberration is astigmatism at large field angles.

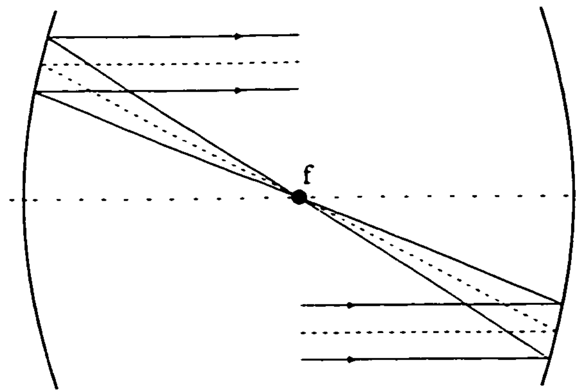

Figure 5.35 A reflecting telescope can be constructed by placing identical parabolic mirrors opposite each other. Only parts of the full parabolas need be used when off-axis collimated beams are used.

Fig. 5.36 shows a CODE V schematic of an all-reflecting unitary telescope. The telescope consists of two 30° off-axis parabolic mirrors with 50.80 mm parent focal lengths and 25.40 mm diameters, obtained from the JANOS catalog. Apart from the components, the entrance pupil diameter, field angles and the afocal settings are identical to the refracting telescope.

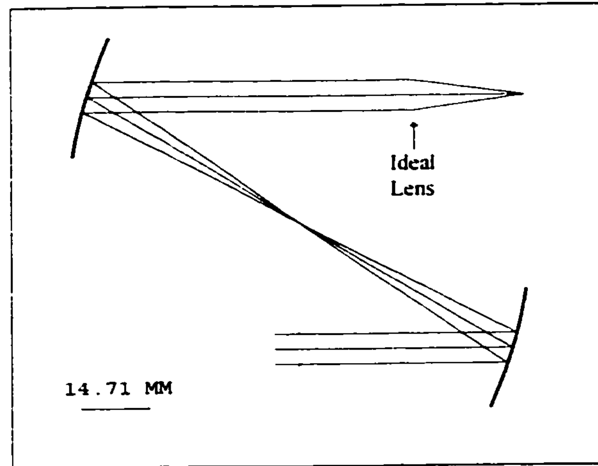

Figure 5.36 Reflecting telescope with a 0° field angle shown. The telescope consists of two off-axis (30°), 50.8 mm parent focal length parabolic mirrors.

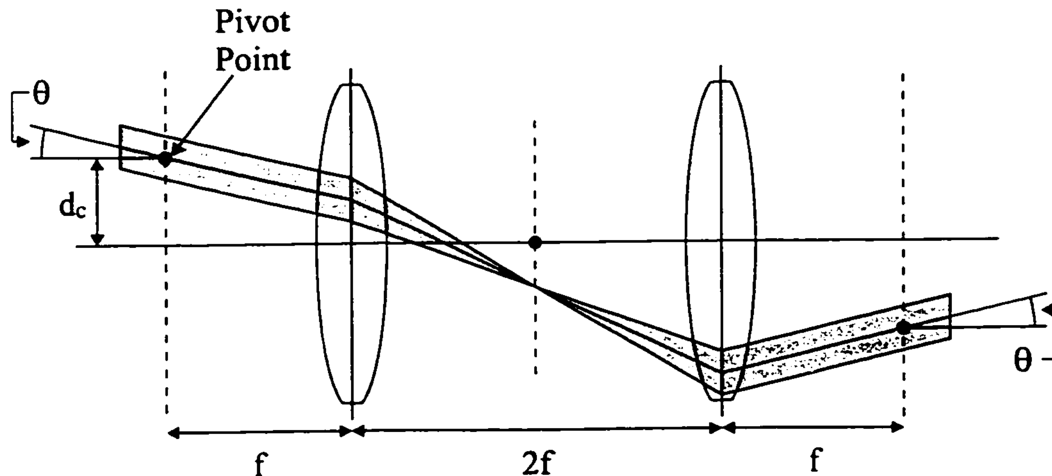

Figure 5.37 Refractive equivalent of the off-axis parabolic reflecting telescope from Fig. 5.36. Note that this configuration was never used in the cslm or for any analysis.

Data for the reflecting telescope can be found in Appendix 6. Due to the off-axis nature of the reflecting telescope its refracting equivalent is not the same as in Fig. 5.33. Fig. 5.37 shows an equivalent refracting version for the system in Fig. 5.36. Basically the incident beam has been moved off-axis and pivots at the focal plane some distance d_c above the lens' focal point. This lens system would have to be extremely well corrected for it to work properly in a real microscope.

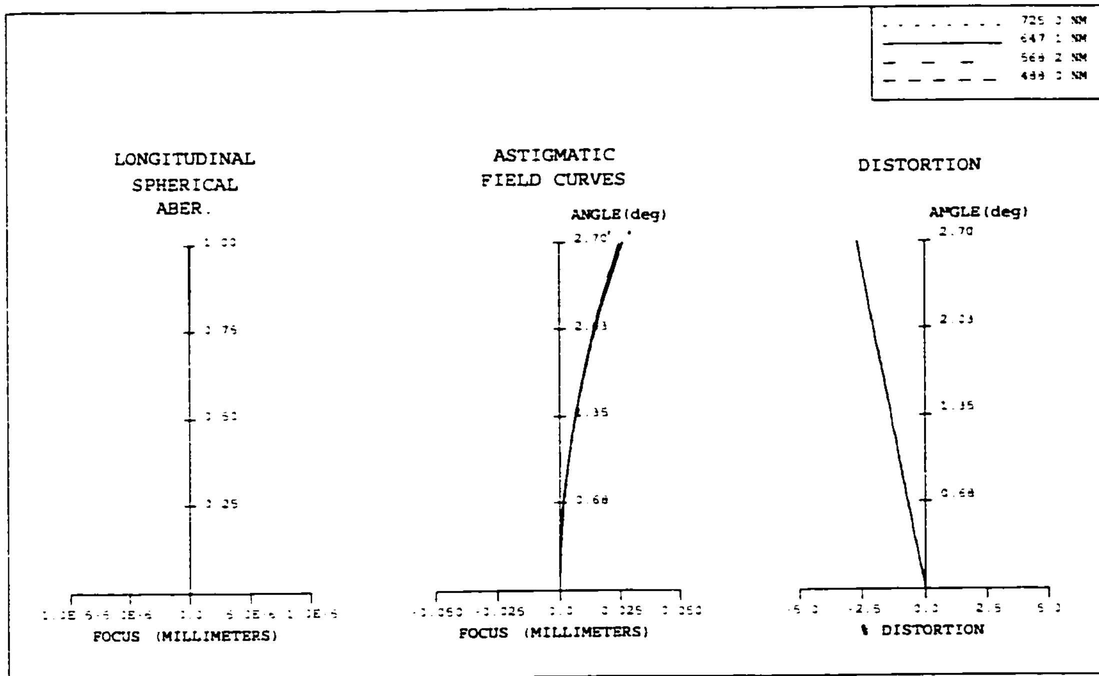

Figure 5.38 Field plot for the reflecting telescope. Notice that chromatic aberrations have disappeared while astigmatism has decreased with respect to the refracting telescope. Unfortunately some distortion is present.

Fig. 5.38 shows a field plot for the reflecting telescope. As expected, spherical and axial chromatic aberration have disappeared. Longitudinal astigmatism is about 25 μm in both sagittal and tangential directions which implies a circularly symmetric blur. The astigmatism is down by a factor of four compared to the refracting telescope and it is in the positive direction unlike the refracting telescope. The distortion is non-zero and reaches a peak of -2.7% at full field angle. Third order aberrations can be misleading at this point since this is a decentered system and consequently the symmetry principle does not strictly apply.

A very convincing way to show which telescope is superior is to plot out PSFs at various field angles for both systems. Given a square field of view, PSFs were plotted for an edge (y = 2.7°, x = 0°) and a corner (x, y = 2.7°) point in Figs. 5.39 and 5.40 respectively. All plots have the same scale with colour representing intensity. At 0°, both telescopes operate at or near the diffraction limit generating 4 and 12 μm spots for the reflecting and refracting cases respectively.

Fig. 5.39 shows PSFs for the edge point. Fig. 5.39a clearly shows the effect of astigmatism on the refracting telescope. The spot has increased significantly in height. The reflecting telescope PSF has doubled in size (compared to 0° field angles) as shown in Fig. 5.39b, but has remained circular. In Fig. 5.40, PSFs were plotted for a corner point on the field of view. The refracting telescope image has deteriorated to a ~ 40 μm diameter oval as shown in Fig. 5.40a. This represents almost a four-fold increase in size compared to the diffraction-limited spot. Fig. 5.40b shows that the reflecting telescope has also aberrated the image. The spot is now 13.8 μm large. Figs. 5.41a and b show encircled energy plots for both the refractive and reflective telescopes, respectively, at 0, (0, 2.7°) and (2.7°, 2.7°) field angles. The 80% encircled energy values of Fig. 5.41 basically show that the refractive telescope gives spot sizes about 3 times worse than the reflective telescope. The refractive telescope has problems mainly with astigmatism, spherical, and chromatic aberration. The reflecting telescope is generally superior even when chromatic aberrations are ignored. Table 5.3 shows 80% encircled energy diameters for the reflecting and refracting telescopes. Only one wavelength was used in Table 5.3, 546.1 nm, the design wavelength for the LAO079 achromats. Also, a 'best focus' routine was run in order to minimize spot sizes at all field angles. In this case the reflecting telescope still outperforms the refracting telescope by about a factor of two. It is interesting to note the minor asymmetry between spot sizes for x and y field angles of the same size for the reflecting telescope. The asymmetry is due to the off-axis, non-centered, nature of the mirror telescope which becomes more pronounced as the field angle and entrance pupil are increased.

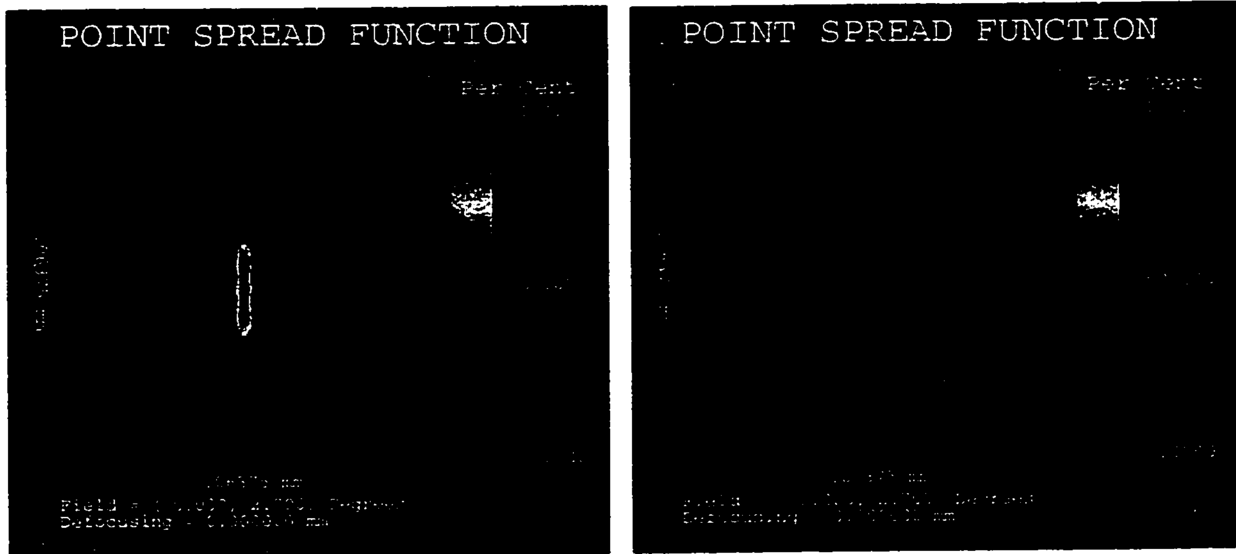

Figure 5.39 PSFs at 2.7 degree field angle for the (a) refracting telescope and (b) the reflecting telescope. The refracting telescope shows clear signs of astigmatism.

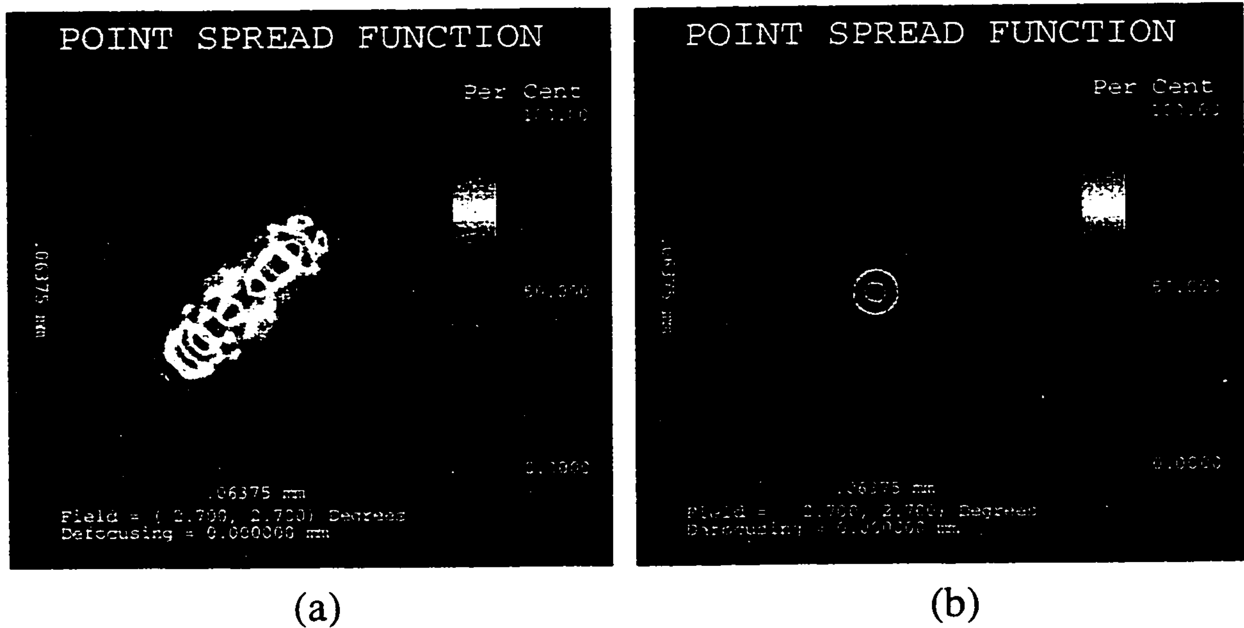

Figure 5.40 PSFs at 2.7 degree x and y field angles for the (a) refracting telescope and (b) the reflecting telescope. The reflecting telescope is the clear winner.

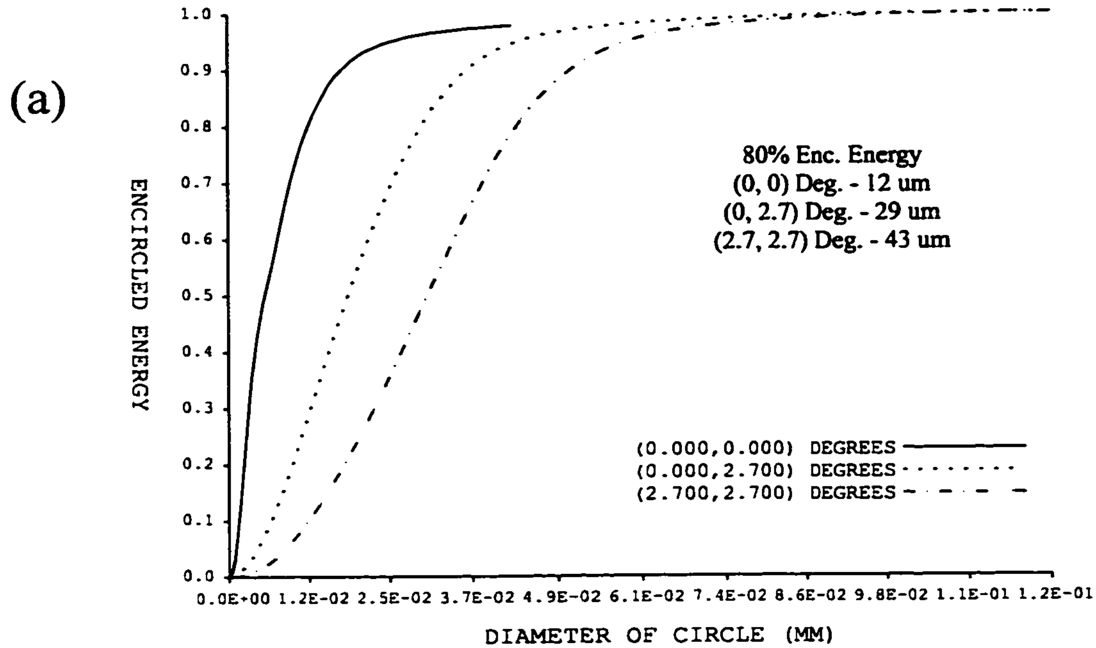

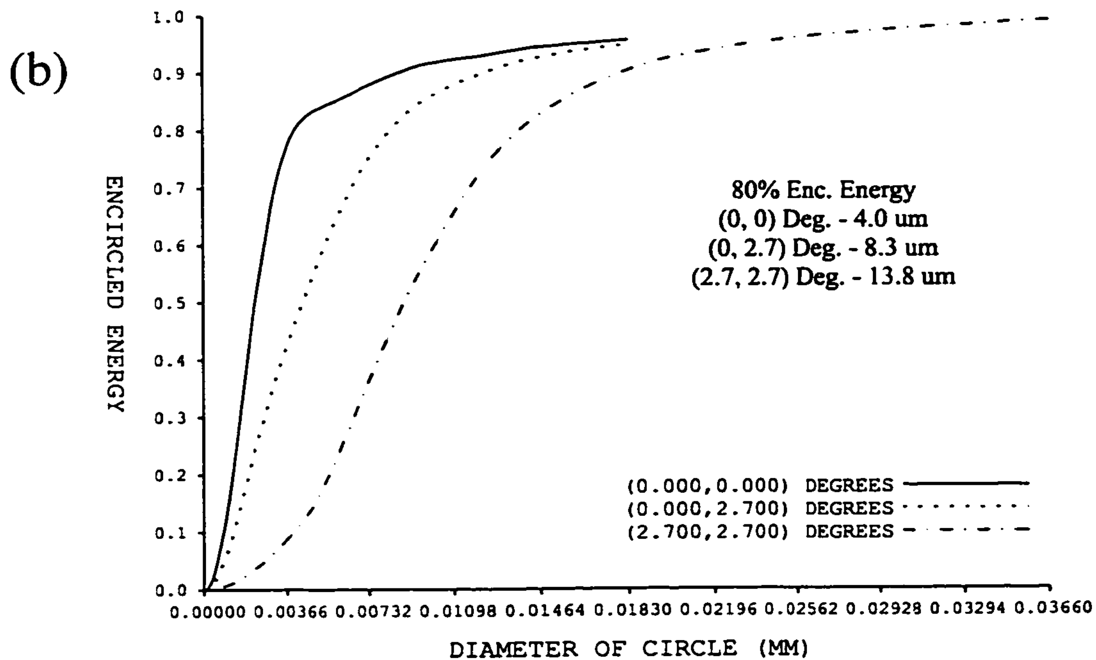

Figure 5.41 (a) Encircled energy vs. diameter for the refractive telescope and (b) for the reflective telescope.

	80% Encircled Energy Diameters (μm)	
Field Angle	Lens Telescope	Mirror Telescope
(0°, 0°)	13	6.7
(0°, 2.7°)	11	3.9
(2.7°, 0°)	11	4.4
(2.7°, 2.7°)	27	9.4

Table 5.3 Comparison of reflecting and refracting telescopes using 546.1 nm light at 'best focus'.

Another property of the reflecting telescope is that virtually any other combination of off-axis parabolic mirrors will yield basically the same results as above (Fig. 5.41b), given the same parent focal lengths. Table 5.4 shows 80% encircled energy diameters for the reflective telescope of Fig. 5.36 and an equivalent telescope made up of 90° off-axis parabolic mirrors. The values are very similar and implies an expanded flexibility for mirror telescope construction.

	80% Encircled Energy Diameters (μm)	
Field Angle	30° Mirror Telescope	90° Mirror Telescope
(0°, 0°)	4.0	4.0
(0°, 2.7°)	8.3	7.7
(2.7°, 0°)	8.5	8.5
(2.7°, 2.7°)	13.8	13.1

Table 5.4 Comparison of 80% encircled energy diameters for unitary telescopes made with 30° and 90° off-axis parabolic mirrors.

The cost for the two off-axis parabolic mirrors is approximately $380, while the cost for two LAO079 achromats is about $360. The results are clear and unambiguous: the reflecting telescope is a superior optical system. Note that the use of spherical mirrors does not work

since they introduce a very large amount of astigmatism even at 0° field angle. The key to the parabolic mirror telescope's success is that it contributes zero aberrations with a 0° field angle. It follows intuitively that small deviations from 'on-axis' operations will lead to small aberrations. The reflecting telescope would significantly improve the image quality on the cslm by providing confocal operation over most of the field of view with little deterioration even when used in photoluminescence. The reflecting telescope also eliminates transmission problems and chromatic aberrations associated with the UV and IR.

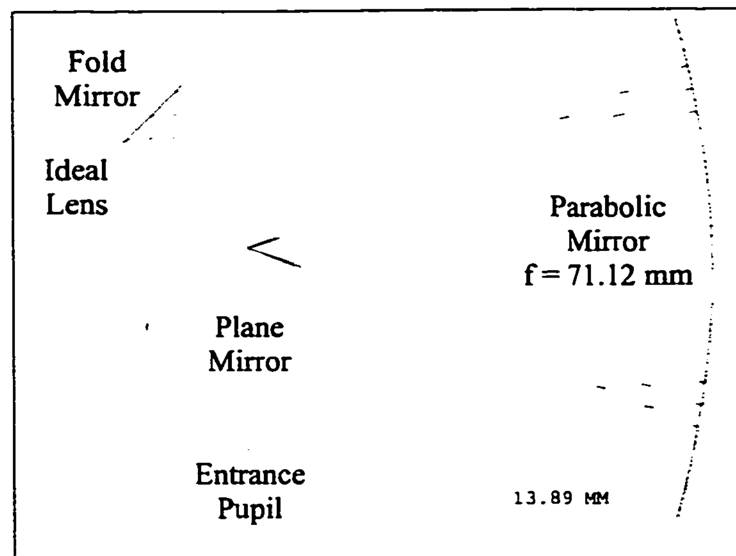

Figure 5.42 A reflecting telescope utilizing a single on-axis parabolic mirror.

The reflecting telescope image quality can be improved at the corners of the field of view by simply increasing the focal length of the off-axis parabolic mirrors. For example, doubling the focal length will produce a PSF at the corner 1.7 times as large as the unaberrated case compared to more than 3 times as large, as in Fig. 5.41b. Unfortunately, the cost of the mirrors also doubles.

Fig. 5.42 shows an alternate, much more compact design for a reflecting telescope which uses parts of a full, on-axis parabolic mirror with a plane mirror sitting at the focal point. In theory this telescope will have the same response as its off-axis counterpart (assuming the same focal length). In practice, the plane mirror will have a diffraction limited spot scanning

over it such that any imperfection will cause significant aberrations. Care should be taken to avoid dust or scratches when mounting the high quality aluminized flat into the system. The price for these two mirrors is about $650. This system is advantageous due to its simplicity and ease of alignment. Fig. 5.42 shows a 76.2 mm diameter, 71.12 mm focal length parabolic mirror coupled with a 12.7 mm diameter flat mirror. The field angle is once again 2.7° and the entrance pupil diameter is 7 mm while the afocal lens setting is 0.14 NA. Fig. 5.43 shows the corresponding encircled energy plotted as a function of circle diameter. The response for the Fig. 5.42 telescope is slightly better than for the Fig. 5.36 telescope due to a longer effective focal length.

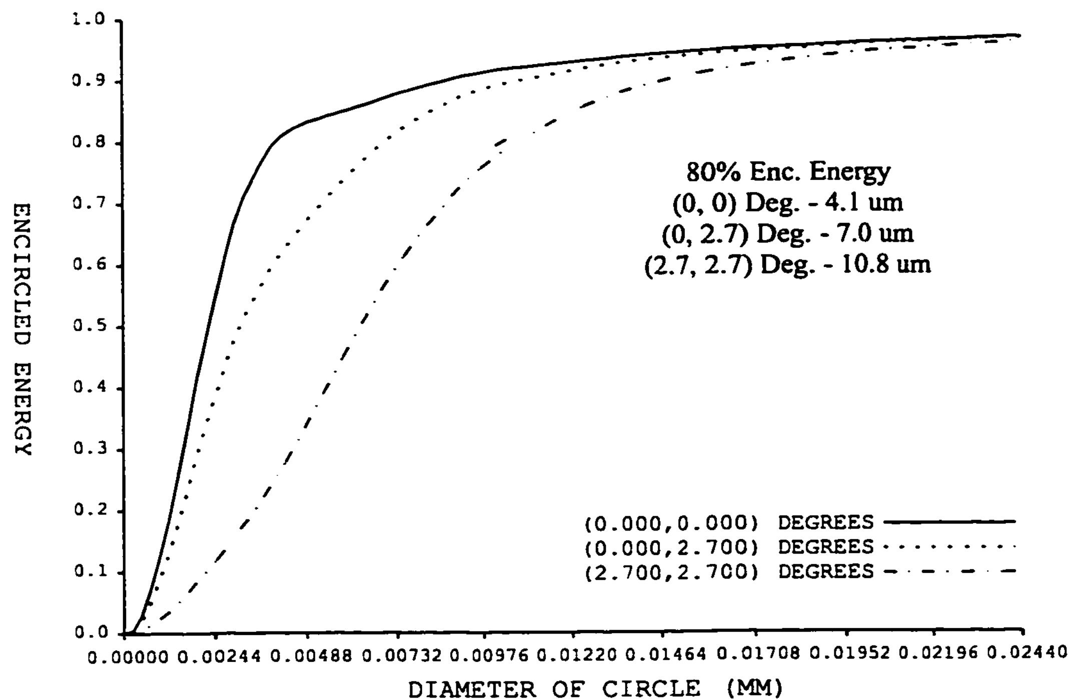

Figure 5.43 This graph plots the energy enclosed by a circle of a given diameter for the reflecting telescope of Fig. 5.42.

A third and final design for a reflecting telescope is shown in Fig. 5.44a. It is a non-unitary 1.5X telescope consisting of a 50.8 mm diameter, 50.8 mm parent focal length off-axis (90°) parabolic mirror in combination with a 50.8 mm diameter, 76.2 mm focal length off-axis (90°) parabolic mirror. The telescope is designed to accept a 10 mm diameter beam with a 4.05° field angle and generate a 15 mm diameter beam with a 2.7° field angle. Fig. 5.44b shows how the entrance and exit angles for non-unitary telescopes are not the same. In general, if a beam is expanded by some factor, the exit angle will be reduced by the same factor. Fig. 5.44b shows a 2X telescope made up of two simple lenses. The beam diameter expands by a factor of two, however, the exit angle is reduced to $\theta/2$ compared to the original θ entrance angle. Alternatively, the beam in Fig. 5.44a could be input from above and undergo a 1.5 reduction. In this case, a 22.5 mm diameter beam at a 1.8° field angle would be reduced to a 15 mm beam at a 2.7° field angle. The aberrations produced by both these configurations are identical. An encircled energy plot is shown in Fig. 5.45 for the expanding beam case. Due the size of the entrance beam the ideal lens was set to a 250 mm focal length (0.03 NA) since any faster lens created a problem with CODE V, therefore, the 0° field angle spot size is about 19 μm. Unfortunately, the edge and corner spot sizes are 5 and 10 times larger, respectively. The off-axis parabolic mirror design seems to reach its limit at about 1 cm diameter beams (for reasonable focal lengths), beyond which aberrations become very large. The same happens for field angles beyond about 5°. This clearly rules out reflecting telescopes for use on the MACROscope. Use on the cslm is possible although the 0.14 NA objective would prove troublesome due to its large entrance pupil.

(a)

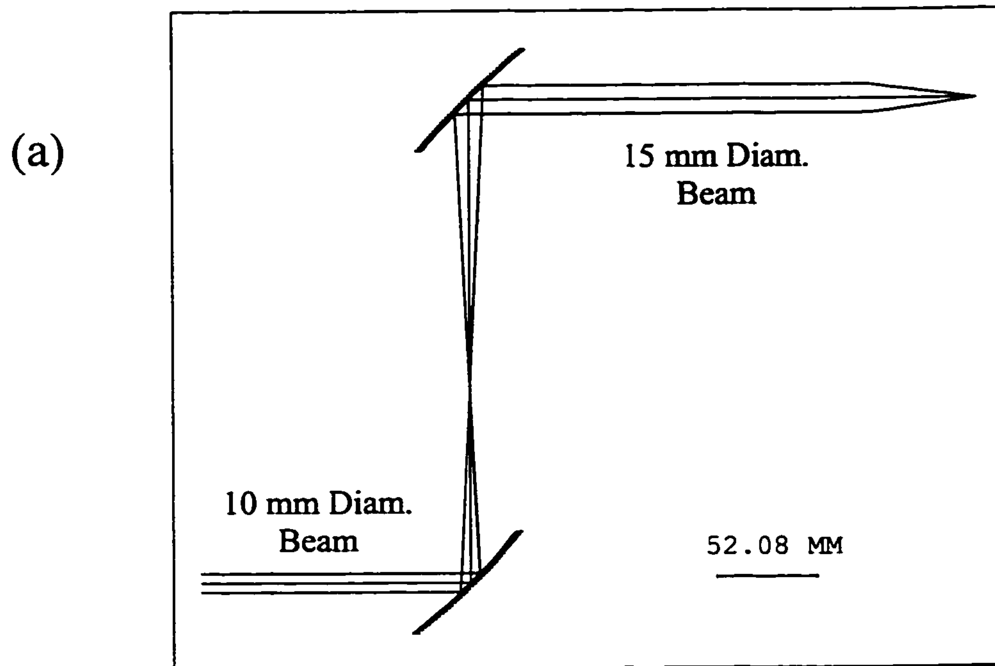

(b)

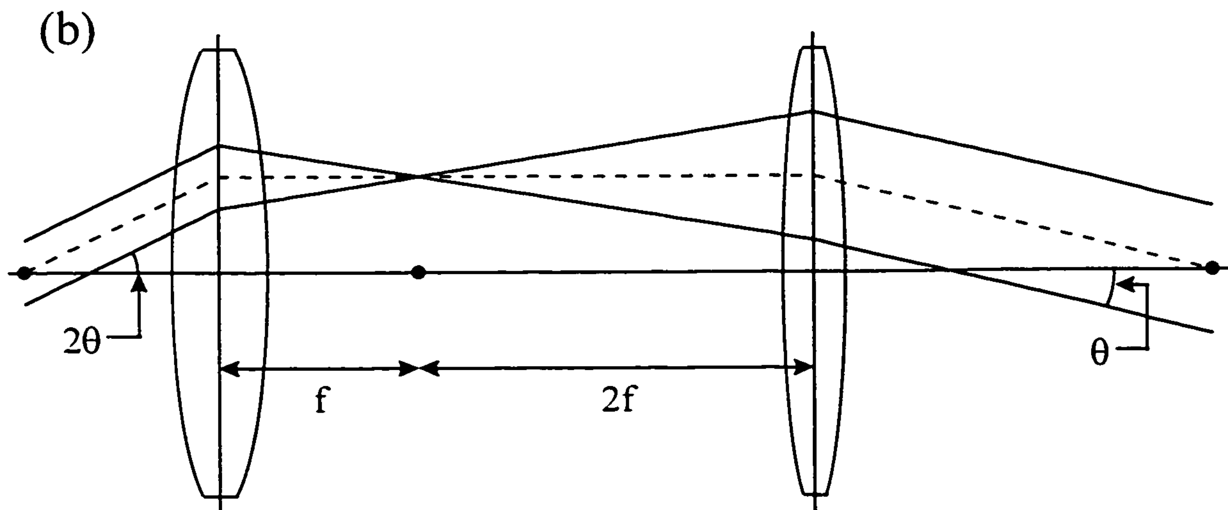

Figure 5.44 (a) Schematic diagram of 1.5X reflecting telescope with a 0° field angle shown. (b) A 2X refracting telescope showing how the exit angle is reduced by a factor of two compared to the entrance angle.

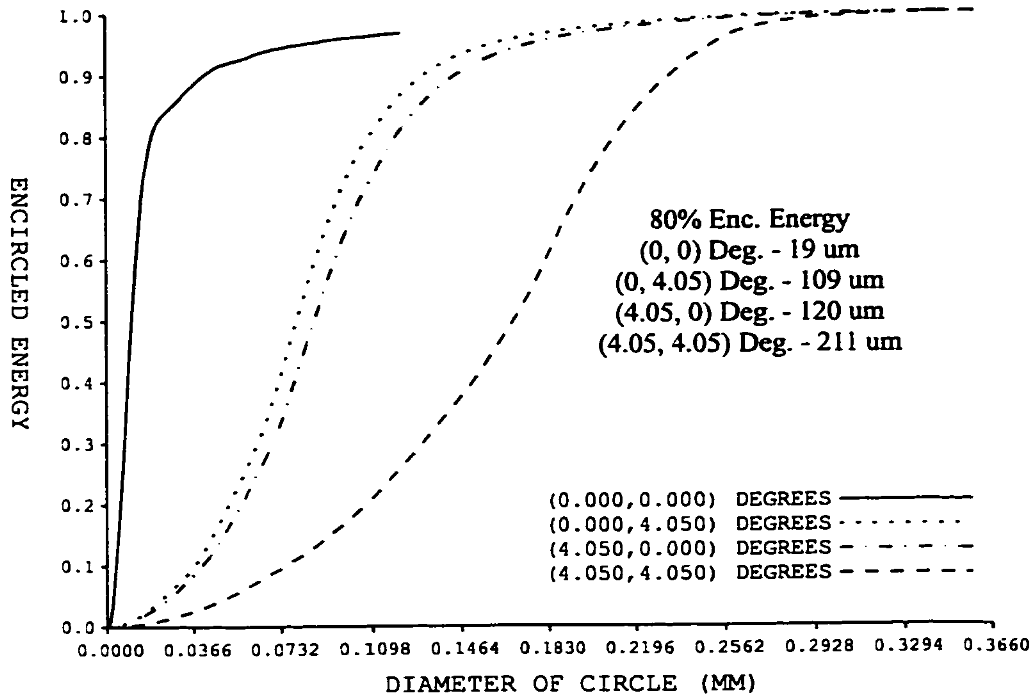

Figure 5.45 Plot of encircled energy for the 1.5X reflecting telescope.

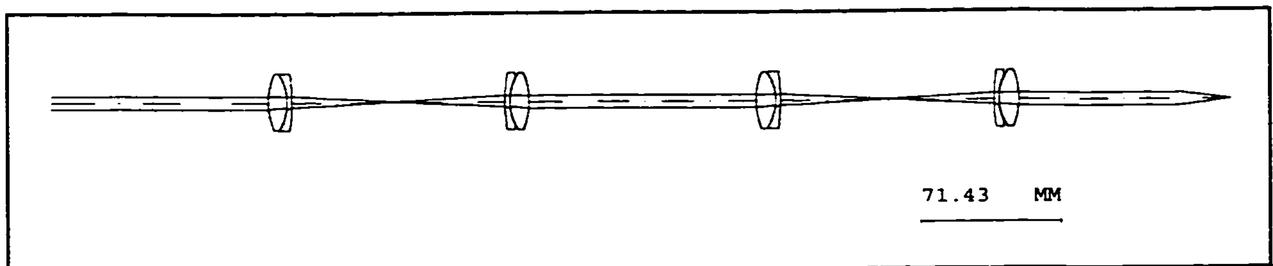

Figure 5.46 Schematic diagram of a two telescope refracting system.

So far only the effect of passing through one telescope has been studied. For the cslm, the beam passes through two telescopes on illumination and two more for emission. This clearly degrades the image further. Fig. 5.46 shows two sets of telescopes with a 0° field angle. The system from Fig. 5.33 was duplicated and assembled to produce a two telescope system. Fig. 5.47 shows the effect on the edge position PSF when another telescope is added. Fig. 5.47a shows the PSF for the single telescope with a y = 2.7°, x = 0° (edge) field angle.

Fig. 5.47b shows the PSF for the double telescope at the same scale and field angle. The image has approximately doubled in size. In general when aberrations are large, such as this case, the image size will go like the number of telescopes. Improving the telescope performance even by a small amount can be significant since its effects will be multiplicative.

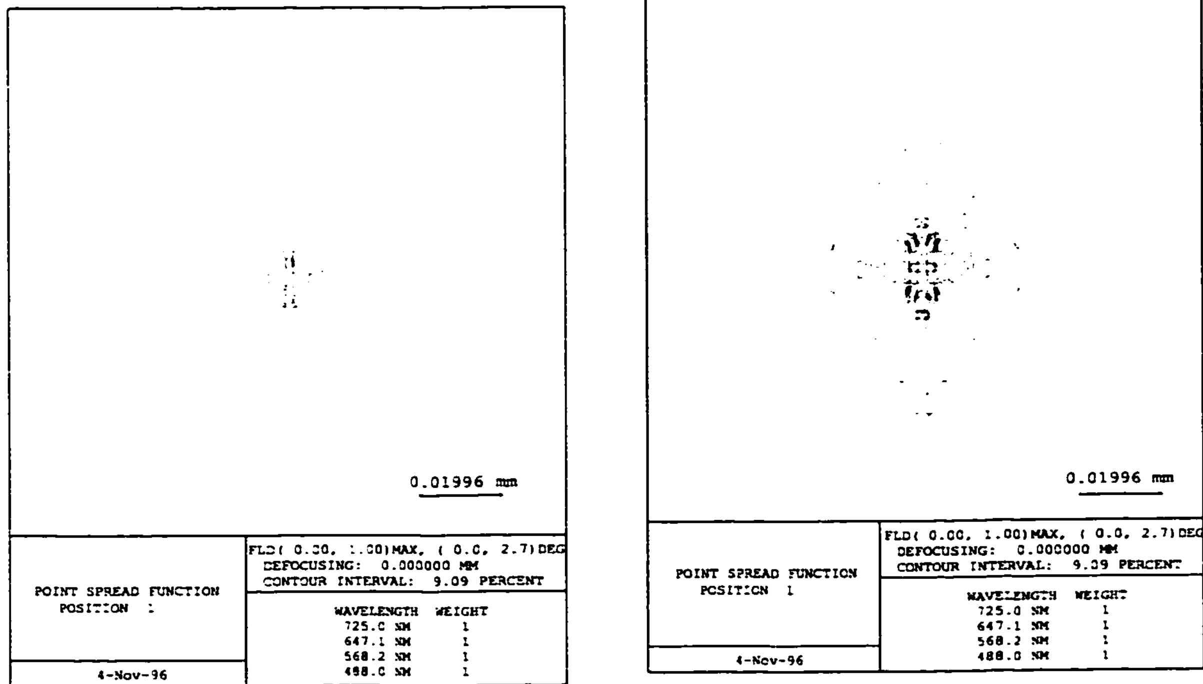

(a) (b)

Figure 5.47 PSFs for refracting telescopes at 2.7 degree field angles (a) single telescope (b) double telescope

5.5.2 Low Cost UV Objective

Most types of optical quality glass transmit poorly or not at all in the UV (<380nm). UV optics are therefore rare and most importantly, expensive. While UV quality singlets can be purchased for about $200, anything more complicated such as an achromat can cost several thousand. Optics for Research sells an air-spaced, 200 mm focal length achromat for about $2000 US. The goal of this section is to suggest a low-cost alternative for under $300 with similar imaging characteristics as the achromat. The specific motivation was to image

fingerprints which have been treated with a dye that photoluminesces at 614 nm and is excited with 325 nm light. The field of view must be at least 2x2 cm. In general, macroscopic UV imaging can be very useful since many materials autofluoresce and little has been done in this field.

Before presenting the results for the proposed designs, two interesting 'failures' will be examined. Fig. 5.48 shows a triplet made up of an equiconvex and two plano-concave singlets.

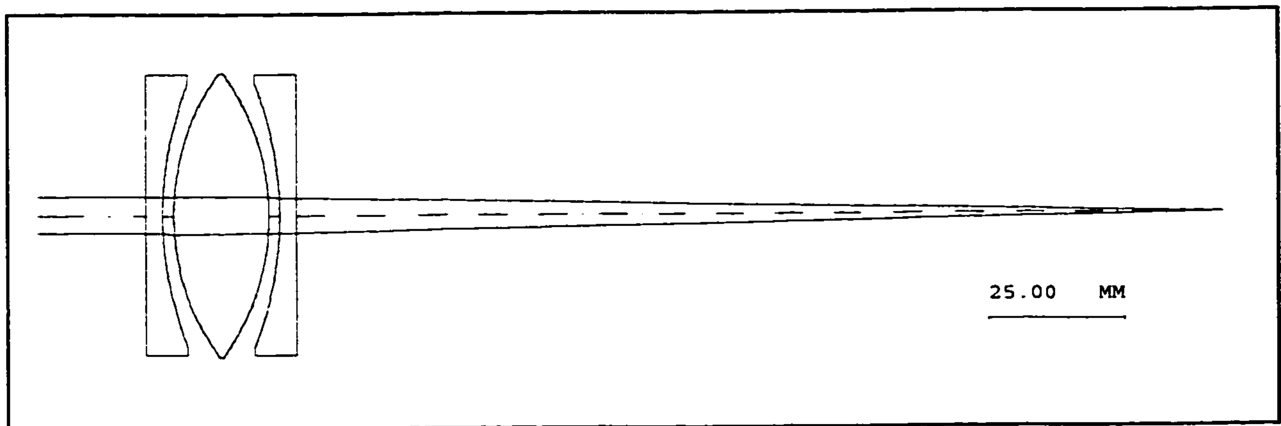

Figure 5.48 A UV triplet made up of stock item singlets.

The lenses were stock items from Edmund Scientific and JANOS made from fused silica and calcium fluoride. An attempt was made to come up with a UV triplet design and then choose stock item lenses that closely fit the CODE V generated lenses. It was found that for the triplet to work properly the last element should be a 'custom' lens and therefore too expensive. The use of all stock item lenses, as in Fig. 5.48, did not give enough degrees of freedom for proper optimization. Even if it had worked, the cost would have been close to \$1000; even singlets are expensive.

Fig. 5.49 shows an all reflecting macroscopic objective which met all the requirements except that it was physically impossible to operate due to the fact that the telecentric plane of the system lay to the right of the convex mirror. This type of reflecting objective is fully described in Smith[13]. Both these designs have a great deal of potential in becoming fully corrected systems.

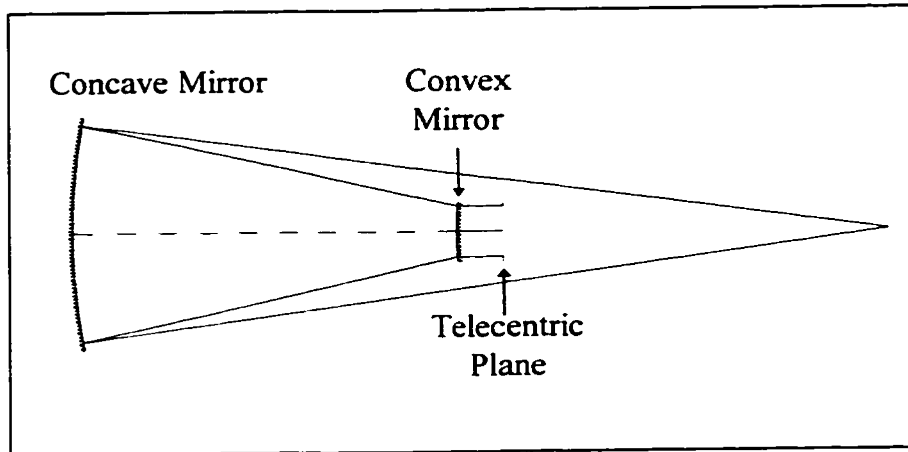

Figure 5.49 A reflecting macroscopic objective with its field angle equal to zero.

A traditional approach would be to create a low magnification all-refracting objective with materials such as fused silica and calcium fluoride. Unfortunately UV refracting objectives tend to be corrected only up to about 550 nm. Fig. 5.49 represents an attempt to design an all-reflective objective which is extremely appealing in multiwavelength applications such as UV PL and IR imaging. A full fledged multi-element, refracting design might ultimately be the solution to macroscopic UV imaging. This would require an expert lens design, high quality materials and possibly tens of thousands of dollars. One intermediate step between $100s and $10000s might be constructing a known UV triplet design. Investment in a reflecting/refracting hybrid might also yield results.

Until recently the UW-CMG has done very little macroscopic scanning beam UV imaging. The best macroscopic UV lens available in the confocal microscopy lab consisted of a 5 cm focal length, fused silica, plano-convex singlet. This lens worked reasonably over approximately a 1 cm field of view. Beyond this point, aberrations become too large. Aberrations can be reduced by increasing the f-number of the system and decreasing the field angle. The easiest approach was to increase the focal length of the singlet. It was decided that the f-number should be around 20 which falls in between the UV achromat (f_{no} 28) and the MACROscope LSL (f_{no} 12).

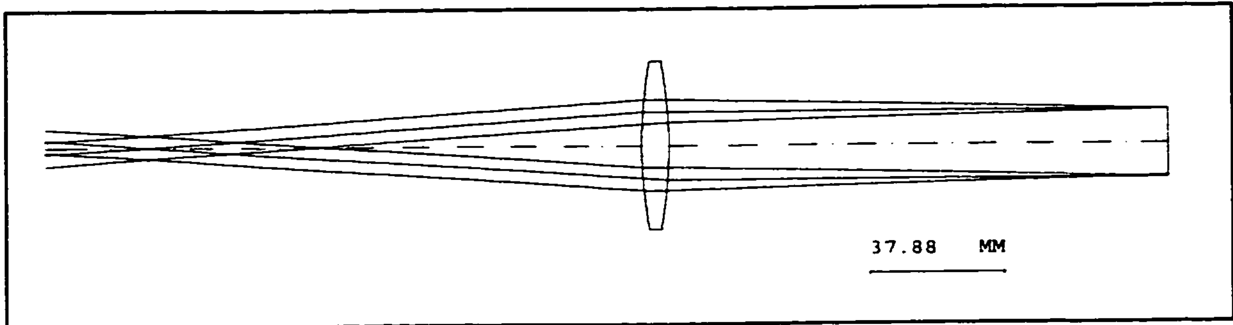

Figure 5.50 UV fused silica singlet with a 150 mm focal length and a 2 cm field of view.

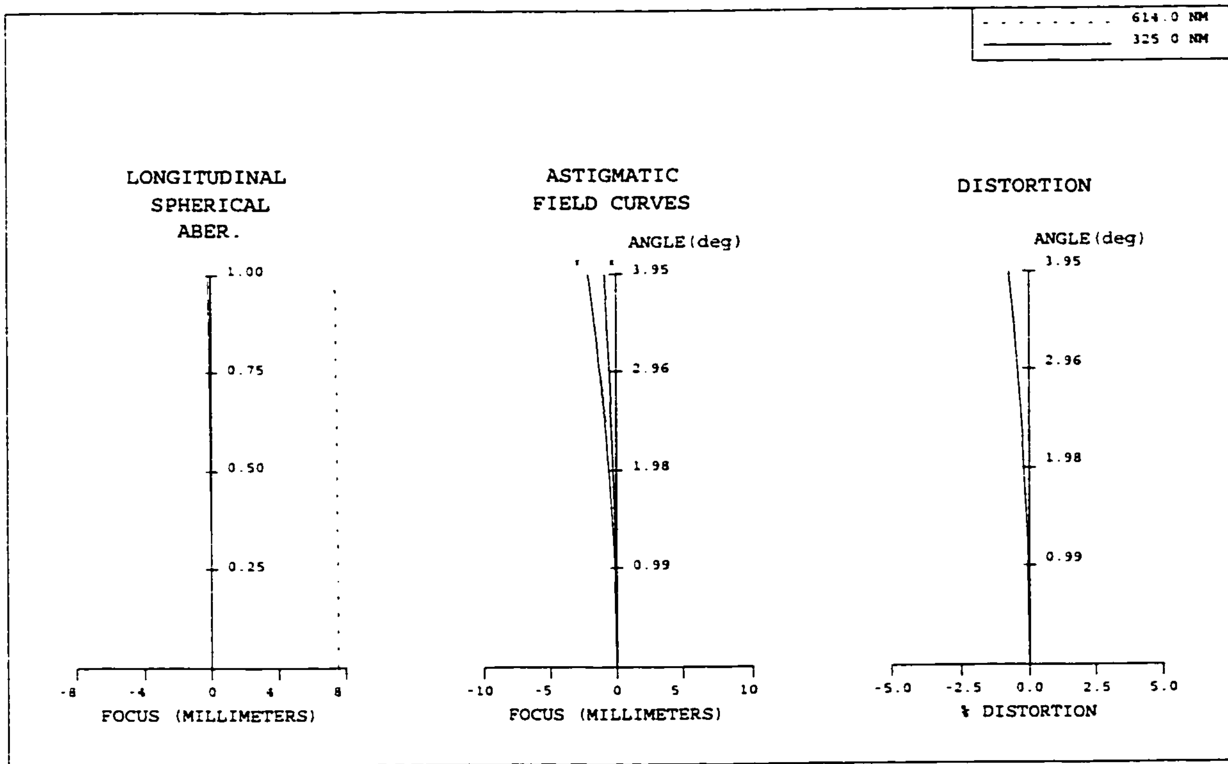

Figure 5.51 Field plot for the 150 mm focal length UV singlet.

Fig. 5.50 shows an Edmund Scientific, equi-convex, fused silica, 150 mm focal length, 50.8 mm diameter lens with a telecentric stop. The beam diameter is 7 mm and the field angle shown is ±3.95 degrees giving a 20x20 mm field of view. The design wavelengths were 614 and 325 nm. Fig. 5.51, a field plot for the above lens, shows that axial chromatic aberration dominates. A list of the third order aberrations (not shown) indicates lateral colour aberration is also quite high. The reference wavelength for this system was 325 nm from which the paraxial focus is calculated. CODE V allows the user to run a best focus routine to find a focal plane which gives the best image over the entire field of view and not just the paraxial area.

Given the large chromatic aberrations encountered with the singlet, a very simple reflecting objective was designed. Fig. 5.52 shows a 76.2 mm diameter, 152.4 mm focal length spherical mirror followed by a plane mirror. The beam diameter is 7 mm while the field angles are ±3.75° (0° is also shown in Fig. 5.52).

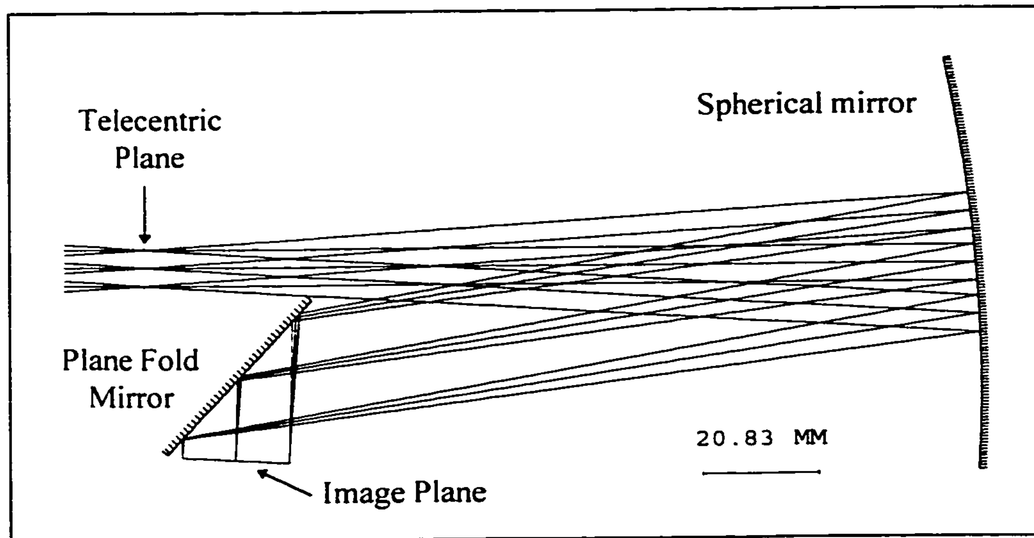

Figure 5.52 Mirror objective consisted of a tilted (4.5°) spherical mirror and a flat mirror.

As was seen in section 5.4.2, the key to reducing aberrations with a single tilted mirror was to minimize the tilt angle. This forces the image plane to be as close as possible to the telecentric plane. A fold mirror was placed as close to the incoming rays as possible and the image plane was positioned very close to the fold mirror. The final result is a mirror tilt of

4.5° which is responsible for mainly astigmatic aberrations. The system was expected to have non-symmetric aberrations. Specifically, positive field angles tend to cancel out the mirror tilt, hence spot sizes in this region will be superior in quality to the ones with negative (downward pointing) field angles. A direct comparison can be made between the UV singlet and the mirror objective by plotting PSFs for both systems at various field angles.

Figs. 5.53a, and 5.54a show PSFs for the fused silica singlet at (x,y) = (0°,0°) and (3.95°,3.95°) field angles, that is at the center and corner positions, respectively. Figs. 5.53b, and 5.54b show PSFs for the reflecting objective at (0°,0°) and (3.75°,3.75°) field angles respectively. For the singlet, the image plane was defocused by -1.2 mm from the paraxial focus in order to minimize axial chromatic aberration as seen in Fig. 5.53a. The defocus degraded the off-axis images in Fig. 5.54a. The final result for the singlet is a resolution not much better than 40 μm throughout its 2x2 cm field of view. Such a badly aberrated lens would not be expected to yield reasonable confocal PL images. The reflecting objective corrects chromatic aberrations but introduces a significant amount of astigmatism. The astigmatism is worse at negative field angles. This can be seen clearly for the corner value in Fig. 5.54b where the resolution is down to about 50 μm. The center value for the reflecting objective are quite reasonable in comparison, resolutions of 20 μm or less can be attained here. It is clear that neither system is terribly good, however, they are low cost (approximately $200 each) and in this case, you get what you pay for.

All of the design and analysis in this section for the two UV systems have assumed confocal operation which implies imaging at 325 <u>and</u> 614 nm. Non-confocal imaging where the confocal aperture is removed, or PL emissions are collected before they reach the objective, offer a greater amount of flexibility. The lateral resolution in non-confocal PL imaging will only depend upon incident beam spot size because emitted light will be collected regardless of descan or aberration by a 'large' detector. Three Edmund Scientific, double-convex, fused-silica singlets were examined with CODE V (f = 50, 100, and 150 mm; #8016, 8019, 8020 respectively) using only 325 nm light and a 7 mm diameter beam.

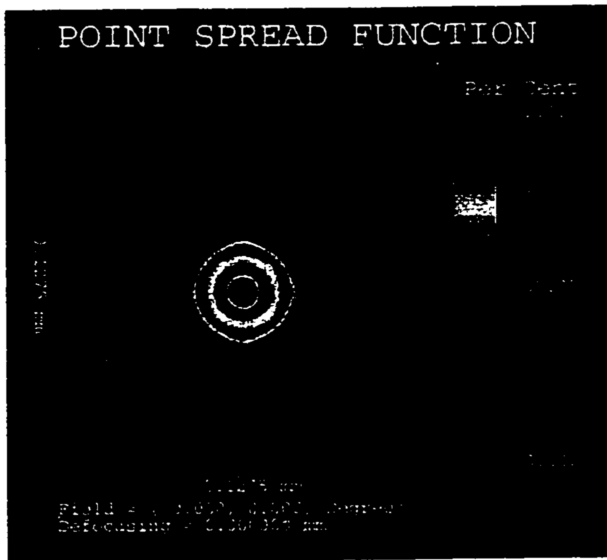

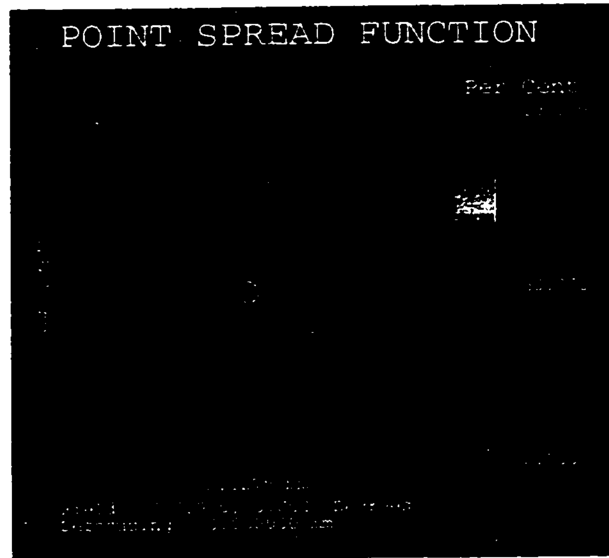

(a) (b)

Figure 5.53 PSFs at 0 degree field angles for the (a) fused silica singlet and (b) the mirror objective. The singlet has a large amount of axial chromatic aberration.

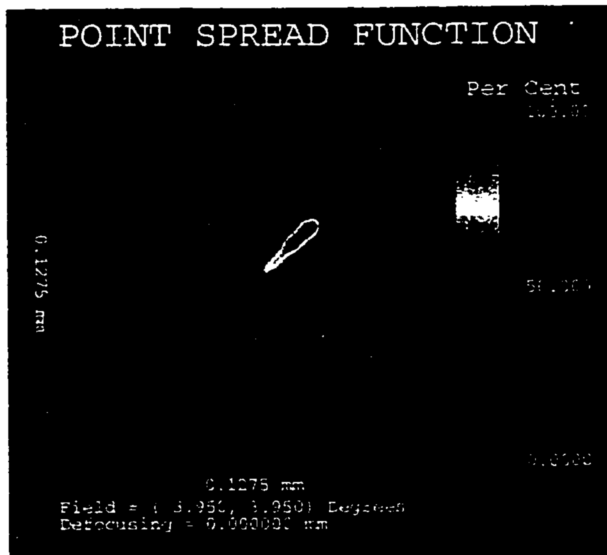

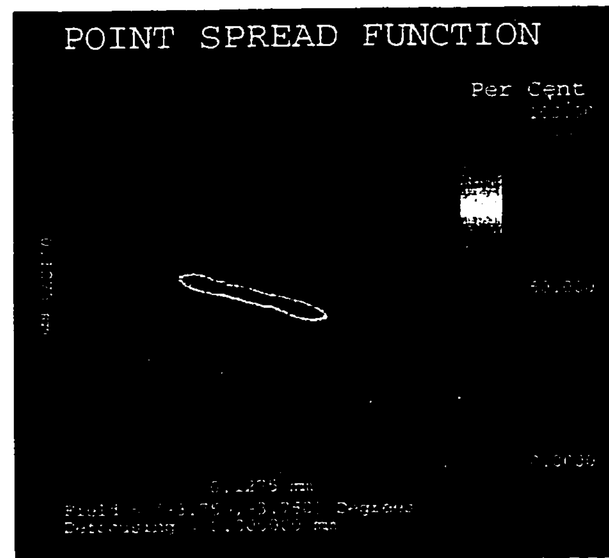

(a) (b)

Figure 5.54 PSFs for the (a) fused silica singlet at a 3.95° x and y field angle and (b) the mirror objective at a 3.75° x and y field angle.

Table 5.5 shows 80% encircled energy diameters for the three lenses at various y-field angles. The field angles were chosen so as to reach a 2 cm diameter field of view while keeping aberrations from exploding. Once the field angles were chosen a 'best focus' routine was run. Monochromatic aberrations are clearly large in singlets, as expected. Even in non-confocal operation the 150 mm focal length lens seems to be the optimum choice providing about 30 μm resolution through its field of view.

f = 50 mm		
y-field Angle	80% Encircled Energy Diameter (μm)	Field of View Diameter (mm)
0	31	0
2	28	3.3
4	45	6.7
6	94	10

f = 100 mm		
y-field Angle	80% Encircled Energy Diameter (μm)	Field of View Diameter (mm)
0	36	0
2	26	6.7
4	43	13
6	131	20

f = 150 mm		
y-field Angle	80% Encircled Energy Diameter (μm)	Field of View Diameter (mm)
0	22	0
1	21	5.5
3	32	17
4	60	22

Table 5.5 Using 325 nm light and a 'best focus' routine, 80% encircled energy diameter is shown at various y-field angles for f = 50, 100 and 150 mm fused-silica singlets using a 7 mm diameter entrance beam.

5.6 The Erfle Eyepiece Telescope

Although data for this section was obtained at the last minute, literally while writing chapter 7, a decision was made to include it due to its importance to the thesis, in the form of a self-contained section. This section describes a proposed design for the least expensive and best corrected relay lens system to date.

There are many types of eyepieces described in the literature[14,15,16,17,18] which are commonly available commercially such as: the Huygens eyepiece, the Ramsden eyepiece, the Kellner eyepiece, the orthoscopic eyepiece, the symmetrical or Plössl eyepiece, and the Erfle eyepiece. The Erfle is probably the most common wide-field eyepiece and is well corrected for all aberrations. However, 'well corrected' does not necessarily apply to the demanding world of confocal microscopy, where the smallest of aberrations can result in noticeable image degradation.

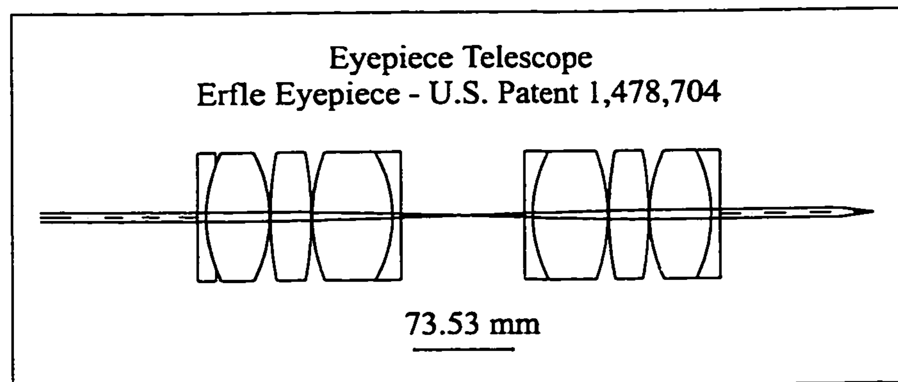

Figure 5.55 Erfle eyepiece telescope as drawn by CODE V.

CODE V has lens data for several eyepieces, including some Erfle designs. One of these Erfle eyepieces was taken, duplicated, flipped, and positioned so as to create a unitary telescope. Fig. 5.55 shows the Erfle eyepiece telescope as drawn by CODE V. Although the eyepieces in Fig. 5.55 will undoubtedly not be the ones used by UW-CMG, this analysis is still intended to give a feeling for what aberrations can be expected. The quality of present day Erfle eyepieces is expected to be equal to or better than the Fig. 5.55 design obtained form the original 1923 patent[19].

Spherical Aberration	0.001292	Distortion	0.000010
Tangential Coma	-0.000011	Axial Colour	0.012427
Tangential Astigmatism	-0.003505	Lateral Colour	-0.000035
Sagittal Astigmatism	0.000524	Petzval Curvature	-0.013176
Petzval Blur	0.002538		

Table 5.6 Third order transverse aberrations for the eyepiece telescope in units of mm. The dominant aberration, in this case, is axial colour while the other aberrations contribute many times less.

The Erfle eyepiece consists of two achromats surrounding a singlet. The first set of beam diameters, field angles, and wavelengths were exactly the same as those used with the refracting and reflecting telescopes of Appendix 6, namely, a 7 mm diameter beam, 0-2.7° field angles, a 0.14 NA ideal lens, and 488, 568.2, 647.1, and 725 nm wavelengths. Table 5.6 shows third order aberrations in mm for the eyepiece telescope.

Fig. 5.56 shows longitudinal spherical, longitudinal astigmatic, and percent distortion field plots for the Erfle eyepiece telescope. Both Table 5.6 and Fig. 5.56 show similar results for spherical and axial chromatic aberrations when compared to the achromatic telescope in Table 5.2 and Fig. 5.34. The astigmatism, however, is many times less for the eyepiece telescope than for the achromatic telescope. Since coma, distortion, and lateral colour are taken care of by the symmetry principal, only astigmatism and field curvature are left as off-axis aberrations. The Erfle eyepiece takes care of astigmatism which is really the only difference between it and the achromat in this case.

Fig. 5.57 shows an encircled energy versus diameter plot for the Erfle eyepiece telescope. It should be clear that this represents the best response of any of the telescopes analyzed in chapter 5. The 80% encircled energy diameter at the optic axis is similar to the diameter obtained with the achromatic telescope. The 80% EE diameter stays relatively constant throughout the entire field-of-view including the 2.7° and (2.7°,2.7°) field angles. This suggests a much 'flatter' response when imaging a mirror as compared to the terrible response obtained with the achromatic telescope.

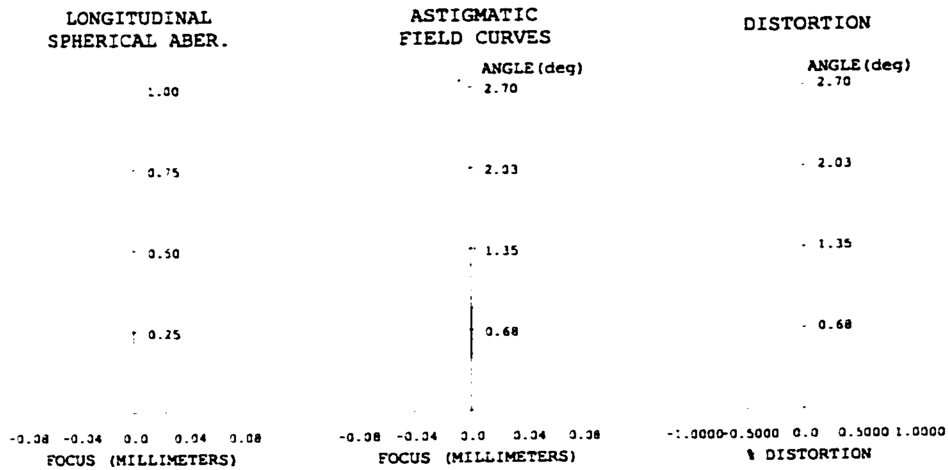

Figure 5.56 Field plot showing longitudinal spherical, longitudinal astigmatism, and percent distortion for the Erfle eyepiece telescope.

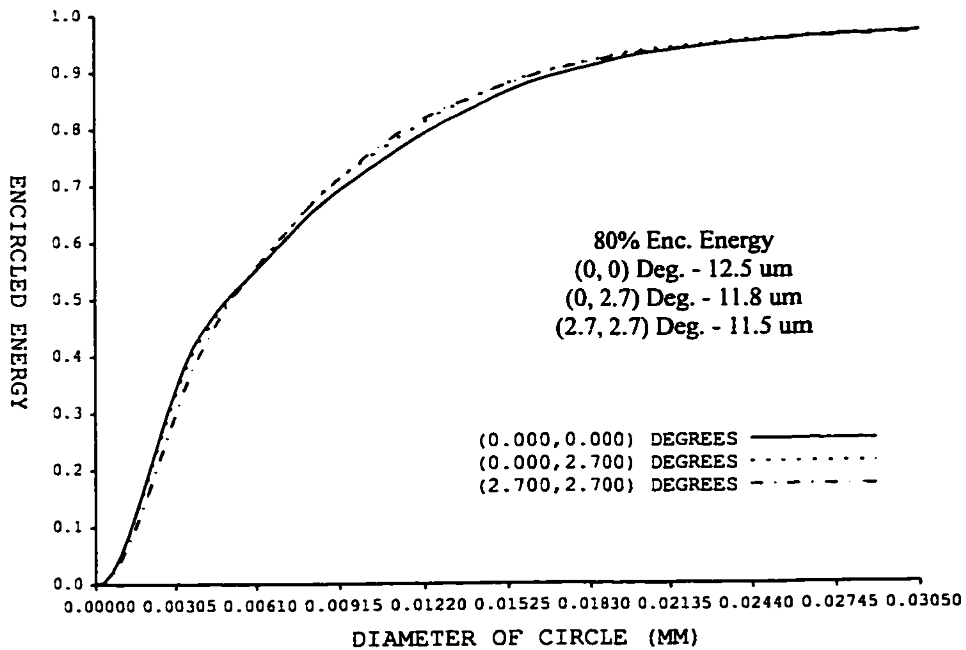

Figure 5.57 Encircled energy as a function of diameter at three different field angles for the Erfle eyepiece telescope.

The results from the eyepiece telescope were so good that it was decided to see how far the design could be pushed without encountering large aberrations. Tables 5.7 and 5.8 show 80% encircled energy diameters as the entrance pupil is progressively increased from 10 to 15 and 20 mm diameters.

	80% Encircled Energy Diameter (μm)	
Field Angle	10 mm Entrance Pupil	15 mm Entrance Pupil
(0°,0°)	20	46
(0°,2.7°)	22	48
(2.7°,2.7°)	22	50

Table 5.7 80% encircled energy diameters for the Erfle eyepiece telescope using 10 mm and 15 mm diameter entrance pupils.

Field Angle	80% Encircled Energy Diameter (μm)
(0°,0°)	75
(0°,2.7°)	78
(0°,5°)	76
(5°,5°)	97

Table 5.8 80% encircled energy diameters for the Erfle eyepiece telescope using MACROscope entrance pupils (20 mm diameter) and field angles.

The 10 mm entrance pupil allows the 0.42 NA Mitutoyo objective to be overfilled while the 15 mm entrance pupil does the same for the 0.14 NA Mitutoyo objective. The 80% EE diameters are relatively constant throughout the field of view. The 10 mm entrance pupil 80% EE diameter is about 21 μm and the 15 mm entrance 80% EE diameter is about 48 μm. The increase in size is primarily due to spherical aberration and axial chromatic aberration which suggests that a search should be made for an apochromatic wide field eyepiece. Only when 20 mm entrance pupil and 5° field angles are used does the Erfle eyepiece telescope show signs of astigmatism in addition to the ever increasing spherical and axial chromatic aberrations. Experimentally all these configurations can and should be tested in order to reveal what effects they have on images.

The above data implies that Erfle eyepieces, in general, have a good probability of providing superior imaging quality than the achromats. Erfle eyepieces are inexpensive and abundant commercially. Edmund Scientific, for example, sells two Erfle eyepieces: one for U.S. $85 and the other for U.S. $187 differing in aperture and focal length. The possibility of providing better performance than the achromatic telescopes, at a lower cost, and with a more compact design is certainly enticing.

5.7 Summary and Discussion

CODE V was initially used to characterize unitary telescopes made with off-axis parabolic mirrors. Their use in the BioRad confocal microscope suggested that they could provide superior performance than the currently used achromatic doublet telescopes. This chapter has analyzed various reflecting telescope configurations and compared them directly with the existing refracting telescope used on the cslm. Care was taken to insure a fair comparison. CODE V allowed simulations with the actual lens specification from the Melles Griot catalog for the achromats, while specifications from the JANOS catalog were used to simulate the parabolic mirrors. This chapter has shown that the reflective telescope is indeed superior to the refractive one, and also allows for a greater flexibility in its construction. Unfortunately the reflective telescope design cannot be used on the MACROscope since both the beam diameter and field angles are too large. Another problem is that JANOS itself has said that its mirrors might not meet imaging quality standards due to a 'large' amount of scatter. Further research is needed to determine their actual quality. For primarily reflected-light imaging and visible light PL imaging the eyepiece telescope seems to hold great promise since it provides a very uniform response over the entire field of view. If the eyepieces are carefully chosen, a relay lens will result with a superior performance, more compact design, and at a reduced cost compared to either the achromatic or reflecting telescope designs.

CODE V was also used in determining the maximum allowable tilt angle for spherical mirrors used in the construction of a beam expander and as part of the detector arm. Generally angles under 5° allowed for near-diffraction-limited operation.

CODE V also proved useful in designing and characterizing a very low cost UV objective to be used in the analysis of fingerprints. The lens chosen for this turned out to be a 150 mm

focal length, fused silica, double convex singlet. It provided about 30 μm resolution over a 2 cm diameter field of view in non-confocal mode. Confocal imaging does not seem to improve imaging quality in this case.

Several new contributions were made in this chapter:

1) The effects of small tilts in spherical mirrors was studied with respect to beam expanders and detector arm optics.
2) The existing unitary telescope was compared to a reflecting telescope and an eyepiece telescope via CODE V.
3) A reflecting telescope made up of off-axis parabolic mirrors has never been analyzed in the literature.
4) The eyepiece telescope represents an innovative, well-corrected relay that has never been described in the literature.

REFERENCES

[1] W. J. Smith, Modern Optical Engineering-The Design of Optical Systems, 2nd Ed., (McGraw-Hill, New York, 1990), p59.

[2] W. J. Smith, Modern Optical Engineering-The Design of Optical Systems, 2nd Ed., (McGraw-Hill, New York, 1990), p58.

[3] W. J. Smith, Modern Optical Engineering-The Design of Optical Systems, 2nd Ed., (McGraw-Hill, New York, 1990), p30.

[4] E. Hecht, Optics, 2nd Ed., (Addison-Wesley, Reading Massachusetts, 1987), p421.

[5] M. Born, E. Wolf, Principles of Optics, 6th Ed., (Pergamon Press, Oxford, 1991), p478.

[6] M. Born, E. Wolf, Principles of Optics, 6th Ed., (Pergamon Press, Oxford, 1991), p479.

[7] E. Hecht, Optics, 2nd Ed., (Addison-Wesley, Reading Massachusetts, 1987), p227.

[8] W. J. Smith, Modern Optical Engineering-The Design of Optical Systems, 2nd Ed., (McGraw-Hill, New York, 1990), p372 - 375.

[9] M. Born, E. Wolf, Principles of Optics, 6th Ed., (Pergamon Press, Oxford, 1991), p398.

[10] M.R. Spiegel, Mathematical Handbook of Formulas and Tables, (Schaum's Outline Series, McGraw-Hill, New York, 1990), p38.

[11] E. Hecht, Optics, 2nd Ed., (Addison-Wesley, Reading Massachusetts, 1987), p510.

[12] J.W. Goodman, Introduction to Fourier Optics, (McGraw-Hill, New York, 1968), p83.

[13] W. J. Smith, Modern Optical Engineering-The Design of Optical Systems, 2nd Ed., (McGraw-Hill, New York, 1990), p415.

[14] E. Hecht, Optics, 2nd Edition, (Addison-Wesley, Reading, Massachusetts, 1987), p188.

[15] W.J. Smith, Modern Optical Engineering-The Design of Optical Systems, 2nd Edition, (McGraw-Hill, New York, 1990), p403.

[16] M.H. Freeman, Optics, 10th Edition, (Butterworths-Heinemann, Oxford, 1990), p199.

[17] G.W. White, Introduction to Microscopy, (Butterworths, London, 1966), p48.

[18] J.H. Richardson. Handbook for the Light Microscope—A User's Guide, (Noyes. Park ridge, New Jersey, 1991), p87.

[19] Erfle, U.S. Patent #1478704, 1923.

CHAPTER 6

THE FULLY INTEGRATED CONFOCAL SCANNING LASER MACROSCOPE / MICROSCOPE

The MACROscope was initially developed as an instrument separate and distinct from a confocal scanning laser microscope (cslm). The MACROscope was designed to act as a scaled-up version of a cslm providing high resolution, large field of view confocal images. It was immediately apparent that a system providing both the confocal microscopic imaging techniques from a cslm and the macroscopic capabilities of the MACROscope would be a very useful combination. In previous chapters, the cslm and MACROscope have referred to separate instruments assembled on different optical platforms. Any reference to a Confocal Scanning Laser MACROscope/Microscope (cslM/m), up to this chapter, has implied the use of two distinct instruments with their own optics and electronics. This combination of instruments can be thought of as a MACROscope/Microscope station with each of the instruments on either side of the user. One of the goals of the UW-CMG is to design and construct a fully integrated cslM/m. A design which integrates the MACROscope and cslm into a common set of optics and electronics is described by Dixon[1] in U.S. patent #5532873. Fig. 6.1 shows a schematic diagram of the cslM/m taken from the above patent. A working instrument based on this design was constructed by S. Damaskinos. The schematic of Fig. 6.1 basically combines features from the cslm of Fig. 3.1 and the MACROscope of Fig. 3.24. In MACROscope mode, the cslM/m suffers beam splitter problems in addition to off-axis aberrations caused by the unitary telescopes. In cslm mode, aberrations caused by the achromatic doublet unitary telescope are present. This chapter aims to investigate possible improvements to the MACROscope and especially the cslm. An improved design for a fully integrated cslM/m will also be presented.

The first section in this chapter examines a commercial confocal microscope (BioRad) in detail, describing its advantages and disadvantages. Many improvements to the cslm and MACROscope can be obtained by studying the BioRad and other commercial confocal

microscopes. In the next section, improvements are described for each part of the cslm and MACROscope. The last section applies these improvements to a fully integrated version of the cslM/m. The primary, new contribution made in chapter was to clearly define features needed on a fully integrated single instrument MACROscope-Microscope.

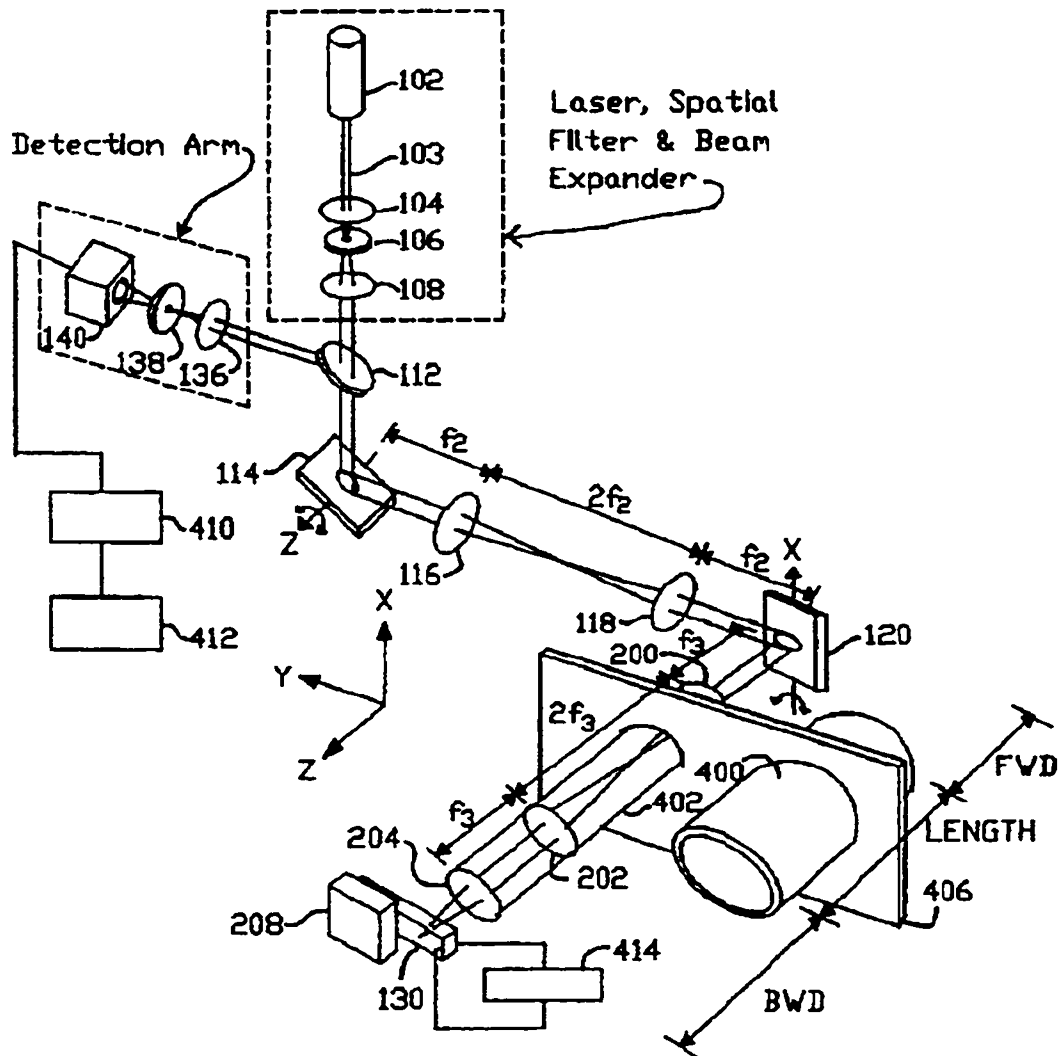

Figure 6.1 A fully integrated version of the cslM/m taken from A.E. Dixon's U.S. Patent #5532873. In microscope mode the instrument is similar to the current version of the cslm. In both modes, the unitary telescopes cause a significant amount of off-axis aberration.

6.1 Commercial Confocal Microscopes

Commercial confocal microscopes have been around since about 1987 and most manufacturers are currently producing second and third generation instruments. Although no single design seems to dominate, much can be learned from the industry. This section studies the BioRad confocal microscope for two reasons: the BioRad closely resembles the UW-CMG cslm and its design has been patented offering a very detailed view of its structure. Advantages and disadvantages of the BioRad will be listed and comparisons with other commercial confocal microscopes will be made.

Fig. 6.2 shows a schematic diagram of a BioRad confocal scanning laser microscope. The diagram was taken from the Confocal Handbook[2] which in turn is taken from a patent by White[3]. A laser beam is inserted via a single-mode optical fiber on the middle-right of the diagram. This has the advantage of de-coupling the laser head and cooling fan from the microscope which reduces vibrations significantly. The laser beam strikes the first dichroic beam splitter which reflects short wavelengths and transmits long wavelengths (this is a standard stock item commercial dichroic unlike the ones used by UW-CMG until recently). The dichroic assembly consists of the dichroic beam splitter, a laser line filter, and a long-pass filter, all encased within a cylindrical holder which is made to be removed and inserted by the user. This cylindrical filter holder allows the user to choose between a wide variety of filter combinations without ever having to touch the filters since there can be one holder for each application. After the filter holder the beam strikes mirror 1, which will be one of two types: multilayer dielectric providing > 98% reflectivity in the visible, or MgF_2-coated aluminum which provides > 90% reflectivity from the UV to the IR. The laser beam is then deflected by the Y-axis scanning mirror, passes through a mirror relay, and then is deflected by the X-axis scanning mirror. The mirror relay consists of two off-axis parabolic mirrors which make up a telescope similar to the ones described in chapter 5 of this thesis. The arrangement offers good telecentricity, no chromatic aberrations, and small off-axis monochromatic aberrations. This type of scanning system has been patented by Amos[4] with BioRad having obtained the rights to it. One disadvantage of this scanner arrangement is that it contains four mirror surfaces which with time will decrease in reflectivity.

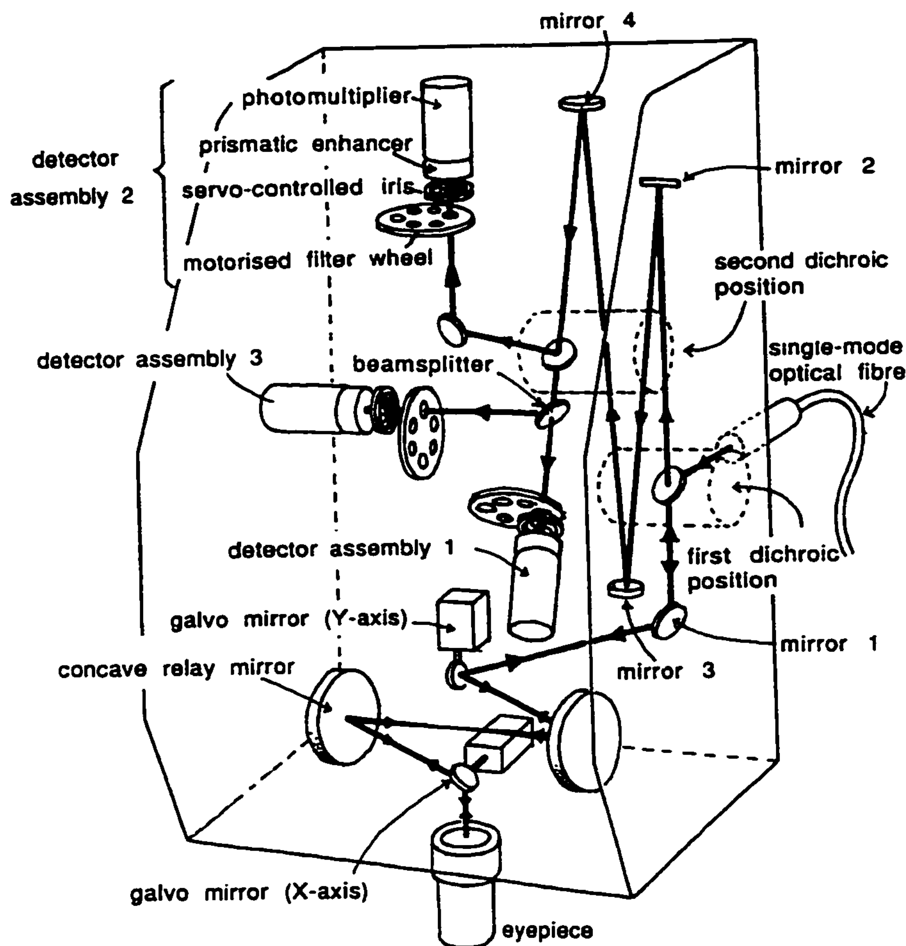

Figure 6.2 Optical arrangement for the BioRad confocal microscope. The BioRad has several innovative features such as a patented off-axis parabolic mirror relay, a 'no detector lens' arrangement, and a PMT prismatic enhancer. The BioRad has a large number of mirror surfaces which can cause problems with alignment and collection efficiency as the mirrors degrade with time. Figure taken from the Confocal Handbook[2].

The single x-y scanning mirror employed by Leica is clearly superior to the BioRad scanner system since four mirrors are reduced to a single surface and off-axis aberrations are eliminated. After the scanning mirror assembly the beam enters the eyepiece of a conventional wide-field microscope. The X-axis scanning mirror sits on the telecentric plane of the combined eyepiece-objective lens optical system which acts like a virtual infinity-corrected microscope objective as shown in Fig. 2.2. The entire BioRad 'box' literally sits on top of a conventional wide-field fluorescence microscope. Almost all commercial confocal

microscopes are built around, and can be operated as wide-field microscopes which gives the user a great deal of added flexibility. In theory, the combination of eyepiece and microscope objective is well-corrected for all aberrations.

Light returning from the specimen is descanned and passes through the first dichroic beam splitter to be deflected by mirrors 2, 3 and 4. These mirrors are used to fold the beam in order to provide a long enough path length such that no detector lens is required. The combination of high microscope objective NA and long objective to detector path length effectively creates a confocal effect. When defocused, the detector will collect very little light from the objective / eyepiece's highly divergent beam. A longer path length will result in increased confocality. The lack of a detector lens allows BioRad to use a servo-controlled iris diaphragm which eliminates alignment problems associated with micron-sized confocal pinholes. Such a large number of mirror surfaces will cause problems with collection efficiency as they degrade in quality with time. Leica avoids the fold mirrors by employing an adjustable, computer-controlled, micron-sized, square pinhole in combination with a detector lens. On the BioRad, the beam reflected from mirror 4 passes through 2 additional beam splitters and enters one of three PMTs providing a wide variety of imaging options such as backscatter imaging (RL), fluorescence imaging, differential phase and interference contrast, etc. The head-on PMT heads are fitted with prismatic enhancers which increase the detector sensitivity to long wavelengths. Fig. 6.3 shows how the enhancer works. All head-on PMTs are enveloped by protective glass or quartz sheaths. By coupling a prism to this sheath, a beam can be inserted at a large enough angle, with respect to the normal of the PMT face, such that the beam will be totally internally reflected between the photocathode and the glass sheath. This technique, described initially by Gunter[5], is shown by Pawley[6] to increase the quantum efficiency by 60% at 520 nm, 180% at 690 nm, and 220% at 820 nm.

In addition to using very efficient optical systems, commercial confocal microscopes also have extensive interface and imaging software which can be important when assessing the overall performance of a cslm. Although the BioRad and other commercial microscopes are well designed, they are by no means perfect.

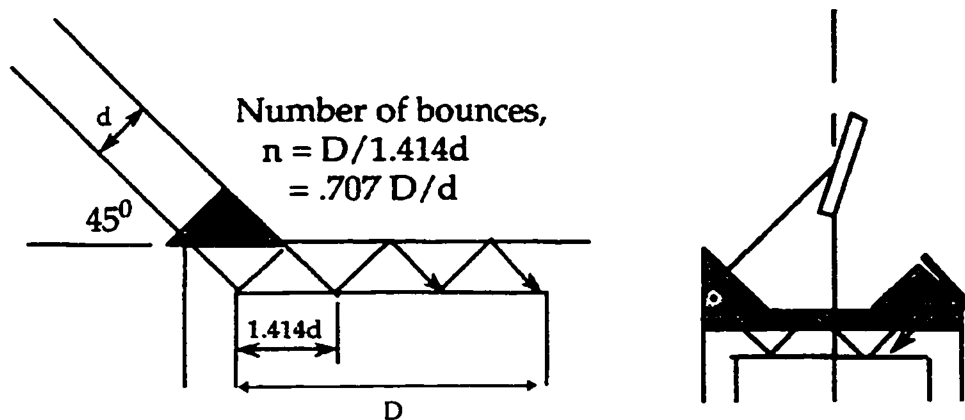

Figure 6.3 Two possible configurations for a PMT prismatic enhancer. The most basic configuration is shown on the left where a 45°-90°-45° prism is coupled to the glass sheath of a head-on PMT such that a beam can be inserted at an angle exceeding the critical angle of the sheath-air interface. PMT operation is enhanced since the reflected part of the beam (from the photocathode) will be totally internally reflected back towards the photocathode. The schematic on the right shows a prismatic enhancer which accepts an incident beam normal to the PMT face in addition to providing an extra set of internal reflections. Figure modified from Confocal Handbook[6].

Like any instrument confocal microscopes must be regularly maintained, the various optics must be aligned occasionally, and as was mentioned several times above, mirrors will require re-coating every couple of years to maintain peak performance. Fig. 6.4a shows a 1 x 1 mm, RL (488 nm) confocal image of a flat mirror taken with a 40X, 0.55 NA Nikon objective on a BioRad MRC 600 confocal microscope. The image is very poor and shows several imaging problems:

1) The x-scanning mirror is misaligned such that the edges of the microscope objective's field-of-view are showing on the left top and bottom corners.
2) The image has a non-uniform intensity distribution which indicates that aberrations are present such as the ones discussed in chapter 3 of this thesis (non-telecentricity, off-axis aberrations, etc.).
3) The circular structures inside the white boxes are not part of the image and are probably caused by internal reflections from dirty optics.

4) The horizontal band structure is most likely caused by vibrations originating from the laser, which was not linked to the microscope via fiber-optic cable.

Fig. 6.4b shows a 1 x 1 mm, RL (488 nm) confocal image of the same mirror taken with a 10X, 0.3 NA Zeiss objective on a Zeiss LSM 410 confocal microscope. The Zeiss microscope was much newer than the BioRad and only shows a restricted field of view caused most likely by non-telecentric operation since two closely spaced scanning mirrors are used in the Zeiss. The images in Fig. 6.4 illustrate one of the major differences between commercial and laboratory microscopes. While laboratory microscopes are continually adjusted and tuned, commercial microscopes must be rugged and reliable, needing few adjustments. This suggests a simple and forgiving microscope design. Fig. 6.4 also shows that the flat mirror imaging 'test' is a difficult test to pass even for a commercial cslm and serves as a good way to gauge the optical quality of a cslm.

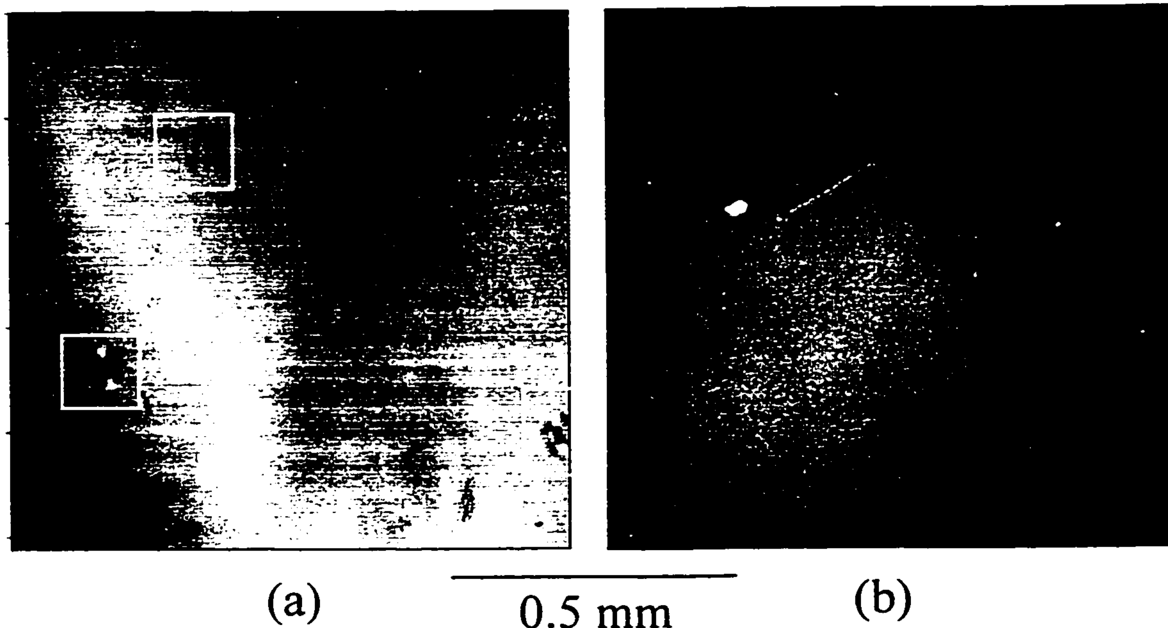

Figure 6.4 (a) Confocal RL (488 nm) image of a flat mirror taken with a BioRad MRC 600 cslm. The image quality is very poor showing signs of aberrations, non-telecentricity, misalignment, and internal reflections. While the BioRad might have a good design it still requires regular maintenance and alignment. (b) Confocal RL image of the same specimen taken with a Zeiss LSM 410. This microscope is newer than the BioRad and seems to show signs of mild non-telecentricity possibly due to its scanning mirror arrangement.

6.2 Possible Improvements for the MACROscope and cslm

In this section of the chapter each part of the cslm and MACROscope will be examined and a set of possible improvements will be suggested with a fully integrated cslM/m in mind.

6.2.1 Laser Arm

The laser arm can be the least or the most expensive part of the cslM/m to improve depending on what is desired. UW-CMG has found the adjustable power multi-line laser capability to be very useful. The Ar-Kr laser, providing red, green and blue laser lines is adequate in most imaging situations. Its major drawback is that the cooling fan produces vibrations which can be problematic in very sensitive situations such as high NA confocal imaging and imaging involving interferometry. The vibration problem is partially alleviated by using an air table or similar vibration isolation system which is needed even if the laser is noiseless. A better alternative is to simply remove the laser from the optical bench with use of an optical fiber. Although fiber-optic coupling adds several thousand dollars to the price of a laser it provides a great deal of flexibility and is commonly used in commercial confocal microscopes. Results from chapter 3 indicate that given a standard TEM_{00} laser beam, spatial filtering only results in a slight increase in performance for the cslm. Intuitively, a very 'clean' spatially filtered beam only becomes important when all of the optics in a confocal microscope are very nearly diffraction-limited. In other words use of spatial filtering should be considered only after problems with the beam splitter, scanning mirrors and relay optics are addressed.

Two-photon imaging[7] has been steadily gaining in popularity over the past several years and some of the commercial manufacturers of confocal microscopes have started offering this capability. The technique involves using short-pulse lasers (pico and femto second) which provide instantaneous intensities on the order of 10^{12} W/cm^2. At such high intensities, two-photon processes can occur where fluorophores absorb two photons of wavelength λ simultaneously. From the point of view of the fluorophore, it is as if a single photon of wavelength $\lambda/2$ has been absorbed. The implication of this is that UV-PL imaging can be done by using visible light (red) excitation without UV optics. More importantly two-photon

events will only occur near or at the focal plane producing a confocal effect without a confocal pinhole. Excitation only at the focal plane means that bleaching is restricted to this area unlike one-photon excitation where bleaching occurs along the incoming and outgoing cones of light. In addition to two-photon imaging, the short pulse lengths allow time resolved and PL lifetime imaging to be performed. The major drawback of ps or fs pulsed lasers is their price, which can reach ~ $150,000.

6.2.2 x-y Scanner

The choice of scanning mirror arrangement for the cslM/m is critical in determining the ultimate performance of the instrument. The x-y scanner must provide adequate telecentricity in microscope mode and also allow wide angle, large beam diameter operation in MACROscope mode with little or no aberrations. The four basic choices of scanner arrangement were outlined in section 2.3.3:

1) Two scanning mirrors with an intermediate telescope or relay optics (Fig. 2.17). The results from chapter 5 show that off-axis parabolic mirror-based relay optics work well in microscope mode but fail in MACROscope mode. A plan-apochromatic relay system which can accommodate 2 cm diameter beams and ± 10° scan angles would undoubtedly involve many elements and be very expensive to manufacture. Unless these kind of telescopes exist commercially it is very doubtful this kind of scanner arrangement is feasible.
2) Two scanning mirrors spaced as close together as possible with no intermediate optics (Fig. 2.18). This is the current scanner arrangement used on the MACROscope, which works reasonably well. Given a 2 cm diameter beam the minimum separation between the scanning mirrors is about 3 cm from center to center. If the 0.7 NA Mitutoyo objective is used with an ideal relay lens (between the scanners and objective), then the best position for telecentric plane is in between and equidistant from the two scanning mirrors. From Fig. 3.31, x = 1.5 cm and f = 2 mm, such that the angle made by the incident beam with respect to the optic axis at the specimen is given by Eqn. 3.5:

$$\alpha = \tan^{-1}\left[\frac{x}{f}\tan\theta\right] = \tan^{-1}\left[\frac{15}{2}\tan 2.7^\circ\right] = 19^\circ$$

This represents a large telecentric error where a ±2.7° scan angle has been assumed.

The x-y mounting brackets for two closely spaced scanners are available commercially and are easy to implement. Although this scanner arrangement works well for MACROscope mode it is doubtful that microscope mode would fair well, especially at high NA.

3) Two closely spaced mirrors with one mirror sitting off to one side of the scanner's rotational axis as shown in Fig. 2.19. The performance of this arrangement in MACROscope mode would probably be comparable to the system in 2). The telecentric error in microscope mode is hard to predict and experimental results are clearly needed at this point. In addition to the two mirror paddle scanner configuration of Fig. 2.19, the 'golf-club' configuration[8] and the 'beam conditioner' configuration[9] provide the same kind of performance (see Fig. 6.5). All the above systems have the advantage of minimizing laser spot movement on the second scan mirror which implies a reasonably sized mirror can be used. A wide beam diameter scanner arrangement of this sort is not available commercially and would therefore have to be developed. Time would probably be better spent developing a single mirror system.

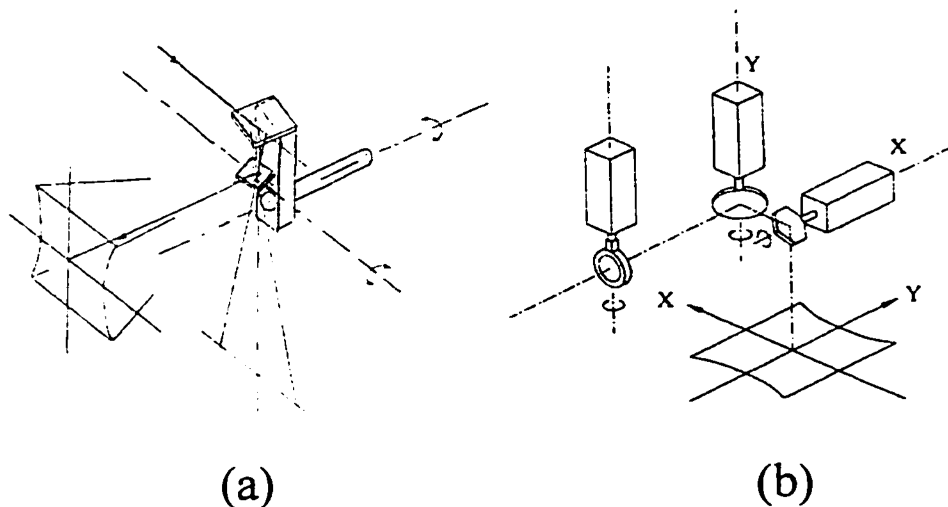

Figure 6.5 (a) 'Golf-Club' two scanning mirror configuration. (b) 'Beam conditioner' two scanning mirror configuration. Both configurations minimize laser spot movement on the second scanning mirror.

4) A single scan mirror which pivots in both x and y direction. In Fig. 2.20 a conventional scanner pivots the mirror in one direction while the other pivot direction is achieved by rotating the entire scan unit such that the center of rotation is coincident with the mirror center. The single mirror scanner has many advantages such as no telecentric error, no aberrations due to intermediate optics and good transfer efficiency since there is only one reflecting surface. The main problem with the one-mirror scanner is that it is not readily available commercially. This does not mean that it is impossible to construct since Leica has developed its own 1 mirror x-y scanner. Even if the Leica scanner can be purchased separately, it might not be suitable since it has most likely been designed to accept < 5 mm diameter beams.

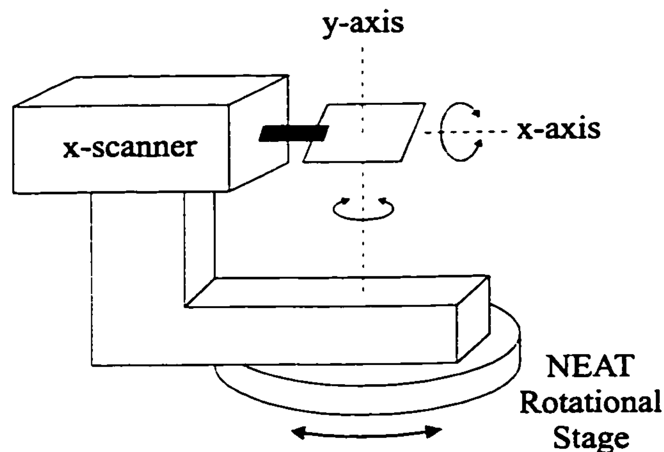

Figure 6.6 A single mirror x-y scanner constructed using existing equipment at UW-CMG. The x-y motion can be achieved by rotating a conventional x-scanning galvanometer such that the axis of rotation of the NEAT stage runs through the center of the mirror.

The easiest and cheapest way to construct a single-mirror scanner is to take an existing galvanometer scan unit (x-scanner) and find a way to rotate it accurately about the mirror center. Fig. 6.6 shows a system which can be constructed with existing equipment at UW-CMG. It consists of a standard Cambridge Technology optical scanner with a suitable mirror (2 cm beam), mounted on a NEAT rotational stage such that the central axis of rotation for the NEAT RT-4-SM stage goes through the center of the scan mirror. The NEAT stage has a resolution of 35 μradians at its most accurate setting which is equivalent to 16 micron

resolution on the MACROscope. Clearly a substantial amount of work must be done before the single mirror scanner achieves commercial grade quality. Although not commercially available, single mirror scanners have been constructed as prototypes especially for strategic defense initiative applications. Two types of single mirror prototypes constructed by General Scanning[9] are shown in Fig. 6.7. The existence of these prototypes give at least some hope of obtaining a single mirror scanner for the cslM/m.

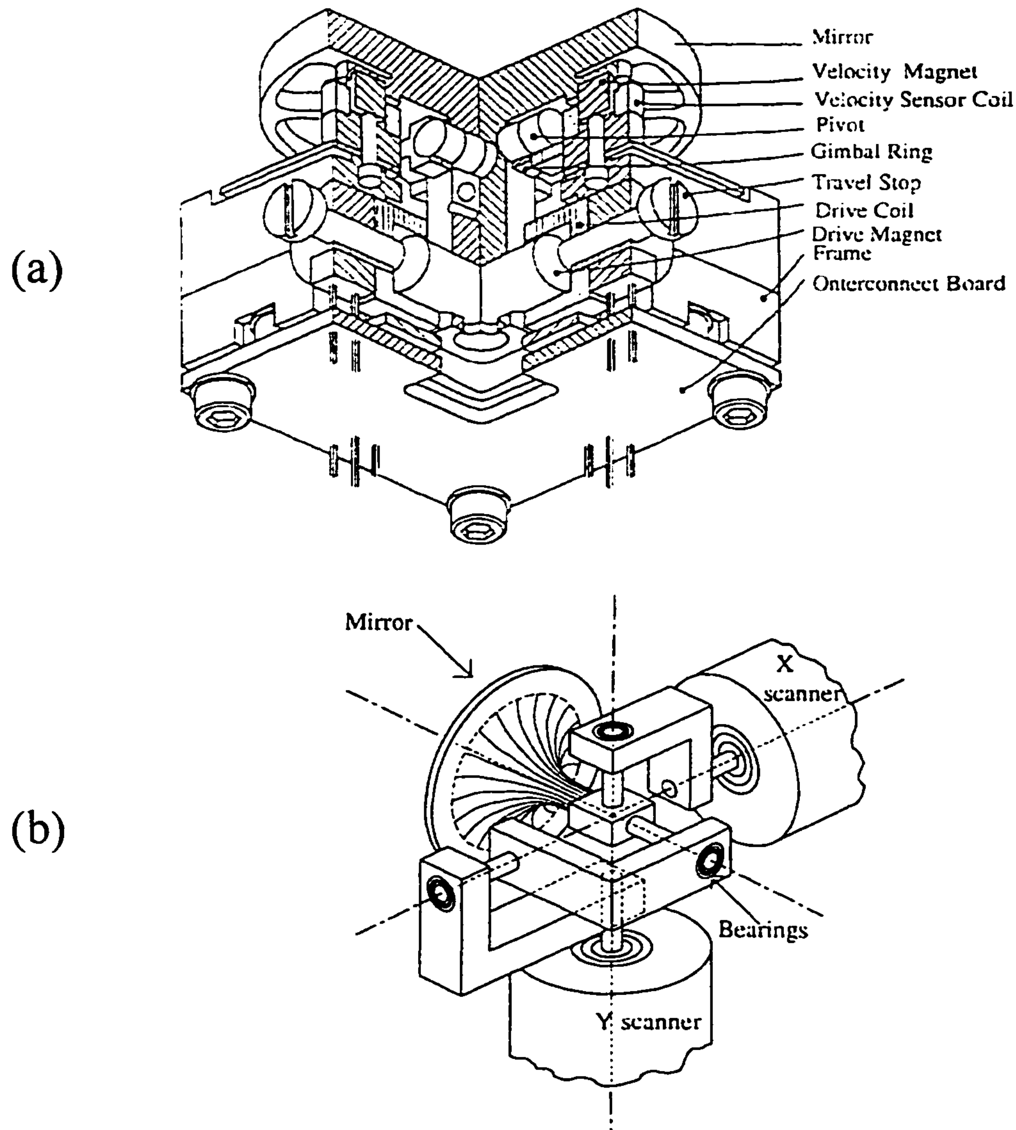

Figure 6.7 (a) Moving magnet, single mirror, two-axis beam scanner developed by General Scanning. This extremely compact design provides a > 30 mm mirror diameter with a ±6° scan angle. (b) Wide angle galvanometer-driven single-mirror scanner. Figures taken from Montagu[9].

6.2.3 Objective and Specimen Stage

Most microscope objectives have their telecentric planes residing inside the objective such that some kind of relay optics are needed to couple with a scanning mirror. UW-CMG has traditionally used telescopes formed by a pair of achromatic doublets as relay optics which results in large off-axis aberrations as shown in chapter 5 of this thesis. This section assumes all plan-apochromatic objectives to be of equal quality regardless of brand name since any small difference between Nikon, Zeiss, Olympus, etc. will be swamped by aberrations from the relay optics.

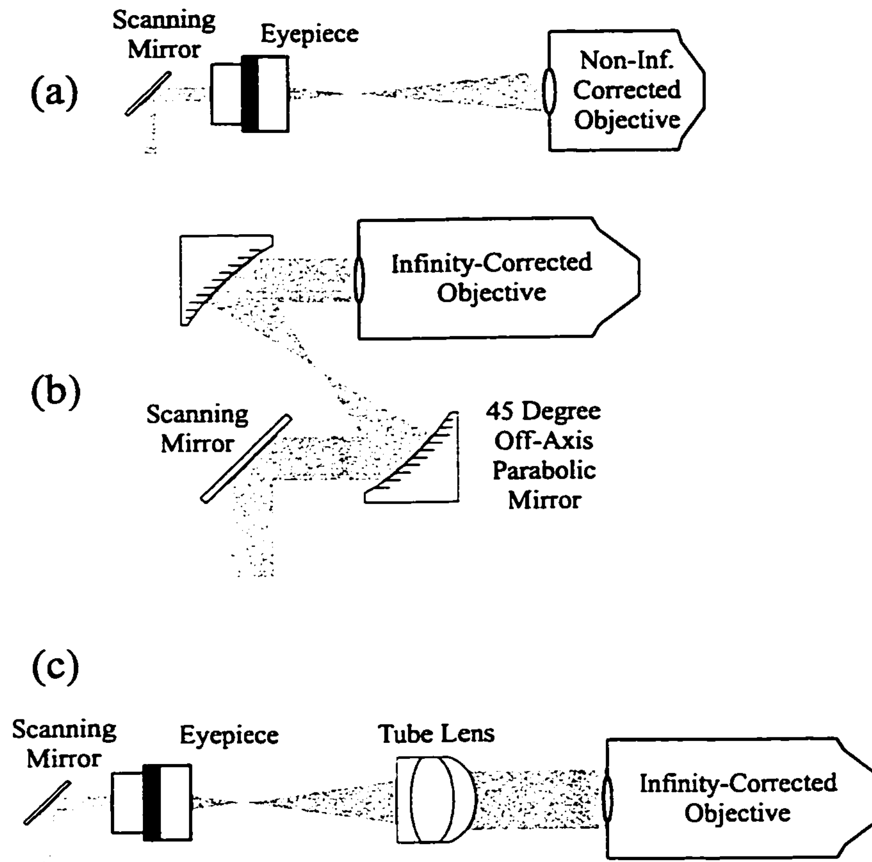

Figure 6.8 (a) BioRad scanning mirror-objective lens configuration. The combination of eyepiece and non-infinity corrected objective results in a virtual infinity corrected objective. The scanning mirror sits on the telecentric plane of the virtual objective. (b) A scanning mirror followed by a unitary telescope optical relay formed by two off-axis parabolic mirrors, in turn followed by an infinity-corrected objective. The UW-CMG configuration uses an all-refractive relay. (c) An all-refractive version of b) where an eyepiece and tube lens make up a telescope relay. In theory this sort of relay has small off-axis aberrations.

Fig. 6.8 shows 3 basic types of relay optics mated to objective lenses. Fig. 6.8a shows the simplest arrangement consisting of an eyepiece and a non-infinity corrected microscope objective. The scanning mirror sits at the telecentric plane of the system which corresponds to a $f_e(f_e + L)/L$ distance from the eyepiece's first principle plane, where f_e is the eyepiece focal length and L is the optical tube length of the microscope. The lens arrangement in Fig. 6.8a corresponds to a conventional wide-field microscope and is identical to Fig. 2.2. The eyepiece can be chosen so that the entrance beam diameter and scanning mirror scan angles are appropriate. Since the microscope objective is assumed to be well-corrected, the limiting optical element will be the eyepiece and therefore it should be of the highest quality. An Erfle[10,11] eyepiece, for example, provides wide-field (± 30°) viewing and is well-corrected for all aberrations. The advantage of this system is that it is simple and all parts are available commercially due to the fact that they form part of a wide-field microscope.

Fig. 6.8b shows an infinity corrected objective in combination with an all-reflecting unitary telescope made up of 45° off-axis parabolic mirrors. The all-mirror relay has no chromatic aberrations present, as discussed in chapter 5 of this thesis. Off-axis parabolic mirrors are provided in many varieties and at low prices by JANOS. Fig. 6.8b shows a 45° version of the relay which is compact but more difficult to implement than a 90° version. Virtually any combination, including non-unitary ones, can be made. This relay system has the advantage of being able to operate in the UV and IR as well as the visible while having the standard degradation disadvantage associated with all mirrors. Another problem has to do with the optical quality of the off-axis parabolic mirrors. JANOS itself has pointed out that their parabolic mirrors might be inadequate for imaging purposes due to a large amount of scatter produced by the diamond-cut surfaces. If higher quality surfaces are required then the cost could increase from several hundred to several thousand dollars.

Fig. 6.8c shows an infinity-corrected microscope objective coupled with a tube lens and an eyepiece representing an all-refracting version of Fig. 6.8b. In telecentric operation the scan mirror sits at the first focal plane of the eyepiece, the second and first focal points of the eyepiece and tube lens, respectively, are coincident, and the second and first focal points of the tube lens and objective lens, respectively, are coincident. The combination of eyepiece and tube lens make up a telescopic optical relay system. In theory, the aberrations associated

with this telescope are less than the aberrations produced by the refracting telescope of chapter 3 due to superior off-axis performance. For the Mitutoyo objectives the matching tube lens has a focal length of 200 mm which results in a long (> 50 cm) distance from the scanning mirrors to the specimen. A more compact wide field microscope version employs non-telecentric operation, where the tube lens is moved towards the objective. The advantage of this system for UW-CMG is that it is probably the least costly to implement since only an eyepiece and a tube lens need be purchased from Mitutoyo. While writing chapter 7, this thesis, the concept of replacing the tube lens with an eyepiece was proposed. If both eyepieces are identical then their combination will form a unitary telescope. If the eyepieces are chosen carefully then this unitary telescope will outperform the achromatic telescope in many respects: it will provide a superior off-axis response, it will have a more compact design, and it will cost less. Refer to section 5.6 for more information on the eyepiece telescope.

The optical performance of systems like the one in Fig. 6.8b have been well defined in this thesis unlike the systems in Fig. 6.8a and c. The optical statistics as well as practical considerations like ease of alignment and mounting must be addressed for all the setups in Fig. 6.8 before any conclusion as to the best system, can be made. Ideally each system should be evaluated on CODE V followed by lateral and axial resolution imaging both in RL and PL, while in practice lateral and axial measurements in RL should suffice.

6.2.4 Detector Arm

The detector arm consists of a beam-splitter, various filters, a detector lens, a confocal pinhole, and a detector. The beamsplitter used throughout this thesis has been a 5 cm diameter, 2 mm thick dichroic purchased from Omega Optical which transmits blue (488 nm) and reflects anything longer than 530 nm. The main problem with this kind of beamsplitter is its flatness. A 2 mm thickness is not enough to guarantee $\lambda/4$ flatness over its entire surface which results in distorted wavefronts especially when large beam diameters are used. One solution to this problem is to ask the manufacturer to use 1/10 wave dual surface optical flats such as those available from Edmund Scientific with a thickness of about 12.5 mm. Another problem, even with an improved beam-splitter, is that it must be custom made and therefore

is inherently expensive. One solution is to reduce the beam size by a factor of about two by inserting a beam expander between the beam splitter and the scanning mirrors as shown in Fig. 6.9. The beam at this point is stationary, hence a simple telescope made up of two achromats or apochromats (if available) is all that is needed.

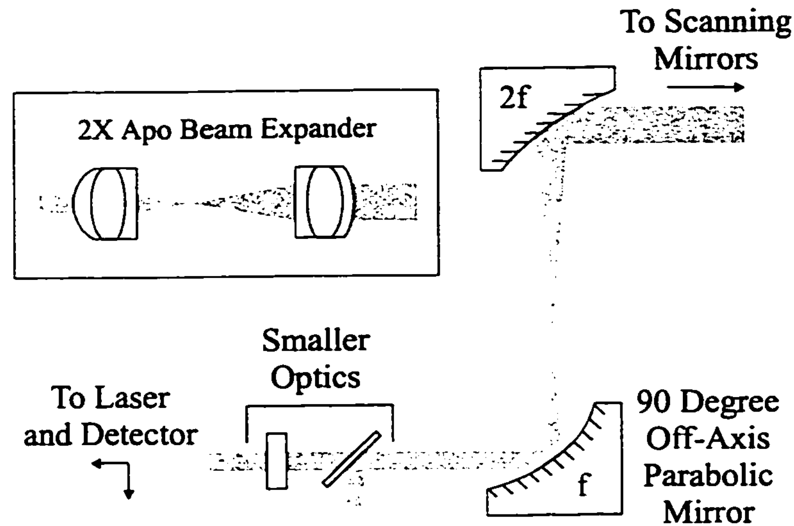

Figure 6.9 Inserting a beam expander in between the beam splitter and the scanning mirrors allows smaller dichroics and filters to be used, as shown above. The use of off-the-shelf optics reduces cost, allows for greater flexibility, and reduces flatness problems associated with large optics. The beam expander can either be made up of mirrors in order to accommodate UV and IR imaging, or can consist of achromats or apochromats (if available) as shown in the box above.

Fig. 6.9 also shows an all-reflecting beam expander made up of two 90° off-axis parabolic mirrors to be used when UV and IR operation is required. Once the beam has been reduced in diameter, commonly available 25 mm diameter stock filters and beamsplitters can be used which enhances the microscope's flexibility and reduces cost.

There are three basic choices for the detector lens / pinhole assembly:

1) No detector lens and a variable iris diaphragm. This is the assembly used by BioRad which requires a set of fold mirrors to provide a long objective to detector path length. The combined long path length and high NA of the objective renders the system effectively confocal when the iris is closed down at the detector. This system avoids all the problems associated with aligning diffraction-limited spots with micron-sized

pinholes. The 'no detector lens' arrangement has two pitfalls: the use of a large number of fold mirrors and the loss of confocality with low magnification objectives. Mirrors tend to degrade in quality much faster than lenses and the effects with several fold mirrors will be much worse. For example, 4 fold mirrors with a reflectivity of 95% will reflect $(0.95)^4$ = 81% of the incident light while 85% reflectivity mirrors only reflect $(0.85)^4$ = 52% of the incident light. The longer the path length the better the confocality, or in other words, good confocal operation requires that the objective to detector path length increase as the NA of the objective decreases. There is a trade off between confocality and the number of fold mirrors, hence the collection efficiency. An extremely long path length would be required for the MACROscope to achieve full confocality. The 'no detector lens' arrangement is better suited to microscopes.

2) A short focal length (≤ 10 cm) detector lens and an adjustable micron-sized pinhole. This is the assembly used by Leica which is very simple, compact, and efficient but requires very accurate lateral and axial alignment of the pinhole such that it sits right on the waist of the diffraction-limited spot as shown in Fig. 6.10. Such precise alignment makes the system more difficult to work with and sensitive to small component deviations and aberrations.

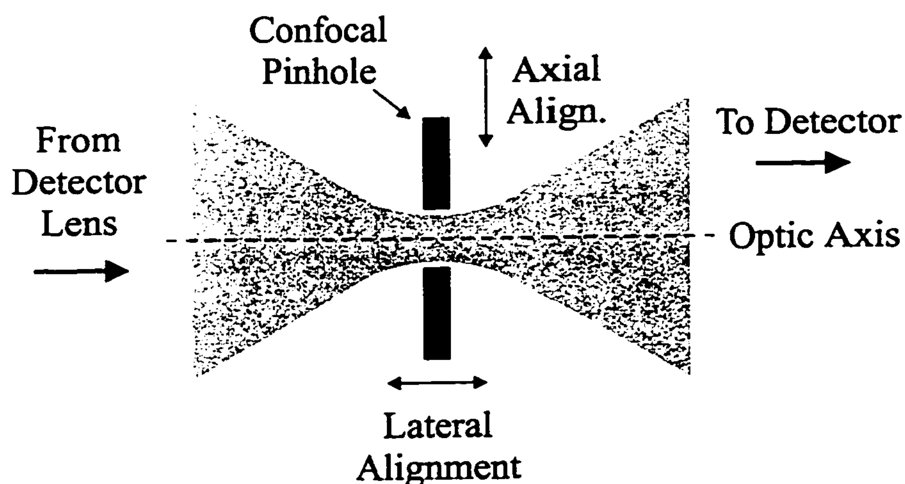

Figure 6.10 Pinhole alignment along the waist of a diffraction-limited spot is critical to achieving confocality.

3) A long focal length (≥ 50 cm) detector lens or mirror and an adjustable micron-sized pinhole. This is an intermediate step between 1) and 2) which would require one or two fold mirrors but provides a larger diffraction spot with a much more forgiving axial alignment. This would allow the use of a less precise adjustable pinhole thus saving on cost. This arrangement is especially useful with the MACROscope LSL where 2 cm diameter beams are used which results in 5 - 10 μm spots (too small) at the pinhole using a 10 cm focal length detector lens.

Notice that in all the above arrangements an adjustable or variable pinhole/iris is always present. This is an essential component since it allows the user to choose from highly confocal to highly light-sensitive imaging. It also allows a constant level of confocality to be maintained when changing to objectives with different entrance pupil diameters, as occurs with the Mitutoyo objectives.

The last component in the detector arm is the detector itself which presently consists of a head-on PMT, more specifically a Hamamatsu R2228 red sensitive PMT. One of the easiest ways of improving the performance of the R2228 is to employ a prismatic enhancer like the ones used by BioRad. Unfortunately it is not clear if they are for sale as separate items and if they would fit the R2228. An alternate solution is to use a superior PMT such as Hamamatsu model R928. The R928 is a side-on PMT, unlike the R2228, with an aperture measuring 8 x 24 mm which is significantly smaller than the R2228's 25 mm diameter active area. Another disadvantage is that side-on PMTs have an inferior spatial uniformity, that is, a variation of sensitivity with respect to detector position. This requires careful centering of the ≤ 5 mm diameter beams at the detector which can easily be achieved with long focal length detector lenses. Apart from these two disadvantages, the R928 outperforms the R2228 in just about every respect. Fig. 6.11 shows a spectral response curve (552 U) for the R928 PMT where quantum efficiency is plotted as a function of wavelength. The R928 combines the excellent UV and blue response of the R292 with the good near-IR response of the R2228 (see Fig. 3.4). In fact, the R928 quantum efficiency is close to double that of the R2228 for nearly all wavelengths.

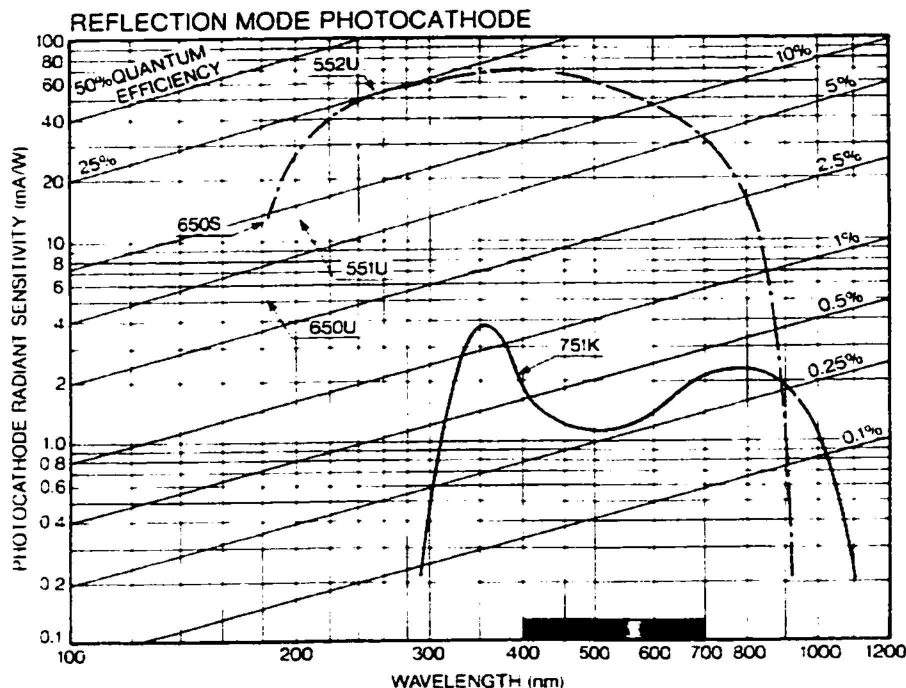

Figure 6.11 Spectral response curve (curve 552 U) for the R928 Hamamatsu side-on PMT. The R928 performs almost as well as the R292 in the blue and outperforms the R2228 in the near-IR. Response curves taken from the 1996 Hamamatsu PMT catalog.

	R292 Head-On	R2228 Head-On	R928 Side-On
Curve Code	400 K	501 K	552 U
Wavelength range (nm)	300 - 650	300 - 900	185 - 900
Peak Wavelength (nm)	420	650	400
Current Amplification ($\cdot 10^5$)	21	7.5	100
Anode Dark Current (nA)	2 - 10	8 - 30	3 - 50
Rise Time (ns)	12	15	2.2
Transit Time (ns)	60	60	22
Active Area	25 mm Diam.	25 mm Diam.	8 x 24 mm
Length	12.5 cm	12.5 cm	9.4 cm
Diameter	2.9 cm	2.9 cm	2.9 cm

Table 6.1 A comparison between two head-on PMTs (R292 and R2228) with a side-on Hamamatsu PMT (R928). The R928 provides superior performance compared to the other two PMTs combined.

Table 6.1 shows various statistics comparing the R292, R2228 and R928 PMTs taken from the Hamamatsu PMT Handbook. The R928 performance is clearly superior to the R292 and the R2228 PMTs combined, providing enhanced quantum efficiency especially in the much needed near-IR and improved current amplification. UW-CMG has traditionally operated its PMTs in current mode, that is, the anode current is converted to a voltage which represents a detected intensity. However, for very low signals, photon counting seems to be the method of choice. Photon counting[12] can be done with a PMT and involves counting the number of pulses generated at each pixel position. Pulses for single photon events are clearly distinguishable from multiple photon events. A discriminator circuit is used to choose only a narrow band of pulse heights which gives an inherently digital output representing detected intensity. Another advantage of photon counting is that it avoids the problem of incomplete integration[12] in which only part of the pixel dwell time is spent collecting intensity data in order to avoid blending adjacent pixels. For example, with a 10 μs pixel dwell time (100 kHz) the integration time would be set to 10/4 μs (400 kHz) to avoid pixel overlap which unfortunately means that the system 'counts' only 25% of the time. BioRad implements both photon counting and current mode with circuits that allow full integration to be performed. Although the majority of commercial confocal microscopes utilize PMTs as detectors, recent advances in photovoltaic detectors, such as avalanche photodiodes[12], has opened several possibilities. Avalanche photodiodes offer advantages such as high quantum efficiency (70%+), low cost, spectral response up to 1 μm wavelength (for Si) and compactness. One significant disadvantage is the lack of electron multiplication. While an avalanche photodiode might generate an electron gain on the order of 10^2, a PMT can generate gains up to 10^7, five orders of magnitude greater. It is unclear, especially at low light levels, if avalanche photodiodes are generally superior to PMTs. Certainly UW-CMG would need superior amplifiers to properly compare the two types of detectors. More experiments and data is required in this area.

6.3 The cslM/m

This section tries to combine the best features from section 6.2 into a design for a fully integrated cslM/m. Fig. 6.12 shows a simplified schematic diagram of the proposed cslM/m.

The laser arm is not shown and a 2 cm diameter variable intensity beam with a good crossection is assumed to enter the filter box from the bottom. Laser line filters, long-pass filters and beam-splitters are expected to be changed often and therefore the filter holder design is adopted from BioRad (MRC 600). Several filter boxes can hold different sets of filters for various applications such that filter handling is minimized. A commercial version of the cslM/m might incorporate a set of mechanized, computer-controlled filter wheels to change filters in addition to a beam reducer (see 6.2.4) in order to utilize stock item filters and dichroic beam-splitters. Upon leaving the filter box, the beam is deflected by a single mirror x-y scanner. A single mirror scanner is absolutely essential to the successful operation of the cslM/m since it avoids aberrations caused by relay optics between two scanning mirrors and eliminates telecentric errors caused by closely spaced scanning mirrors. Single mirror scanners also simplify the optics which helps with alignment and improved throughput. Unfortunately single mirror systems do not seem to be available commercially. Although obtaining a scanner from Leica is a possibility, it is more likely that UW-CMG will have to develop its own single mirror scanner or pay a lot to buy one. After the single-mirror scanner, the beam enters the laser scan lens (LSL) which has its telecentric plane or front focal plane sitting outside of its casing, a very convenient feature. Future LSL designs will include full colour correction to allow for confocal PL imaging. The existing non-colour-corrected LSL has been successfully used in non-confocal mode where a beam splitter is inserted in between the LSL and the specimen thereby maximizing light collection. The advantage here is that chromatic aberrations from the LSL have little effect, and the resolution is determined by the excitation spot size. Cathodoluminescence[13] is the scanning electron microscope equivalent of non-confocal scanning laser imaging where the resolution is determined by the electron-hole pair generation volume.

In microscope mode, relay optics are required to pivot the beam at the telecentric plane of the objective. A pair of 90° off-axis parabolic mirrors, forming a unitary telescope, serve as the relay. This is by no means a final design since all refractive optics, as described in section 6.2.3, might prove superior. Regardless of the final design it is clear that the microscope arm should be parfocal, that is, it should focus on the specimen at the same z-level as the LSL.

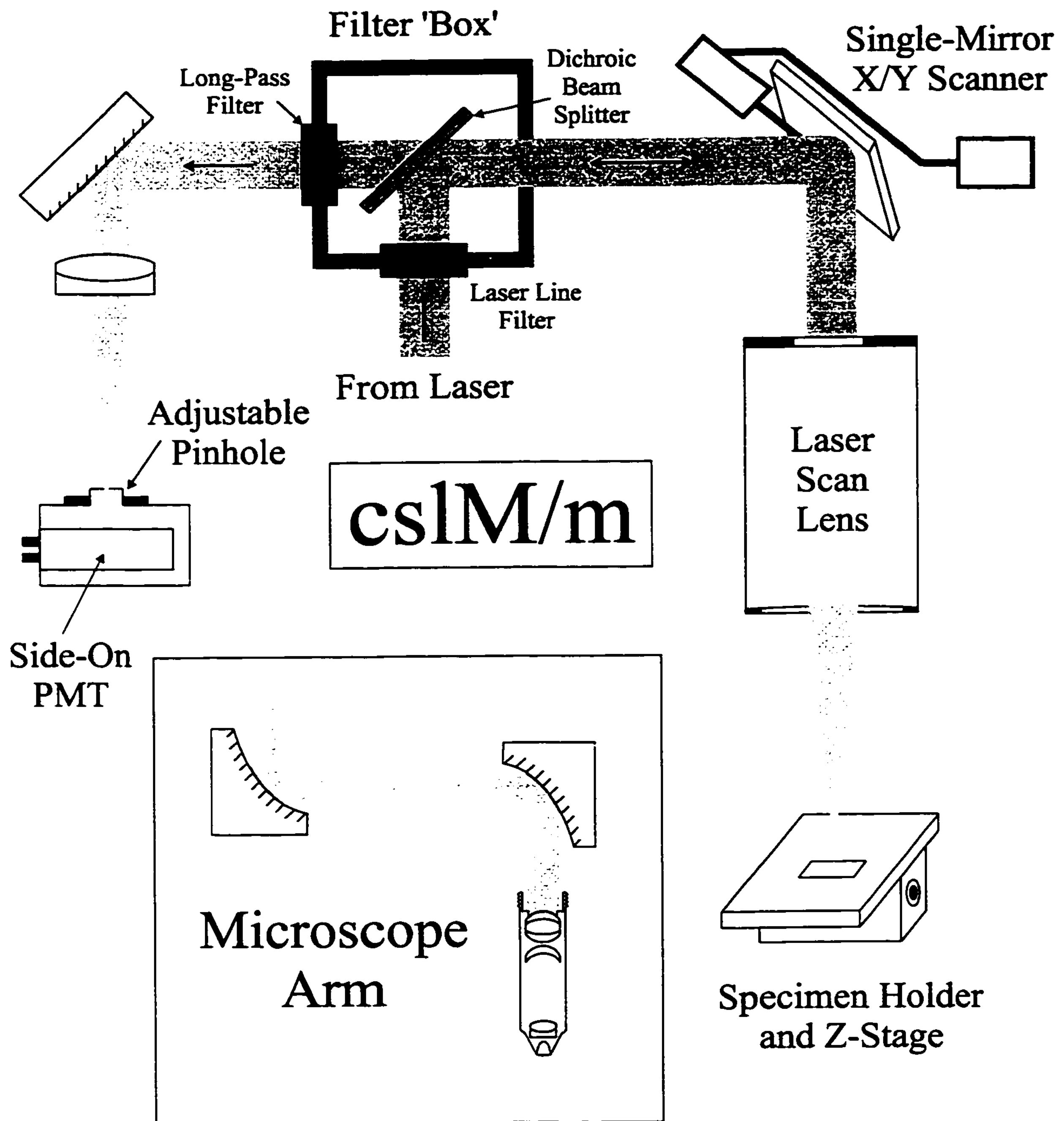

Figure 6.12 A proposed fully integrated Confocal Scanning Laser MACROscope-Microscope (cslM/m). The fundamental innovation requires the use of a single mirror x/y scanner which solves the problem of non-telecentricity in microscope mode and telescope dependent aberrations in MACROscope mode. The microscope arm is improved by abandoning unitary telescopes utilizing achromats. Confocality is better controlled with an adjustable pinhole. The proposed design stresses simplicity and superior optical performance.

The most common specimen holder consists of a standard microscope stage with coarse and fine vertical height adjustments as well as lateral movement. In order to perform confocal slicing the z-motion must be computer controlled and motorized in some way to provide at least 50 nm resolution. UW-CMG has traditionally used 100 nm resolution NEAT stages, while commercial confocal microscopes use stepping motors connected to the microscope stage, or piezo stages, both with position feedback. Regardless of the system is should be able to resolve 50 nm and have position feedback to ensure accuracy and repeatability. Suitable vibration-isolation should also be provided.

Light from the specimen is descanned and reaches the detector arm which in this case consists of a positioning mirror, a medium focal length lens, an adjustable pinhole, and a R928 Hamamatsu side-on PMT. The critical and essential improvement in the detector arm is the variable pinhole (manual or motorized). An adjustable pinhole is necessary to insure flexibility in the degree of confocality for RL (light abundant) and PL (light deficient) imaging. This flexibility is also needed to maintain confocality with a widely ranging spot size at the pinhole due to different entrance pupil diameters for each objective. For example, the 0.7 NA objective has an entrance pupil diameter equal to 2.8 mm compared to the LSL with a 20 mm diameter. This would effectively result in spot sizes at the detector pinhole differing by more than a factor of 7. The detector lens can be easily replaced by a long focal length mirror in order to produce larger diffraction spots at the confocal pinhole or if UV and IR operation is needed. The detector is a side-on, Hamamatsu model R928 PMT which, as shown in section 6.2.4 offers good response from the UV into the IR and effectively outperforms both the R2228 and the R292 Hamamatsu PMTs.

The central theme of the proposed cslM/m is simplicity, which is immediately apparent when Fig. 6.12 is compared with the cslm in Fig. 3.1. This has many advantages such as ease of alignment and maintenance of the optical components, good throughput and collection efficiency, generally more rugged and less susceptibility to vibration problems, and the system is more easily compacted. Due to its simplicity the cslM/m also lends itself to IR and UV imaging where most of the components must be reflecting rather than refracting.

6.4 Summary and Discussion

The purpose of this chapter was to propose a design for a fully integrated cslM/m stressing simplicity and optimum performance.

The first section of the chapter took a detailed look at the BioRad confocal microscope. The cslm forms part of the cslM/m and it is therefore natural to adopt the best design from commercial confocal microscopes. BioRad holds a patent on its design which shows a very detailed view of its components from which many useful concepts can be deduced.

In the second section a series of possible improvements was suggested for each part of the cslM/m. The suggestions were based in part on the data and experiences gathered from chapters 3 to 5 (this thesis) as well as concepts adopted primarily from the BioRad and Leica confocal microscopes.

The last section distills the various possible improvements from section 2 into a design for a fully integrated version of the cslM/m. A single mirror x-y scanner is the most significant improvement on the cslM. The design of the cslm stresses simplicity, high collection efficiency, and high quality optical performance.

The most significant, new contribution in this chapter was to clearly establish the main requirements for a fully integrated cslM/m. A single mirror x-y scanner, and an adjustable pinhole are essential in a cslM/m.

References

[1] A.E. Dixon, U.S. Patent #5532873, 1996.

[2] J.B. Pawley (Editor), Handbook of Biological Confocal Microscopy, 2nd Edition, (Plenum, New York, 1995), p584.

[3] J.G. White, U.S. Patent #5144477, 1992.

[4] W.B. Amos, U.S. Patent #4997242, 1991.

[5] W.D. Gunter, G.R. Grant, S. Shaw, Appl. Optics **9** (1970) 251.

[6] J.B. Pawley (Editor), Handbook of Biological Confocal Microscopy, 2nd Edition, (Plenum, New York, 1995), p25.

[7] J.B. Pawley (Editor), Handbook of Biological Confocal Microscopy, 2nd Edition, (Plenum, New York, 1995), chapter 28.

[8] F.A. Goodman and A.E. Prentakis, U.S. Patent #4685775, 1987.

[9] J. Montagu, SPIE, **1920** (1993) 162.

[10] E. Hecht, Optics, 2nd Edition, (Addison-Wesley, Reading Massachusetts, 1987), p 190.

[11] W.J. Smith, Modern Optical Engineering, 2nd Edition, (McGraw-Hill, New York, 1990), p 407.

[12] J.B. Pawley (Editor), Handbook of Biological Confocal Microscopy, 2nd Edition, (Plenum, New York, 1995), chapters 2, 12.

[13] D.B. Holt and D.C. Joy (Editors), SEM Microcharacterization of Semiconductors, (Academic Press, 1989), chapter 8.

CHAPTER 7

DISCUSSION, PERSONAL CONTRIBUTIONS AND RECOMMENDATIONS

In this chapter a general discussion and review will be given for chapters 2-6. Any conclusions and my personal contributions will also be presented. Recommendations will be given in the second section for developing and improving the confocal scanning laser MACROscope/Microscope (cslM/m).

7.1 Discussion, Conclusions and Personal Contributions

This thesis has several purposes:

1) To document my research for the past several years and present it in a well-organized and intelligible format.
2) To formalize and record many topics discussed by UW-CMG. Much of this material can be found in chapters 2 and 6 in addition to being scattered throughout the other chapters.
3) To generate data for the cslm and MACROscope which can be used as a benchmark to compare with future instrument improvements and designs.

In general, many topics in this thesis are new to UW-CMG but not necessarily new to the confocal microscopy community. This section will try to distinguish between these two situations.

7.1.1 Chapter 2 - Introduction to Confocal Microscopy

Chapter 2 gives an introduction to thin lenses, the confocal effect, lateral and axial resolutions and cslms in general. The section on thin lenses is especially relevant since many concepts in this thesis are explained using thin lenses. A description of wide-field or conventional microscopes is also relevant since they are commonly incorporated into commercial cslms. UW-CMG, until now, has used commercial, infinity-corrected microscope objectives (Mitutoyo and Olympus) in combination with laboratory-made relay

optics (achromatic telescopes) instead of commercial eyepieces and tube lenses. Appendix 1 deals with eyepiece-objective lens configurations and how they can be treated as virtual infinity corrected objectives with the telecentric plane lying some distance away from the eyepiece. Appendix 2 illustrates how an infinity corrected objective becomes a virtual non-infinity corrected objective with the addition of a tube lens. Both these appendices serve to link chapter 3, where the current cslm is discussed, with chapter 6, where future cslm configurations are entertained such as one that incorporates a wide field microscope.

7.1.2 Chapter 3 - Characterization of the Confocal Scanning Laser Microscope and MACROscope

Chapter 3 gives data on efficiency, lateral and axial resolutions, and limitations such as the unitary telescopes and non-telecentricity, for both the cslm and MACROscope. Both instruments were examined in detail, part by part.

The UW-CMG cslm was assembled in the mid-1980s and is currently in need of modifications. The scanning mirrors are too small, which means that the 0.42 NA and 0.14 NA Mitutoyo objectives are underfilled, and the mirrors need to be recoated. The unitary telescopes show clear signs of off-axis aberration and the confocal field-of-view is limited to zoom 2 or 4 regardless of the objective used. The axial resolution measurements do not seem to indicate any on-axis aberrations caused by optics other than the objectives. Lateral resolutions were reasonable except that the resolution targets were not of sufficient quality to test the 0.7 and 0.9 NA objectives. Clearly, resolution targets with submicron features are required both for reflected-light and photoluminescence imaging. No lateral or axial resolution data was obtained with photoluminescence due to lack of targets. The Mitutoyo microscope objectives have proven to be very flexible due to their ultra-long working distances. Bowron[1] and Atkinson[2] have both done axial resolution measurements with the Mitutoyo objectives. My new contribution was to measure relative intensities in conjunction with the axial resolution measurements. The optimum pinhole maximizes both axial resolution and relative intensity. Plots of relative intensity over FWHM as a function of pinhole size can help to determine if there are any aberrations or problems present in the cslm.

Probably the most interesting discovery I made on the cslm is that it could never generate a satisfactory image of a flat mirror. After much experimenting I was able to trace this back to the unitary telescopes. In retrospect, it is easy to see that the achromats making up the telescope might pose a problem since Melles Griot itself does not rate them much beyond 1°. M.R. Atkinson had noted that same aberration and come to the same conclusion, as to the reason, while working with the confocal scanning laser opthalmoscope in the optometry department at the University of Waterloo. Unfortunately I learned about this after I had formed my own conclusions and after Atkinson had left to work for 3M. The experimental characterization (as well as the CODE V simulations which will be discussed later) of the unitary telescope aberrations are new for UW-CMG.

The MACROscope of Fig. 3.24 seems to be an optimum design. Its transmission efficiency is very good due to its simplicity. Image degradation at a single wavelength is apparently caused by wavefront distortion due to a non-flat beam splitter or a distorted beam from the laser. The non-telecentric error should therefore have a negligible effect once this problem is fixed and axial resolution should also improve as a consequence. The prototype LSL has exceeded all expectations, providing an enormous variety of confocal and non-confocal, reflected-light, photoluminescence, and OBIC images. At the time of its construction, monetary constraints and expected imaging applications resulted in a non-colour-corrected LSL design. Not surprisingly, the prototype LSL makes confocal photoluminescence imaging difficult. Fortunately all the specimens imaged in this thesis were under 10 μm in thickness and therefore completely flat from the point of view of the LSL. Future designs for new LSLs will most likely be colour-corrected. A cslM/m made for EG&G in 1996 included a colour-corrected LSL with a 2.5 x 2.5 cm field of view and an NA of 0.05. Recently a colour-corrected 0.2 NA LSL with a 1 x 1 cm field of view has been designed for UW-CMG. The MACROscope axial measurements were previously done by K.M. Beesley, however, intensity measurements were not included. The transmissions efficiency measurements were new for both the cslm and the MACROscope. The effect and concept of telecentric error, introduced in Fig. 3.31, was both new to UW-CMG and the confocal microscopy community. Stelzer[3] mentions the non-telecentric error but never describes its effect.

Although I have participated in the continuing design, construction, assembly, alignment, etc., of both the cslm and especially the MACROscope, most of my contributions have been in the area of analysis and characterization.

Section 3.3 was originally intended to include spectrally resolved data from the UW-CMG scanning stage microscope. Unfortunately I was unable to generate reproducible and reliable spectra based on the fact the confocal pinhole is inherently unstable (spectrally). Bowron[1] pointed out that spectral discrimination is best done separate from the spatial filtering. The main lesson I learned from this is to always use a slit and not a pinhole for spectrally resolved measurements.

7.1.3 Chapter 4 - MACROscope/cslm Applications and Imaging Results

Chapter 4 was used to present imaging results from both the MACROscope and cslm for two types of semiconductor specimens, solar cells and porous silicon (PSi). MACROscope and cslm applications were an integral part of their characterization and development.

Solar cells were a natural specimen to image on both instruments for several reasons:

1) Commercial cells of many types are both inexpensive and abundant.
2) S. Damaskinos was very familiar with solar cell characterization from working at IEC and possessed many high quality thin film solar cell prototypes.
3) H.F. Tiedje produced several thin film solar cells which required spatially resolved characterization for the purpose of quality control.
4) Solar cells and similar devices are excellent test specimens for both the MACROscope and the cslm since they require micro and macroscopic analysis using reflected-light, photoluminescence and OBIC.

The cslM/m was shown to be an excellent instrument for quality control where many cells could be compared to a control cell. The cslM/m built for EG&G was designed basically for this purpose. Some innovative imaging techniques such as multi-wavelength, semi-confocal OBIC, and non-telecentric OBIC imaging were demonstrated. Two limitations of OBIC were shown: 'ringing' caused by scanning faster than the solar cell can respond, and non-linear OBIC response to increases in laser intensity. The latter limitation can affect the accuracy of quantitative OBIC imaging and can result in poor contrast. A rigorous approach to solar cells

would be to obtain linearity data on a wide variety of cells and try to operate within the linear regime. A short section in this chapter compared and contrasted EBIC with OBIC. In general EBIC provides approximately the same resolution as OBIC except for shallow junctions or edge-scanning. EBIC, however, has many disadvantages such as: it can damage specimens, it will charge dielectric layers which ultimately results in imaging problems, multiwavelength analysis is impossible, and encapsulated cells cannot be imaged.

Based on the solar cell imaging results I was able to publish two articles: an MRS conference proceeding[4] and a paper to Solar Cells[5]. These papers highlight the fact that the MACROscope-cslm system provides OBIC, confocal reflected-light, and confocal photoluminescence images at macroscopic and microscopic levels.

PSi, the novel form of silicon which luminesces in the visible at room temperature, could contribute to the development of all-silicon optoelectronics such as flat panel displays and optical interconnects. Before this potential revolution in the optoelectronics can occur, a clear understanding of PSi must be achieved at many levels. I have, with the aid of the cslM/m, contributed to development of PSi materials and devices by characterizing many specimens created by P.M. Fauchet's research group. Specifically for PSi materials, I provided imaging data on photoluminescence uniformity, imaging evidence of lateral etching, evidence of enhanced etching due to RIE and evidence of bleaching and passivation. Several PSi devices were created by the Rochester group which I helped to characterize in reflected light, photoluminesce and OBIC. I-V and spectral response data taken by H.F. Tiedje in addition to OBIC data showed S.P. Duttagupta's PSi solar cell to be 8% efficient, although the state of the PSi junction is unclear. A series of PSi 'dot' devices were successfully shown to contain nanoporous light emitting PSi in addition to producing an OBIC signal. The smallest 'dots' were 5 μm in diameter which, at the time, represented the smallest PSi devices created.

I published two PSi-cslM/m articles: a Surface Science[6] conference proceedings, and a letter to Applied Physics[7]. The latter article was one of the first to show confocal images of PSi concurrently with Nassiopoulos[8].

Chapter 4 demonstrated that the cslM/m is a versatile instrument and excellent for characterizing solar cells and porous silicon. UW-CMG aided in helping to characterize many

PSi materials and devices from the Rochester group which could have not been done with many other instruments.

7.1.4 Chapter 5 - Quantitative Lens Analysis with CODE V

This chapter begins by giving a brief introduction to primary monochromatic and chromatic aberrations. Some examples of CODE V analysis options are also shown. The core of chapter 5 was intended to be a comparison between two types of unitary telescopes: refractive telescopes made with a pair of achromats, and reflective telescopes made with a pair of off-axis parabolic mirrors. In addition to the telescopes, a set of designs involving an all-mirror beam expander and a detector mirror were also analyzed. The last section attempted to come up with an inexpensive UV objective lens.

The analysis of the detector mirror and 30X mirror beam expander resulted in the following conclusion: if off-axis parabolic mirrors are unavailable then a long focal length, tilted spherical mirror can be used as a substitute as long as the tilt is kept small (< 5°).

As expected from chapter 3, the refracting telescope was found to have a large amount of astigmatism at 2.7° field angles. Spherical and axial chromatic aberrations contributed to an 80% encircled energy (EE) diameter, at 0° field angle, 3 times the diffraction-limited diameter. The (2.7°, 2.7°) field angle 80% EE diameter was more than three times larger than the optic axis value. The reflective telescope was found to generate smaller spot sizes and was generally less aberrated. Lack of chromatic aberrations resulted in 80% EE diameters one third as large as the refractive telescope diameters. A reduced amount of monochromatic aberrations meant that the reflective telescope outperformed the refractive telescope even with monochromatic light. Unfortunately Fig. 5.41b still shows that the corner 80% EE diameter is triple that of the center diameter, a significant aberration which can only be fixed by using larger focal length parabolic mirrors.

Both telescopes were tested using a 7 mm diameter beam and a maximum 2.7° field angle. It is clear that neither system can serve as a relay lens on the MACROscope where beam diameters can reach 2 cm and field angles reach 10°.

Not surprisingly, the best UV objective for under $300 turned out to be a fused-silica singlet. A f=150 mm double convex singlet was found to give the best results confocally and non-confocally. A 30 μm lateral resolution (non-confocal) was possible over a 22 mm diameter field of view.

I am the first person at UW-CMG to study the telescopes quantitatively both experimentally and theoretically. The problems with the achromatic telescopes prompted me to search for alternate relay lenses. We tried to use a pair of Nikon f_{no} 1.4 camera lenses as unitary telescopes but they failed to work properly. After reading Stelzer's chapter[3] in the Confocal Handbook and seeing the BioRad diagram[9,10,11] I decided to learn CODE V and try off-axis parabolic mirrors for use on the cslm <u>and</u> the MACROscope. The analysis performed for the off-axis parabolic mirrors does not appear anywhere in the literature although it is extremely likely that either Amos or someone at BioRad must have done similar analysis.

CODE V has proven to be an extremely useful tool. It has given UW-CMG very good estimates of the aberrations associated with various existing and proposed lens designs as well as aiding in the development of new imaging systems.

7.1.5 Chapter 6 - The Fully Integrated Confocal Scanning Laser MACROscope-Microscope

This chapter was intended to suggest the best current design for a single unit confocal scanning laser MACROscope/Microscope (cslM/m) based on all the data and knowledge obtain from previous chapters. It was clear that I should write this kind of a chapter since we had learned so much throughout the years about the MACROscope and cslm. In addition to summarizing a series of suggested improvements, chapter 6 also served to clarify the course of future research and point out what needs to be done to obtain a more viable commercial cslM/m. There are three main developments this chapter investigated:

1) An adjustable confocal pinhole. A variable pinhole is absolutely essential to the cslM/m in order to control the degree of confocality or light collection ability, and to adjust to widely varying laser beam diameters. Manually inserting different size pinholes is

unacceptable since it leads to constant misalignment and mismatch due to the finite number of pinhole sizes available. A manually or electronically adjustable pinhole is required.

2) An x-y single mirror scanner. The MACROscope works perfectly well with the two closely spaced scanning mirrors configuration (Fig. 2.18). The cslm works reasonably well with a telescope between the scanning mirrors (Fig. 2.17). Unfortunately neither system works well when combined into a cslM/m since telescopes cannot operate with the large beam diameters and scan angles used on the MACROscope, and the cslm will only work well with very closely spaced mirrors, i.e. small mirrors. The only viable solution is a single mirror x-y scanner (Fig. 2.20) which solves both problems and offers increased collection efficiency. The question as to whether or not such a scanner is obtainable at a reasonable price is unclear and must be investigated.

3) The microscope objective-relay lens system. The choices for this are basically a, b or c in Fig. 6.8. All of the configuration of Fig. 6.8 must be easily portable or movable in order to coexist with the MACROscope lens, which in most cases implies that the cslM/m cannot be constructed around a wide-field microscope (at least not all of it). This in turn means that each of the lenses in Fig. 6.8 must be purchased separately which might prove to be a problem for the tube lens in Fig. 6.8c (it might not exist as a single lens). The configuration of Fig. 6.8a offers the simplest design involving an eyepiece and a non-infinity corrected objective. The eyepiece and objective can be taken from an existing wide-field microscope, which ensures compatibility because they are designed to work together. Another approach is to purchase a parfocalized set of very high quality objectives and separately purchase the highest quality eyepiece available since it will ultimately determine the total aberrations of the combined lens system. Both Figs. 6.8b and c offer designs which incorporate infinity-corrected objectives. This is of particular interest to UW-CMG since it allows the use of the existing Mitutoyo objectives. Fig. 6.8b offers a relay which has a wavelength independent design allowing for IR-visible-UV-imaging. The off-axis parabolic mirror focal lengths must be large for good optical performance and the question of surface quality is unclear.

Fig. 6.8c basically involves a telescope made up of an eyepiece and a tube lens from a microscope using an infinity corrected objective. Unfortunately in the case of the Mitutoyo objective this would involve a f = 200 mm 'tube lens' which might or might not exist as a single lens. An alternative which has come to light recently, in fact just as this chapter was being written, involves substituting another eyepiece for the tube lens in Fig. 6.8c. This opens up an entire host of possibilities. First, any type or combination of eyepiece is available including unitary and non-unitary configurations. Second, CODE V can be utilized to simulate this configuration since it contains several eyepiece designs from patents. Section 5.6 includes CODE V analysis of a unitary telescope made by combining two Erfle[12] eyepieces. Although the Erfle eyepieces used in section 5.6 were obviously intended for telescopes the simulation can still give a feel for what aberrations will arise. Briefly, the 'eyepiece unitary telescope' has similar axial chromatic and spherical aberrations as the achromatic telescope but it greatly reduces the astigmatism. The 'eyepiece telescope' therefore produces 80% EE diameters similar to the achromatic telescopes at (0°, 0°) field angle over the <u>entire</u> field of view. Erfle eyepieces have been commonly available for decades and can be purchased in many varieties from various companies. Edmund Scientific, for example, sells an Erfle eyepiece for $85 U.S. Given the above cost and similar performance to that encountered in section 5.6, this represents, by far, the best visible light relay lens system design to date. Using this basic design a wide variety of combinations can be constructed involving different focal lengths, wider entrance pupils, and even non-unitary configurations.

The proposed cslM/m design of Fig. 6.12 is not intended to be constructed as such rather it embodies many of the suggested improvements and stresses simplicity.

7.2 Recommendations

In this section specific recommendations will be made with respect to improving the cslM/m. Each part (laser arm, scanning arm, objectives and relay, and the detector arm) of the cslM/m will be treated separately. The theme is simplicity and modularization.

7.2.1 Laser Arm

When imaging photoluminescing specimens, like porous silicon, there have been times when more excitation intensity was needed. For most specimens there should be enough laser power to saturate and/or bleach them. My recommendation is to purchase a laser in the 30 mW, 450 nm range with convection air cooling to eliminate vibrations.

For multiple wavelength operation there are two routes: use several convection air cooled lasers, or a single multiwavelength laser (ArKr) with fiber optic coupling. The former could prove to be the least expensive but the latter will undoubtedly prove to be the most flexible and compact. If multiple wavelengths including UV and IR are used simultaneously then an all-mirror beam expander should be used.

In anticipation of improved optics, the laser beam should be spatially filtered and over-expanded so as to utilize the homogeneous central portion of the beam. This is another reason why excess laser power is needed.

Although the purchase of a laser for use in two-photon imaging is extremely expensive, UW-CMG should nevertheless consider entering this field be it via a grant or collaboration. The MACROscope could make important contributions to two-photon imaging. Biomedical Photometrics is in fact currently designing a cslM/m to be used at the University of Toronto for two-photon imaging.

7.2.2 Scanning Arm

My sole recommendation in this section is to obtain a single mirror x-y scanner. This scanner is critical for the proper operation of a cslM/m. Inquiries should be made to companies like General Scanning, Cambridge Technologies, Leica, etc. Inquiries can also be made to the authors of various articles dealing with single mirror x-y scanners. An effort should be made to at least assess what scanners are available and to obtain an approximate cost.

If it turns out that single mirror x-y scanners are unavailable then the best alternative is to use two closely spaced scanning mirrors of reduced size. The mirrors should be large enough to accommodate a 1 cm diameter beam (at most) such that the center to center scanning mirror distance is small. This would result in a lower NA for the MACROscope but better, more

telecentric performance from the high NA microscope objectives. There are many different configurations that can be adopted to stress superior MACROscope or cslm operation, but not both without a x-y single mirror scanner.

7.2.3 Microscope Objective, Relay Optics, and Specimen Stage

Quite simply the various relay-objective lens configurations in Fig. 6.8, including the 'eyepiece telescope' described in Appendix 7, must be evaluated experimentally. Questions must be answered with respect to the quality of the parabolic mirrors from JANOS, the cost of each configuration, resolution, aberrations, and throughput efficiency.

UW-CMG in particular will likely choose to continue using the Mitutoyo objectives since so much money has been invested in them. The 'eyepiece telescope' should be examined first for use with the Mitutoyo objectives because it theoretically offers the best response in the visible, and is also less expensive than the achromatic telescope. Performing a search for apochromatic eyepieces would also be useful. Assuming the Mitutoyo objectives are still to be used, I recommend UW-CMG purchase a 0.9 NA Mitutoyo objective in order to replace the Olympus objective and thereby parfocalize the system. Purchasing a 0.025 NA Mitutoyo objective (17 x 17 mm field of view) would allow the present cslm a more macroscopic view without having to add all the components needed for a cslM/m. Assuming a single-mirror x-y scanner is used, the question of parfocality versus telecentricity for the Mitutoyo objectives still remains. The Mitutoyo objectives were designed to operate parfocally and therefore they should be run this way, however, the question of where to pivot the beam remains open especially for the high NA, small focal length objectives. A series of diagrams, like Fig. 3.31, can be drawn to determine to amount of clipping that occurs when the limiting aperture and the telecentric plane do not coincide. Designs for a hybrid scanning beam and stage cslM/m using a single LSL should also be considered.

I recommend that UW-CMG purchase proper resolution targets for reflected-light and photoluminescence imaging. At the very least, a submicron reflected light target for the cslm should be obtained. It is very difficult to properly characterize new instruments without proper standards.

The specimen stage should be integrated with a conventional microscope stage, if possible, and should provide 50 nm z-resolution with position feedback. There are many ways to do this and a search must be done for the most efficient and cost-effective way.

7.2.4 Detector Arm

The most important recommendation in this section is to use an adjustable pinhole. This is essential in a cslM/m to both control the degree of confocality and to adapt to changing beam diameters when the objectives are changed. A search for adjustable pinholes and their cost, accuracy, size, specification, etc., should be done.

The easiest and least costly way to improve PMT performance is to implement the prismatic enhancer described by Pawley[13]. An attempt should be made to ascertain whether or not a prismatic enhancer can be obtained from BioRad, or someone else, and at what cost. If this fails then the R-928 Hamamatsu side-on PMT should be considered (see section 6.2.4). Photon counting as well as using avalanche photodiodes should be considered for future research. Low-level light imaging should be implemented into every new design.

The filters and beam splitters should be mounted in a modular fashion like on the BioRad (Fig. 6.2). Apart from the specimen stage and confocal pinhole this is one part of the microscope which is constantly being changed and is therefore prone to misalignment. With respect to the beam splitter, an optically-flat beam splitter should be ordered and tested to see how much distortion it produces on a 2 cm diameter collimated beam. Also a spatial filter should be used on the MACROscope's beam expander.

7.2.5 Top 5 Recommendations

1) Use a single mirror x-y scanner
2) Use an adjustable pinhole
3) Investigate objective-relay lens options
4) Obtain resolution targets
5) Implement and investigate single photon counting

References

[1] J.W. Bowron, Ph.D. Thesis, 1993, Physics Department, University of Waterloo, Waterloo, Canada.

[2] M.R. Atkinson, Ph.D. Thesis, 1991, Physics Department, University of Waterloo, Waterloo, Canada.

[3] J.B. Pawley (Editor), Handbook of Biological confocal Microscopy, 2nd Edition, (Plenum, New York, 1995), Chapter 9.

[4] A.C. Ribes, S. Damaskinos, H.F. Tiedje, A.E. Dixon, D.E. Brodie, S.P. Duttagupta, and P.M. Fauchet, Materials Research Society Symposium Proceedings, **426** (1996) 581.

[5] A.C. Ribes, H.F. Tiedje, S. Damaskinos, A.E. Dixon, and D.E. Brodie, Solar Energy Materials and Solar Cells **44** (1996) 439.

[6] A.C. Ribes, S. Damaskinos, A.E. Dixon, K.A. Ellis, S.P. Duttagupta, and P.M. Fauchet, Progress in Surface Science, **50** (1995) 295.

[7] A.C. Ribes, S. Damaskinos, A.E. Dixon, G.E. Carver, C. Peng, P.M. Fauchet, T.K. Sham, and I. Coulthard, Applied Physics Letters, **66** (1995) 2321.

[8] A.G. Nassiopoulos, S. Grigoropoulos, L.T. Canham, A. Halimaoui, I. Berbezier, E. Godolides, D. Papodimitriou, Thin Solid Films **255** (1995) 329.

[9] J.B. Pawley (Editor), Handbook of Biological confocal Microscopy, 2nd Edition, (Plenum, New York, 1995), page 584.

[10] J.G. White, U.S. Patent #5144477, 1992.

[11] W.B. Amos, U.S. Patent #4997242, 1991.

[12] Erfle, U.S. Patent #1478704, 1923.

[13] J.B. Pawley (Editor), Handbook of Biological confocal Microscopy, 2nd Edition, (Plenum, New York, 1995), page 25.

APPENDIX 1

USING A WIDE-FIELD MICROSCOPE AS A CSLM

In Chapter 6 (this thesis) it will be important to know the FFL and the BFL for the system in Fig. 2.2. Defining the specimen as the object then $f_1 = f_o$ and $f_2 = f_e$ and using Eqns. 2.7 and 2.8:

$$FFL = \frac{f_o(f_e + L + f_o - f_e)}{f_e + L + f_o - (f_o + f_e)} = \frac{f_o(L + f_o)}{L} \quad \textbf{(A1.1)}$$

$$BFL = \frac{f_e(L + f_e)}{L} \quad \textbf{(A1.2)}$$

Given an 8X eyepiece (f_e = 254/8 = 31.8 mm) and a standard L = 160 mm tube length, then BFL = 38.1 mm. On a BioRad microscope this defines the distance from the scanning mirror to the first principal plane of the eyepiece. Note this does not correspond to the definition of BFL in chapter 5. The diameter of the beam entering the eyepiece will be magnified by $L/f_e \cong$ 5X at the entrance pupil of a high magnification/NA objective lens. This agrees with the arguments given by Stelzer in the Confocal Handbook where the magnification of the scan lens or eyepiece is given by:

$$M_{SL} = \frac{f_e + L}{BFL} = \frac{L}{f_e} \quad \textbf{(A1.3)}$$

Stelzer, like many other authors defines optical tube length differently in his formulas which relates to L as follows:

$$L = L_S + L_A \quad \textbf{(A1.4)}$$

where L_S = optical tube length defined by Stelzer, the distance from the intermediate image to the flange of the objective lens, and L_A = the distance from the flange to the first principal plane. L_A is not a constant for different objectives in the same parfocal family.

Given a standard 20 mm maximum height for the intermediate image, the maximum scan angle is given by:

$$\tan\theta_{MAX} = \frac{10\,mm}{f_e} \quad \textbf{(A1.5)}$$

which is obtained from the diagram on the next page.

Eqn. A1.5 does not agree with the equation given by Stelzer ($\tan\theta_{MAX}$ = 10 mm/BFL) which seems to be a typographical error.

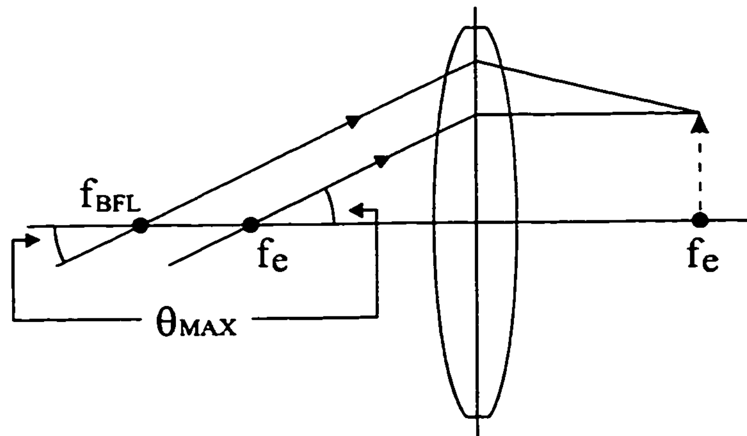

Continuing with the 8x eyepiece example, θ_{MAX} is given by:

$$\theta_{MAX} = \tan^{-1}\left(\frac{10}{31.8}\right) = 17.5^{\circ} \qquad \textbf{(A1.6)}$$

which seems a bit large for a scan angle. With a 2X eyepiece the scan angle becomes a more reasonable, ± 4.5°, while the beam diameter magnification becomes 1.25.

APPENDIX 2

INFINITY-CORRECTED OBJECTIVES

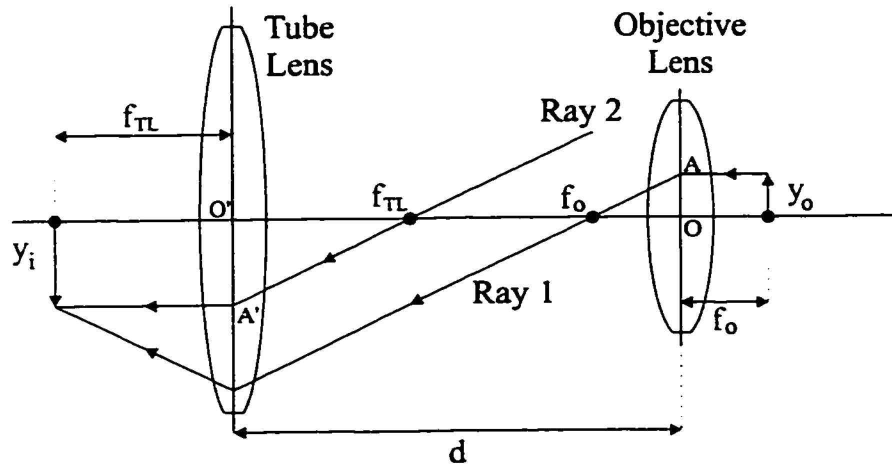

An infinity-corrected objective does not generate an intermediate image of the object at any finite distance. It must be therefore combined with a tube lens such that this combination reverts back to a non-infinity corrected configuration which replaces the objective in Fig. 2.2. Shown above is a diagram combining a tube lens of focal length f_{TL} and an objective of focal length f_o. This sort of arrangement gives the lens designer some flexibility with the tube lens - objective lens separation, d.

For an infinity-corrected objective the object is placed at the focal plane of the objective. In the above diagram, ray 1 starts out parallel to the optic axis and therefore passes through the objective's second focal point. Since the object is at the focal plane of the objective lens, all rays from a given point on the object will emerge parallel to each other after passing through the objective lens. Upon passing through the tube lens, ray 1 must come to focus at the tube lens' second focal plane. To determine the height on the focal plane, ray 2 is drawn which is a ray parallel to ray 1 passing through the first focal point of the tube lens. Ray 2 emerges parallel to the optic axis after passing through the tube lens and intersects the focal plane at height y_i.

The magnification $M = y_i/y_o$ can be determined by noting that triangles AOf_o and $A'O'f_{TL}$ are similar triangles, therefore :

$$M = \frac{y_i}{y_o} = \frac{f_{TL}}{f_o} \qquad \textbf{(A2.1)}$$

The magnification of an infinity-corrected objective is uniquely determined by its focal length and the tube lens, regardless of the value of d.

APPENDIX 3

EFFECTIVE NA

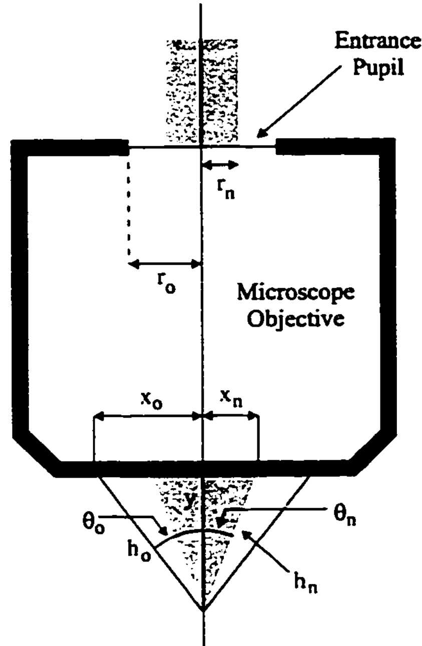

A microscope objective, such as the one shown above, will only operate with its full NA when its entrance pupil is fully filled. If the objective is underfilled with a beam of radius r_n instead of the full radius r_o, then the effective NA will be reduced. To calculate the effective NA first consider that:

$$\frac{r_o}{r_n} = \frac{x_o}{x_n}, \text{ and also:} \tag{A3.1}$$

$$NA_o = \sin\theta_o = \frac{x_o}{h_o} \tag{A3.2}$$

$$y^2 = h_o^2 - x_o^2 = x_o^2\left(NA_o^{-2} - 1\right) \tag{A3.3}$$

Eqns. (2) and (3) also apply for the x_n, h_n, etc. coefficients, therefore

$$x_o^2\left(NA_o^{-2} - 1\right) = x_n^2\left(NA_n^{-2} - 1\right) \tag{A3.4}$$

$$NA_{EFFECTIVE} = NA_n = \left[\left(\frac{r_o}{r_n}\right)^2\left(NA_o^{-2} - 1\right) + 1\right]^{-\frac{1}{2}} \tag{A3.5}$$

APPENDIX 4

ESTIMATE OF QUANTUM EFFICIENCY

The PL quantum efficiency of a specimen is an important parameter especially when it is used to define the minimum signal requirements for the MACROscope or cslm. Obtaining a rough estimate of the quantum efficiency requires two sets of calculations. The first step requires an estimate of the number of photons per second collected by the LSL necessary to produce a given PMT anode current. A specular reflector, such as a mirror, will cause all incident light to return along the same path. By measuring the incident beam power and using a mirror specimen of known reflectivity (90%) the number of photons per second entering the MACROscope can be obtained. The set-up of Fig. 3.24 with a 633 nm HeNe laser is used as an example:

The amount of light incident on the mirror specimen was measured to be 1.88 μW with the calibrated silicon detector of section 3.1.1.4 which resulted in a 460 μA PMT anode current. The number of photons/s required to produce a μA of anode current is given by:

$$\frac{\text{Incident Power(W)}}{1.60\cdot 10^{-19}\left(\text{W}\cdot \text{s}/_{\text{eV}}\right)}\cdot\left(\frac{1240\ (\text{nm}\cdot\text{eV})}{\text{Incident Wavelength(nm)}}\right)^{-1}\cdot\frac{\text{Mirror Reflectivity}}{\text{Anode Current}} \quad \textbf{(A4.1)}$$

$$=\frac{1.88\cdot 10^{-6}\,\text{W}}{1.60\cdot 10^{-19}\left(\text{W}\cdot \text{s}/_{\text{eV}}\right)}\cdot\left(\frac{1240\ (\text{nm}\cdot\text{eV})}{633\ \text{nm}}\right)^{-1}\cdot\frac{0.90}{460\,\mu\text{A}}$$

$$= 1.17\cdot 10^{10}\,(\text{Photons/s})\,/\,\mu\text{A}$$

The second step in the quantum efficiency calculation involves estimating the fraction of light collected by the MACROscope from a luminescent specimen. Given the NA on the MACROscope is restricted to 0.04 by the scanning mirrors, then the collection NA will be approximately the same. At this point, the assumption of an isotropic emitter is made. The luminescence is assumed to originate from a point which radiates equally in all directions, i.e. it is an ideal point source. If this assumption is valid, then the amount of light collected with 0.04 NA will be a known fraction of the total light emitted. The percentage of light collected

is given by Eqn. 3.2 and turns out to be $4.17 \cdot 10^{-2}$ %. Using the PL image of Fig. 4.10b as an example with a PMT anode signal of 1.78 μA this corresponds to a total emission rate of:

$$\frac{\text{PL Anode Current} \cdot (\text{Eqn A4.1})}{\text{Collection Fraction}} =$$

$$\frac{1.78\mu\text{A} \cdot 1.17 \cdot 10^{10} (\text{photons/s})/\mu\text{A}}{4.17 \cdot 10^{-4}} = 5 \cdot 10^{13} \text{ photons/s} \quad \textbf{(A4.2)}$$

The above emission rate occurred with 1.6 mW incident power at 488 nm (2.54 eV) excitation, hence:

$$\frac{1.6 \cdot 10^{-3}\text{W}}{1.6 \cdot 10^{-19}\left(\text{W} \cdot \text{s}/\text{eV}\right)} \cdot \frac{1}{2.54\text{eV}} = 3.94 \cdot 10^{15} \text{ photons/s}$$

The quantum efficiency is given by:

$$\frac{\text{Emitted Light}}{\text{Incident Light}} = \frac{5 \cdot 10^{13}}{3.94 \cdot 10^{15}} = 1.27\% \quad \textbf{(A4.3)}$$

APPENDIX 5

INTENSITY VERSUS NA

The spot intensity at a specimen depends on the beam power but more significantly on the spot size and consequently the NA of focusing objective. The table below shows intensities as a function of objective NA for NAs ranging from 0.04 to 0.9 assuming perfect optics. The wavelength was assumed to be 488 nm while the beam power was taken to be 1 mW. The spot radius is given by:

$$r = \frac{1.22\lambda}{2NA} \quad \textbf{(A5.1)}$$

The intensity in kW/cm^2 is given by:

$$I = \frac{BeamPower(kW)}{\pi r(cm)^2} \quad \textbf{(A5.2)}$$

Intensity is therefore proportional to NA^2.

NA	Spot Radius µm	Axial Resolution µm	Intensity kW/cm^2
0.04	7.44	268	0.58
0.10	2.98	42.8	3.59
0.14	2.13	21.8	7.04
0.20	1.49	10.6	14.4
0.30	0.99	4.66	32.3
0.40	0.74	2.57	57.5
0.42	0.71	2.32	63.4
0.50	0.60	1.60	89.8
0.60	0.50	1.07	129
0.70	0.43	0.75	176
0.80	0.37	0.54	230
0.90	0.33	0.38	291

APPENDIX 6

LENS DATA FROM CODE V

Refracting telescope

```
RDY                THI       RMD         GLA
  OBJ:          INFINITY           INFINITY
  STO:          INFINITY          58.365089
    2:          39.49000           9.990000          SK11_SCHOTT
    3:         -27.80000           2.470000          SF5_SCHOTT
>   4:        -100.93000         107.251999
    5:         100.93000           2.470000          SF5_SCHOTT
    6:          27.80000           9.990000          SK11_SCHOTT
    7:         -39.49000          58.365089
    8:          INFINITY          24.750000
    9:          INFINITY          24.750000
  IMG:          INFINITY           0.000000

SPECIFICATION DATA
   EPD         7.00000
   AFI        24.75000
   DIM              MM
   WL           725.00    647.10     568.20     488.00
   REF               2
   WTW               1         1          1          1
   XAN         0.00000      0.00000      2.70000
   YAN         0.00000      2.70000      2.70000
   VUX         0.00000      0.00000      0.00000
   VLX         0.00000      0.00000      0.00000
   VUY         0.00000      0.00000      0.00000
   VLY         0.00000      0.00000      0.00000

APERTURE DATA/EDGE DEFINITIONS
   CA
   CIR S2    EDG            15.000000
   CIR S3    EDG            15.000000
   CIR S4    EDG            15.000000
   CIR S5    EDG            15.000000
   CIR S6    EDG            15.000000
   CIR S7    EDG            15.000000

REFRACTIVE INDICES
    GLASS CODE      725.00       647.10       568.20       488.00
   SK11_SCHOTT    1.558870     1.561341     1.564814     1.570128
   SF5_SCHOTT     1.662215     1.667307     1.674856     1.687123
```

```
INFINITE CONJUGATES
   EFL        -24.7500
   BFL         24.7500
   FFL          0.0000
   FNO         -3.5357
   IMG DIS     24.7500
   OAL        273.6522

   PARAXIAL IMAGE
    HT          1.1672
   ANG          2.7000

   ENTRANCE PUPIL
    DIA         7.0000
    THI         0.0000

   EXIT PUPIL
    DIA     0.1928E+11
    THI    -0.6816E+11
```

Reflecting Telescope

```
                  RDY               THI       RMD       GLA
> OBJ:          INFINITY          INFINITY
  STO:          INFINITY         58.094552
   2:          -101.60000       -101.600000             REFL
      CON:
      K   :    -1.000000   KC  :      100
      XDE:      0.000000   YDE:    27.223640    ZDE:     0.000000
      XDC:       100       YDC:      100        ZDC:      100
      ADE:      0.000000   BDE:     0.000000    CDE:     0.000000
      ADC:       100       BDC:      100        CDC:      100

   3:           101.60000         58.094552             REFL
      CON:
      K   :    -1.000000   KC  :      100

   4:           INFINITY          24.750000
      XDE:      0.000000   YDE:    27.223640    ZDE:     0.000000
      XDC:       100       YDC:      100        ZDC:      100
      ADE:      0.000000   BDE:     0.000000    CDE:     0.000000
      ADC:       100       BDC:      100        CDC:      100

   5:           INFINITY          24.750000
 IMG:           INFINITY           0.000000


SPECIFICATION DATA
   EPD         7.00000
   AFI        24.75000
   DIM              MM
   WL           725.00    647.10    568.20    488.00
   REF               2
   WTW               1         1         1         1
   XAN         0.00000       0.00000       2.70000
   YAN         0.00000       2.70000       2.70000
   VUX         0.00000       0.00000       0.00000
   VLX         0.00000       0.00000       0.00000
   VUY         0.00000       0.00000       0.00000
   VLY         0.00000       0.00000       0.00000

APERTURE DATA/EDGE DEFINITIONS
   CA
   CIR S2                    12.700000
   ADY S2                   -27.223600
   CIR S3                    12.700000
   ADY S3                    27.223600
```

```
No refractive materials defined in system

No solves defined in system

No pickups defined in system

        This is a decentered system.  If elements with power are
        decentered or tilted, the first order properties are probably
        inadequate in describing the system characteristics.

INFINITE CONJUGATES
   EFL        -24.7500
   BFL         24.7500
   FFL         14.5891
   FNO         -3.5357
   IMG DIS     24.7500
   OAL         39.3391

   PARAXIAL IMAGE
    HT          1.1672
   ANG          2.7000

   ENTRANCE PUPIL
    DIA         7.0000
    THI         0.0000

   EXIT PUPIL
    DIA        11.8753
    THI        66.7377
```

IMAGE EVALUATION TEST TARGET (QA-3)

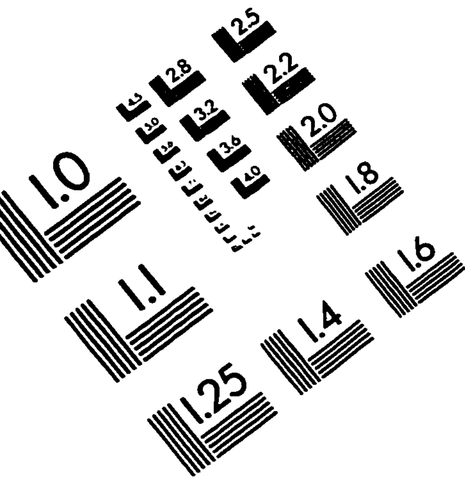
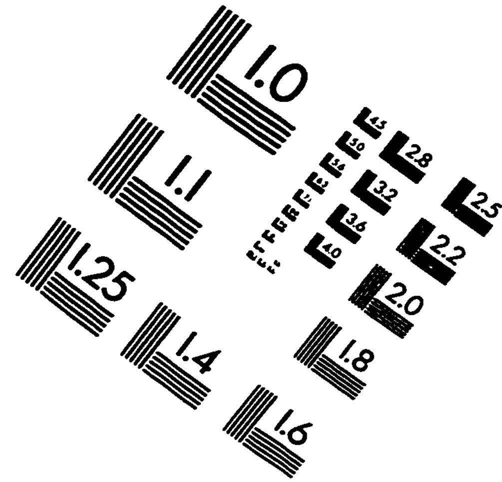
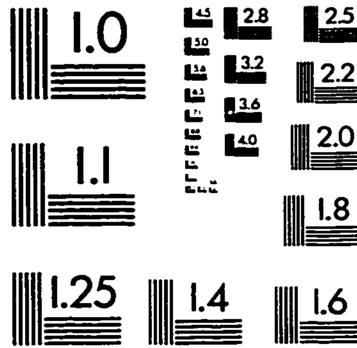
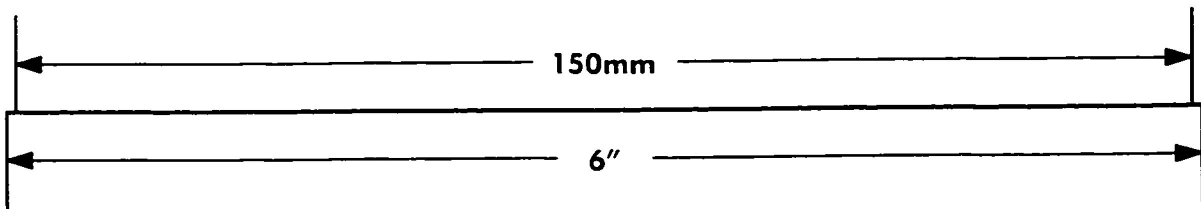

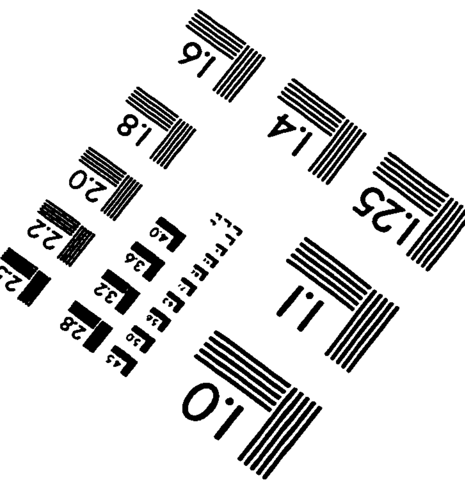

APPLIED IMAGE . Inc
1653 East Main Street
Rochester, NY 14609 USA
Phone: 716/482-0300
Fax: 716/288-5989

© 1993, Applied Image, Inc., All Rights Reserved